Frictional properties of faults: from observation on the Longitudinal Valley Fault, Taiwan, to dynamic simulations

Thesis by
Marion Y. Thomas

In Partial Fulfillment of the Requirements for the degree
of
Doctor of Philosophy

CALIFORNIA INSTITUTE OF TECHNOLOGY
Pasadena, California
2014
(Defended July 31st 2013)

Acknowledgements

This is the last section I am writing for this PhD manuscript, and I cannot find a better way to end this long journey, since this work is first and foremost the result of collaborations, meetings and support I got along the way, since I discovered how awesome it would be to become a geologist.

My first experience with the academic world and most of all, geology, was thanks to Dr Philippe Davy, who welcomed me in his lab when I was 14 years old, for a quick internship of one week. I discovered then what "plate tectonics", "field geology", and "analogical and numerical experiments" meant, and went back home, really excited, to told my mum that one day I would become a geologist... Well I guess this day finally happened! Thanks a lot, Philippe.

I find myself lucky to do what I love and to wake up every day, happy and excited about the day to come. This has been possible firstly thanks to the unconditional support and love from my family and my boyfriend. We went through difficult times together, right before I came to California, but despite the distance we stayed close and I am just wordless to find the appropriate way to thank them.

A PhD is undoubtedly a big, rich, challenging and unexpected part of someone's life. The journey has not always been easy but, I found my advisor Jean-Philippe Avouac unfailingly willing to provide support, contagious enthusiasm, inspiration, and skillful guidance. I cannot recall even one time when he did not welcome me with a smile when I knocked (and I did quite often!) at the door of his office. He encouraged me to discover new fields, enlarge my knowledge to better embrace Earth Sciences. A genuine thank to you Jean-Philippe, I did learn a lot!

I would like also to express my sincere gratitude to Nadia Lapusta who has been a very supportive advisor during all those years at Caltech. She has been patient and always tried to find (and succeed) the right words to encourage me when I was lacking confidence. Thanks to her I discovered a new field in Earth Science that I really enjoy and I decided to keep working on it during my postdoc.

As I mentioned at the beginning, this work is the result of many collaborations I feel the privileged to have established during my PhD: a grateful thank to Jian-Cheng Lee who made me discover the geology of Taiwan and fall in love with its "cuisine"; to Jean-Pierre Gratier who found some time in his busy schedule to go with me and Jean-Philippe to the field and who helped doing all the analysis presented in the third chapter; to all the people I met in CEA with a special thanks to Philippe Loreaux, Guillaume Quin, Laurent Bollinger and Béatrice Puysségur for their precious assistance during the two months I spend there; to Mark Simons from whom I have learned much and got useful advices; and finally to Romain Jolivet, Thomas Ader, François Ayoub, Nadaya Cubas and Piyush Agram for all the help I got and the scientific discussions, but also for their precious friendship.

I would like to thank the members of my thesis committee, Professors Tom Heaton, Paul Asimow, Brian Wernicke, Jean-Philippe Avouac, Nadia Lapusta and Mark Simons for supporting me, *following my progress, and reviewing this thesis.*

My thanks also go to the current and former members of the TO with a special thought to Heather Steele and Lisa Christiansen. They all made the third floor of North Mudd an awesome place to work in: I always found someone to help, provide helpful advices or just be there to chat about science or anything else.

Throughout this five years far from my family, the friends I have met here are what made me feel home and I am going to miss you a LOT. It is going to be hard to appropriately acknowledge all of them but I like to give a special thanks to Elsa and Romain for their most supportive attitude during this two months of writing the manuscript! François, I cannot believe I am saying that but I am going to miss you teasing me... Catherine, James, that was wonderful to spent time with you guys: no matter how tough is our past history, British and French go along pretty well! Laurent was at Caltech during my first years as a gradstudent: thanks for helping me going through the hard time of the beginning. "Grand" Thomas, Stephanie you were the sister and the brother I was missing: it was so much fun to share a home with you. Manue, Nadaya thanks for all the time we spend together which make my life more "real" and not all about science! Last but not least, Thomas, my PhD "twin", I am really glad we made this long journey together, you helped me to become more confident.

J.M.G. Le Clézio
(L'Inconnu sur la terre)

"Vivre, connatre la vie, c'est le plus léger, le plus subtil des apprentissages. Rien à voir avec le savoir."

"To live, to experience life, it is the lightest, the most subtle way of learning. Nothing to do with knowledge"

Abstract

Faults can slip either aseismically or through episodic seismic ruptures, but we still do not understand the factors which determine the partitioning between these two modes of slip. This challenge can now be addressed thanks to the dense set of geodetic and seismological networks that have been deployed in various areas with active tectonics. The data from such networks, as well as modern remote sensing techniques, indeed allow documenting of the spatial and temporal variability of slip mode and give some insight. This is the approach taken in this study, which is focused on the Longitudinal Valley Fault (LVF) in Eastern Taiwan. This fault is particularly appropriate since the very fast slip rate (about 5 cm/yr) is accommodated by both seismic and aseismic slip. Deformation of anthropogenic features shows that aseismic creep accounts for a significant fraction of fault slip near the surface, but this fault also released energy seismically, since it has produced five $M_w > 6.8$ earthquakes in 1951 and 2003. Moreover, owing to the thrust component of slip, the fault zone is exhumed which allows investigation of deformation mechanisms. In order to put constraint on the factors that control the mode of slip, we apply a multidisciplinary approach that combines modeling of geodetic observations, structural analysis and numerical simulation of the "seismic cycle". Analyzing a dense set of geodetic and seismological data across the Longitudinal Valley, including campaign-mode GPS, continuous GPS (cGPS), leveling, accelerometric, and InSAR data, we document the partitioning between seismic and aseismic slip on the fault. For the time period 1992 to 2011, we found that about 80-90% of slip on the LVF in the 0-26 km seismogenic depth range is actually aseismic. The clay-rich Lichi Mélange is identified as the key factor promoting creep at shallow depth. Microstructural investigations show that deformation within the fault zone must have resulted from a combination of frictional sliding at grain boundaries, cataclasis and pressure solution creep. Numerical modeling of earthquake sequences have been performed to investigate the possibility of reproducing the results from the kinematic inversion of geodetic and seismological data on the LVF. We first investigate the different modeling strategy that was developed to explore the role and relative importance of different factors on the manner in which slip accumulates on faults. We compare the results of quasi dynamic simulations and fully dynamic ones, and we conclude that ignoring the transient wave-mediated stress transfers would be inappropriate. We therefore carry on fully dynamic simulations and succeed in qualitatively reproducing the wide range of observations

for the southern segment of the LVF. We conclude that the spatio-temporal evolution of fault slip on the Longitudinal Valley Fault over 1997-2011 is consistent to first order with prediction from a simple model in which a velocity-weakening patch is embedded in a velocity-strengthening area.

Contents

List of Figures

List of Tables

Introduction

This thesis presents an investigation of fault mechanics based on the detailed study of a prime example of an active fault, the Longitudinal Valley fault (LVF) in Taiwan, combined with dynamic modeling of the seismic cycle.

The Longitudinal Valley fault was chosen as the focus of this work because of its exceptionally fast slip rate (of about 4.5 cm/yr), its ability to produce aseismic as well as seismic slip (with 5 $M_w > 6.5$ events since 1950, including the M_w 6.8 Chengkung earthquake of 2003) and the wealth of geodetic and remote-sensing data available. These geodetic data record the deformation during the interseismic, coseismic and postseismic periods, providing a unique opportunity to image the time evolution of the fault slip and to compare with dynamic models of the seismic cycle. In addition, the fault has a thrust component, which has resulted in exhumation of the fault zone, making fault-gouge accessible for various microstructural investigations of rock deformation mechanisms.

In the first chapter, we provide some background information about the tectonic setting of the LVF based on a review of the literature. Chapter 2 presents the analysis of the remote-sensing (including InSAR results provided by our collaborator Johann Champenois from CNES, France) and GPS data (provided by the Central Weather Bureau). We also use data from the Taiwan accelerometric network to constrain the source model of the Chengkung earthquake (provided by Yih-Min Wu from National Taiwan University). We derive a kinematic model describing the time evolution of the fault slip over the last 20 years. Chapter 3 presents a detailed analysis of the geological setting and fault rocks from the LVF. This chapter is based on my own field work, and various analytical techniques applied to the samples collected in the field or from drill cores. Access to the drill cores was enabled by our partner Jian-Cheng Lee from the Institute of Earth Sciences in Taipei (Academia Sinica). Jean-Pierre Gratier (ISTerre Grenoble) provided guidance on some aspects of the study. The major objective of this chapter is to elucidate the deformation mechanisms and conditions favoring aseismic creep on the LVF. The following chapter discusses the possibility of simulating the seismic cycle on faults, and more particularly on the LVF, using numerical simulations. Recent studies have shown that fully-dynamic models based on the rate-and-state formalism can successfully reproduce many aspects of the seismic cycle and the model parameters can be adjusted to reproduce quantitatively the observations (e.g., *Barbot et al.*, 2012).

However, this approach is extremely costly computationally. We therefore explore in Chapter 4 the possibility of resorting to the least costly quasi-dynamic approach. Chapter 5 presents our attempt at producing a first order model of the seismic cycle on the LVF. The point of this chapter is to identify the key features which are used to guide the design of the fault model (most importantly the assumed spatial distribution of fault rheology) and discuss the merit and limitations of the proposed model.

The manuscript includes three appendices in addition. The first one provides a brief summary of the few documented examples of creeping faults in continental settings. Several fault in the San Andreas Fault system (California) have long been recognized to creep aseismically. Aseismic creep has been observed to be either continuous or episodic, in the case of the San Andreas Fault system. Similar observations have been made on few other examples, but the mechanism governing fault creep is still poorly understood. The second appendices is a short review of rock deformation mechanisms. The last one discusses in more detail the origin of the key formation that leads to aseismic creep of the LVF, the Lichi Mélange.

Chapters 2, 3 and 4 are meant to be submitted for publication in peer-reviewed journals. Chapter 5 will be augmented with additional modeling results before submission to a journal.

Chapter 1

Geological and plate tectonic setting of the Longitudinal Valley Fault

1.1 Tectonic setting of Taiwan

The Longitudinal Valley fault runs parallel to the East coast of Taiwan and is one of the major active faults accommodating the present day 9 cm/yr convergence rate between the Eurasian and the Philippine Sea Plate (Figure 1.1a). South of Taiwan this convergence is absorbed along the Manila trench by the eastward subduction of the oceanic crust of the South China Sea beneath the Philippine Sea Plate, leading to the creation of the Luzon volcanic arc (zone I in Figure 1.1b and section (a) in Figure 1.2).

Figure 1.1: Bathymetry (See next Page). Shaded relief map showing regional tectonic setting of Taiwan. (a) Off shore bathymetry. Location of the three E-W seismic profiles shown in Figure 1.3 (red lines). The black line A-A represents the topographic profiles shown in (c) and red triangles are the currently active volcanoes of the Luzon arc. (b)Regional Tectonic of Taiwan. The South China Sea crust subducts beneath the Philippine Sea Plate along the Manila Trench, leading to the formation of the Luzon arc. The Henchung Peninsula represents the exhumed accretionary prism. North of 21°'N, the North Luzon arc collided collied obliquely with yhe Eurasian continent. The collision resulted in deformation of the western part of the North Luzon Trough (fore-arc basin), creating the Huatung Ridge with backthrusting eastward. The Luzon arc and its forearc basin are ultimately accreting on eastern Taiwan, forming the Coastal Range. I-intraoceanic collision zone. II-intial arc-continent collision. III-advanced arc-continent collision. (c) Topographic and seismic profiles across Taiwan along line A-A ligne from *Shyu et al.* (2006).

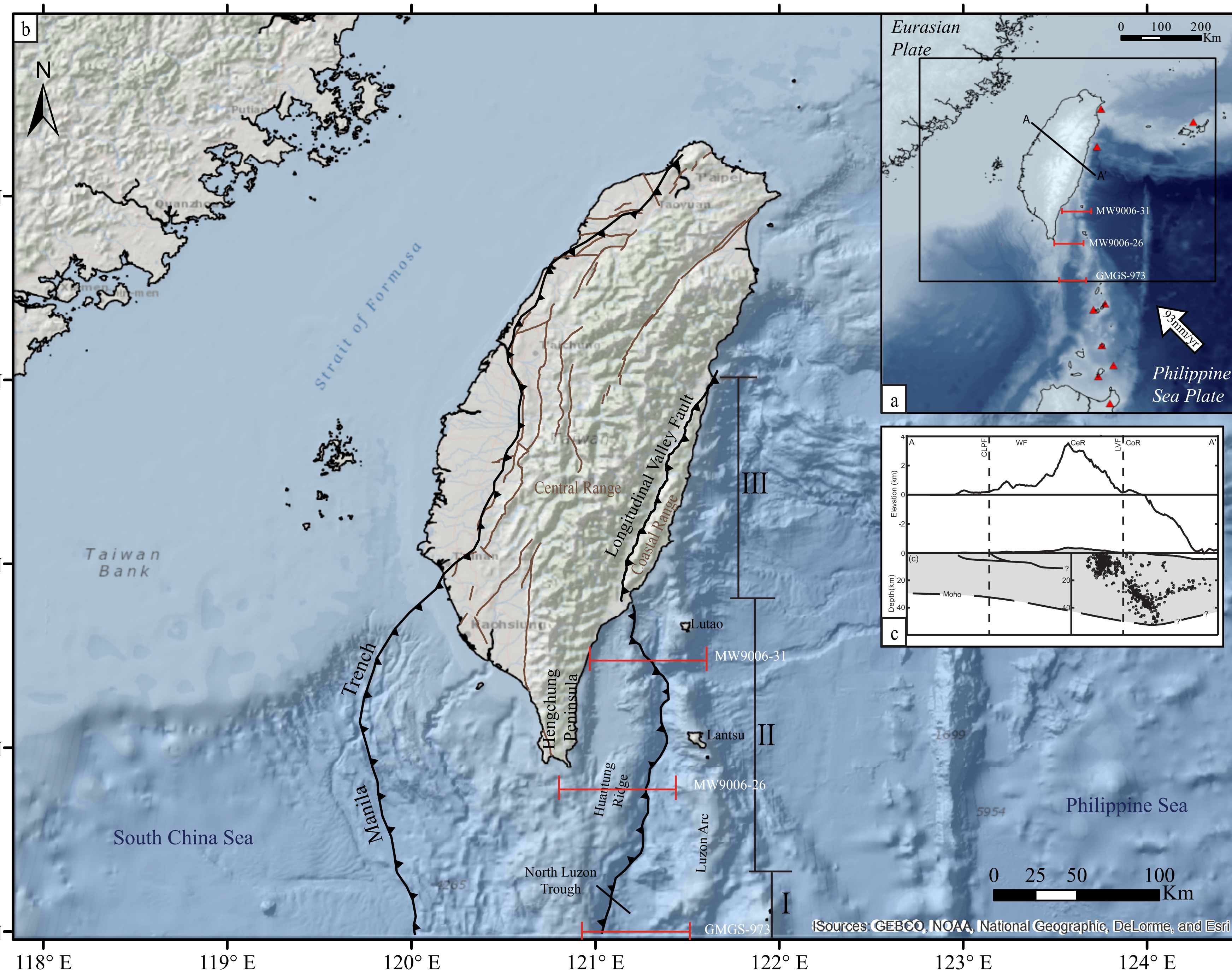
b
N
Strait of Formosa
Taiwan Bank
South China Sea
Philippine Sea
Manila Trench
Central Range
Longitudinal Valley Fault
Coastal Range
Hengchung Peninsula
Huantung Ridge
North Luzon Trough
Luzon Arc
Lutao
Lantsu
MW9006-31
MW9006-26
GMGS-973
I
II
III
0 25 50 100 Km
Sources: GEBCO, NOAA, National Geographic, DeLorme, and Esri
25° N
24° N
23° N
22° N
21° N
118° E
119° E
120° E
121° E
122° E
123° E
124° E
a
Eurasian Plate
Philippine Sea Plate
93mm/yr
0 100 200 Km
A
A'
c
CLPF
WF
CeR
LVF
CoR
Elevation (km)
Depth(km)
Moho

In Taiwan, the continental shelf of South China has now entered the subduction, resulting in a collisional orogeny, at the origin of the formation of the Taiwan Island (e.g., *Barrier and Angelier*, 1986; *Teng*, 1990; *Chang et al.*, 2001; *Malavieille et al.*, 2002; *Huang et al.*, 2006a; *Simoes et al.*, 2007b). The Henchung Peninsula, at the southern tip of Taiwan, represents the exhumed accretionary prism. North of 21°'N, the North Luzon arc collided obliquely with Eurasian continent. The collision has resulted in deformation of the western part of the North Luzon Trough (forearc basin), creating the Huatung Ridge with backthrusting eastward (see seismic profiles in Figure 1.3 and section (b) in Figure 1.2). The Luzon arc and the forearc basin have ultimately been accreted onto eastern Taiwan over the last 5 Ma (*Chang et al.*, 2001; *Huang et al.*, 2006a), forming the Coastal Range (Figure 1.4). As the collision developed, the deformation of the continental passive margin of the South China Sea led to the exhumation of its metamorphic basement, forming the core of the Central Range (section (c) in Figure 1.2). The Longitudinal Valley Fault marks the western border of the Coastal Range and is generally interpreted to form the suture zone between the continental margin of South China and the Luzon arc.

The next section provide some background information on the geography and stratigraphy of the Coastal Range.

1.2 Coastal Range

1.2.1 Physiography: location, relief and drainage system

The Coastal Range is a narrow trending NNE between Hualien (north) and Taitung (south) along the eastern coast of Taiwan. The range, quite straight and uniform in width, is roughly 150 km long and the average width is about 15 km. The Coastal Range faces the Pacific Ocean to the east and is separated from the Central Range to the west by the narrow (about 4 km) Longitudinal Valley (Figure 1.5).

The Coastal Range, extending from 22°46'N to 23°56'N in latitude and 121°10'E (southern extremity) to 121°37'(northern extremity) in longitude, can be subdivided into three main geographic domains (*Hsu*, 1956). The northern part, north of the Hsiukuluan river, is the lowest in elevation. The highest peak, Paliwanshan, reaches only 922 m in altitude. The central part, between the Hsiukuluan river and Chengkung city, encompasses the highest peaks of the Coastal Range, among which Hsinkangshan (1682 m) reaches the highest elevation in the whole range. The southern part extends from Chengkung to Taitung city. In this area, all the peaks but Tuluanshan (1190 m) are below 1000 m in elevation (*Hsu*, 1956) (Figure 1.5).

There are two main drainage systems in the area: the Longitudinal Valley system and the coastal system. The Longitudinal Valley system consists of several subsequent rivers with tributaries mainly from the Central Range. The three main rivers of this system are the Hualien River, the Peinan

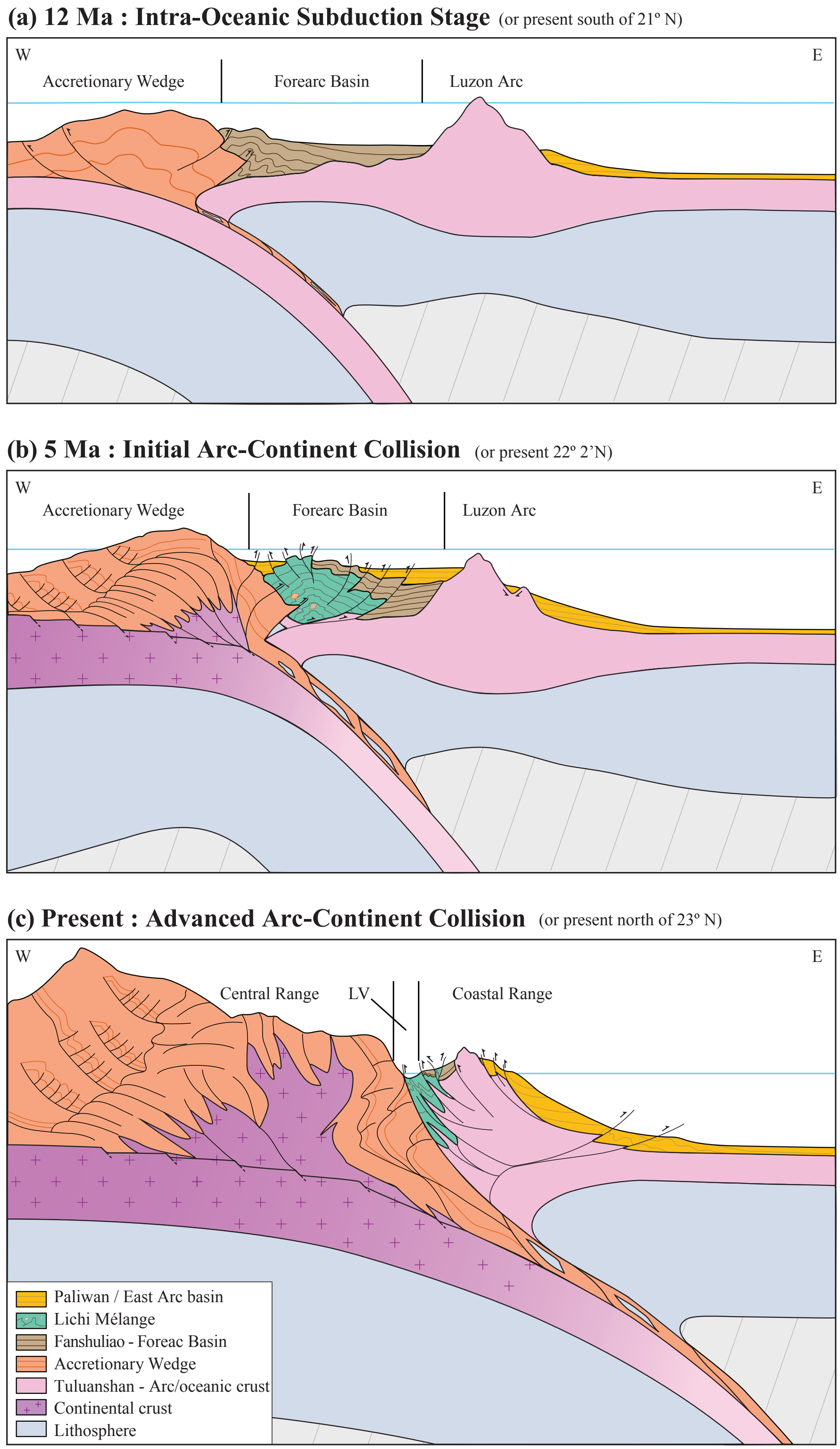

Figure 1.2: Tectonic sketching on the formation of the Coastal Range. (a) Tectonic setting at 12 Ma (or present south of 21°N): intra-oceanic subduction stage. (b) Tectonic setting at 5 Ma (or present 22°2'N): initial arc-continent collision. (c) Current tectonic setting (or present north of 23°N): advanced arc-continent collision. See chapter 3 for the stratigraphic and structural observation used to substantiate these tectonic scenari. The sections (a), (b) and (c) correspond, respectively, to zones I, II and III in Figure 1.1.

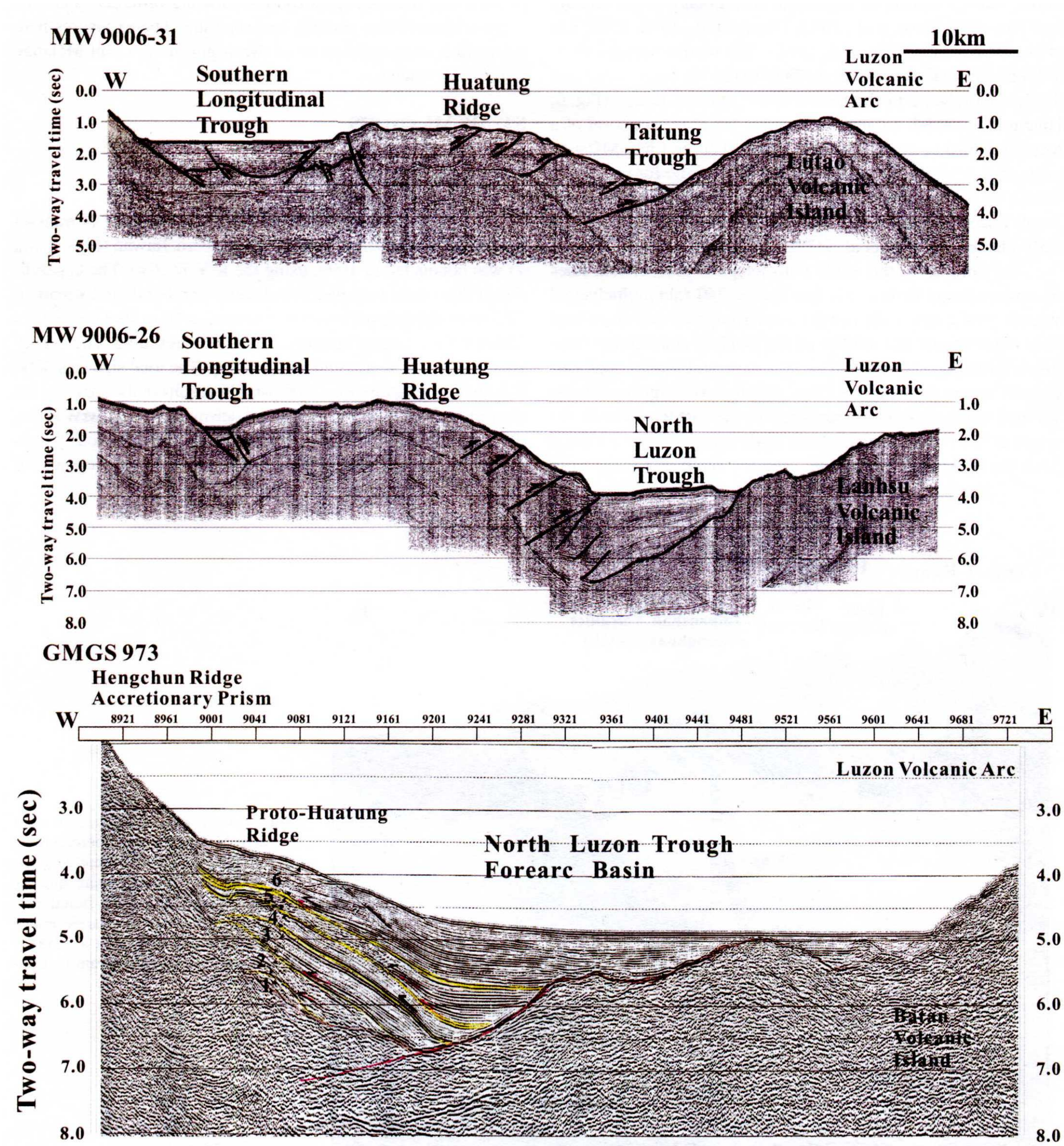

Figure 1.3: Three seismic profiles, from north to south (see Figure 1.1 for location) showing progressive formation of the Huatung Ridge and closure of the North Luzon forearc basin. Line GNGS973 further revealed syndeformational sedimentation in the North Luzon Trough, with six sequences of strata separated by five unconformities. Profiles from *Huang et al.* (2008)

River and the Hsiukuluan River (Figure 1.5). The Hualien River flows north along the valley until it reaches the Pacific Ocean in Hualien while the Peinan flows south to Taitung. The Hsiukuluan River, which drains the middle part of the valley low into the Pacific Ocean at Takangkou. The rivers on the eastern slopes of the Coastal Range form the Coastal Range drainage system and flow directly toward the Pacific Ocean.

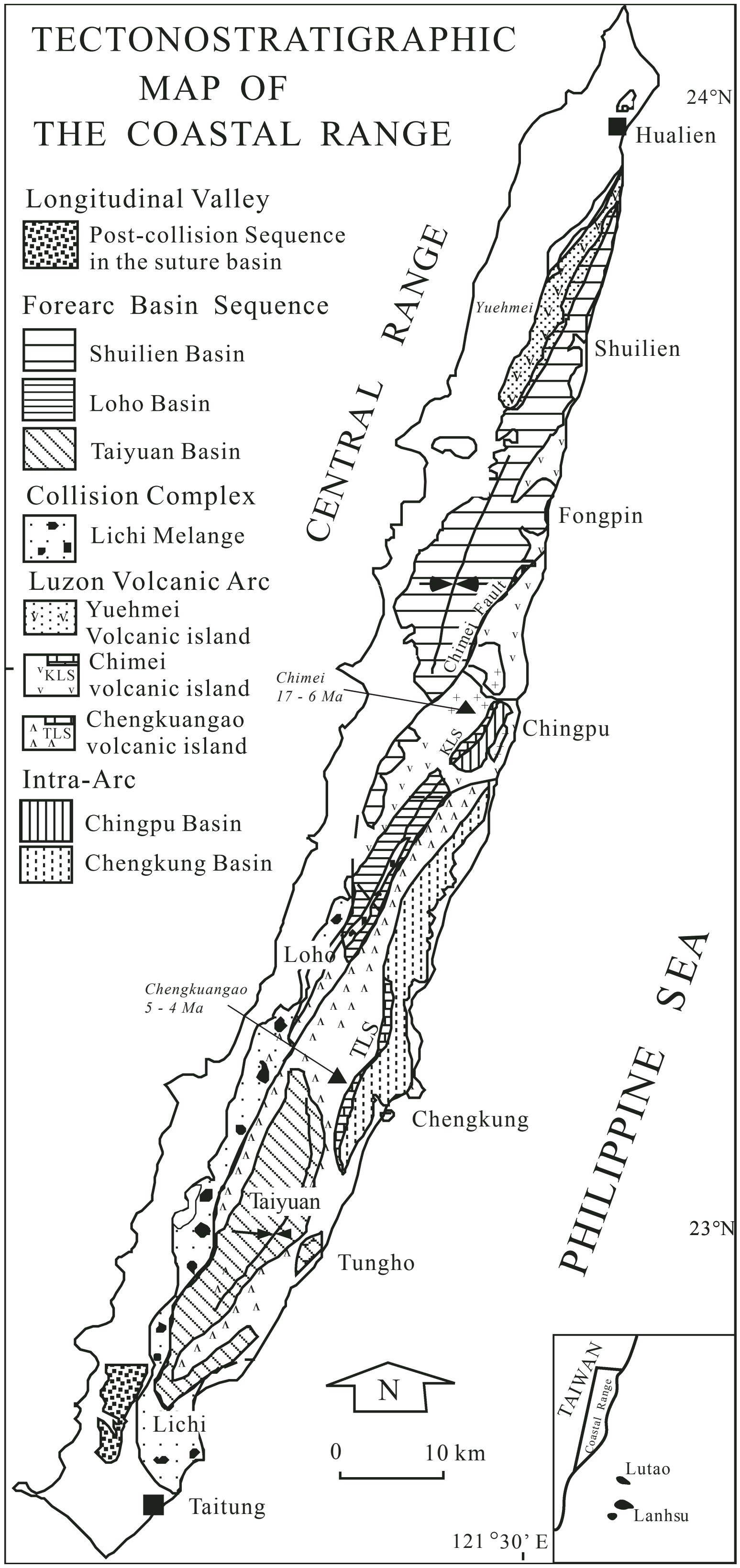

Figure 1.4: Tectonostratigraphic map of the Coastal Range, showing three accreted volcanic islands, three remnant forearc basins, two intra-arc basins, and the Lichi Mélange (modified from *Huang et al.* (2006a)). Age data on the volcanic sequences compiled from *Yang et al.* (1988), *Chen et al.* (1990) and *Lo et al.* (1994).

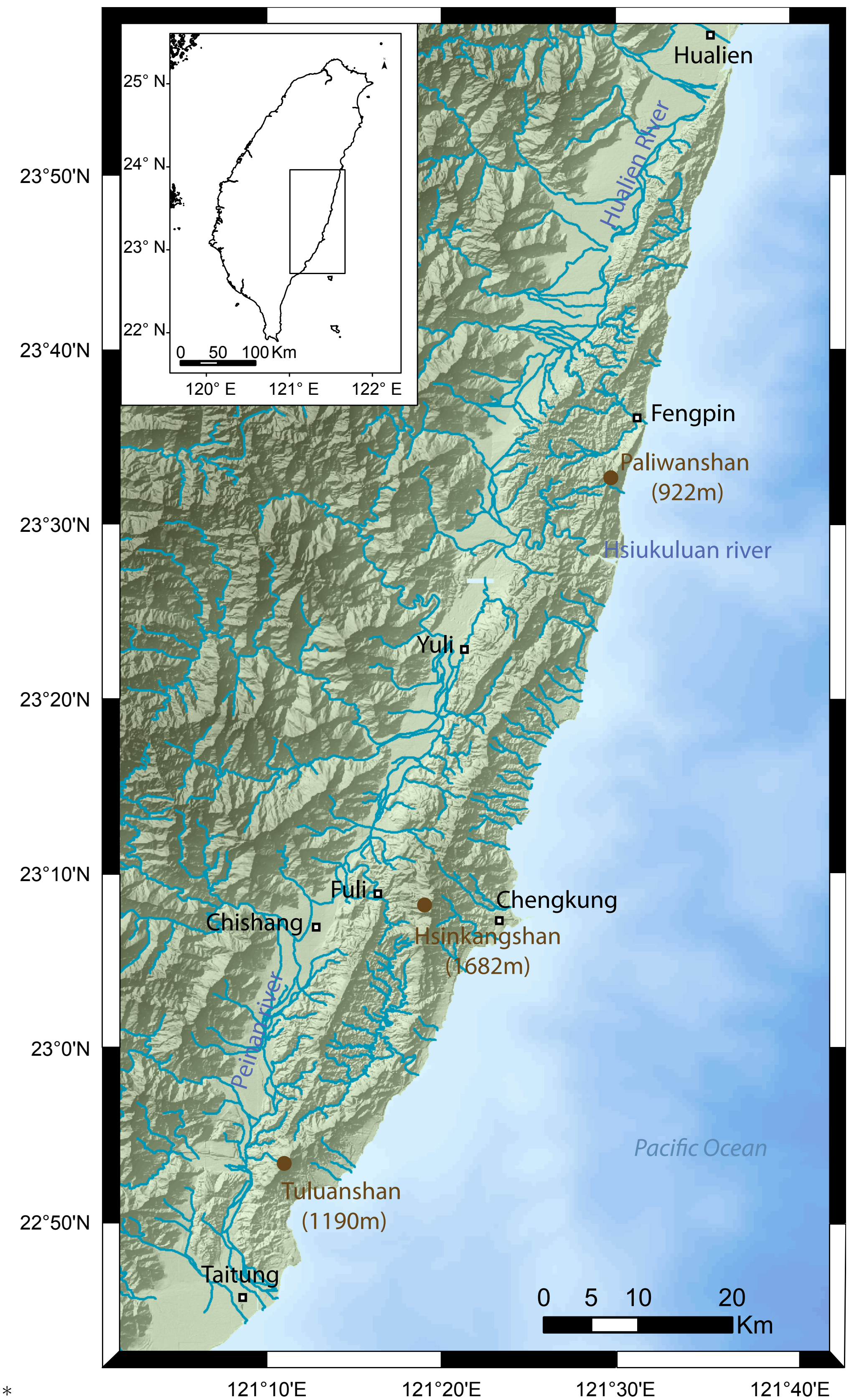

*

Figure 1.5: Geographic map of the Longitudinal Valley in Taiwan. Main towns are located by black squares, and the highest peaks in the Coastal Range are indicated on the map through brown circles. Blues lines correspond to the drainage system.

1.2.2 Stratigraphy of the Coastal Range

Stratigraphic and geochemical studies have shown that the Costal Range is composed of formations from three accreted Miocene-Pliocene volcanic islands, three remnants of Plio-Plesitocene forearc basins, two intra-arc basins, and the Pliocene collision Lichi Mélange (*Huang et al.*, 2006a, 2008) (Figure 1.4). Five rock units can be distinguished in the Coastal Range: the Tuluanshan arc formation, the Fanshuliao volcanoclastic deposits and the Lichi Mélange can be grouped as the pre-collision island-arc lithofacies, whereas the Paliwan lithic flysch and the Peinanshan and Wuho conglomerates (molasse) are the the latter two syn/post-collision lithofacies (Figure 1.6).

The accreted Miocene-Pliocene volcanic islands (from north to south: Yuehmei, Chimei and Cheng-kuangao) are composed of andesite, agglomerates and tuff of the Tuluanshan formation, whereas the remnant forearc basins (Shuilien, Loho and Taiyuan) and the intra-arc basins (Chingpu and Chengkung basin) are filled with turbidites derived from the accretionary prism and the volcanic islands (*Huang et al.*, 1992, 1995, 2008) (Figures 1.4 and 1.6). The Takangkou formation, which represents with the Lichi Mélange the sedimentary facies of the Coastal Range, is usually subdivided in two stratigraphic layers, the Fanshuliao and the Paliwan formations, reflecting the variation of sedimentary sources with time.

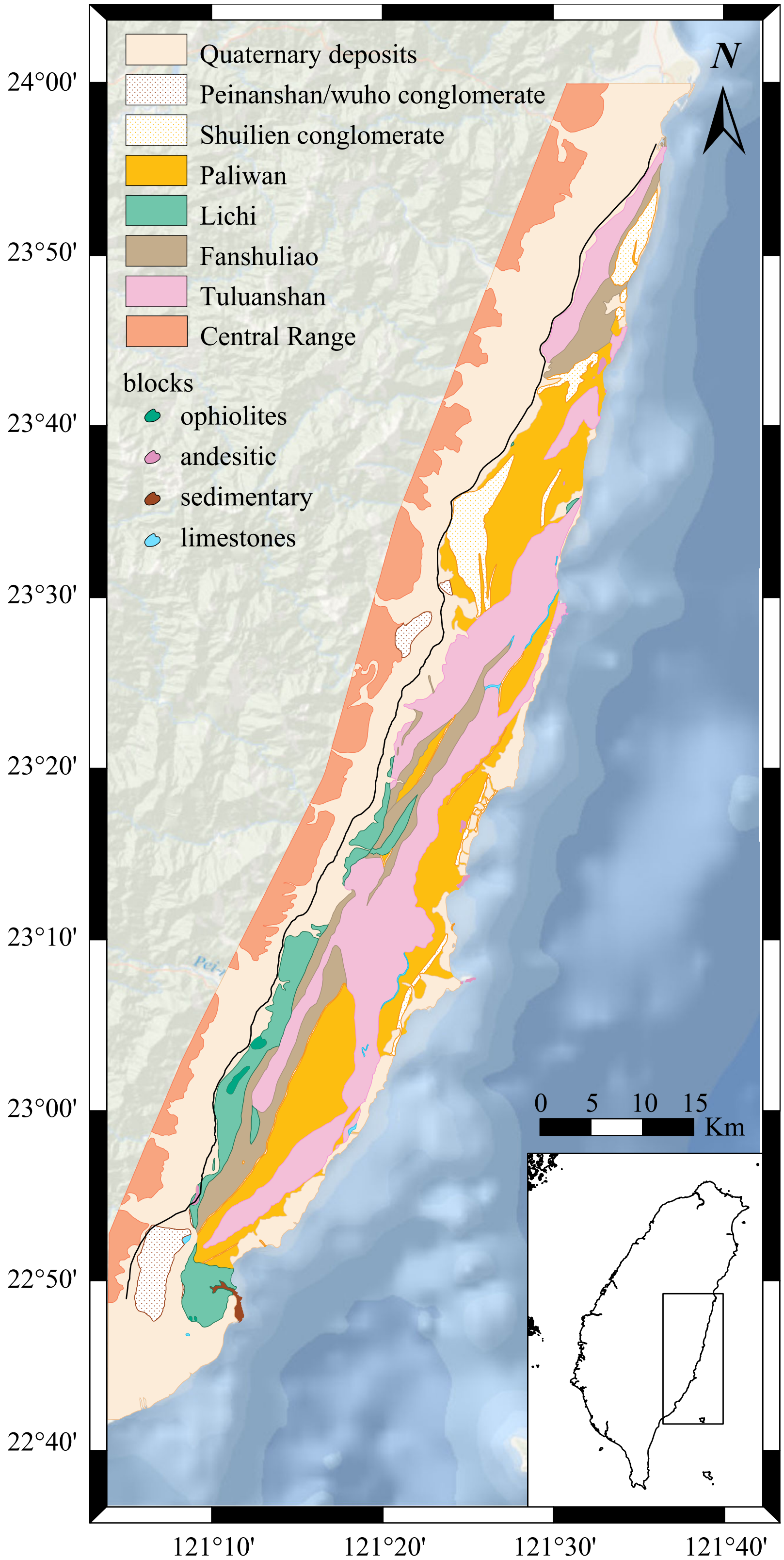

Figure 1.6: Geological map of Eastern Taiwan, modified from *Wang and Chen* (1993), based on field work detailed in chapter 3. Continuous black line shows trace of Longitudinal Valley Fault.

Chapter 2

Spatio-temporal evolution of seismic and aseismic slip on the Longitudinal Valley Fault, Taiwan

Marion Y. Thomas, Jean-Philippe Avouac, Johann Champenois and Jian-Cheng Lee

Abstract

The Longitudinal Valley Fault (LVF) in Eastern Taiwan is a high slip rate fault (about 5cm/yr) which exhibits both seismic and aseismic slip. Deformation of anthropogenic features shows that aseismic creep accounts for a significant fraction of fault slip near the surface whereas a fraction of the slip is also seismic since this fault has produced large earthquakes with five $M_w > 6.8$ events in 1951 and 2003. In this study, we analyze a dense set of geodetic and seismological data around the LVF including campaign-mode Global Positionnig System(GPS) measurements, times-series of daily solutions for continuous GPS stations (cGPS), leveling data and accelerometric records of the 2003 Chenkung earthquake. To enhance the spatial resolution provided by these data, we complement them with Interferometric Synthetic Aperture Radar (InSAR) measurements produced from a series of Advanced Land Observing Satellite (ALOS) images processed using a persistent scatterer (PS) technique. The combined dataset covers the entire LVF and spans the period from 1992 to 2010. We invert this data to infer the temporal evolution of fault slip at depth using the Principal Component Analysis-based Inversion Method (PCAIM). This technique allows the joint inversion of diverse data, taking the advantage of the spatial resolution given by the InSAR measurements and the temporal resolution afforded by the cGPS data. We find that (1) seismic slip during the 2003 Chengkung earthquake occurred on a fault patch which had remained partially locked in the interseismic period; (2) the seismic rupture propagated partially into a zone of shallow aseismic interseismic creep but failed to reach the surface; (3) that aseismic afterslip occurred around the area that ruptured seismically. We find consistency between geodetic and seismological constraints

on the partitioning between seismic and aseismic creep. About 80-90% of slip on the LVF in the 0-26 km seismogenic depth range is actually aseismic. We infer that the clay-rich Lichi Mélange is the key factor promoting aseismic creep at shallow depth.

2.1 Introduction

Fault slip can be either aseismic or seismic (i.e., radiating potentially damaging seismic waves). Geodetic and remote sensing techniques, combined with seismology, provide now the tools to quantify the partitioning between these two modes of slip and to investigate the various factors that control their spatial and temporal variations. A number of subduction zones studies have demonstrated, using these techniques, spatio-temporal variations of the mode of slip in the 0-50 km seismogenic depth range: fault slip might be dominantly aseismic at places, as a result of steady creep in the interseismic period or transient afterslip following large earthquakes, and dominantly seismic at others (*Heki et al.*, 1997; *Freymueller et al.*, 2000; *Wallace et al.*, 2004; *Cross and Freymueller*, 2007; *Fournier and Freymueller*, 2007; *Chlieh et al.*, 2008; *Perfettini et al.*, 2010; *Loveless and Meade*, 2011; *Miyazaki et al.*, 2011; *Evans et al.*, 2012). Similarly, strong spatial variations of slip mode have been documented on some continental faults (*Burgmann et al.*, 2000; *Titus et al.*, 2006; *Murray et al.*, 2001; *Jolivet et al.*, 2012; *Kaneko et al.*, 2013). However, how the partitioning between seismic and aseismic slip varies in time and space, and what are the factors governing this behavior (such as temperature, lithology, pore fluids), remain poorly understood questions. This is an important issue in seismotectonics since the seismic potential of any fault depends primarily on the partitioning between seismic and aseismic slip.

The objective of this study is to investigate this issue based on the modeling of the spatio-temporal evolution of slip on the Longitudinal Valley Fault (Figure 2.1). This fault runs parallel to the East coast of Taiwan and marks the suture zone between the continental margin of South China and the Luzon arc on the Philippine Sea Plate (*Lee et al.*, 2001; *Chang et al.*, 2009) (Figure 2.1a and 2.2). We chose to focus on this particular example as this fault is known to creep near the surface (*Angelier et al.*, 1997; *Lee et al.*, 1998, 2000, 2001, 2005; *Chang et al.*, 2009; *Champenois et al.*, 2012) but has also produced $M_w > 6.8$ earthquakes including 4 events in 1951 (*Shyu et al.*, 2007), and the Mw 6.8 Chengkung earthquake of 2003 (*Wu et al.*, 2006a; *Hsu et al.*, 2009a; *Mozziconacci et al.*, 2009). In addition the surface strain is well documented from campaign mode GPS (*Yu and Kuo*, 2001), continuously recording GPS stations (cGPS) of the Taiwan Earthquake center (http://gps.earth.sinica.edu.tw/), leveling data (*Ching et al.*, 2011; *Chen et al.*, 2012), creepmeters (*Lee et al.*, 2001, 2005; *Chang et al.*, 2009) and InSAR (*Hsu and Burgmann*, 2006; *Peyret et al.*, 2011; *Champenois et al.*, 2012). Finally, the slip rate on the Longitudinal Valley Fault is extremely fast, absorbing nearly half of the 9 cm/yr horizontal convergence rate between the Philippine Sea

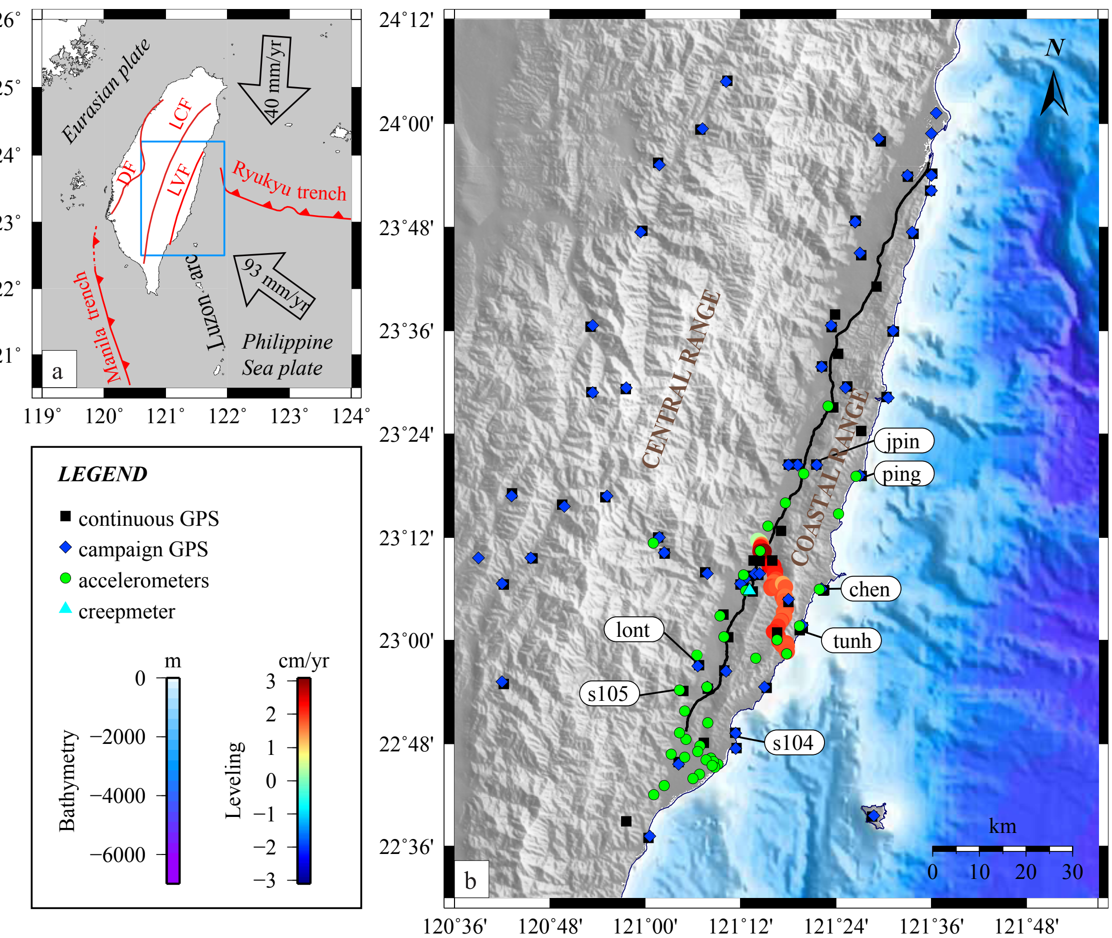

Figure 2.1: (a) Regional tectonic setting of the Longitudinal Valley Fault. Blue rectangle corresponds to the location of Figure 2.1b.DF-deformation front; LCF-Lishan-Chaochou Fault; LVF-Longitudinal Valley Fault.(b) Location of accelerometric, geodetic and leveling data used in this study. Black squared, blue diamonds, green circle and cyan triangle stand for the 67 permanent GPS stations(http://gps.earth.sinica.edu.tw/), the 38 accelerometers (*Wu et al.*, 2006a), the 45 campaign GPS sites (*Yu and Kuo*, 2001) and the creepmeter (*Chang et al.*, 2009; *Lee et al.*, 2005) respectively. We labeled the stations corresponding to the times series shown in Figure 2.4. Colored-scale circles show location of leveling measurements from 9/1/2007 to 31/20/2010 (*Chen et al.*, 2012).

Plate and South China (*Lee and Angelier*, 1993.; *Yu et al.*, 1997; *Hsu et al.*, 2003; *Shyu et al.*, 2006; *Huang et al.*, 2010)(Figure 2.1).

Hereafter, we first describe the dataset used in the study. It consists of a compilation of geodetic and remote-sensing data enhanced with new InSAR measurements. This dataset covers the period from 1992 to 2011. We next present our modeling results starting with the secular interseismic creep rates. We then discuss the coseismic slip distribution related to the Chengkung event, and finally we analyze the spatio-temporal variations of creep rates observed over the study period, in particular due to postseismic relaxation following the 2003 earthquake.

2.2 Data used in this study

In order to achieve the best possible resolution in our inversions of spatio-temporal variations of fault slip, we assembled all the data available on geodetic surface strain (Figure 2.1 and 2.2). We used in particular the data from the continuously recording GPS stations which were installed by the Central Weather Bureau and the Institute of Earth Sciences (http://gps.earth.sinica.edu.tw/), Academia Sinica of Taipei. We also compiled data from the literature. They include campaign GPS data (*Yu and Kuo*, 2001), accelerometric data (*Wu et al.*, 2006a), times-series of creepmeter measurements (*Lee et al.*, 2000, 2001, 2003, 2005; *Chang et al.*, 2009), leveling data (*Chen et al.*, 2012; *Ching et al.*, 2011) and the mean ground velocities measured from the Persistent Scatterer technique (PS) applied to PALSAR ALOS synthetic aperture radar (SAR) images covering the 2007-2010 period (*Champenois et al.*, 2012). These data cover the southern half of the Longitudinal Valley. We extended the existing SAR dataset with new measurements so as to cover the northern portion of the Longitudinal Valley (*Champenois*, 2011). The following sub-sections present these various data in more details.

There is also a leveling data set covering the whole island of Taiwan over the time period of 2000-2008 (*Ching et al.*, 2011). We use this dataset to check the consistency with the cumulative vertical displacements predicted by our model (see supplement Figure S11).

2.2.1 PS mean velocities from the ALOS PALSAR dataset

We used L-band PALSAR images (23.6 cm) provided by the ALOS satellite from the JAPAN Aerospace Exploration Agency (JAXA) to enhance the spatial resolution afforded by the GPS and leveling data and we supplement the results of *Champenois et al.* (2012) obtained on the southern portion of the Longitudinal Valley to achieve a full coverage of the study area (*Champenois*, 2011). We processed a 3 year long time-series, from 01/12/2007 to 09/07/2010, using the Persistent Scatterer (PS) approach (*Ferretti et al.*, 2001; *Hooper et al.*, 2007). The dataset consists of twelve SAR images which were acquired along the ascending path 444 every 3 months on average, except for a

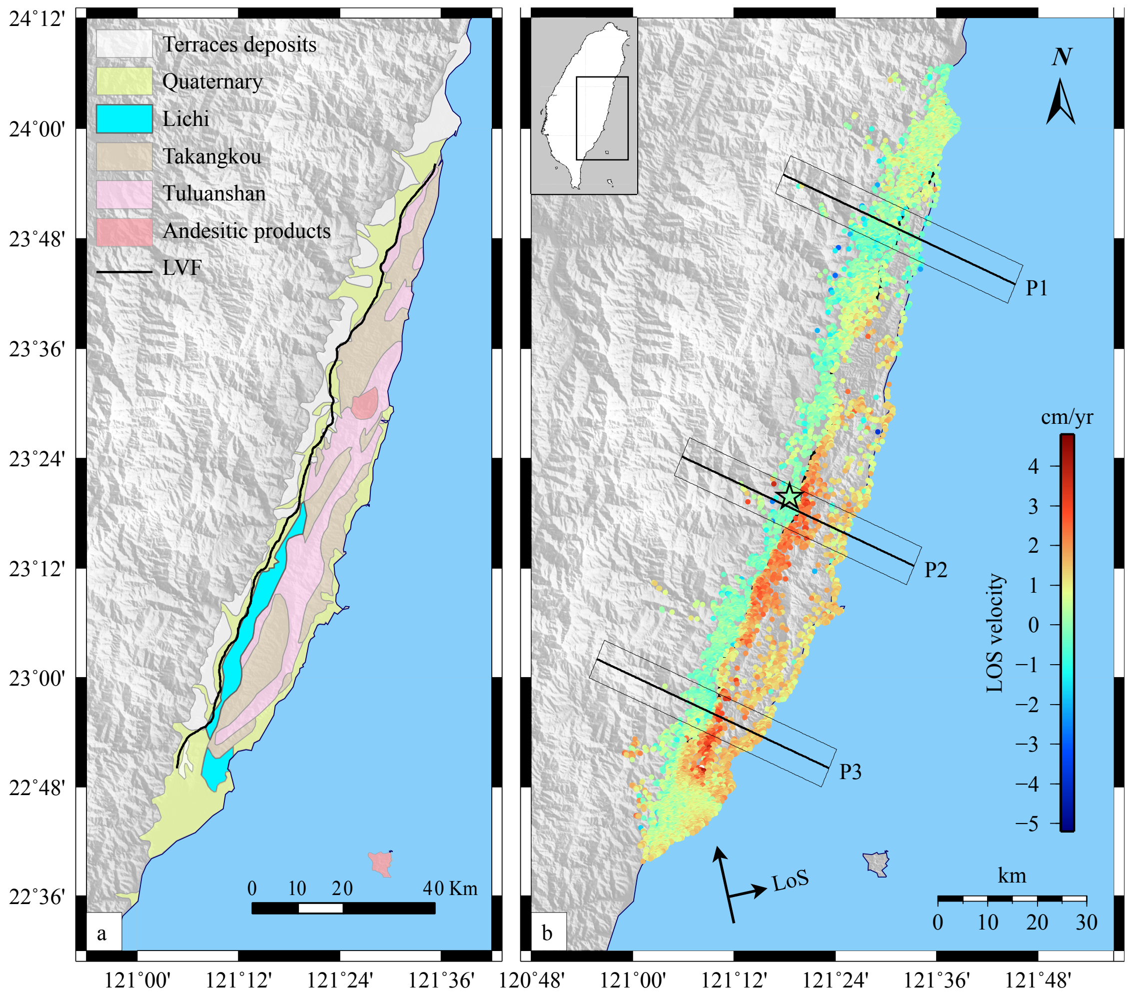

Figure 2.2: (a) Simplified geological map of eastern Taiwan. Coastal Range is composed of three accreted Mio-Pliocene volcanic islands (Tuluanshan formation), three remnants of Plio-Plesitocene forearc basins and intra-arc basins (Takangkou), and the Pliocene collision Lichi Mélange, which is related to the suturing of the subduction zone due to the collision between the Luzon arc (see Figure 2.1a) and the continental margin of South China (*Chang et al.*, 2000, 2001, 2009; *Huang et al.*, 2006b, 2008).(b) Mean line-of-sight (LoS) velocity (in cm/yr) around the Longitudinal Valley Fault derived from the Persistent Scatter technique applied to PALSAR ALOS data acquired between 1/29/2007 and 6/2/2010. Measurements from the southern portion (*Champenois et al.*, 2012) were complemented to cover the whole study area. Velocities are expressed relative to the mean velocity of a reference area, indicated by the black star. Black arrows show the ascending track direction and the LoS which has an incidence of about 35° on average (relative to the vertical). Boxes show location of swath profiles, P1, P2 and P3, plotted on Figure 2.3.

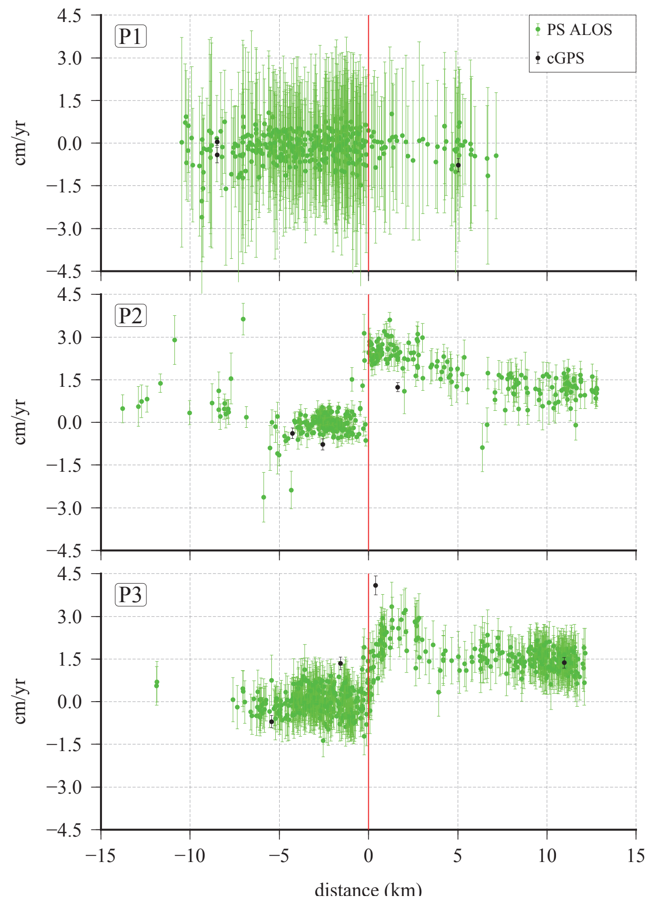

Figure 2.3: LoS velocities along swath profiles P1, P2 and P3. For location see Figure 2.2. Green dots show the PS mean velocity values, black dots show, for comparison, the velocities determined from cGPS times series, for the corresponding period and projected along the LoS. Red lines tag the location of the LVF at surface. PS ALOS Data display a net discontinuity across the fault for the profiles P2 and P3 whereas no jump is observed along profile P1. This discontinuity indicates clearly surface creep on the southern portion of the LVF as reported from field observations at a few sites (*Angelier et al.*, 1997; *Lee et al.*, 2005, 2006).

notable 9 months gap between January 2008 and October 2008. Because of the strong tropospheric effects affecting the time series we used these data to determine the mean LOS mean velocity over the 01/12/2007 to 09/07/2010 time period. Interferograms were generated using ROIPAC (*Rosen et al.*, 2004) with the 10/17/2008 acquisition chosen as the master image and a 40 m horizontal resolution digital elevation model (DEM) for topographic corrections (this national DEM was derived from aerial photogrammetry). We then applied the Stanford Method for Persistent Scatterers (StaMPS) (*Hooper et al.*, 2007). StaMPS uses both amplitude dispersion and phase stability to determine the pixels which can be considered as PS. No a-priori model of deformation is required, nevertheless it assumes that deformation, and consequently interferometric phase, is spatially correlated. The technique yielded a total of 147,737 PS with a density of about 120 - 140 PS per km^2. StaMPS allows estimating the mean ground velocities averaged over the time period covered by the time series, projected along the Line of Sight (LoS) of the satellite, at the location of each PS. Results are displayed in Figures 2.2 and 2.3. Mean velocities were computed with respect to a reference area, corresponding to the city of Rueisuei, near Yuli (black star on the map). Uncertainties estimated through the StaMPS method are of the order of 3-4 mm/yr on average (Table 2.2.1).

	σ_H	σ_V	σ
ALOS (*LoS*)			3.5 mm/yr
cGPS - daily position - secular rate - coseismic	 4 mm 0.1 mm/yr 1 mm	 16 mm 0.5 mm/yr 4 mm	
creepmeter - daily position - secular rate			 2 mm 0.1 mm/yr
campaign GPS	0.2 mm	0.4 mm	
Leveling$_a$		0 to 19 mm	
accelerometers	2.6 mm	1.8 mm	

Table 2.1: Summary of uncertainties associated to the various datasets used in this study (given at the 67% confidence level). (a) Leveling data are referred to the initial point in the survey. The uncertainty of elevation change measurement increases linearly as a function of distance from this point

The highest density of PS was retrieved in urban areas, in particular within the two largest cities in the Longitudinal Valley, Hualien in the North and Taitung in the South. For the same reason, we observe a greater density of PS inside the valley, where urbanization is the most developed, whereas PS are sparser in the Coastal Range, and mostly absent in the Central Range. The rugged topography and dense vegetation are most likely the reason for a lack of PS in those areas. The map of LoS velocities (positive toward the satellite) retrieved from this study shows a clear step in the velocity field along the LVF, south of 23°30 (Figure 2.2 and 2.3). This discontinuity is clear evidence of aseismic slip near the surface for the southern portion of the LVF. This observation is consistent with previously reported field observations of creep at a few sites (*Angelier et al.*, 1997; *Lee et al.*, 2005, 2006) and former InSAR studies (*Hsu and Burgmann*, 2006; *Peyret et al.*, 2011; *Champenois et al.*, 2012). We took advantage of the great spatial resolution to better define the surface trace of the fault in the South. In the North the ALOS PS measurements span the fault trace mapped by (*Shyu et al.*, 2005) but show no clear discontinuity (at the detection level of the technique which we estimate to about 2 mm/yr at the 67% confidence level) (Table 2.2.1), suggesting the shallow portion of the fault has remained locked over the 2007-2010 period.

2.2.2 Continuous GPS stations

A remarkable network of cGPS stations has been deployed in Taiwan. For the purpose of this study, we used times series data from 67 stations spanning the Longitudinal Valley, the Coastal Range, the western part of the Central Range and the Ludao island (Figure 2.1) (http://gps.earth.sinica.edu.tw/). Times series starts on 1/1/1994 for the earliest stations. We analyzed data collected until 11/26/2010 (Figure 2.4).

The dominant sources of signal over this time period are the interseismic loading, the coseismic and postseismic displacements due to the 2003 Mw 6.8 Chenkung earthquake (*Chen et al.*, 2006; *Lee et al.*, 2006; *Wu et al.*, 2006a; *Ching et al.*, 2007; *Hu et al.*, 2007; *Kuochen et al.*, 2007; *Savage*, 2007; *Wu and Wu*, 2007; *Cheng et al.*, 2009; *Hsu et al.*, 2009a; *Huang et al.*, 2009; *Mozziconacci et al.*, 2009). The southernmost stations in the Longitudinal Valley have also recorded displacements due to the 2006 Mw6.1 Peinan earthquake (*Wu et al.*, 2006b; *Chen et al.*, 2009). This earthquake did not take place on the LVF but on a fault bounding the Central Range (*Wu et al.*, 2006b; *Chen et al.*, 2009). Therefore, for the purpose of this study, we corrected the GPS times series for the effect of the 2006 Peinan earthquake and its subsequent postseismic relaxation, by solving the following equation:

$$\begin{aligned} u^i(t) = u_0^i + v^i(t) + \sum_j h_j^i \mathcal{H}(t - t_k) \\ + \sum_k r_k^i \mathcal{H}(t - t_k) \log(1 + (t - t_k)/\tau) \\ + \sum_p \left(s_p^i \sin\left(\frac{2\pi t}{T_p}\right) + c_p^i \cos\left(\frac{2\pi t}{T_p}\right)\right), \end{aligned} \tag{2.1}$$

where i = (north, east, up), u_0 is a constant offset, $v(t)$ correspond to the secular velocity, $\mathcal{H}$ is a Heaviside step function standing for coseismic displacement, t_k is the time at which the step occurs and the Heaviside step function multiply by the logarithmic function follows the postseismic

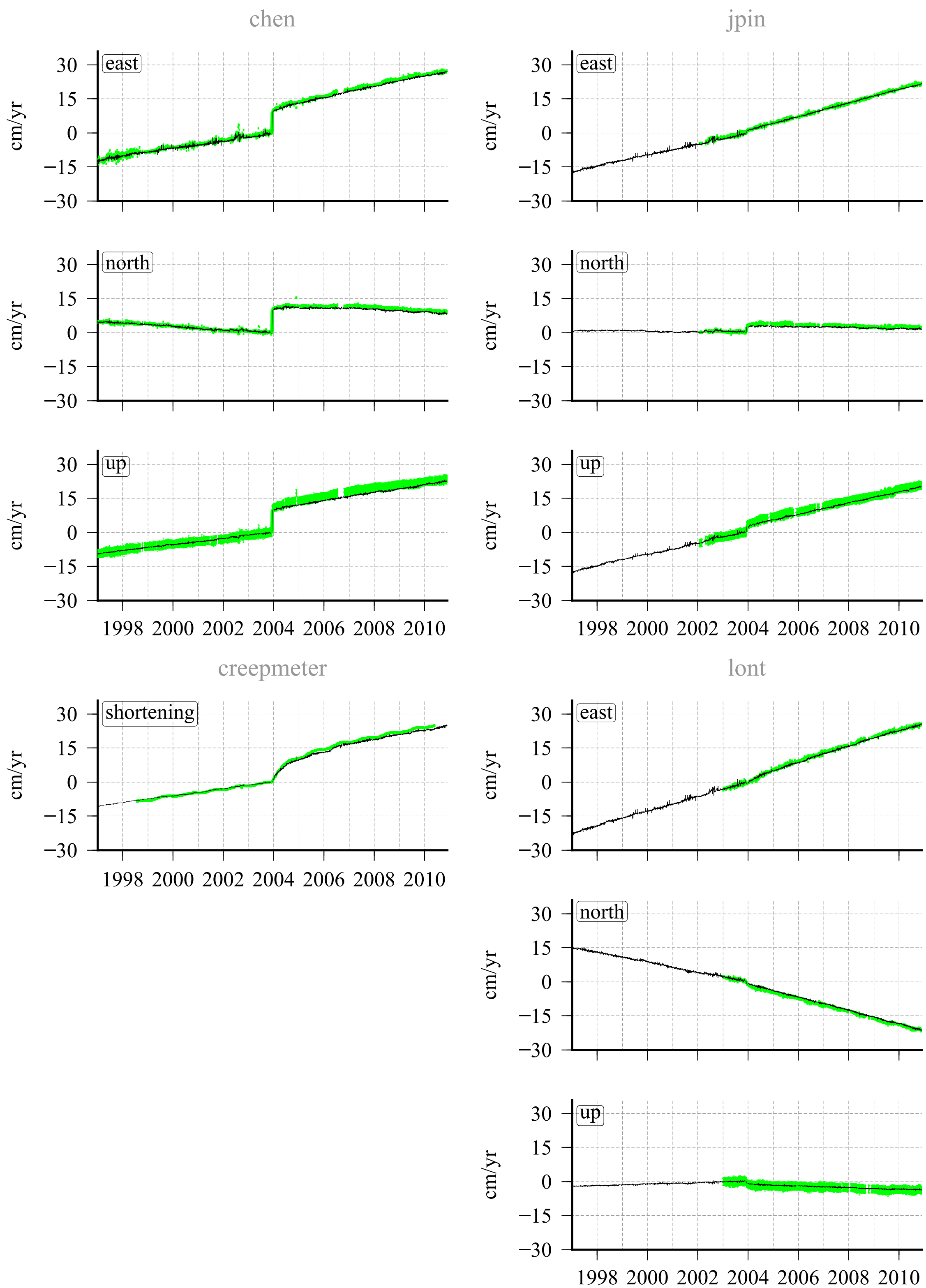

chen
jpin
creepmeter
lont
east
north
up
shortening
cm/yr
30
15
0
−15
−30
1998
2000
2002
2004
2006
2008
2010

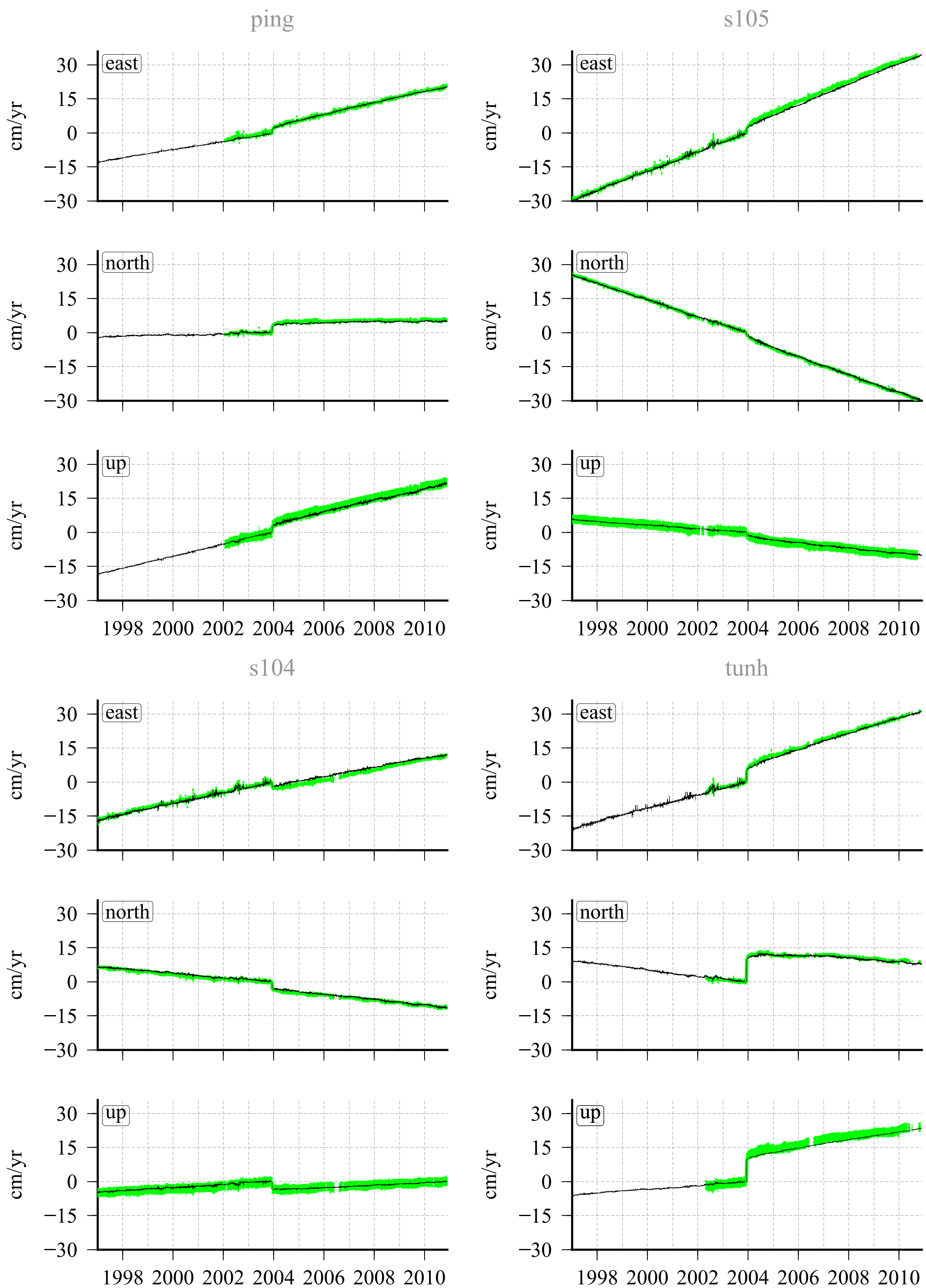
ping
s105
s104
tunh
east
north
up
cm/yr
30
15
0
−15
−30
1998 2000 2002 2004 2006 2008 2010

Figure 2.4: Plots of times series recorded at CGPS stations chen, jpin, lont, ping, s104, s105, tunh (http://gps.earth.sinica.edu.tw) and creepmeter measurements (*Chang et al.*, 2009; *Lee et al.*, 2005). See Figure 2.1 for location. We show a selection of stations with long time records and surrounding the coseismic and postseismic area. See supplements for other times series (Figures S1, S2 and S3). Blue dots with 1-sigma errors bars represents the original dataset. Predictions from the inversion of Coseismic slip and PCAIM inversions of preseismic and postseismic periods are plotted in black To facilitate the comparison we have corrected the model predictions for the mean residual velocities over the pre and post-seismic period represented in Figures 2.17 and 2.19.

relaxation with τ, the characteristic time constant. To model annual variations in equation (2.1) we used sine waves of period T_p. We explored two periods: one year and half a year. The linear parameters u_0^i, v^i, h_j^i, r_k^i, s_p^i and c_p^i are estimated through a standard least-squares inversion. Artificial steps due to maintenance operations, small local earthquakes or equipment malfunction might also affect the signal. We removed them from the times series by applying the same process (equation 2.1). Based on the residuals obtained from fitting the corrected time series with a linear regression (equation 2.1), we estimate the uncertainties on daily positions to be about 4 mm for the East and the North component and 16 mm for the vertical components (Table 2.2.1).

2.2.3 Creepmeter data

Creep on the Chihshang segment of the LVF has been measured daily over the last 15 years thanks to a network of creepmeters (*Lee et al.*, 2000, 2001, 2003, 2005; *Chang et al.*, 2009). We used data from 7/26/1998 to 5/24/2010 from the three creepmeters installed at Chinyuan site (Figure 2.1) but did not include the records from the Tapo site because gravity driven slumping is thought to interfere with fault-slip at this site (*Lee et al.*, 2003). Creepmeters have been set up across the three major splay faults within a 120 m-wide deformation zone. Each creepmeter provides a scalar measurement of the horizontal shortening along the baseline of the instrument ($N113°$, $N156°$ and $N164°$). We projected and sum the time series along the direction of maximum shortening ($N146°$) defined by trilateration method and GPS interseismic vectors at the same site (*Angelier et al.*, 1997; *Lee et al.*, 2006).

No detectable coseismic slip occurred at the surface during the 2003 Chengkung earthquake. By contrast, accelerated creep (*i.e.*, postseismic creep) was observed during the year following the event (Figure 2.4). All three creepmeters at Chinyuan site show strong seasonal variation of fault creep with fast creep during wet season and quiescence during the dry season. This behavior is interpreted to result from pore-pressure variations case by rainfall, as suggested by the correlation with piezometric measurements in a local well (Chang et al, 2009). Based on the residuals obtained from fitting the time series with a linear regression (equation 2.1), we estimate the uncertainty on the individual creepmeter measurements to be 2 mm at the 67% confidence level (Table 2.2.1).

2.2.4 Campaign GPS measurements and secular GPS velocity field.

Annual GPS survey at 45 campaign sites have been conducted across the Longitudinal Valley between 1992 and 1999 (*Yu and Kuo*, 2001) (Figure 2.1). Estimated uncertainties based on (*Yu and Kuo*, 2001) is 0.2 mm for the East and the North component and 0.4 mm for the vertical components (Table 2.2.1). These velocities were combined with the secular velocities at the continuous GPS stations were also computed based on equation (2.1). The corresponding uncertainties are 0.1 mm/yr for the northern and eastern components and 0.5 mm/yr for the vertical (Table 2.2.1).

2.2.5 Leveling data

We used vertical displacements derived from leveling survey in southern part of the Coastal Range (Figure 2.1). Those measurement were acquired on an annual basis between 9/1/2007 and 31/20/2010 along a leveling line crossing the Chihshang segment of the Longitudinal Valley fault (*Chen et al.*, 2012). We used these data to estimate the average vertical rates (relative to the first station along the leveling line) over the 9/1/2007 and 31/20/2010 period. Uncertainties varies from the initial reference point (0 mm) up to 19 mm for the last point (Table 2.2.1).

2.2.6 Accelerometric data

In order to constrain coseismic slip due to the 2003 Mw6.8 Chengkung earthquake, we used the static displacements measured from the offsets in the cGPS records together with the static displacements determined by Wu et al. (*Wu et al.*, 2006a; *Hu et al.*, 2007) from the accelerometric measurements recorded at 38 stations from the TSMIP network (Figure 2.1). TSMIP stations, operating under low-gain mode, sample the signal at 200 Hz (*Wu et al.*, 2006a). Uncertainties were inferred to be 2.9 mm for the horizontal components and 1.9 mm for the vertical (*Wu et al.*, 2006a) (Table 2.2.1).

2.3 Modeling approach and assumptions

The dataset presented above was used to estimate the time-evolution of slip on the LVF. We assume that that the medium surrounding the fault is behaving elastically and apply the *Okada* (1985) semi analytical solution to relate slip at depth to surface displacement. This solution assumes an elastic half space. Heterogeneities of elastic properties and topographic effects are neglected. This approach is known to provide a good first order approximation in general (*Segall*, 2010). This approach requires some model of the fault geometry at depth and some inversion procedure.

2.3.1 Fault geometry and forward modeling

We defined a 3-D fault geometry based on the location of aftershocks at depth of the Chengkung event (*Kuochen et al.*, 2007; *Wu et al.*, 2007, 2008b) and surface trace of the LVF determined from the discontinuity in PS ALOS velocity field (Figure 2.2) and the geomorphologic expression of the fault for the northern part (*Shyu et al.*, 2005) (Figure 2.5). Both, the relocated seismicity as well as local tomographic results (*Kuochen et al.*, 2007; *Wu et al.*, 2007, 2008b) suggest the LVF is a listric fault with a dip angle decreasing gradually from about 62° at shallow depth (0-14m) to 19° at 27 km depth and thereafter. This geometry is relatively well constrained for the central to southern portion of the LVF, because of the intense aftershocks activity following the Chengkung earthquake. We assume that the same listric geometry holds for the northern portion of the LVF although we have no direct constraints there. Fault is subdivided in 44 x 15, 3.16 x 3.16 km^2 patches. The fault extends over about 140 km along strike (the length of the Longitudinal Valley) and about 47 km along dip.

Assuming a linear purely elastic half-space, displacements at surface are related to the fault slip distribution through a Fredholm integral equation of the first kind, which, if we use k measurements and discretize the fault plane in l patches, gives in the matrix from:

$$\mathbf{d} = \mathbf{G}\mathbf{m}, \tag{2.2}$$

where $\mathbf{d}$ is the input data vector, $\mathbf{G}$ is the kxl Green's functions matrix that relates slip at depth and surface displacements, and $\mathbf{m}$ is the vector of parameters we are solving for, i.e. strike-slip and dip-slip components of the slip vector. For an elastic half-space the Green functions depend only on the Poisson ratio which is fixed to 0.25. The rigidity modulus is fixed to as standard value of 30 GPa and used only to convert slip potency (integral of slip over fault area) to moment (expressed in N.m).

2.3.2 Inversion procedure

The slip distribution needed to account for the observed surface displacements $\mathbf{d}$, is solved through a standard linear inversion. In order to take into account the uncertainties on the measurements we normalize the data using C_d, the data covariance matrix. This procedure allows combining data with different noise characteristics, such as GPS and InSAR obervations with appropriate relative weighting. Equation (2.2) then becomes:

$$\mathbf{C_d}^{-1}\mathbf{d} = \mathbf{d}^* = \mathbf{C_d}^{-1}\mathbf{G}\mathbf{m} = \mathbf{G}^*\mathbf{m}. \tag{2.3}$$

This is the equation that we seek to solve for fault slip, $\mathbf{m}$. In principle a linear inversion of that equation provides the solution which minimized the weighted rms of the difference between the observed and predicted displacement, with the weighting of each data point being determined by its uncertainty. This is equivalent to minimizing a reduced Chi-squared criterion defined as:

$$\chi^2_{red}(\mathbf{m}) = 1/n \parallel \mathbf{G}^*\mathbf{m} - \mathbf{d}^* \parallel^2, \tag{2.4}$$

where n is the number of data point.

However the inversions described below are poorly constrained due to the large number of unknowns (1320) and trade-offs among model parameters. To regularize the inversion, we impose fault slip distribution to be smooth. Following an approach suggested by *Lohman* (2004), we weight the constraint put on smoothing according to local resolution of the inversion. Therefore, fault slip is retrieved by minimizing some combination of the model ability to fit the data and the penalty imposed on the roughness of the slip distribution which is quantified from its Laplacian:

$$\phi_d = \parallel \mathbf{G}^*\mathbf{m} - \mathbf{d}^* \parallel^2 + \frac{1}{\lambda} \parallel \mathbf{S\Lambda m} \parallel^2, \tag{2.5}$$

where $\mathbf{\Lambda}$ is the Laplacian matrix, $\mathbf{S}$ is a diagonal smoothing shape matrix that weight each row of $\mathbf{\Lambda}$ and λ define the weight attributed to the penalty. $\mathbf{S}$ is defined as the inverse of the width of the best-fitting gaussian curve to each row of the resolution matrix (see supplement from *Ader et al.* (2012) for details). Consequently, well resolved patch have small or no smoothing applied, whereas, poorly resolved mesh grids are strongly smoothed with their neighbourhood.

Figure 2.6 illustrates the resolution for the various inversions described below. The resolution is expressed here in terms of the characteristic size of smallest inhomegeneities of coupling which could in principle be resolved given the spatial distribution and the uncertainties of the measurements. For each case we take into account the distribution of data and their uncertainties and plot, at the location of each cell of the fault model, the width of the best-fitting gaussian curve to each row of the resolution matrix. This is in effect representing the width of the equivalent Gaussian distribution that is retrieved if one inverse the displacements predicted for a unit slip at the considered cell. These maps show that, past the coastline, the resolution on fault slip at depth becomes quite poor as expected given the absence of any offshore constraints except for the cGPS station on Ludao island (Figure 2.1). Features smaller than about 10 km cannot in principle be resolved there. Updip of the coastline the resolution is generally better than about 5 km.

To illustrate the resolution power of our inversions, we show in Figure 2.7 the result of the inversion of a synthetic source model. The input is a rectangular source with a uniform slip or 1 m. The location and size of the source was chosen so that this source is comparable to that of the M_w 6.8 earthquake. Synthetic displacements were computed at the location of the GPS and

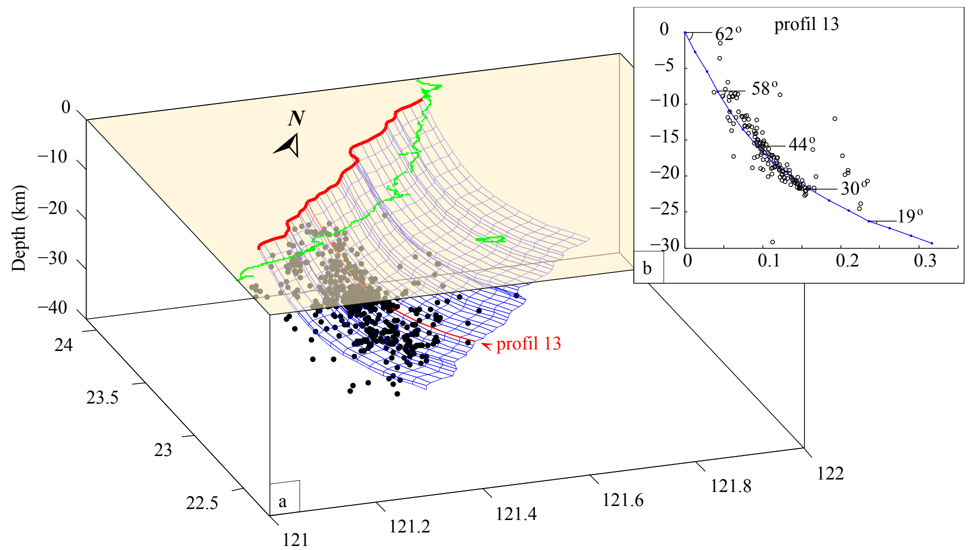

Figure 2.5: (a) 3-D fault geometry (blue grid) determined from the surface fault trace (red line) and relocated seismicity(black dots) for events of $M_w \geq 2.5$ (*Wu et al.*, 2008a). The geometry at depth is well constrained only in the Chengkung earthquake area due to the intense afterschocks activity. (b) Profile shows the variation of dip angle with depth. Black dots corresponds to seismic events.

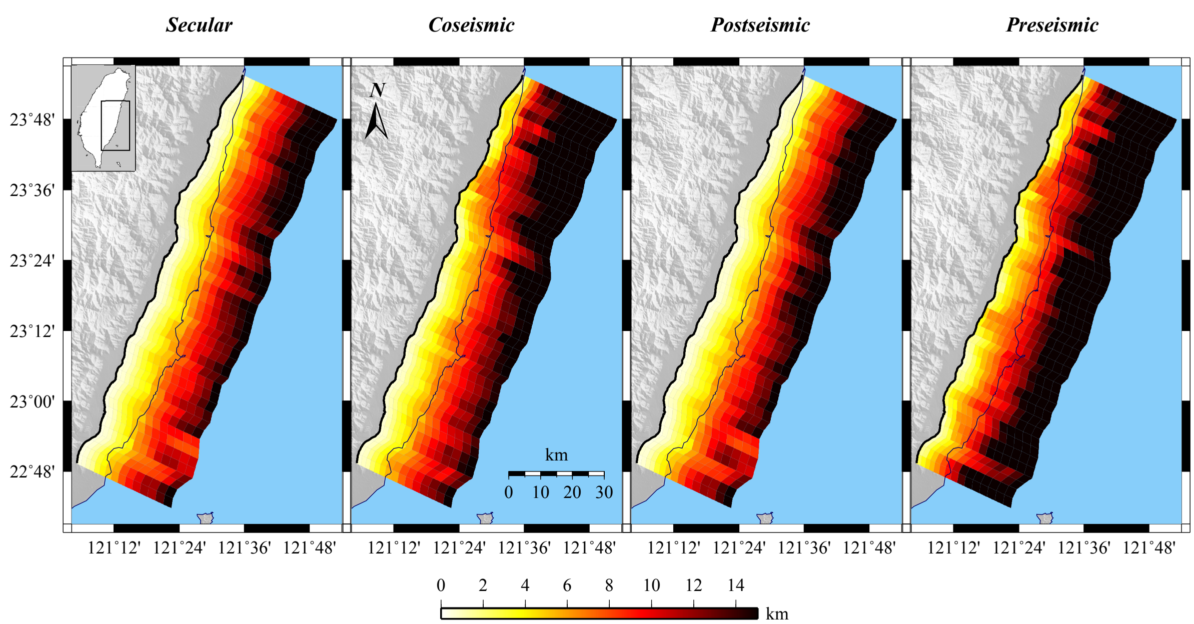

Figure 2.6: Resolution of the various inversions described in this study. The width of the best-fitting gaussian curve to each row of the resolution matrix is plotted at the location of each cell of the fault model. This is in effect representing the width of the equivalent Gaussian distribution that is retrieved if one inverse the displacements predicted for a unit slip at the considered cell.

accelerometric stations and were assigned the same uncertainties as the original observations.

2.3.3 Block model correction

Before any inversion for fault slip rate with depth, the surface displacements must first be referred to a local reference frame. In effect, we need to determine the long term motion of the Coastal Range and Central Range which are bounding the Longitudinal Valley Fault to the east and west respectively. As is customary in plate tectonics or continental deformation studies, we use the Euler pole formalism to describe the long term motion of the Coastal Range (CoR) and Central Range (CeR) blocks. Given that all the GPS stations are closed to the LVF, it is not possible to determine these Euler poles reliably without taking into account interseismic strain. We therefore first determine jointly the secular pattern of fault slip (time-averaged fault slip over the study period) and the Euler poles of the CeR and CoR blocks relative to ITRF2005 (section 2.4). Then we infer coseismic slip due to the Chenkung earthquake. Both coseismic and secular interseismic model are determined simply from solving equation (2.5) in which $\mathbf{d}$ represents the surface displacements. To retrieve the temporal variations of fault slip for the period preceding and following the 2003 event, we used the PCAIM method (*Kositsky and Avouac*, 2010), explained in more details in section 2.6.1.

2.4 Secular Interseismic Model

2.4.1 Data used

We determine in this section the secular Model of fault slip rate on the LVF, in the interseismic period. For that purpose, we use GPS campaign measurements, leveling data, PS ALOS mean velocity and secular velocities determined with the continuous GPS and creepmeters time-series (as determined from least squares fitting of the time series with equation (2.1)). The leveling and ALOS datasets were acquired more than three years after the 2003 Chengkung earthquake. According to the GPS and creepmeter postseismic relaxation was mostly over by this time. Therefore, these data are incorporated in the secular inversion, which improves significantly the spatial resolution. Uncertainties assigned to these datasets are displayed in Table 2.2.1.

2.4.2 Euler pole correction

In order to get a secular model of slip on the LVF we need to evaluate the long term motion of the CoR and CeR blocks. Evidence for active thrusting offshore the eastern coast of Taiwan (*Malavieille et al.*, 2002; *Huang et al.*, 2010) dismisses the CoR block as part of the Philippine Sea Plate. In addition, the Philippine Sea Plate motion is very poorly constrained as this plate is bounded only by subduction zone and the few GPS sites on this plate might be affected by plate-boundary strain.

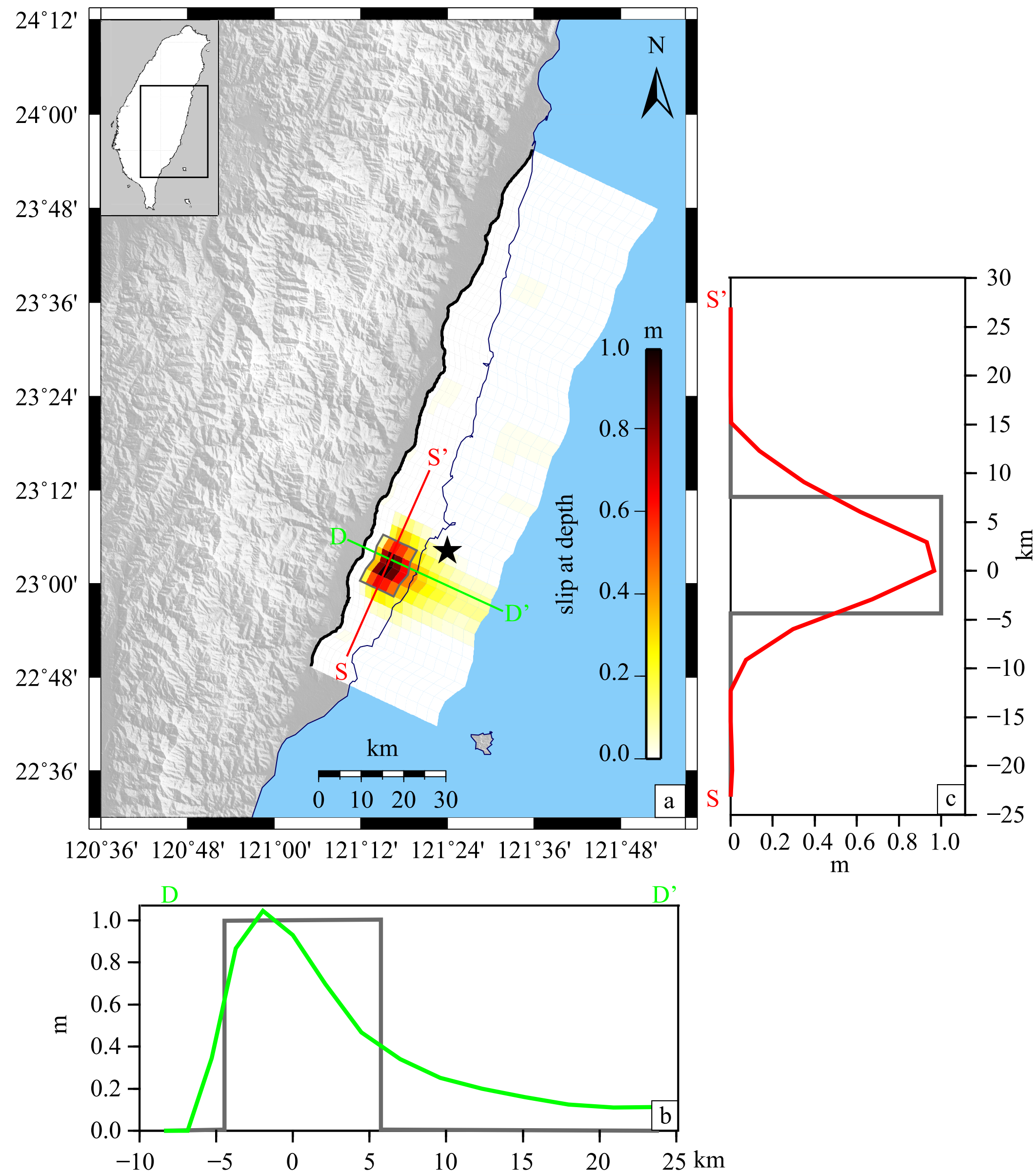

Figure 2.7: Resolution test. The input is theoretical displacements computed for a rectangular source (black box) with a uniform slip or 1m. The location and size of the source was chosen so that this source be comparable to that of the Mw 6.8 earthquake. Synthetic displacements were computed at the location of the GPS and accelerometric stations and were assigned the same uncertainties as the original observations. The left and bottom panels show the input and inverted slip distribution along strike (SS) and along dip (DD) respectively. Locations of profiles are reported in the map view.

We therefore need to determine the secular motion of that block. This requires to take into account the interseismic strain associated with the LVF since all the geodetic data are located less than ~ 20 km away from the fault. Similarly, the CeR blocks is not fixed with respect to South China due to active thrusting along the western foothills of Taiwan (*Hsu et al.*, 2003) and none of the GPS data can reliably be considered to represent the long term motion of the CeR block. Therefore, we use a simple 2 steps procedure to evaluate the Euler poles describing the long term motion of these two blocks, with the Philippine Sea Plate chosen as a reference. We first express the GPS velocities with respect to the Philippine Sea Plate by using the Euler pole (ITRF-Ph) computed by *DeMets et al.* (2010), (Table 2.4.2 and Figure 2.8).

Then, using the backslip modeling approach (*Savage*, 1983) we invert for slip at depth using the campaign GPS data and the secular velocities derived from the continuous GPS times series, for stations East of the LVF. This model is then used to predict the GPS velocities at stations in the footwall (West of LVF) to further compare them with the secular velocities measured at those locations. If the LVF is assumed to be the only source of strain in the study area, then the residuals represent the long term motion of the footwall with respect to the Philippe Sea plate. Residuals for stations in the Central Range are then used to compute the Euler pole of the CeR block from a linear least-squares inversion (CeR/Ph pole in Table 2.4.2 and Figure 2.8). Next we use the CeR/Ph Euler pole to express the secular velocities of the western stations in the local CeR reference frame. These data are now inverted for the coupling on the LVF using the backslip approach. Similarly to the previous step, we predict displacements at stations lying on the eastern side of the LVF and compute the residuals with the secular velocities at those sites, expressed in the CeR reference frame. We can now use these residuals to compute an Euler pole describing the motion of the CoR relative to CeR (see CeR/CoR pole in Table 2.4.2 and Figure 2.8). It is now possible to express the geodetic data in either the CeR or CoR reference frame, and predict the long term slip on the LVF fault needed to accommodate the relative block motion between the Central Range and Coastal Range (Figure 2.9). The computation assumes that the blocks behave rigidly in the long term. This is only a first order approximation as the LVF is not strictly planar.

	Ph/ITRF	CeR/Ph	CeR/CoR	CoR/Ph
Latitude	47.1	32.15	-23.34	-19.42
Longitude	150.4	133.30	-54.93	-58.11
Ω(°/Myr)	-0.9251	-2.1351	7.0154	-4.94

Table 2.2: Location of axis and angular rotation rates of Euler poles used to describe the relative motions of the Philippine Sea Plate (Ph), Central Range block (CeR), and Coastal Range block (CoR).

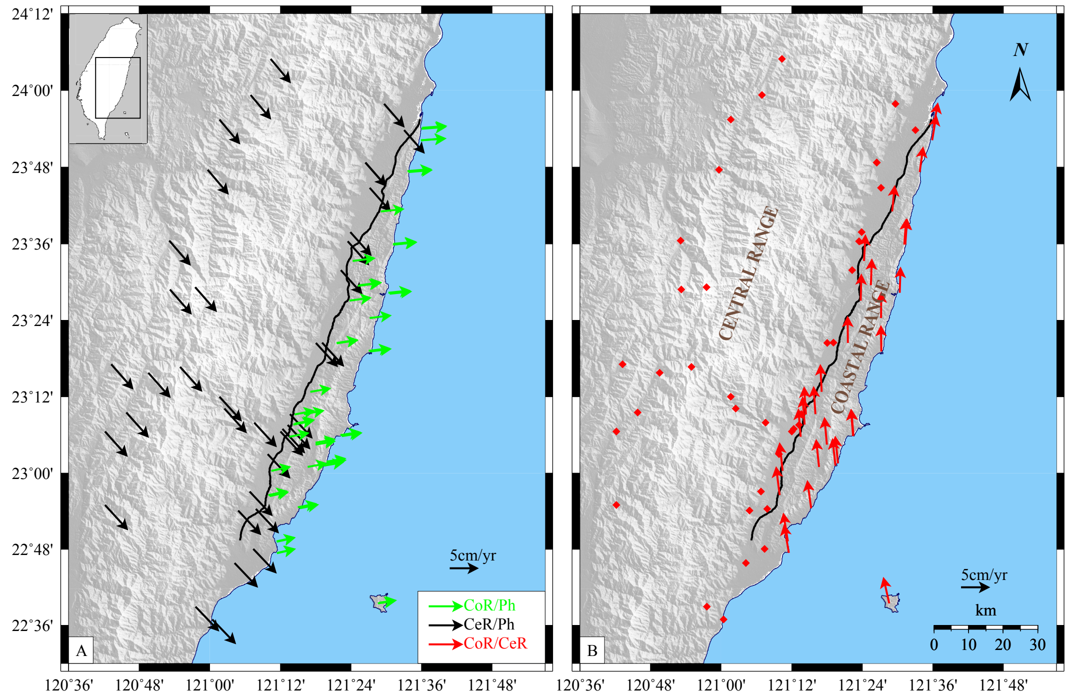

Figure 2.8: (a) Secular motion of the Central Range (black arrows) and Coastal Range (green arrows) blocks relative to the Philippine Sea Plate as defined by Philippine/ITRF (*DeMets et al.*, 2010). (b) Secular motion of the Coastal Range relative to the Central Range. Pole parameters are listed in Table 2.4.2.

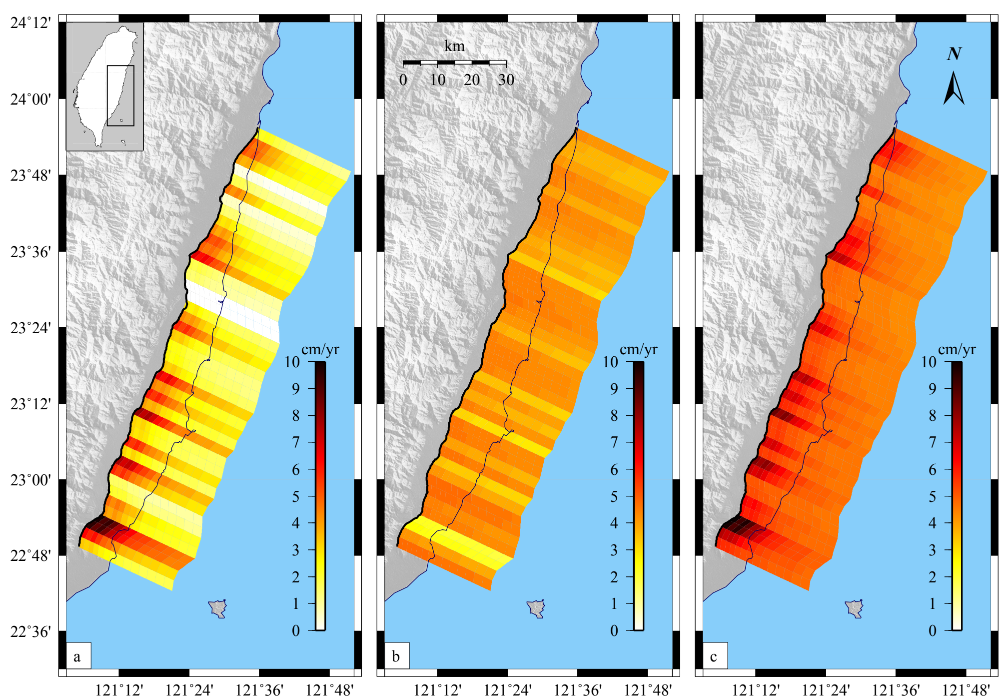

Figure 2.9: Dip-slip component (a), strike-slip component(b) and magnitude (c) of long term slip rate on the LVF predicted from the secular relative motion between the Central Range and Coastal Range. This computation is based on the CoR/CeR pole listed in Table 2.4.2.

2.4.3 Interseismic slip and coupling on the LVF

We now use the complete dataset of InSAR, GPS and leveling measurements to determine the time-averaged pattern of slip rate on the LVF in the interseismic period. We assume that the deeper continuation of the fault is slipping at the long term slip rate imposed by the relative block motion between the Central Range and Coastal Range, as predicted by the CeR/CoR Euler pole established in the previous section. Because of the very limited sensitivity of our data to slip at depth, we limit the inversion to the fault portion shallower than 26 km (corresponding to 15 cells of our gridded fault along the downdip direction). We first predict the theoretical displacements at stations by assuming that the fault is fully locked from the surface to a depth of 26 km. To compute such model we use again the backslip approach (*Savage*, 1983). The CeR/CoR pole Euler pole characterize the long-term surface velocities and the backslip model is added to account for locking of the LVF down to a 26 km depth. We then substract the velocities predicted by this model from the measured velocities. These residual must contain the signal due to creep on the LVF. We can now inverse the residuals to get the spatial variation of secular slip rate on the LVF in the 0-26 km depth range of our model. We apply this procedure to all the data, including continuous and campaign GPS data, leveling measurements and PS ALOS mean velocities. The slip rate distribution obtained from this inversion, as well as the comparison between the model predictions and the observations are plotted in Figures 2.10(a), 2.11, 2.12 and 2.13. This model highlights the sections of the fault which are creeping from the ones which remain locked. As previously recognized, the southern portion of the fault is creeping near the surface (*Angelier et al.*, 1997; *Lee et al.*, 2000, 2001, 2003, 2005; *Hsu and Burgmann*, 2006; *Lee et al.*, 2006; *Chang et al.*, 2009; *Cheng et al.*, 2009; *Hsu et al.*, 2009b; *Huang et al.*, 2010; *Peyret et al.*, 2011; *Champenois et al.*, 2012; *Chen et al.*, 2012; *Chuang et al.*, 2012). Our study highlights that, on the contrary, the northern part is mostly locked. Pattern at depth is more complex, with areas creeping at high rate, connecting the deeper and the upper part, while others seem to be locked or partially locked. Moreover, epicenters of historical earthquakes on the LVF (1938,1951,2003) (*Chung et al.*, 2008) seem to correlate with the location of partially locked patches (Figure 2.10b).

We can next estimate the interseismic coupling (ISC) which quantifies the degrees of locking of the fault. ISC is defined as the ratio of slip deficit divided by the long term slip rate.

$$ISC = 1 - \frac{V_{int}(x)}{V_{pl}(x)}, \tag{2.6}$$

where V_{pl} is the long-term slip rate on the fault and V_{int}, the slip rate during the interseismic period. In principle, if no transient events occurs during the time period considered to compute V_{int}, ISC values should be between 0 and 1. If $ISC = 1$, then patch is fully locked, accumulating stress to be released during transient slip events (earthquakes or aseismic slow slip events for example). On the

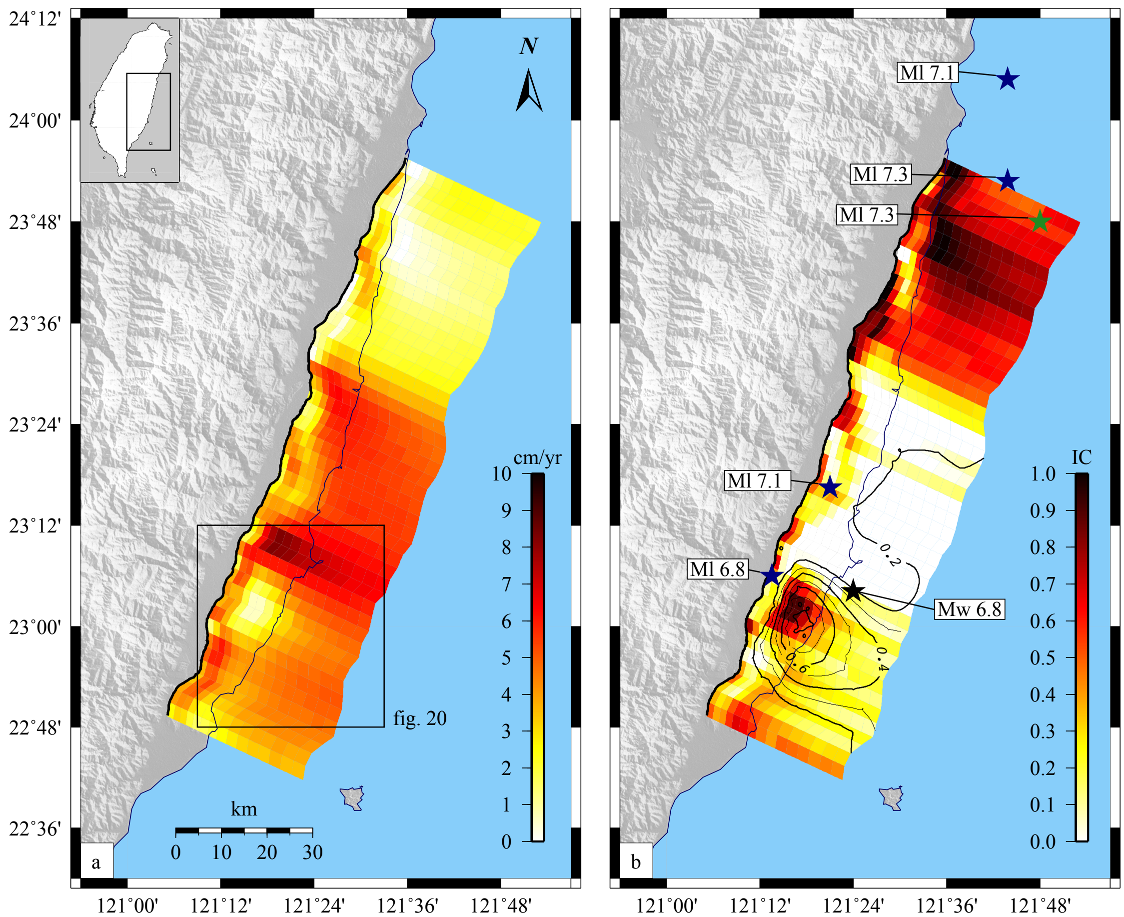

Figure 2.10: Secular interseismic model. (a) Slip rate distribution derived from the inversion of campaign GPS data, secular interseismic velocities inferred at cGPS stations, creepmeter secular rate, leveling data and PS ALOS mean velocities. Black rectangle shows locations of the map view displayed in Figure 2.20. (b) Interseismic coupling (ISC) distribution derived from the interseismic slip rate distribution shown in (a). ISC quantifies the degrees of locking of the LVF fault. If $ISC = 1$, then patch is fully locked, whereas $ISC = 0$ means that the patch is creeping at the long-term slip rate. Black, green and blue stars indicate the epicenter of the 2003 Chengkung earthquake, the 1938 earthquake and the 1951 earthquakes sequence respectively (*Chung et al.*, 2008). Back curves show contour lines of coseismic slip distribution for the 2003 Mw 6.8 Chengkung Earthquake (Figure 2.14).

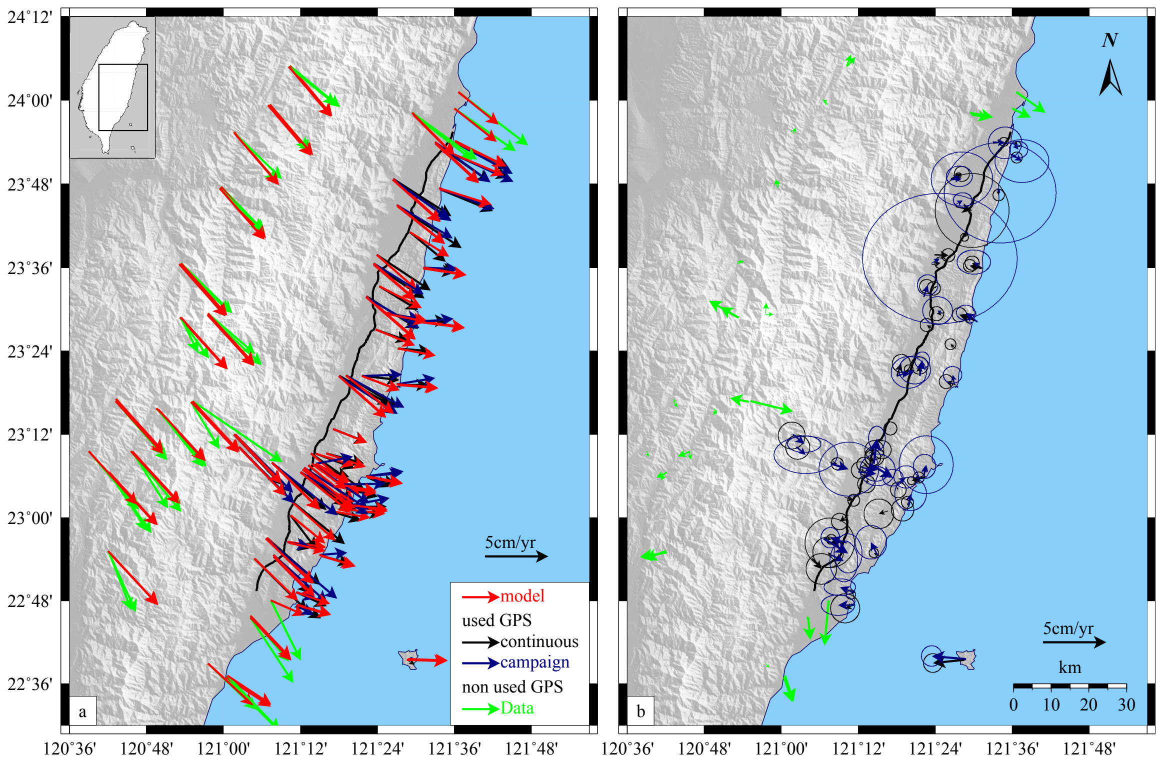

Figure 2.11: Interseismic coupling model, fit to geodetic data. (a) Comparison between observed and predicted horizontal velocities. The reference frame is the Philippine Sea Plate. The GPS data used in this inversion are plotted respectively as dark blue and black arrows for the campaign and continuous GPS measurements. Green arrows stand for the GPS stations that were not used in the inversion but which are plotted for reference. Predictions from the interseimic coupling model are displayed in red. (b) Residuals from the inversion with corresponding error ellipses. Same color attributions as in (a).

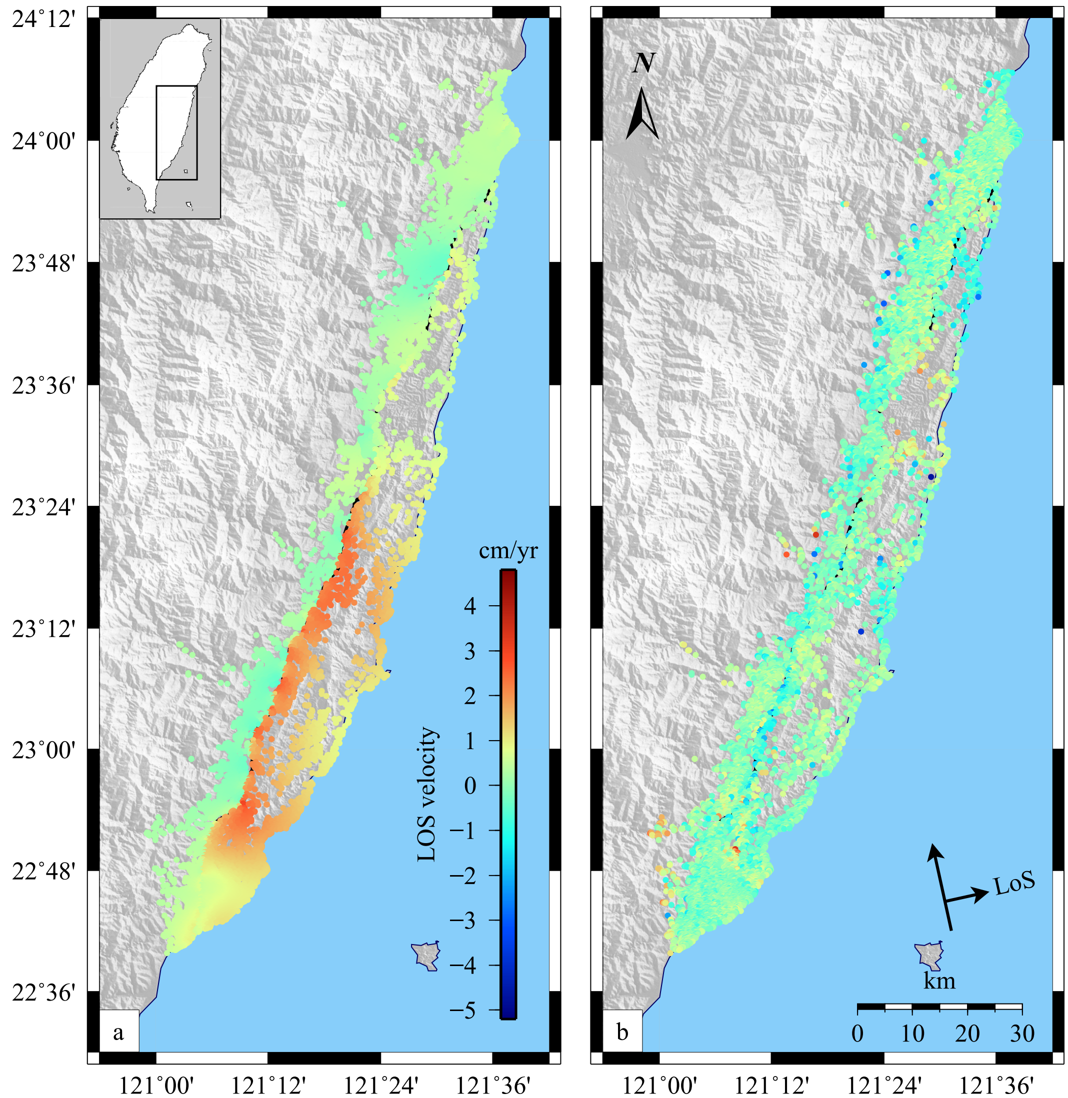

Figure 2.12: Interseismic coupling model, fit to PS ALOS mean velocity. (a) Line of Sight velocities predicted from the secular interseismic model. For comparison with observations see figure 2.2. (b) Residuals from the inversion with same color scale as in (a).

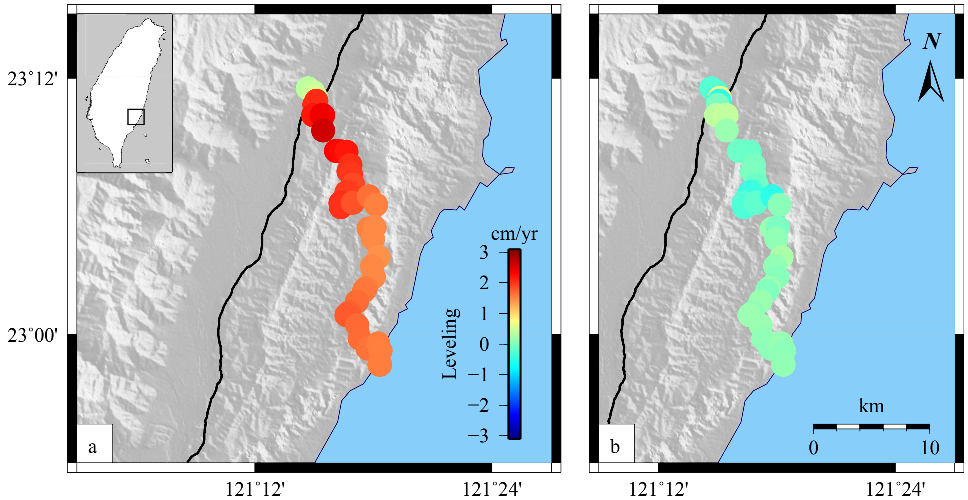

Figure 2.13: Interseismic coupling model, fit to leveling data. (a) Vertical velocities predicted from the secular interseismic model. See Figure 2.1 for corresponding observations. (b) Residuals from the inversion with same color scale as in (a).

contrary, $ISC = 0$ means that the patch is creeping at long-term slip rate. To compute the ISC on the LVF we divide the slip rates derived from the inversion of surface strain with the long term slip rate predicted by the CeR/CoR Euler pole (Figure 2.9). The inferred distribution of ISC is dispayed in Figure 2.10b.

2.5 Source model of the 2003 Chengkung earthquake

We present here our determination of the slip distribution related to the Chengkung earthquake. This event, which occurred on December 10^{th} 2003, ruptured the south-eastern portion of the LVF. Several source models have already been established with different assumptions regarding the fault geometry or elastic structure (*Wu et al.*, 2006a; *Ching et al.*, 2007; *Hu et al.*, 2007; *Mozziconacci et al.*, 2009; *Cheng et al.*, 2009; *Hsu et al.*, 2009a). We produce our own model to allow for a consistent comparison with interseismic and postseismic slip models.

coseismic slip on the LVF is determined based on the estimate of static displacements derived from the cGPS (33 sites) and accelerometric (38 sites) records (*Wu et al.*, 2006a; *Wu and Wu*, 2007; *Hu et al.*, 2007). The coseismic displacements and the associated uncertainties at the cGPS stations are derived from the least squares fit to the times-series using equation (2.1). The 1-sigma uncertainties are of the order of 1 mm and 4 mm for the horizontal and vertical components respectively. With regard to the coseismic displacements retrieved from the accelerometric records, we initially use the uncertainties estimated by *Wu et al.* (2006a) which are reported to be 2.9 mm for the horizontal components and 1.9 mm for the vertical. Fault slip is determined from a standard least squares inversion of these data, as described in section 2.3. In equation (2.5) λ is chosen to offer the best compromise between smoothness and fit to the data, which lead to $1/\lambda = 0.005$, for more details see Figure S4 in supplement that plots the variation of χ^2 against λ. Uncertainties are renormalized to balance the relative contribution of the accelerometric and GPS data. We imposed the reduced χ^2 to be equal to 1 when computed on each data set separately, *i.e* accelerometric uncertainties must be multiplied by 4.8 whereas uncertainties for inferred coseismic jumps from GPS times series must multiplied by 6.6. These renomalization factors suggest that some sources of errors are not properly taken into account in the initial estimates of the uncertainties (such as those due to heterogeneities of the elastic medium or topography). The renormalized uncertainties seem reasonable (of the order of a few cm)

Our coseismic model (Figure 2.14) is in good agreement with previously published geodetic inversions (*Ching et al.*, 2007; *Hu et al.*, 2007; *Mozziconacci et al.*, 2009; *Cheng et al.*, 2009; *Hsu et al.*, 2009a), but somewhat smoother than the kinematic model of *Mozziconacci et al.* (2009) which incorporates GPS data as well as teleseismic and accelerometric waveforms. According to our model most of the slip occurred on a $10x10\text{km}^2$ patch and peaked to a maximum of 0.91 m at 17 km depth (Figure 2.14). The location of the rupture area is close to what *Mozziconacci et al.* (2009) obtained. Their source is more compact with a peak slip twice as large, probably because of the enhanced resolution afforded by the seismic waveforms (in fact in such a joined inversion the static displacements constrain essentially the final slip distribution while the waveforms provide constrains on the time history of slip). Our model shows no significant slip near the surface (Figure 2.14). This finding is in agreement with field observations and the absence of coseismic offset in the creepmeter record which is located updip of the zone with maximum slip. Few patches display 0.15 to 0.27 m of fault slip, but most of them show a displacement lower than 0.1 m.

The equivalent seismic moment released (M_0) was computed as the sum of the seismic moment of all individual subfaults, assuming a shear modulus (μ) of 30 GPa:

$$M_0 = \mu \sum_i S_i \Delta u_i, \tag{2.7}$$

where S_i is the area of the subfault and Δu_i the computed slip on S_i. Our model estimates the seismic moment to be $1.87.10^{19}$ N.m., in close agreement with the moment of $2.07.10^{19}$ N.m. determined by *Mozziconacci et al.* (2009) assuming a shear modulus of 32 GPa. The equivalent moment Magnitude ($M_w = 6.8$), estimated using *Hanks and Kanamori* (1979) relation :

$$M_w = \frac{2}{3}\left(\log_{10} M_0 - 9.1\right), \tag{2.8}$$

is consistent with the value reported in the Harvard-CMT catalogue.

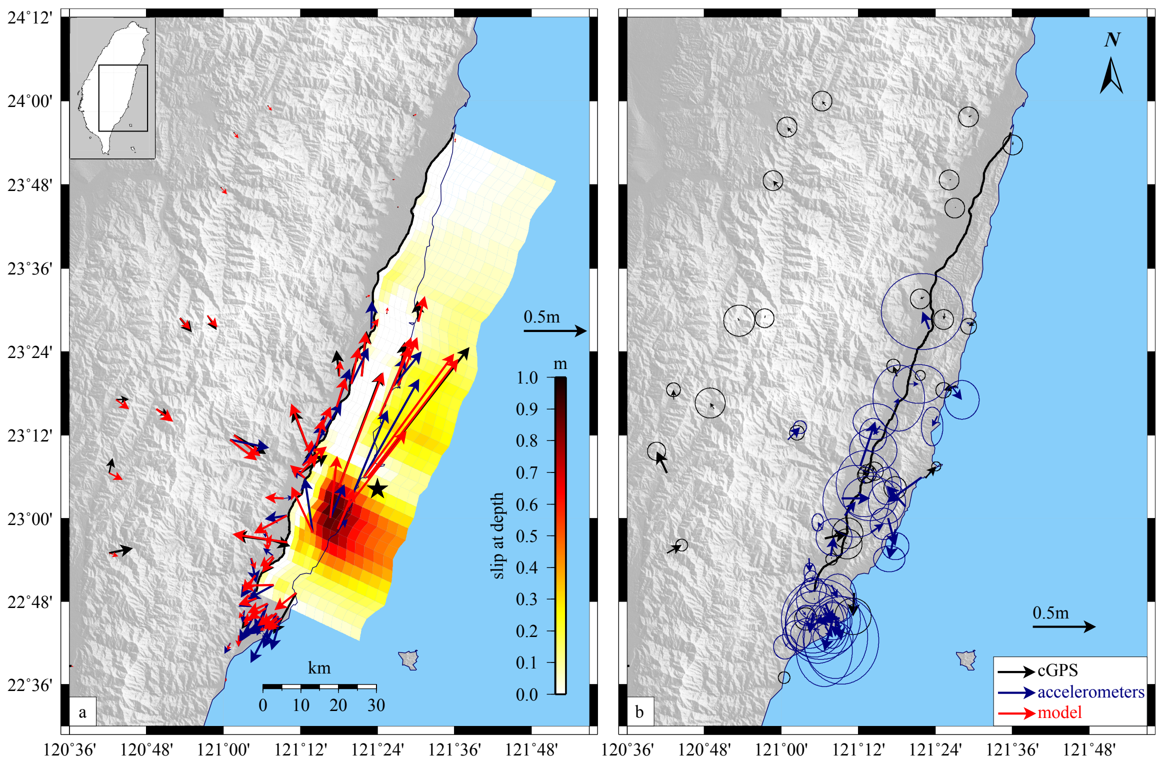

Figure 2.14: Coseismic slip distribution model of the 2003 Mw 6.8 Chengkung Earthquake. (a) The grid shows slip on the fault inferred from the inversion of the static coseismic displacements determined at the CGPS and accelerometric stations, indicated by black and blues arrows respectively. Predictions from our best-fitting coseismic model are plotted in red. (b) Residuals between observed and predicted horizontal displacements. Black star indicates the epicenter of the Chengkung earthquake and black line represents the fault trace of the Longitudinal Valley Fault.

2.6 Pre- and postseismic temporal variation of fault slip rate

2.6.1 Inversion procedure

We now determine the temporal variation of slip at depth before and after the 2003 Chenkung earthquake from modeling the geodetic time series. We use the PCAIM technique (*Kositsky and Avouac*, 2010) since this method has been designed to deal with any kind of time variations of fault slip and allow integrating simultaneously different kind of geodetic measurements and remote sensing data (see also *Lin et al.* (2010); *Perfettini et al.* (2010); *Wiseman et al.* (2011); *Copley et al.* (2012) for examples of applications of that technique). The method is computationally cheap and allows to take advantage of the spatial resolution afforded by the remote sensing data, which are sparse in time but dense in space, with the temporal resolution of the GPS time series which are sparse in space but dense in time.

Times-series are combined to build a data matrix X_0 of dimension $m \times n$ where each row corresponds to the time series of 1 scalar quantity (either shortening measurement from a creepmeter or one component (east, north, up) of a GPS stations), and each column corresponds to a given epoch of data acquisition (all data acquired at a given are listed under the same column). Therefore X_{ij} represents the displacement at station i at the j^{th} step in time. Infinite uncertainties is assigned to missing data measurement. The data matrix is then centered (equation 2.9) before applying a Singular Value Decomposition (SVD):

$$X(i,j) = X_0(i,j) = \mu \sum_i S_i \Delta u_i, \tag{2.9}$$

$$X = U.S.V^t, \tag{2.10}$$

where the column vectors of U are the eigenvectors of the spatial covariance matrix XX^t, the column vectors of V are the eigenvectors of the temporal covariance matrix X^tX, and S is the rectangular diagonal matrix with elements equal to the eigenvalues of X, ordered decreasingly (*Kositsky and Avouac*, 2010). The components are determined from a weighted least squares procedure that takes into account data uncertainties. The principle of PCAIM is to combine Principal component analysis (PCA) (equation 2.10) with the inversion for slip at depth based on the theory of dislocation in an elastic half space (equation 2.2). Therefore, each column vectors of U are inverted to get the corresponding principal slip distribution l defined by:

$$U = G.l. \tag{2.11}$$

This equation is solved from the standard least-squares procedure with Laplacian regularization described in section 2.3. The fault slip history is retrieved by linear composition:

$$X = (G.l)\,.S.V^t = G.\left(l.S.V^t\right), \tag{2.12}$$

where $(l.S.V^t)$ is the slip on each patches of the fault over time. Only statistically relevant Principal Components (PCs) of the decomposition should be kept. The number of useful components is assessed from computing the fraction of variance of the data matrix accounted by the k^{ith} component which is simply:

$$\frac{\lambda_k^2}{\sum_{i=1}^{r} \lambda_i^2}, \tag{2.13}$$

where r is the rank of the diagonal matrix S (number of non zero eigenvalues). One can also consider the variation of the χ^2 as a function of the number of principal components used and determine the number of useful components using a f-test (*Kositsky and Avouac*, 2010).

A dataset very sparse in time, such as the PS-ALOS data or the campaign GPS data, cannot be incorporated in the PCA decomposition but can be used to place constraints on the inversion of the principal components. The set of linear equation (2.12), considering only the meaningful components, is then inverted jointly with the condition that the slip distribution, at the appropriate epochs, predict the sparse dataset. Consequently these data bring constraints on the spatial distribution of the principal slip distribution represented by the vectors l but not on the time functions V. As in section 2.5, we balance the weight put on each data used in PCAIM by rescaling the uncertainties so that the weighted rms of the residuals (or χ^2_{red}, equation 2.4), computed for each dataset separately, is equal to 1. Weighting is adjusted iteratively, generally only 1 or 2 iterations are necessary. Assessing the appropriate weighting to assign to a sparse dataset, relative to the weight placed on fitting the U vectors is not straightforward. For example, in the case of a dataset consisting of cGPS and SAR data the GPS time series should bring a stronger constrain since they provide a daily, uncorrelated record of absolute position. However, through the PCAIM procedure, we reduce drastically the number of input parameters by a applying an SVD. Therefore ALOS dataset becomes over-predominant whereas there is an inherent redundancy in the information provides by PS, directly correlated with the StaMPS procedure itself. As the data covariance is not an output of the StaMPS processing, to circumvent that issue, we arbitrarily penalize the ALOS dataset by increasing estimated errors 10 times (Table 2.6.2). Others data uncertainties have been renormalized to get a χ^2_{red} of 1.

We carry on separate inversions for the periods preceding and following the earthquake. The two inversions are thus independent and any similarity between these solutions has to come from the data rather from the decomposition.

2.6.2 Postseismic inversion

We model the time-evolution of fault slip on the LVF over 7 years following the Chengkung earthquake using all the geodetic data and InSAR data available over that period. A PCA decomposition is applied to the cGPS and creepmeters stations time series. Based on variation of the misfit as a function of the number of principal components we determine that the first four components are significant (Figure 2.15 and Figure S5 in supplements). These four components capture well the spatio temporal variation of postseismic relaxation and the seasonal variations of surface displacement. The weight put on Laplacian smoothing and renormalization factors are listed in Table 2.6.2 along with the rms values obtained from our inversion

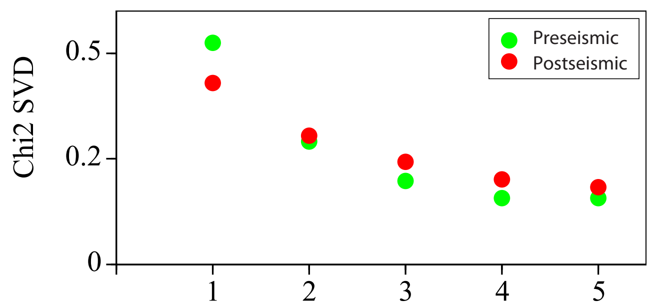

Figure 2.15: Misfit between times series (GPS and creepmeter stations) and reconstructed displacements from the PCA decomposition as the number of principal components increases. Misfit is quantified from reduced chi-square as defined in equation 2.5.

	Secular		Coseismic		Postseismic		Preseismic	
$1/\lambda$	0.1		0.005		0.04		0.06	
	f	rms	f	rms	f	rms	f	rms
ALOS	5	3.8 (mm/yr)			10	3.0 (mm/yr)		
cGPS	60	4.9 (mm/yr)	6.6	6.7 (mm)	0.3	6.5 (mm)	0.3	10.3 (mm)
creepmeter	60	0.5 (mm/yr)			0.3	2.2 (mm)	0.2	1.8 (mm)
campaign GPS	40	2.6 (mm/yr)					8.9	9.0 (mm/yr)
leveling	0.2	2.6 (mm/yr)			3.9	3.3 (mm/yr)		
accelerometers			4.8	8.3 (mm)				

Table 2.3: root mean square (rms) and normalization factors (f).

Figure 2.16 shows the slip distribution model over this time period. Temporal variation of slip at depth is discussed in more details in section (2.7). The fit to the cumulative displacements measured at the cGPS stations is presented in Figure 2.17, and the fit to the InSAR and leveling data is presented in supplementary Figures (S7 and S8). Time variations of surface displacements predicted by the model are plotted in Figure 2.4 for cGPS and the creepemeter time series at a few sites surrounding the coseismic area. Others times-series predictions can be found in supplementary materials (Figures S1, S2 and S3). The principal slip distribution l and their associated time

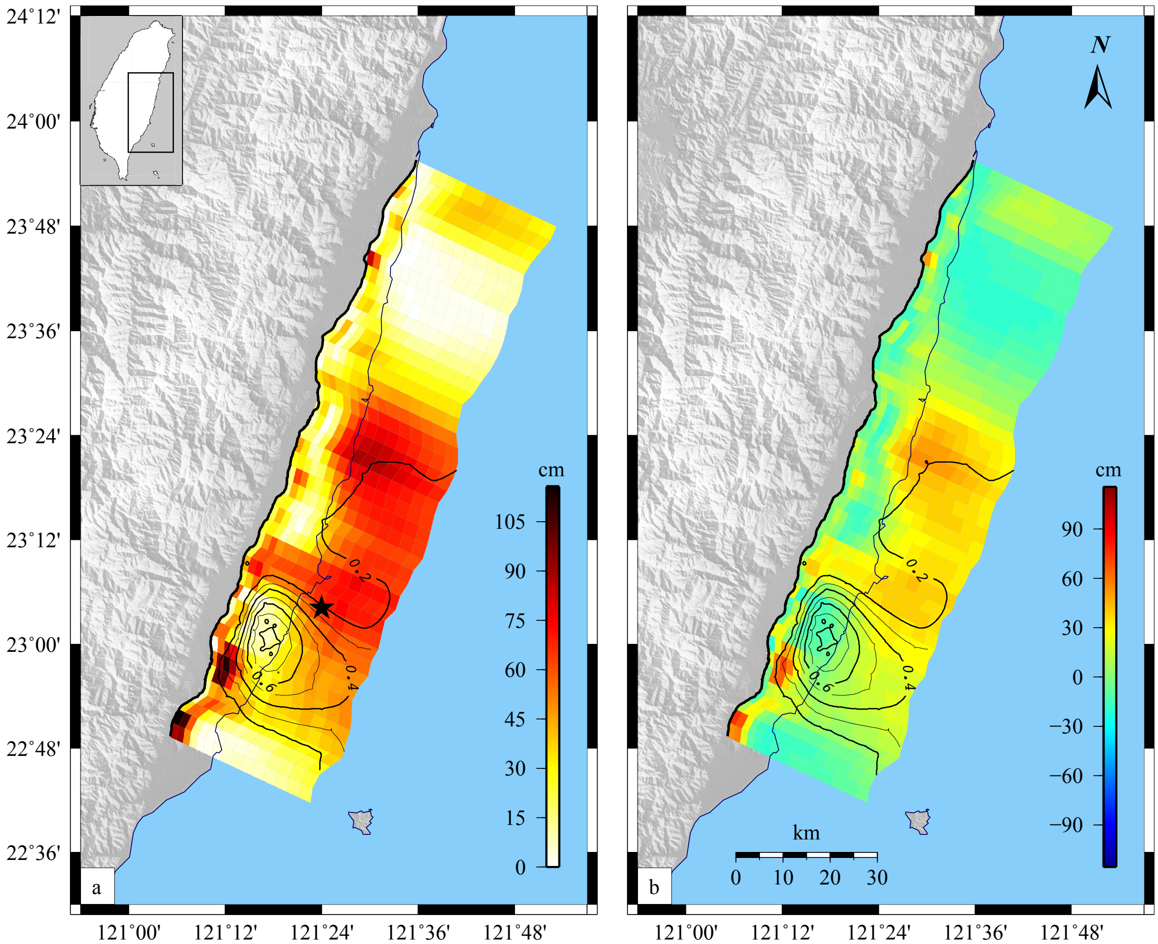

Figure 2.16: Postseismic slip distribution model following the Mw 6.8, Chengkung earthquake of 2003. (a) Cumulative slip on the LVF over the period between 12/11/2003 and 11/26/2010, determined from PCAIM inversion of CGPS and creepmeters time series, leveling data (from 9/1/2007 to 31/20/2010) and PS ALOS cumulative displacement between 1/29/2007 and 6/2/2010. Black star indicates the epicenter of the 2003 Chengkung earthquake. Back curves show contour lines of coseismic slip distribution model of the Chengkung earthquake (Figure 2.14). (b) Difference between postseismic slip and secular slip predicted from the secular model of (Figure 2.10).

functions V are shown in supplementary Figure S6 and S5.

The spatial pattern of aseismic creep in the postseismic period (Figure 2.16a) turns out to be very similar to the secular pattern (Figure 2.10a) with enhanced slip of up to 72 cm around the coseismic rupture (Figure 2.16b). According to this model (Figure 2.16b), afterslip over the 7 years following the Chengkung earthquake have released the cumulative moment of $1.53.10^{19}$ N.m, about 0.8 times the coseismic moment.

2.6.3 Preseismic slip model

We also used the PCAIM procedure to analyze the temporal variation of fault creep before the 2003 earthquake, between January 1997 and December 2003. The spatial resolution is much worse than

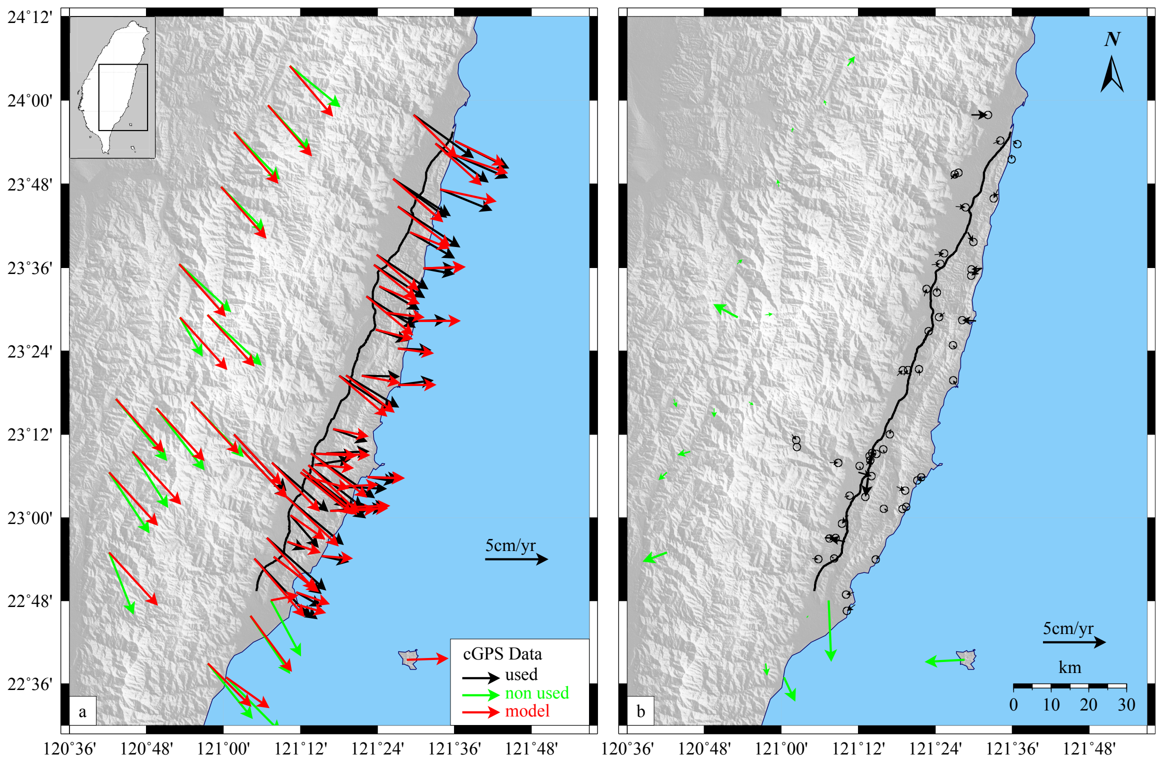

Figure 2.17: Postseismic slip distribution model, fit to geodetic data. (a) Comparison between observed and predicted horizontal displacement over the time period from 12/11/2003 to 11/26/2010. The reference frame is Philippine Sea Plate fixed. The cGPS data which were used or not in the inversion are plotted respectively as black and green arrows. Corresponding predictions of the postseismic slip model of 2.16 are displayeds in red. (b) Residuals from the inversion with corresponding error ellipses. Same color coding as in (a).

in the postseismic period since only 20 continuous GPS stations are available for this time period and among them, only 4 stations have records before 2002. To improve the resolution power of the inversion, we augment the dataset with the campaign GPS measurements which were acquired between 1992 and 1999. These data are treated as sparse in the PCAIM inversion. Creepmeter time series have also been incorporated in this inversion since we have strain measurements across the fault back to 1998.

Variation of the total χ^2 in function of the number of principal components show that 3 components only are significant (*i.e.*, needed to reconstruct the original time series within uncertainties). Most of the signal is explained by the first component (Figure 2.15) which is linear in time (Figure S9 in supplements). The weight put on Laplacian smoothing and renormalization factors are listed in Table 2.6.2 along with the rms values obtained from our inversion. The principal slip distributions l and their associated time functions V are shown in supplementary Figures S10 and S9.

The distribution of slip rate averaged over the preseismic period is plotted in Figure 2.18. Fit to the mean surface velocities at the continuous GPS stations and GPS campaign sites is displayed in Figure 2.19. Time variations of surface displacements predicted by the model are plotted in Figure 2.4 at few continuous GPS stations and for the creepemeter. Comparison of observed and predicted times-series at other stations can be found in supplementary materials (Figures S1, S2 and S3).

As Figure 2.18(b) emphasizes, the interseismic model derived from the PCAIM procedure and the secular slip rate model are very similar. Differences between the two models is most likely related to the lower resolution of the time-dependent interseismic inversion. This modeling indicates that aseismic slip over the 7 years preceding the Chengkung earthquake has been essentially steady-state and released a cumulative moment of $3.86.10^{19}$ N.m, which is about 2 times the coseismic moment which was released during the Chengkung earthquake.

2.7 Slip history on the LVF in the Chengkung earthquake area over the 1997-2011 period

Based on the results presented above it is now possible to describe the time evolution of slip on the LVF over the study period. Here we focus on the Chengkung earthquake area where the temporal variations are the most noticeable. Also, contrary to the Northern portion of the Longitudinal Valley fault, this area is probably not influenced by the Ryukyu subduction zone. The rest of the fault is not showing any significant temporal variation.

Figure 2.20 provides a synthetic view of the time evolution of slip in the Chengkung earthquake area. The map view shows a close-up view of the distribution of interseismic creep rates which was derived from the inversion of the secular surface strain rate (Figure 2.10a). We also show the time

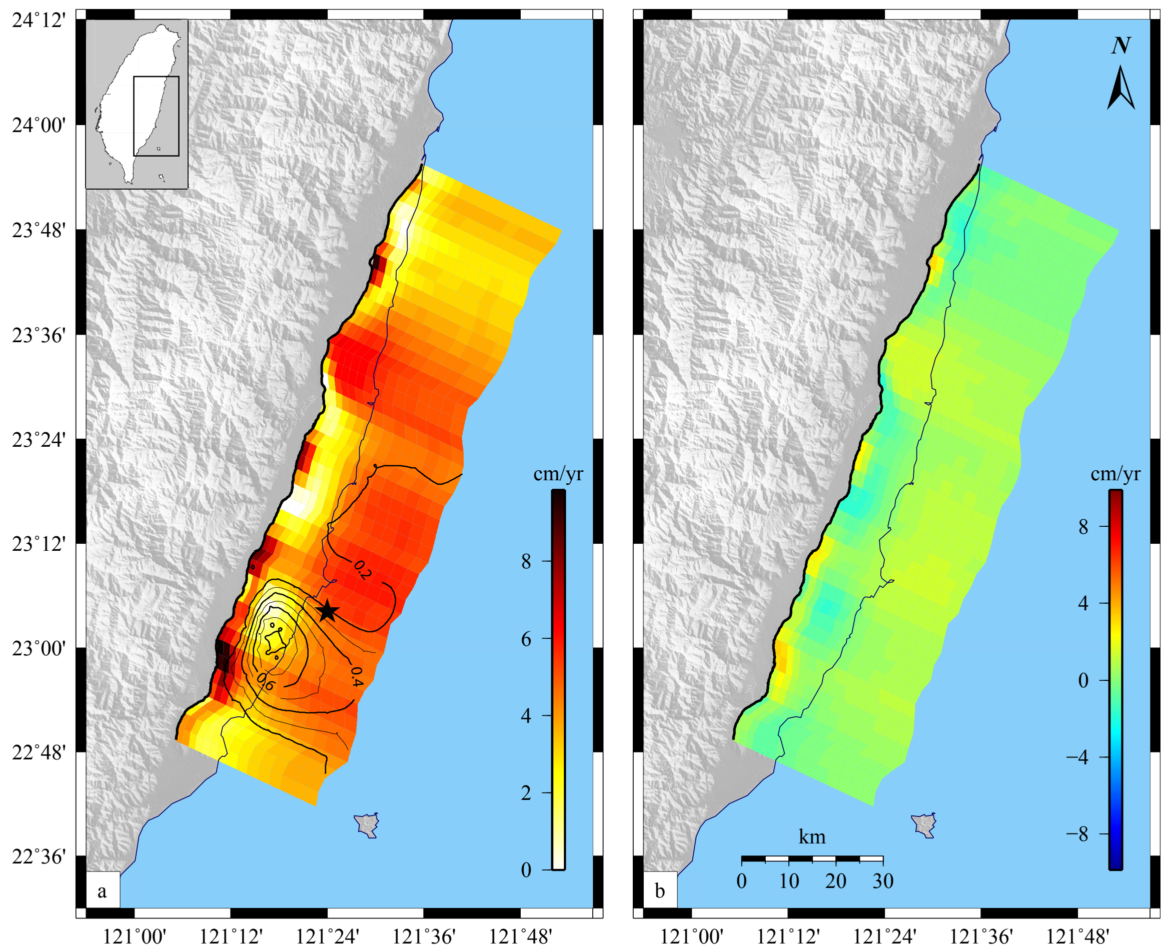

Figure 2.18: Preseismic slip distribution model. (a) Mean slip rate on the fault over the 1/1/1997 to 12/12/2003 period, inferred from PCAIM inversion of the campaign GPS data, the CGPS and creepmeter time series. Black star indicates the epicenter of the 2003 Chengkung earthquake. Back curves are contour lines of the coseismic slip distribution model for the 2003 Mw 6.8 Chengkung Earthquake (Figure 2.14). (b) Difference between preseismic slip rate and secular slip rate predicted from the secular model of (Figure 2.10).

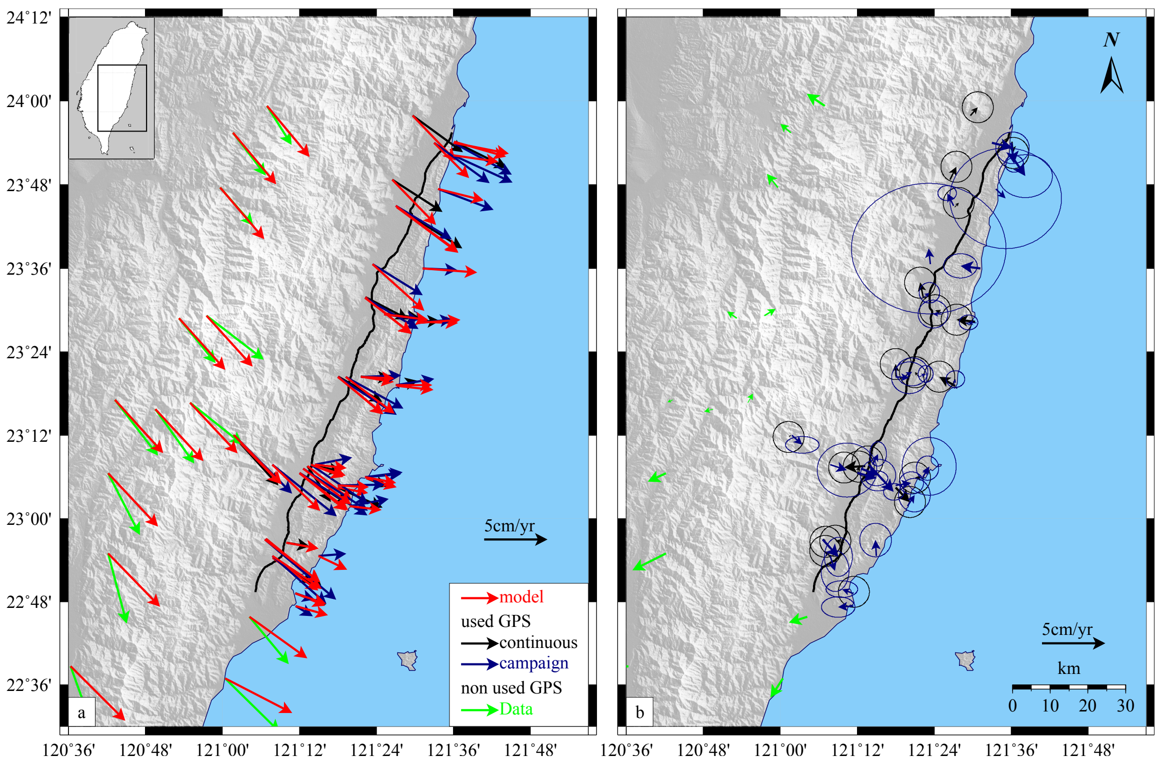

Figure 2.19: Preseismic slip distribution model, fit to geodetic data. (a) Comparison between observed and predicted horizontal velocities, averaged over the time period (from 1/1/1997 to 12/12/2003). The reference frame is Philippine Sea Plate fixed. The GPS data used in this inversion are plotted respectively as dark blue and black arrows for the campaign and continuous GPS measurements. Green arrows stand for the GPS stations that were not used in the inversion but which are plotted for reference. Corresponding predictions of the interseimic coupling model are displays in red. (b) Residuals from the inversion with corresponding error ellipses. Same color coding as in (a).

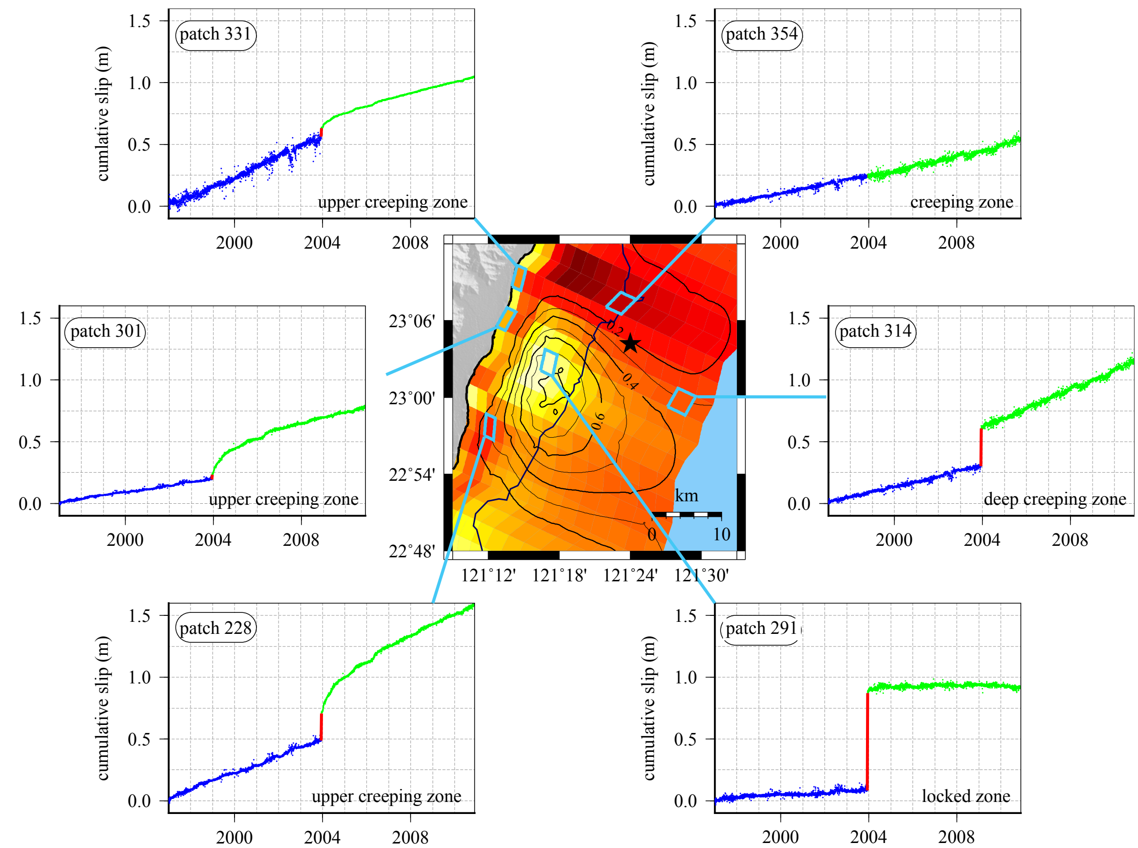

Figure 2.20: Slip at depth through time obtained from combining PCAIM inversions of pre- and post-seismic period and coseismic slip due to the Chengkung earthquake. Map view shows a close-up view of the secular slip rate distribution over the whole study period (see Figure 2.10a for location), with contour lines of the coseismic slip model (black lines) and epicenter (star) of the 2003 Chengkung earthquake. Graphs around the map view show the time evolution of slip at 6 patches along the direction of the slip vector predicted by the block motion of the Coastal Range relative to the Central Range. Patch 331, 301, and 228 sample the upper creeping zone. Patch 291 is characteristic of the zone which was locked before the Chengkung earthquake, slipped during the event and relocked immediately after. Patches 314 and 354 illustrate the behavior of deeper fault portion which is most poorly resolved.

evolution of slip at a number of representative patches, retrieved from combining the source model of the earthquake with the PCAIM models for pre- and post-seismic periods. The cumulative slip vector at each epoch is projected on the direction of the long term slip vector predicted by the block motion of the Coastal Range relative to the Central Range. Our model indicates that over the 14 years between 1997 and 2011 this fault area has slipped by a total of 1 m to 1.5 m. This is approximately the cumulative slip for that period of time expected from the long term oblique convergence between the Coastal Range and the Central Range. The results show that slip resulted from a combination of steady creep, unsteady creep and seismic slip in proportions that vary in space.

Comparison of the secular pattern of creep rate with the slip contour lines of the coseismic rupture during the Chengkung earthquake clearly shows that the rupture extent coincides closely with an area that has remained mostly locked in the interseismic period and relocked immediately after. Time evolution of slip for patch 291 is instructive in that regard (Figure 2.20). This patch lies at depth of about 15 km in the middle of the zone with peak seismic slip. According to our model, this patch slipped by about 0.8 m and relocked immediately after the earthquake. The earthquake nucleated at the edge of this locked zone (see epicenter in Figure 2.20), ruptured this entire patch and did not propagate much into the surrounding creeping areas, except at depth where the overlap could be partially due to the smoothing induced by the regularization of our inversions, as Figure 2.7 illustrates. The rupture failed in particular to propagate across the shallow portion of the fault at depth less than about 7 km (see slip history at patch 301 in Figure 2.20) in agreement with the absence of surface ruptures observed in the field (*Lee et al.*, 2006) and the other source models of this earthquake (*Wu et al.*, 2006a; *Hu et al.*, 2007; *Wu and Wu*, 2007; *Mozziconacci et al.*, 2009).

The secular slip rate on the upper part of the fault, which is creeping in the interseismic period as the InSAR and creepmeter measurements indicate, varies along strike (Figure 2.20). Patches 331 and 228 show similar behavior for the interseismic period: high creep rate was inferred (8.2 cm/yr for 331 and 6.7 cm/yr for 228) whereas patch 301 displays smaller creep velocity (2.9 cm/yr), likely because it is in the stress shadow of the locked segment (see for example *Hetland and Simons* (2010) for a modeling study illustrating this effect). During coseismic patches 331 and 301, which corresponds to the uppermost part of the fault, record only few centimeters of slip. On the contrary, patch 228, which stands at 9 km depth, recorded a coseismic jump of $\sim$ 20 cm. The creep rate increased abruptly right after the earthquake and then relaxed, leading to an approximately logarithmic increase of slip with time, but at different rate for the 3 patches. The maximum displacement is recorded at patch 228, where the slip rate after 7 years is 1.2 times higher than before December 2003. Patch 301 also slip at faster rate (4.8 cm/year, *i.e* 1.6 times faster), but patch 331 on the contrary undergoes a decrease in slip velocity after the Chengkung earthquake (4.8 cm/yr).

Evidence for transient afterslip at depth below the rupture is less clear due to the poor resolution of the inversions. No transient is seen at patch 354, which seems to have been creeping at a nearly constant rate (3.3cm/yr) throughout the study period. Patch 314 which, according to our model has been creeping in the preseismic period at 4.8 cm/yr, slipped during the Chengkung earthquake (0.3 m) and creeps more rapidly in the post-seismic period (6.7 cm/year) but we do not observe the typical logarithmic behavior seen at shallower depth, suggesting a possible way longer relaxation time. Nevertheless it is hard to tell if this observation is really required by the data and warrants interpretation.

2.8 Discussion

2.8.1 Spatial distribution of seismic and aseismic creep, role of the Lichi Mélange

The dataset assembled in this study demonstrates that most of the southern portion of the LVF is creeping at the surface, though at a rate lower than the long term slip rate required by the block motion of the Coastal Range with respect to the Central Range. By contrast, no surface creep is detected along the northern half of the LVF, which displays a high stress-build up (Figure 2.10b).

Comparison with surface geology support earlier inferences (e.g., *Hsu et al.*, 2009a) than the Lichi Mélange would be responsible for promoting aseismic creep. This clay-rich formation, interpreted as a collision ḿlange (*Chang et al.*, 2000, 2001, 2009; *Huang et al.*, 2006b, 2008), crops out in the Coastal Range and seems to fringe the creeping segment of LVF (Figure 2.2a). This formation does not extent along the northern segment of the LVF, where only isolated outcrops have been interpreted to correspond to that particular formation (*Teng*, 1980a). It is noteworthy that the seismic crisis of 1951, with its 4 $M_w > 6.8$ shocks, did produce surface ruptures only along the northern portion of the LVF (*Shyu et al.*, 2007; *Lee et al.*, 2008). The southern segment of the fault can nevertheless also produces large seismic event as the Chenkung earthquake demonstrates. However the rupture occurred in the 10-20km depth range and didnt reach the surface. Our interseismic model indicates that the earthquake actually ruptured a fault patch that was locked before 2003 and relocked immediately after and is surrounded by a zone that is dominantly creeping. The Lichi ḿlange is an important factor controlling along strike variations of creep rate but whether it is through the intrinsic properties of its dominant minerals or whether it is related to the hydrological properties of this formation is unclear at this point.

2.8.2 Seismic and aseismic slip budget, implication for the return period of $M_w > 6.8$ earthquakes on the LVF

Our modeling results allow estimating the relative proportion of seismic and aseismic slip on the LVF and draw inferences regarding the return period of large earthquakes in this area. The reader should be aware of the large uncertainties involved in this discussion. It is particularly difficult to formally take into account all the possible sources of errors due not only to the measurements uncertainties but also to the modeling assumptions. For example, it is probably not correct to assume that the CeR and CoR blocks can be consider rigid in the long run nor to neglect the strain associated with the complicated junction with the Ryuku subduction zone north of the Longitudinal Valley. However it is still worth illustrating the kind of questions which can be addressed based on the modeling attempt presented in this study.

Interseismic strain implies a rate of accumulation of slip-potency ($SP_{deficit}$), or equivalently, moment deficit which can be computed from integrating the slip-rate deficit over the locked fault zones (section 2.4.3 and 2.4.2):

$$M_{0_{deficit}} = \mu.SP_{deficit} = \mu \sum_i V_i.ISC_i.S_i, \tag{2.14}$$

where S_i is the area of the subfault, V_i is the long-term slip rate inferred in section 2.4.2 based on the CeR/CoR pole and the interseismic coupling coefficient ISC_i quantifies the degree of locking defined in section 2.4.3. We estimated the moment deficit rate to be $2.77.10^{18} N.m.yr^{-1}$ for the whole LVF. If we consider the southern section only, with the upper boundary defined as the transition between the creeping section and the locked zone in the north (Figure 2.10b), we obtain a value of $1.12.10^{18} N.m.yr^{-1}$ (Table 2.8.2). Then given the cumulative moment released by the coseismic slip and the following afterslip (Table 2.8.2) inferred in this study, the return period of earthquake similar the Chengkung earthquake can be estimated from the equation:

$$T = \frac{M_{0_{coseismic}} + M_{0_{postseismic}}}{M_{0_{deficit}}}. \tag{2.15}$$

Based on this equation, we get a return period of $\sim$ 13 years if we considered the whole LVF, and $\sim$ 34 years for the southern section. These estimate seems reasonable given that 5 earthquakes with $M_w \geq 6.8$ occurred over the last century (*Shyu et al.*, 2007; *Chung et al.*, 2008; *Lee et al.*, 2008; *Wu et al.*, 2008a). Therefore, this analysis shows there is no need for larger or more frequent earthquakes than those known historically to balance the deficit of slip due to the pattern of locking on the LVF in the interseismic period.

	Models	Moment	equivalent M_w
ISC (deficit)$_a$	all LVF	$3.31.10^{18}$ N.m.yr^{-1}	6.28
	south LVF	$1.35.10^{18}$ N.m.yr^{-1}	6.02
Preseismic$_a$	all LVF	$7.69.10^{18}$	6.52
	south LVF	$5.20.10^{18}$	6.41
Coseismic	all LVF	$2.50.10^{19}$ N.m	6.86
	south LVF	$2.26.10^{19}$ N.m	6.83
Postseismic$_b$	all LVF	$1.92.10^{19}$ N.m	6.79
	south LVF	$2.34.10^{19}$ N.m	6.85

Table 2.4: Moments and moment Magnitudes inferred from inversion models. (a) Moments and moment Magnitudes values are cumulated over one year. (b) cumulative value after $\sim$ 7 years, for the afterslip only, *i.e* minus the secular model.

It is then instructive to compare our estimate of the return period of a $M_w > 6.8$ earthquakes on the LVF with the frequency-magnitude distribution of instrumental earthquakes in the area, displayed in Figure 2.21. For that purpose we used the 1991-2010 seismicity catalog from *Wu et al.*

(2008b), selecting events laying on the southern half portion of the LVF, where our model is best constrained (see seismicity map in Figure S12). Seismic data follows the Gutenberg-Richter law:

$$\log_{10}(N(m > M_w)) = a - bM_w, \tag{2.16}$$

where N is the number of events which have a moment magnitude greater or equal to M_w; a and b are constants with a typical value of 1 for the b parameter in seismically active regions. We divided the dataset in three time periods: from 1/1/1991 to 12/31/2009 (all catalog), from 1/1/1991 to December 9^{th} 2003 (before 2003 Chenkung Earthquake) and from December 10^{th} 2003 and thereafter. Above their magnitude of completeness (which is about 1.8) those three subsets of the main catalog return a similar b value of 0.95 for the complete dataset to 0.94 and 0.89 for seismicity selected before and after the main shock respectively (Figure 2.21). The return period of Chengkung-type earthquake inferred from this study can be plotted in this diagram (Figure 2.21). It shows a nice consistency with the instrumental catalog since the Gutenberg-Richter distribution defined above yields a return period of $\sim$ 24 years for $M_w = 6.8$ earthquake if we were considering the whole LVF and $\sim$ 36 years if we only selects earthquakes in the southern section of the LVF (Figure 2.21).

We can also estimate the fraction of slip potency (or equivalently release moment) which results from aseismic (α), or seismic (γ) over the long term average, assuming that known seismicity is representative of the long term behavior. The fraction of aseismic slip is

$$\alpha = \frac{T.\sum_i V_i.(1 - ISC_i).S_i + M0_{postseismic}/\mu}{T.\sum_i V_i.S_i}. \tag{2.17}$$

This calculation tends to provide an overestimate as it assumes that all of the measured geodetic strain results from aseismic creep, except for the effect of the Chengkung earthquake. We estimated this fraction to about 77% for the whole LVF. If we focus on the southern portion where the model is more reliable (not biased by interseismic strain associated with the Ryuku subduction zone), we get an even larger value of 92%. This estimate is probably representative of the long term average as the study period is long enough compared to the return period of large earthquakes so that the average interseismic creep pattern is reasonably well constrained, and the contribution of transient aseismic creep due to afterslip following the Chenkgung earthquake is only a small fraction of the total budget. This estimate has a large uncertainty, in relation with uncertainties on our slip models among other factors. The fraction of seismic slip is :

$$\gamma = \frac{\sum M_{0_i}}{\mu.t_{cat}.\sum_i V_i.S_i}, \tag{2.18}$$

where the numerator accounts for the moment released by all earthquakes on the LVF during the study period t_{cat}. This quantity can be bracketed if we consider on one end only the Chengkung

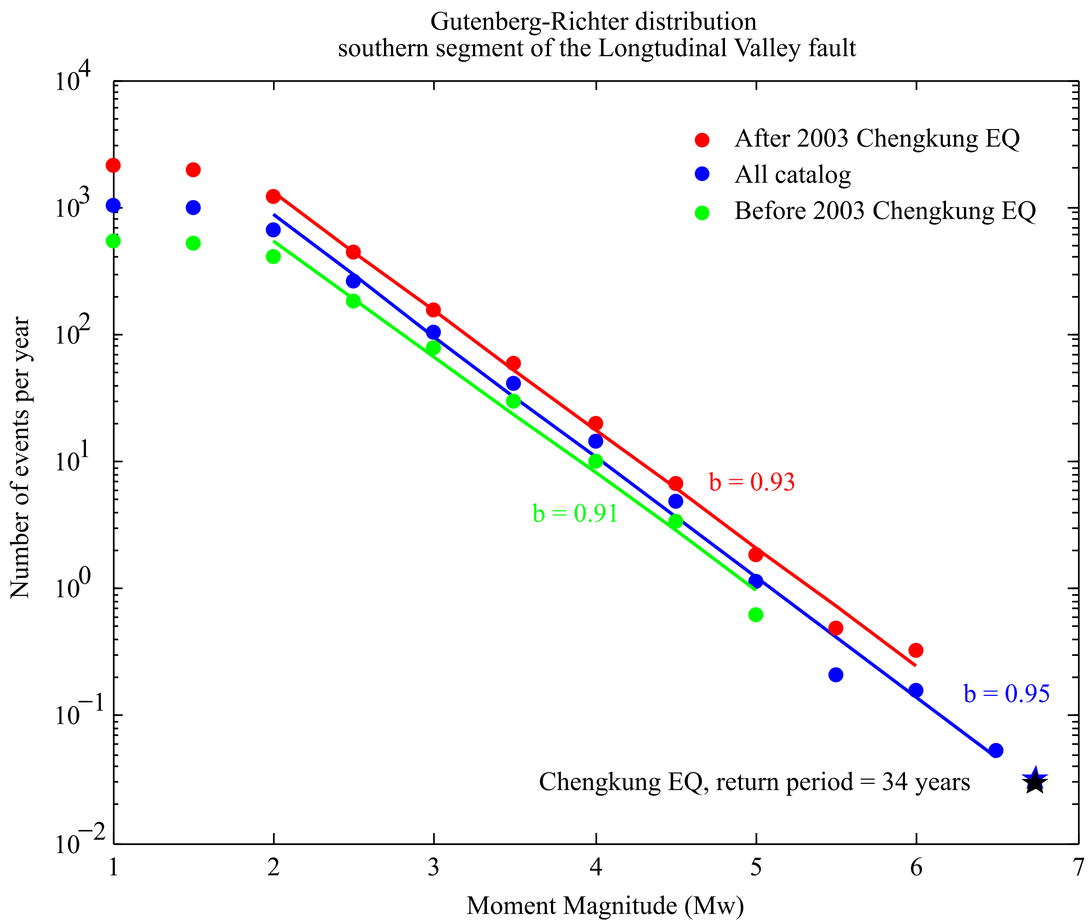

Figure 2.21: Frequency-magnitude distribution of seismicity from 1991 to 2010 on the Longitudinal Valley, using the catalog from *Wu et al.* (2008b), for the southern portion of the fault (see S12a in supplements for location). The graph shows, in ordinate, the number of events with moment magnitude equal or larger than a given value reported in abscissa. We divided the catalog in three time periods: in blue from 1991 to 2010 (all catalog), in green from 1991 to December 9^{th} 2003 (before 2003 Chenkung Earthquake) and in red from December 10^{th} 2003 and thereafter. Lines are Gutenberg-Richter distribution computed for magnitude $M_w \geq 2$. Returned b value are respectively 0.95 for the all catalog, 0.92 before the Chengkung earthquake and 0.95 for seismicity selected after the main shock. Black star shows the return period computed from this study for Chengkung-type earthquake ($M_w = 6.8$) from balancing the seismic and aseismic slip budget on the LVF. .

earthquake, which unambiguously occurred on the LVF, and on the other end assume that all the earthquakes which recorded in the study area over the study period occurred on the LVF and add their scalar seismic moments by extrapolating the number of earthquakes with magnitude below the detection threshold based on the Gutenberg-Richter law (Figure 2.21). We thus estimate the numerator to between $1.87.10^{19}$ and $2.77.10^{19}$ for the all fault, and between $1.68.10^{19}$ and $2.40.10^{19}$ for the southern segment. The fraction of seismic slip is then estimated to between 14% and 21% if all the LVF is considered. It is estimated to between 20% and 28% considering only the southern section where most of the aftershocks occur (see supplement S12). This estimate is not necessarily representative of the long term average given that the earthquake catalog does not cover several earthquake cycles so that the moment released by the largest earthquakes on the LVF in the long run is poorly constrained. Despite all the uncertainties in those estimate it is interesting to note that the slip budget approximately closes up.

2.9 Conclusion

This study demonstrates that a large fraction of the long term slip budget on the Longitudinal Valley Fault (LVF) in the 0-26km seismogenic depth range (as defined by local seismicity) is actually the result of aseismic creep. We estimate that fraction to about 80-90%. The spatial pattern of aseismic creep on the LVF is very heterogeneous, showing both along dip and along strike variations. Creep is observed at the surface along the southern portion of the LVF where it seems to correlate with Lichi Mélange. The Mw 6.8 Chenkgung earthquake of 2003 ruptured entirely a 12.5 km x 15.8 km patch that had remained locked in the interseismic period which extends at depth between 8 and 20 km. The earthquake seems to have nucleated at the boundary of the locked zone, where stress must build up fast in the interseismic period. Then it propagated through the locked patch but fail to propagate much into the surrounding creeping areas Figures 2.10, 2.14 & 2.18). Afterslip, due to enhanced creep in the immediate vicinity of the rupture, released a moment equivalent to 0.8 time the seismic moment of the earthquake and increased approximately logarithmically with time. This time evolution is consistent with the time evolution of afterslip excepted from velocity-strengthening friction (*Marone et al.*, 1991; *Perfettini and Avouac*, 2004). These observations suggest that the location and the extent of seismic asperities are largely controlled by permanent rheological properties of the fault zone, which, in the present case, seems to relate to the lithology.

To first order, this simple picture compares well with theoretical models of seismic cycle based of lateral and depth variation of frictional properties of faults (e.g. *Lapusta et al.*, 2000; *Rice and Ben-Zion*, 1996; *Scholz*, 1998). In those models, aseismic slip occurs in velocity strengthening areas during the interseismic period until instability occurs at the boundary between velocity strengthening and velocity-weakening zones, leading to the nucleation of seismic events that ruptures previously locked velocity weakening zones. Depending on the size and on the frictional properties of the velocity strengthening zones, seismic events are able to propagate through the creeping sections or are stopped by them (*Kaneko et al.*, 2010). Then, relaxation of coseismic stress results in acceleration of aseismic slip in the velocity strengthening areas until it comes back to interseismic rates. Our study thus confirms the suggestion that aseismic patches tend to play a key role in arresting seismic ruptures, presumably because aseismic creep prevent stress build up and because of the presumably rate-strengthening rheology absorbs energy during seismic rupture propagation (*Kaneko et al.*, 2010). We see no clear evidence that Thermal Pressurization could have facilitated propagation of the rupture into the creeping segment as could happen according to numerical simulation (*Noda and Lapusta*, 2010, 2013). The LVF thus stands out as a candidate example where a dynamic model of the seismic cycle could be designed and calibrated from comparison with geodetic and seismic data as has been done on the Parkfield segment of the San Andreas Fault (*Barbot et al.*, 2012).

Seismic and aseismic slip on LVF - Supplementary material

July 23, 2013

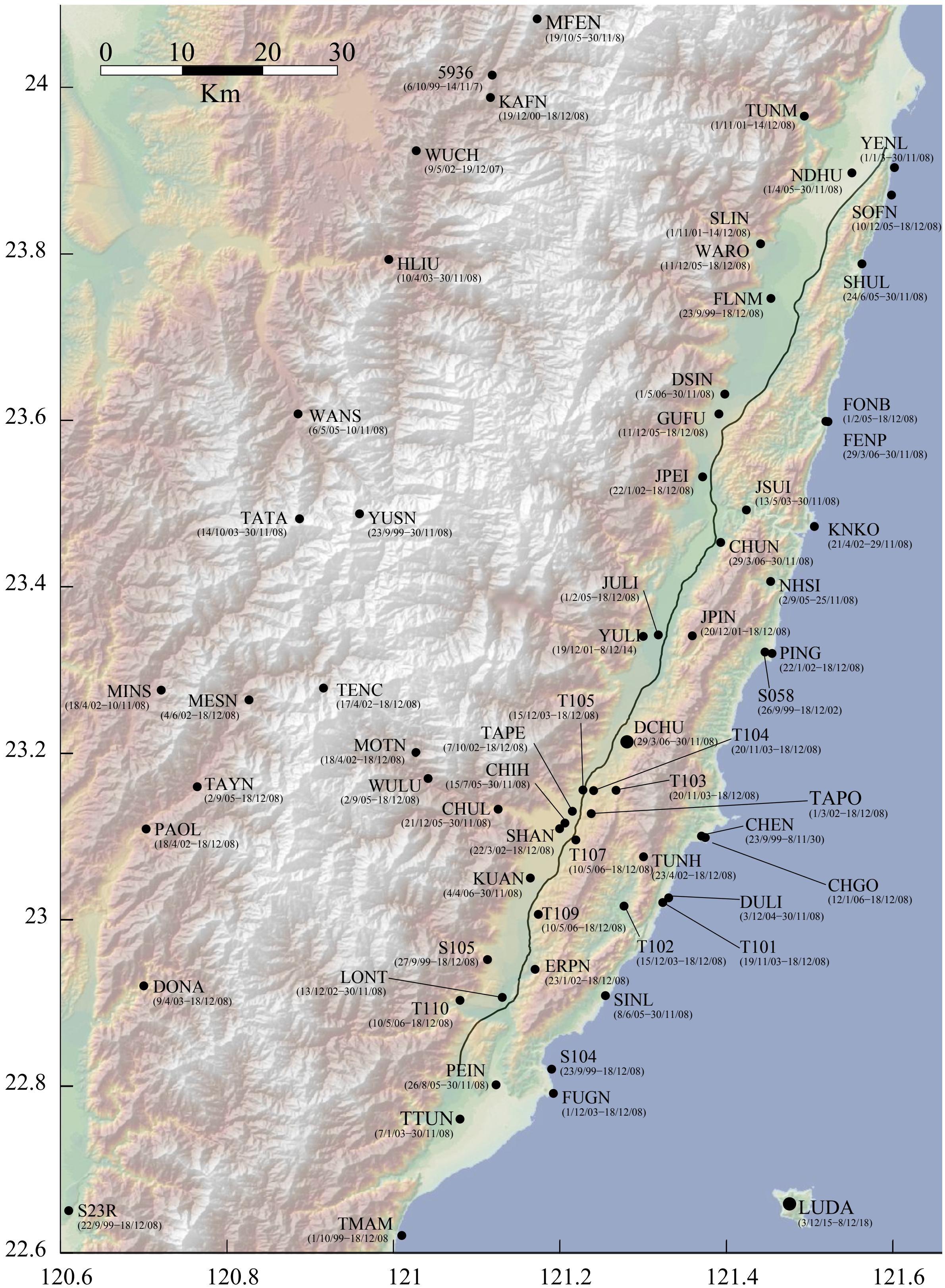

Figure S1: Locations of continuous GPS stations with the corresponding date of records.

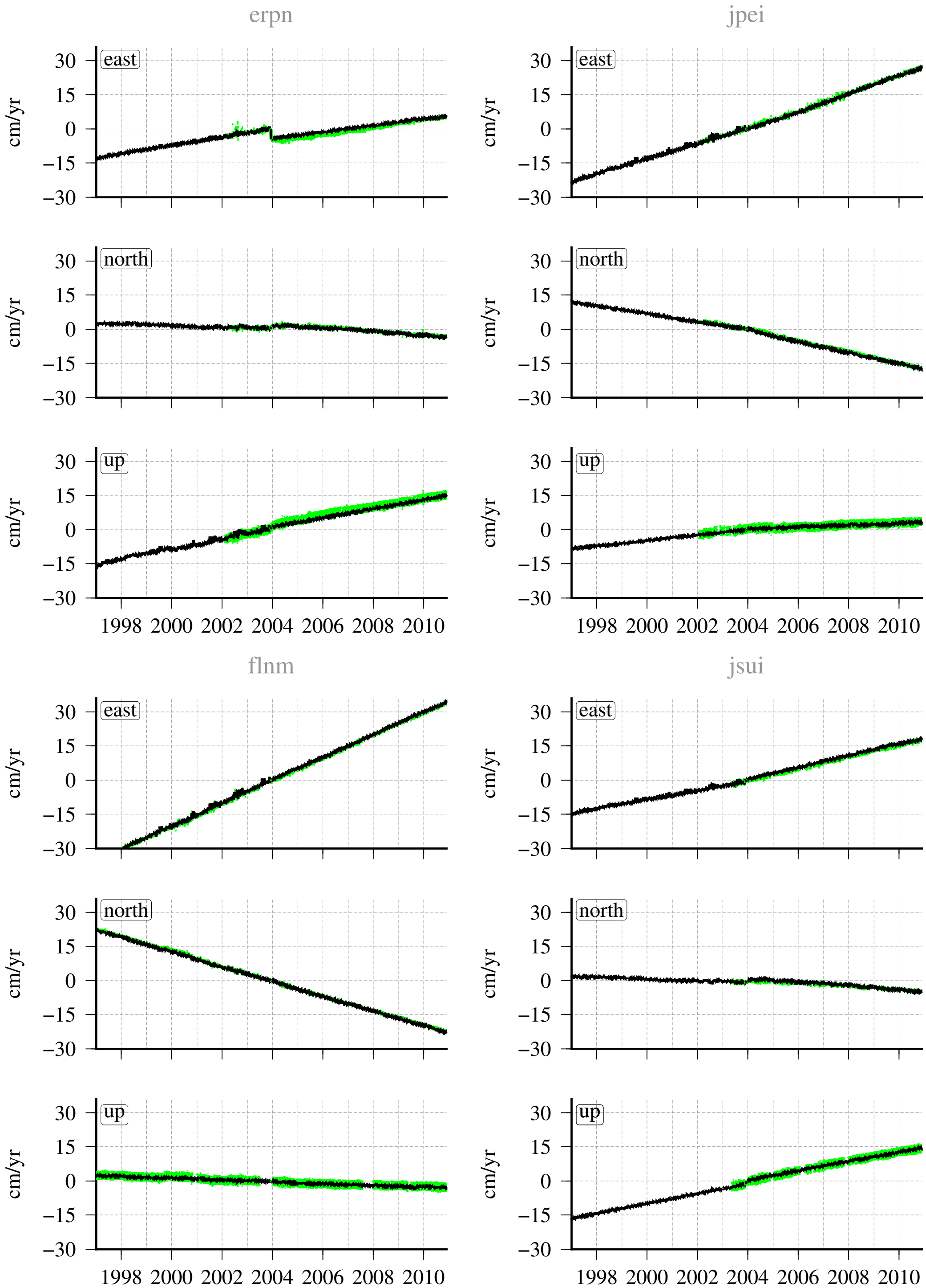
erpn
jpei
flnm
jsui
east
north
up
cm/yr
30
15
0
–15
–30
1998
2000
2002
2004
2006
2008
2010

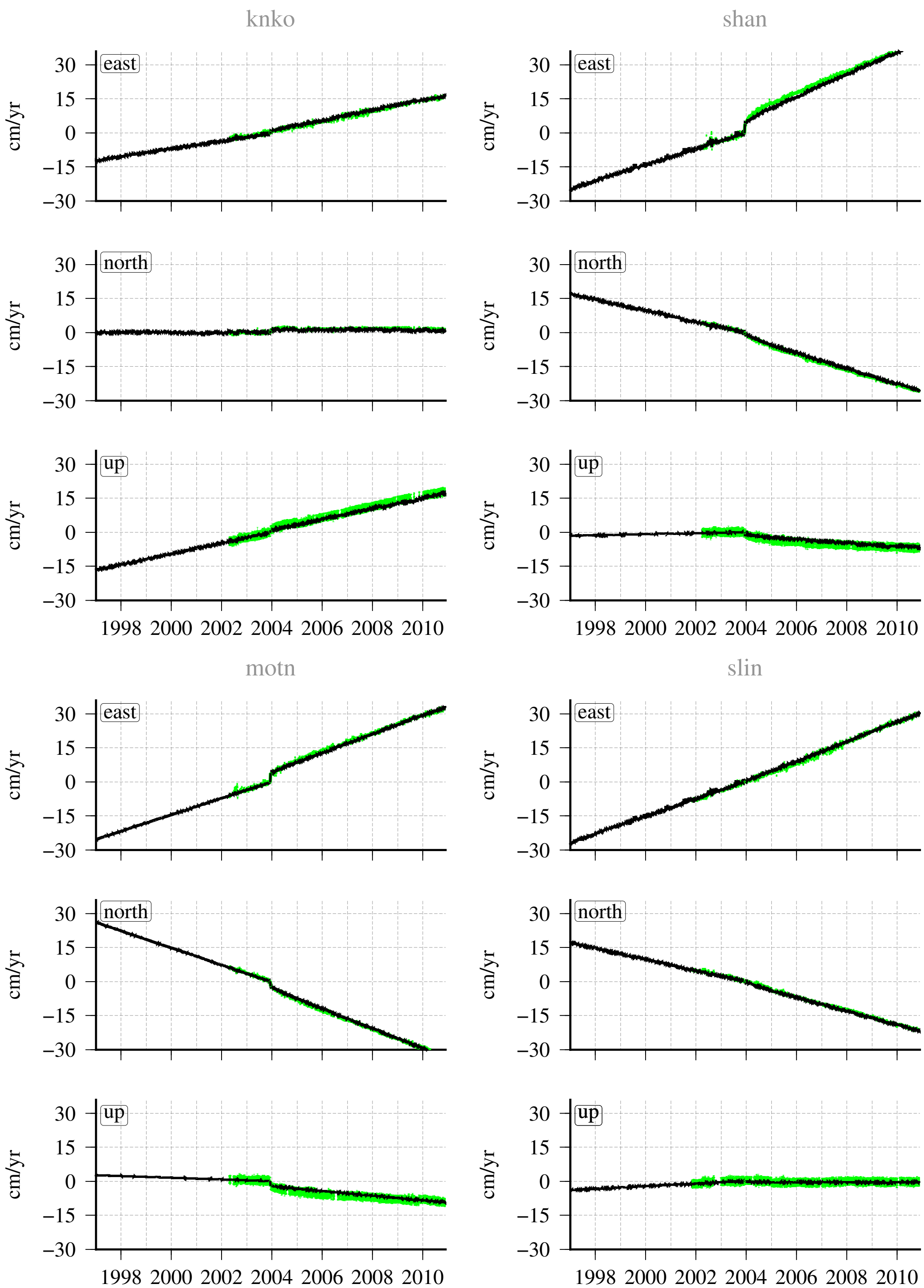
knko
shan
motn
slin
east
north
up
cm/yr
30
15
0
–15
–30
1998 2000 2002 2004 2006 2008 2010

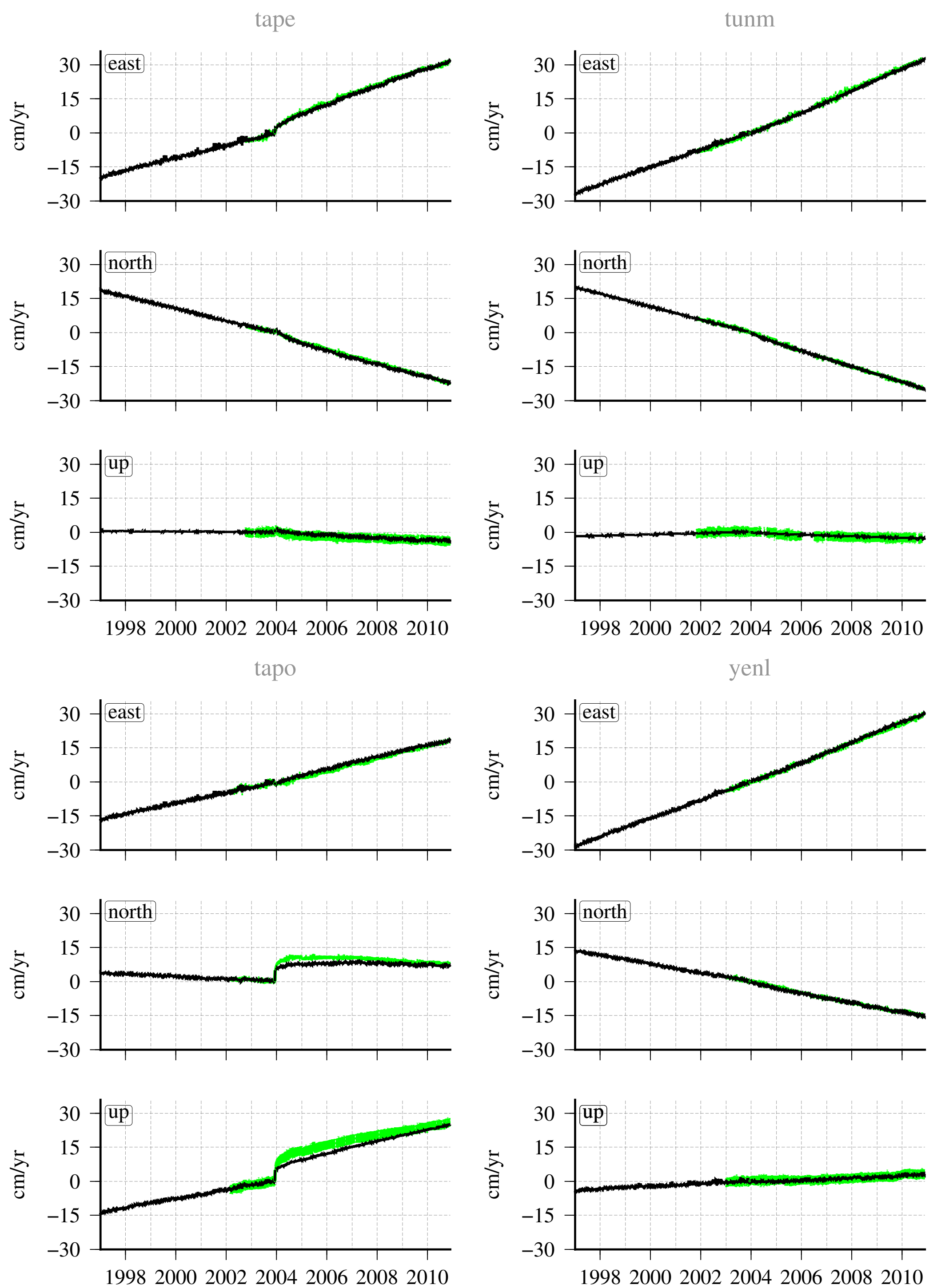
tape
tunm
east
north
up
cm/yr
30
15
0
−15
−30
1998 2000 2002 2004 2006 2008 2010
tapo
yenl

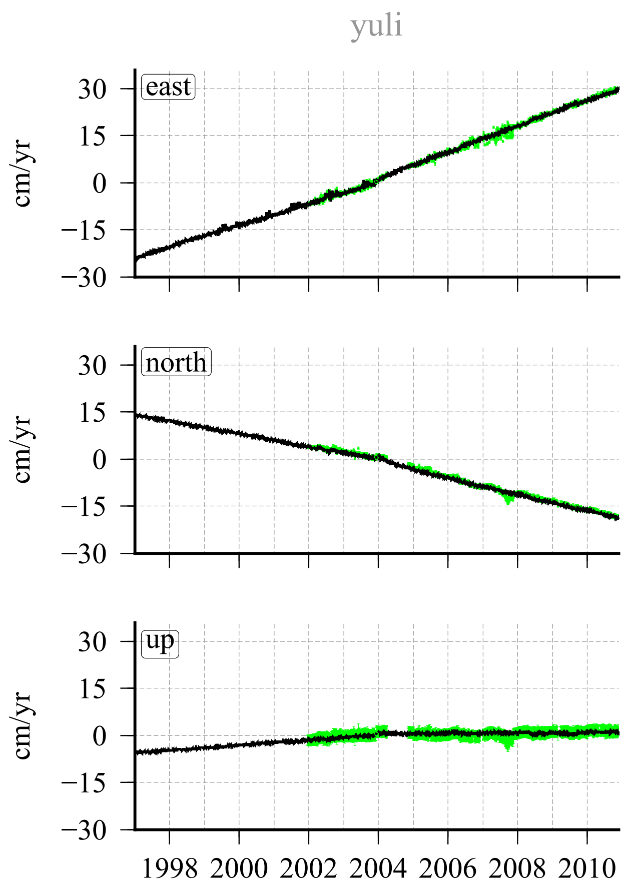

Figure S2: Plots of cGPS times series for which we have records before and after the 2003 Chengkung earthquake. See Figure S1 for location. Green dots with 1-sigma errors bars represents the original dataset. Predictions from the inversion of coseismic slip and PCAIM inversions of preseismic and postseismic periods are plotted in black. To facilitate the comparison we have corrected the model predictions for the mean residual velocities over the pre and post-seismic period represented in Figures 17 and 19.

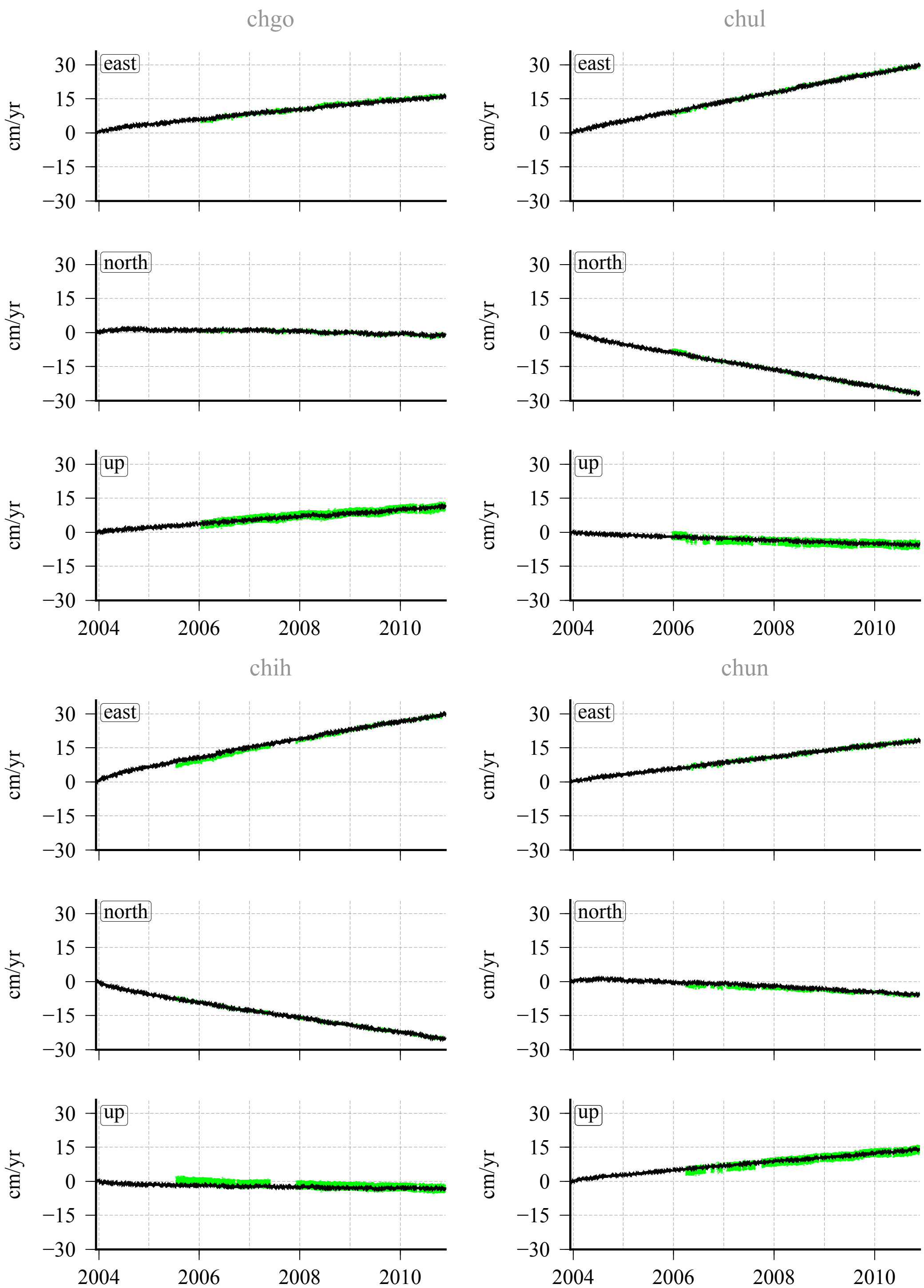
chgo
chul
chih
chun
east
north
up
cm/yr
30
15
0
−15
−30
2004
2006
2008
2010

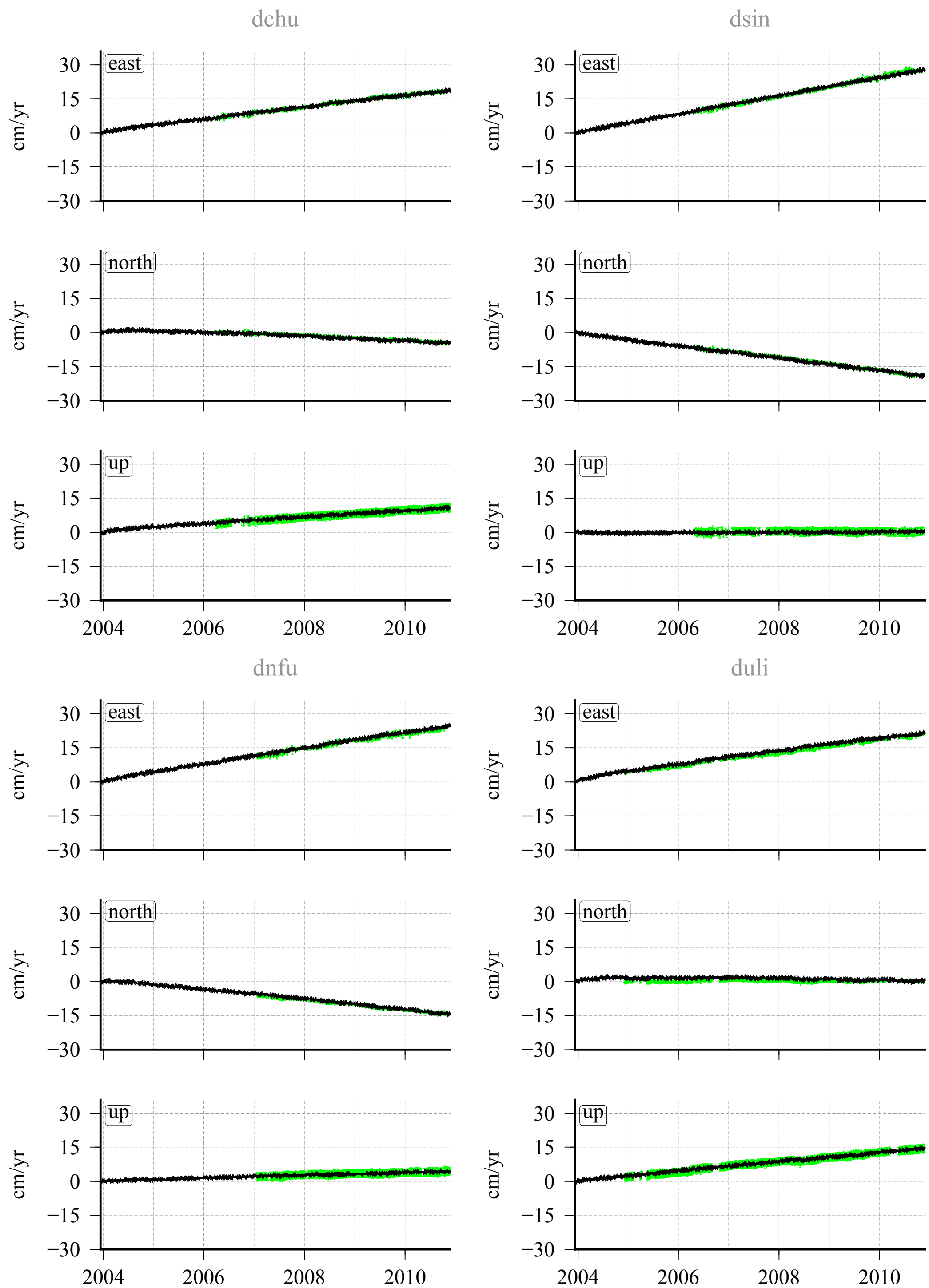
dchu
dsin
dnfu
duli
east
north
up
cm/yr
30
15
0
−15
−30
2004
2006
2008
2010

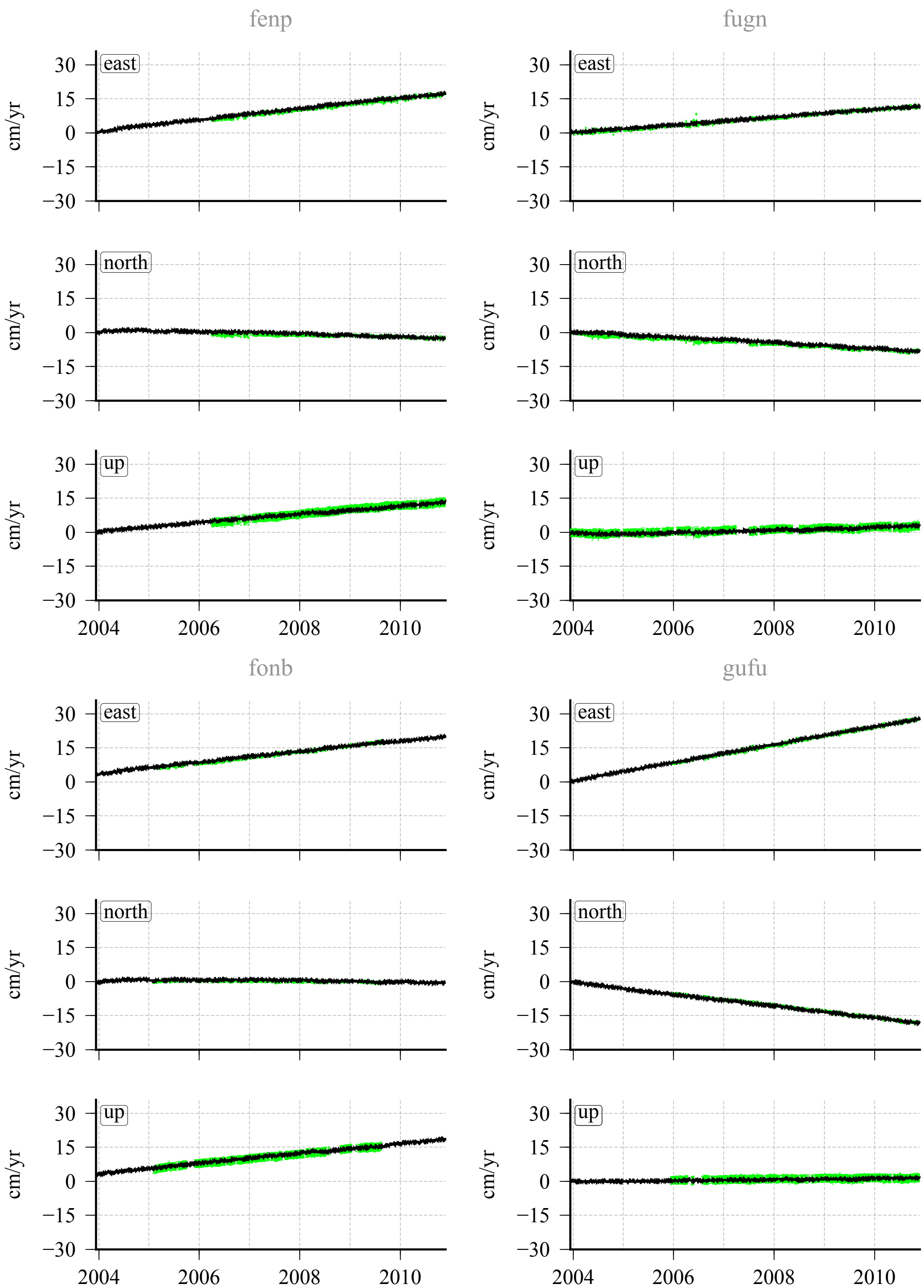
fenp
fugn
fonb
gufu
east
north
up
cm/yr
30
15
0
−15
−30
2004
2006
2008
2010

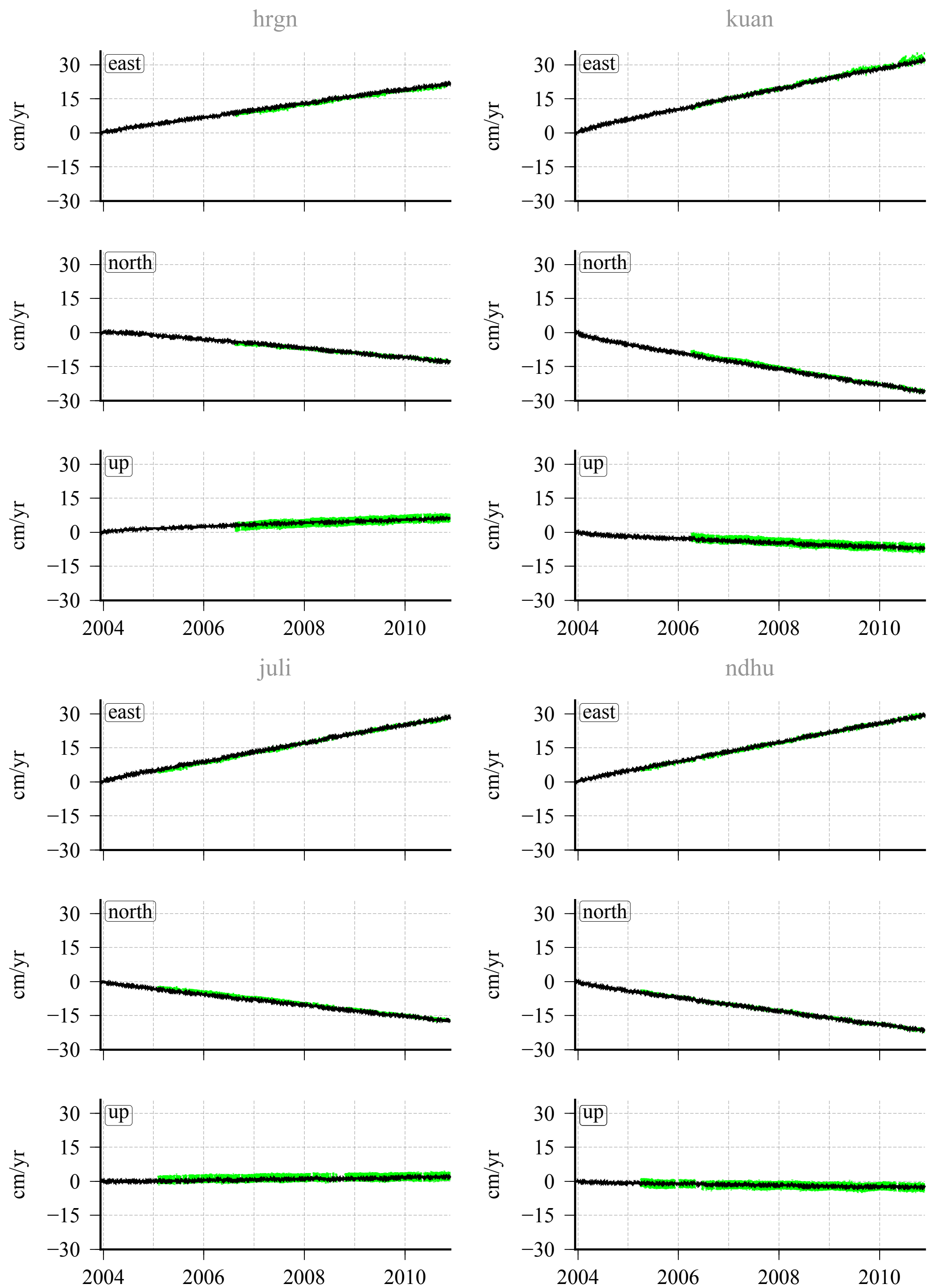
hrgn
kuan
juli
ndhu
east
north
up
cm/yr
30
15
0
−15
−30
2004
2006
2008
2010

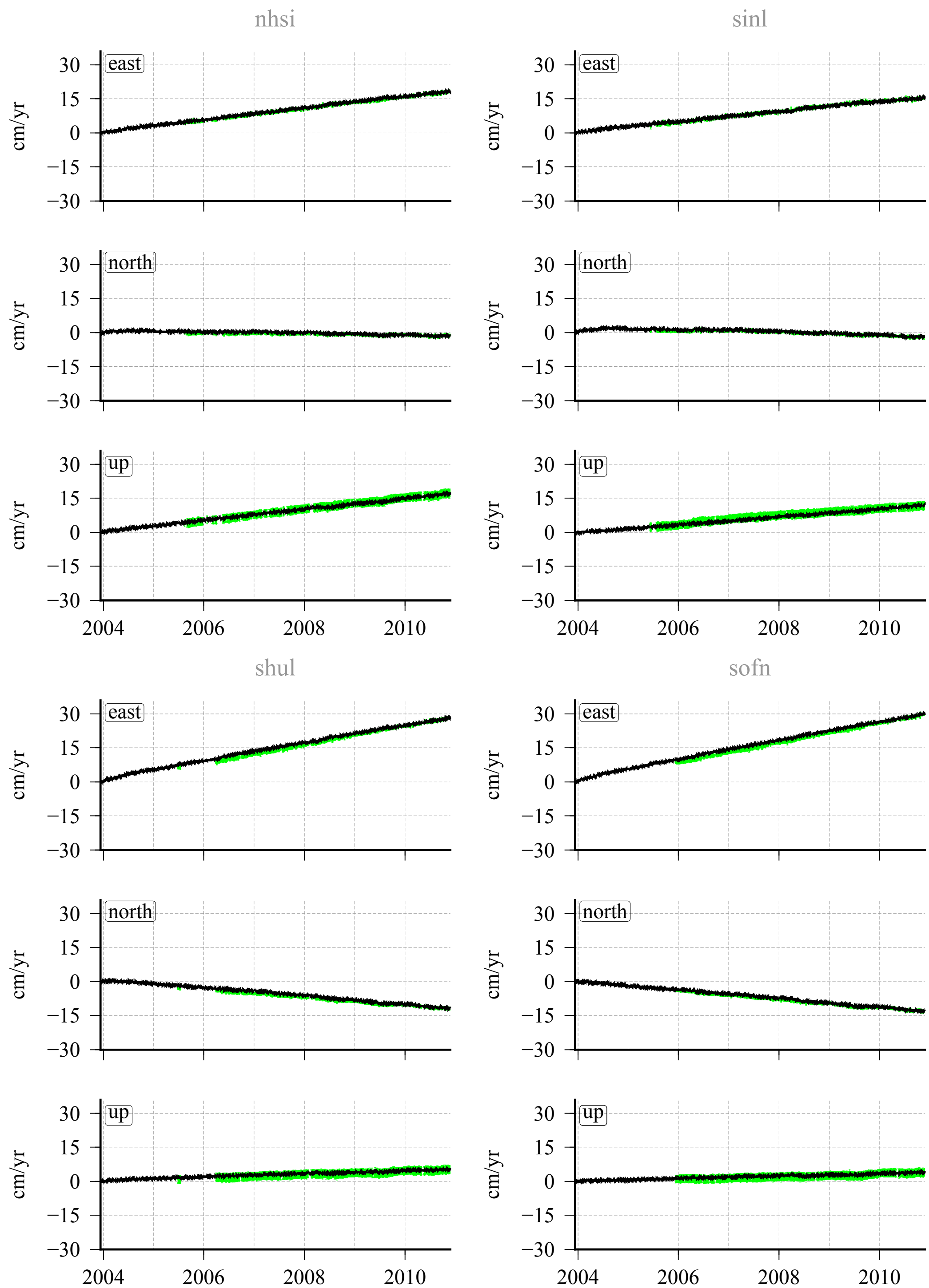
nhsi
sinl
shul
sofn
east
north
up
cm/yr
30
15
0
−15
−30
2004
2006
2008
2010

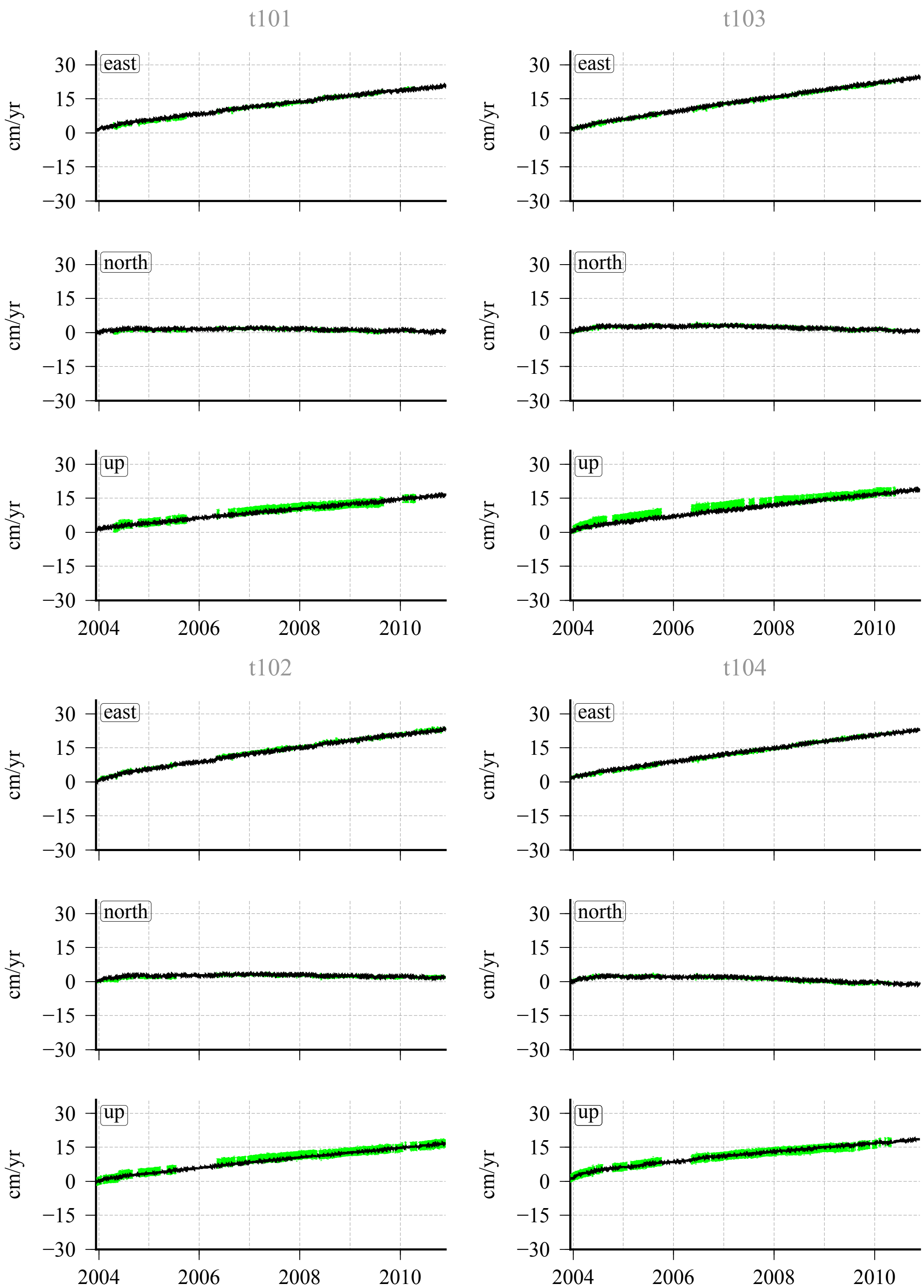
t101
t103
t102
t104
east
north
up
cm/yr
30
15
0
−15
−30
2004
2006
2008
2010

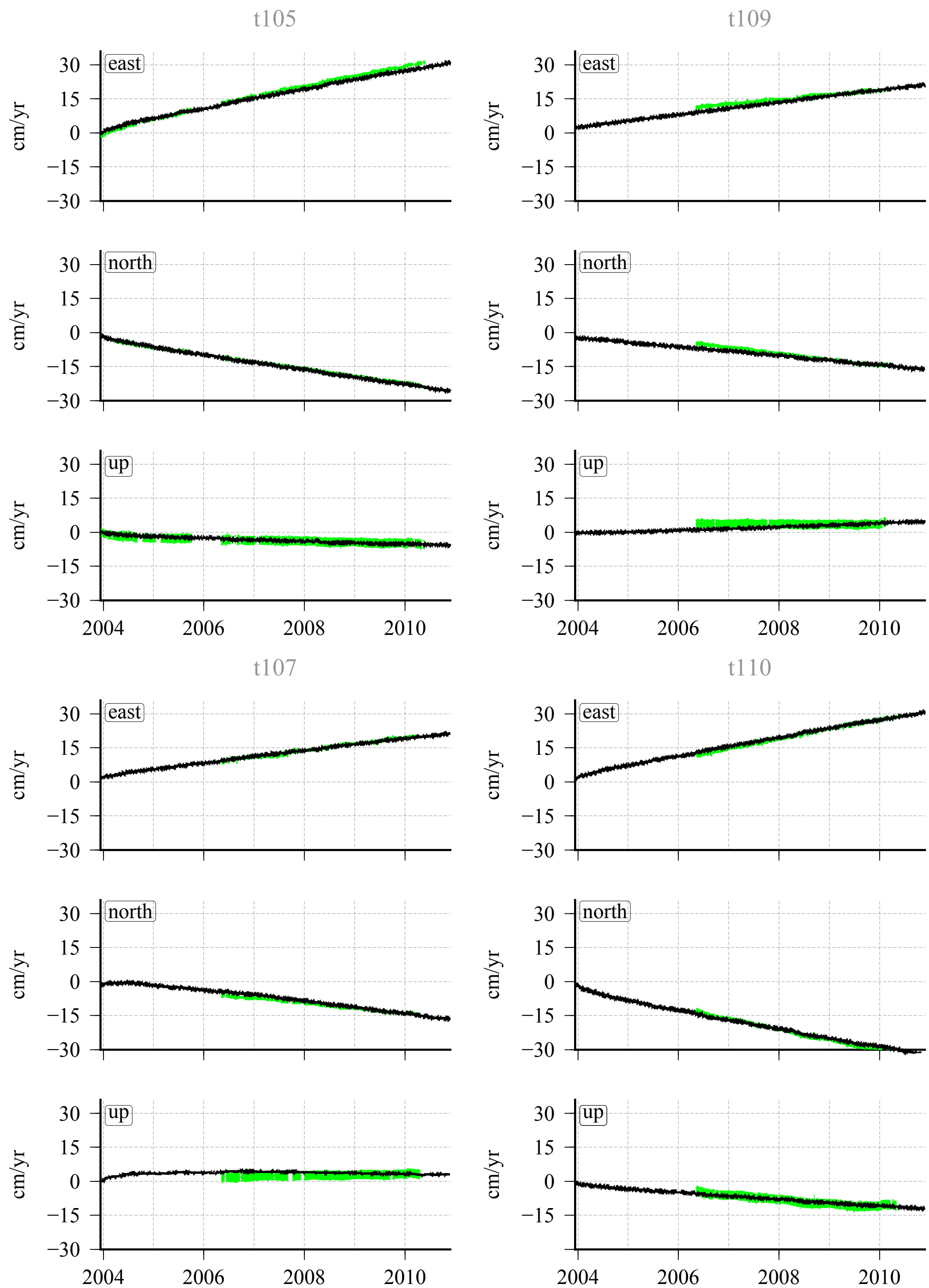
t105
t109
t107
t110
east
north
up
cm/yr
30
15
0
−15
−30
2004
2006
2008
2010

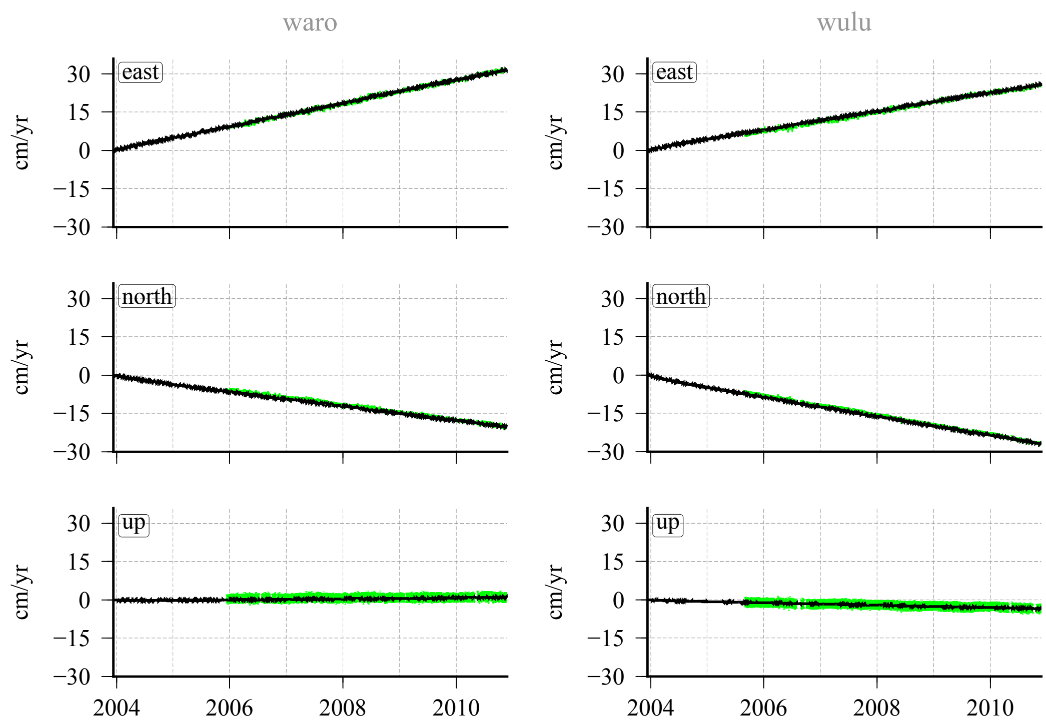

Figure S3: Plots of cGPS times series for which we have records only after the 2003 Chengkung earthquake. See Figure S1 for location. Green dots with 1-sigma errors bars represents the original dataset. Predictions from the inversion of coseismic slip and PCAIM inversions of preseismic and postseismic periods are plotted in black. To facilitate the comparison we have corrected the model predictions for the mean residual velocities over the pre and post-seismic period represented in Figures 17 and 19.

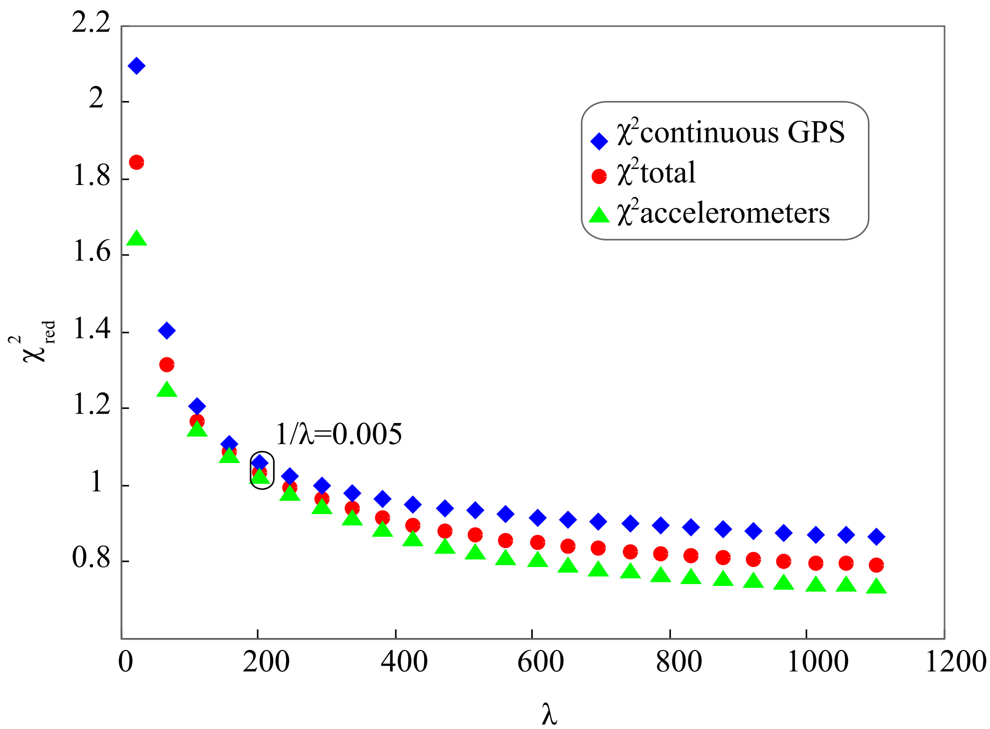

Figure S4: Misfit between measured and reconstructed displacements as the weight put on smoothing (λ) increases. Misfit is quantified from reduced chi-square as defined in equation (4), after renormalization of uncertainties. We choose $1/\lambda = 0.005$ to represent the best compromise.

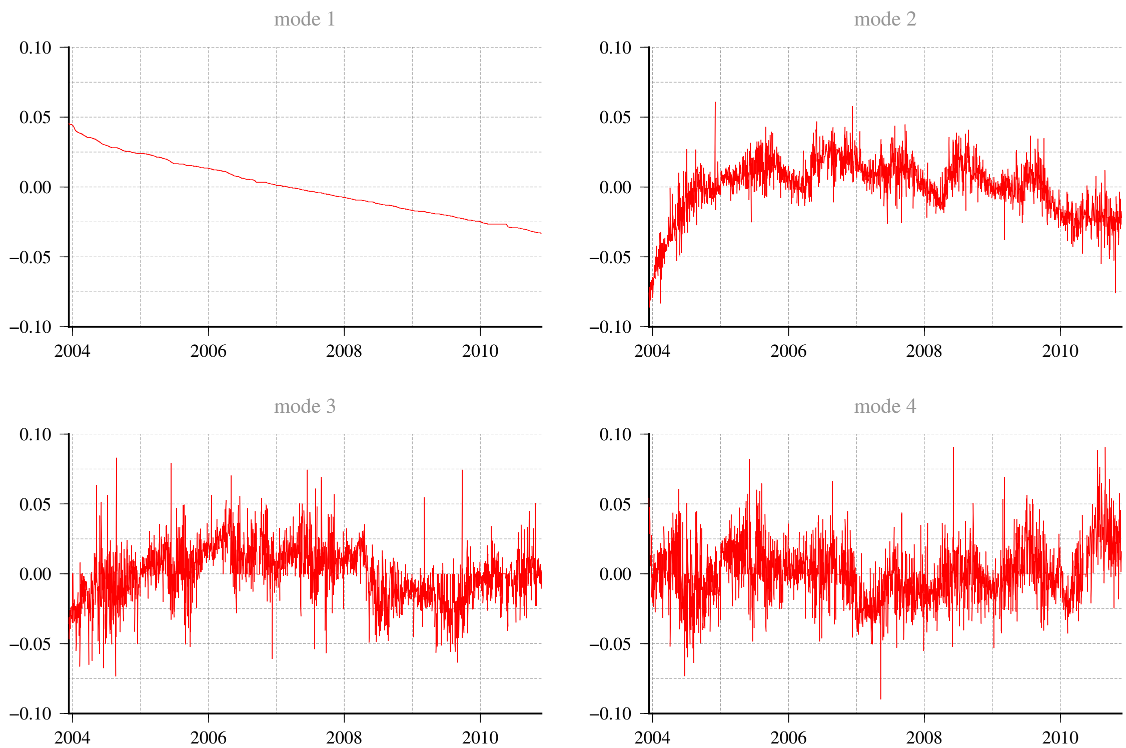

Figure S5: Time functions of the first four principal components for the postseismic modelling. Note that higher-order components (> 2) are more erratic than lower-order components, but do contain significant signals related to postseismic deformation or annual variation of creep rate.

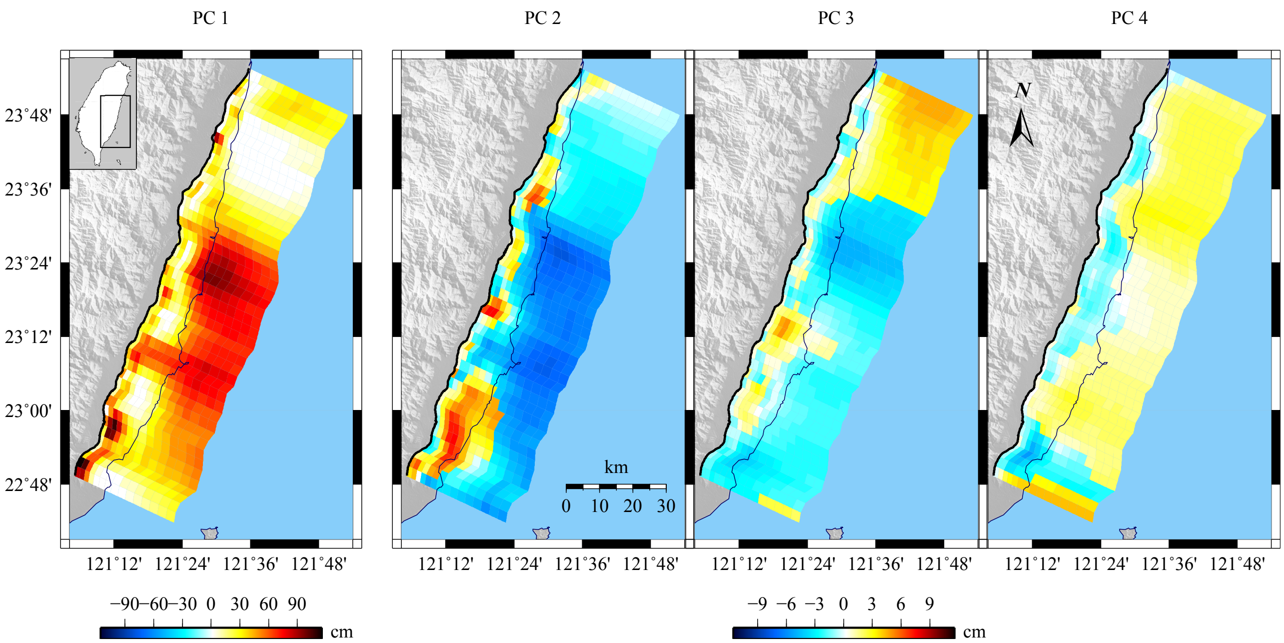

Figure S6: Postseismic principal slip distribution for the four first principal components (PC). Plots display the cumulative slip on the LVF over the period between 12/13/2003 and 11/26/2010, determined from PCAIM inversion of principal components. The range of the color scale is 10 times smaller for PC2, PC3, PC4 than for PC1.

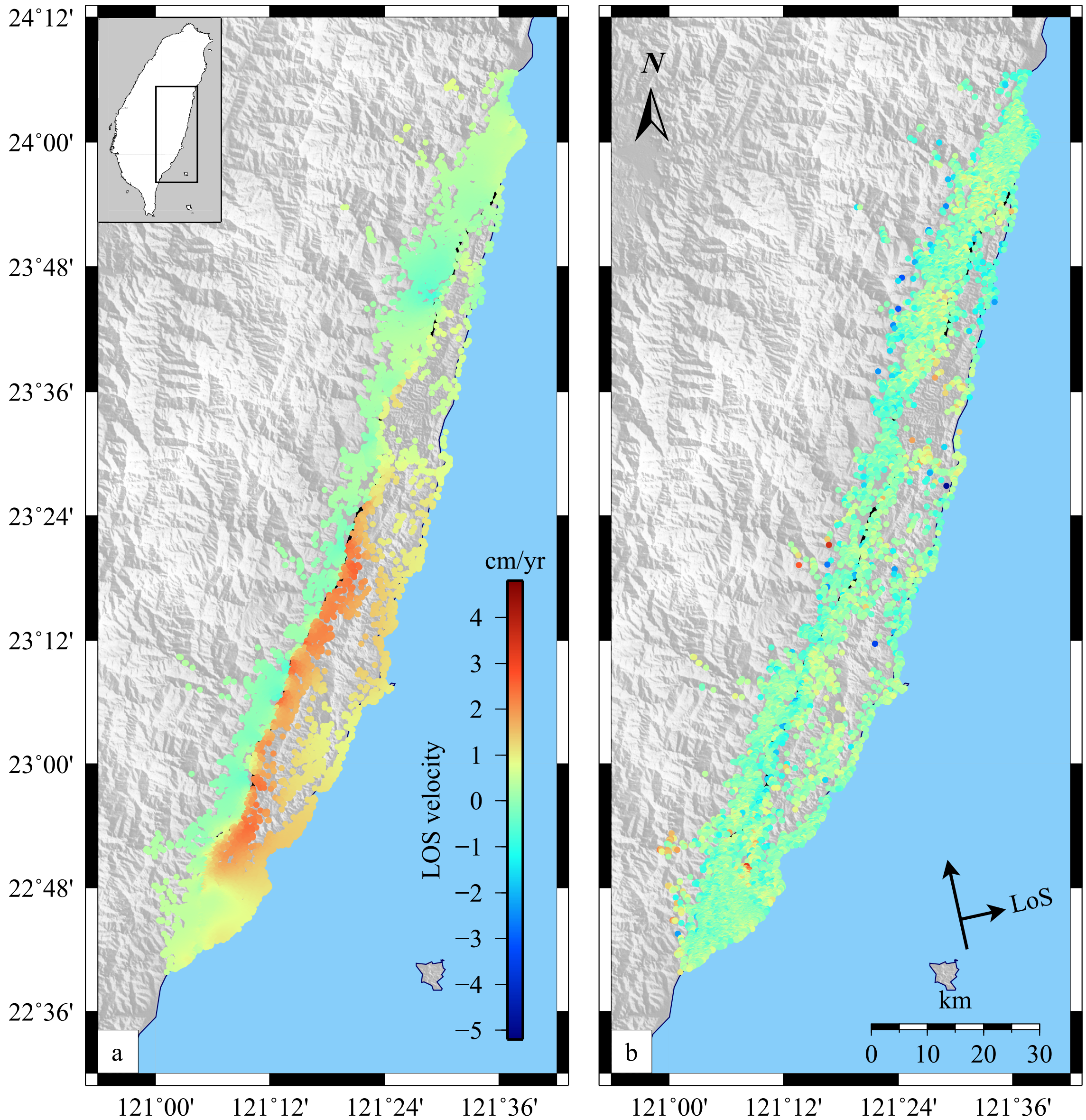

Figure S7: Postseismic model, fit to PS ALOS mean velocity. (a) Line of Sight velocities predicted from the secular interseismic model. For comparison with observations see Figure 2. (b) Residuals from the inversion with same color scale as in (a).

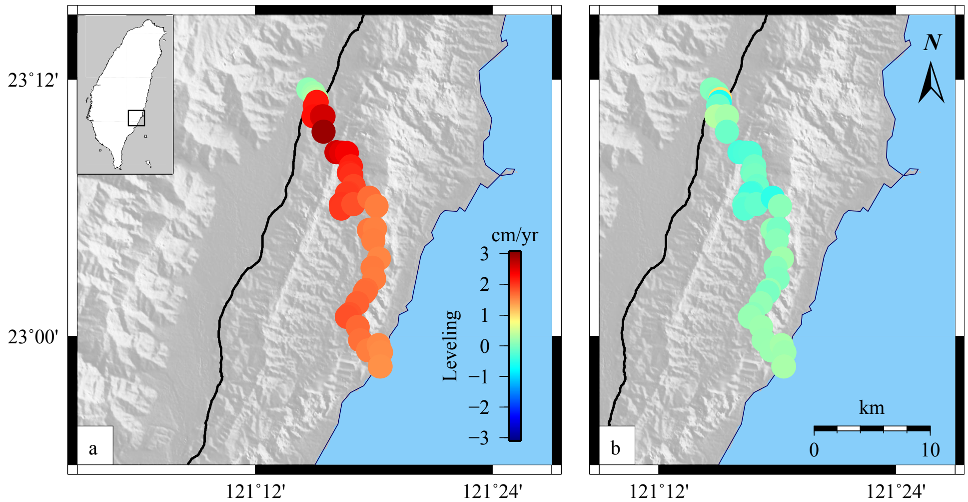

Figure S8: Postseismi model, fit to leveling data. (a) Vertical velocities predicted from the secular interseismic model. See Figure 1 for corresponding observations. (b) Residuals from the inversion with same color scale as in (a).

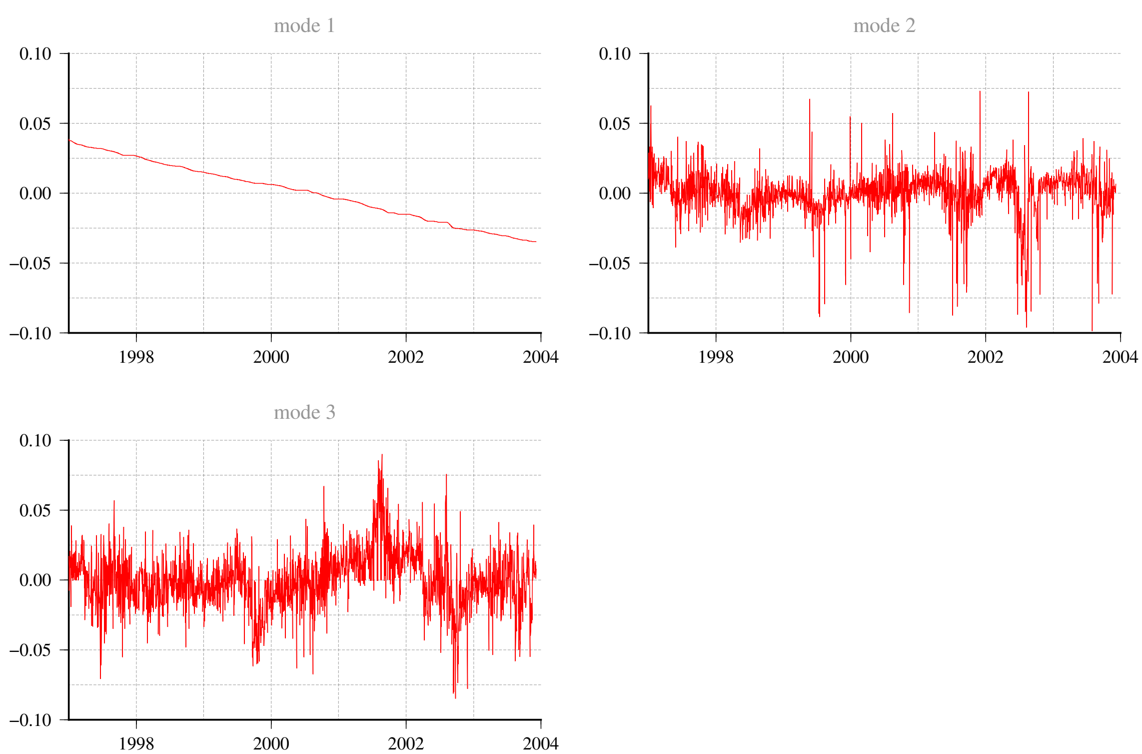

Figure S9: Time functions of the first three principal components for the preseismic modelling.

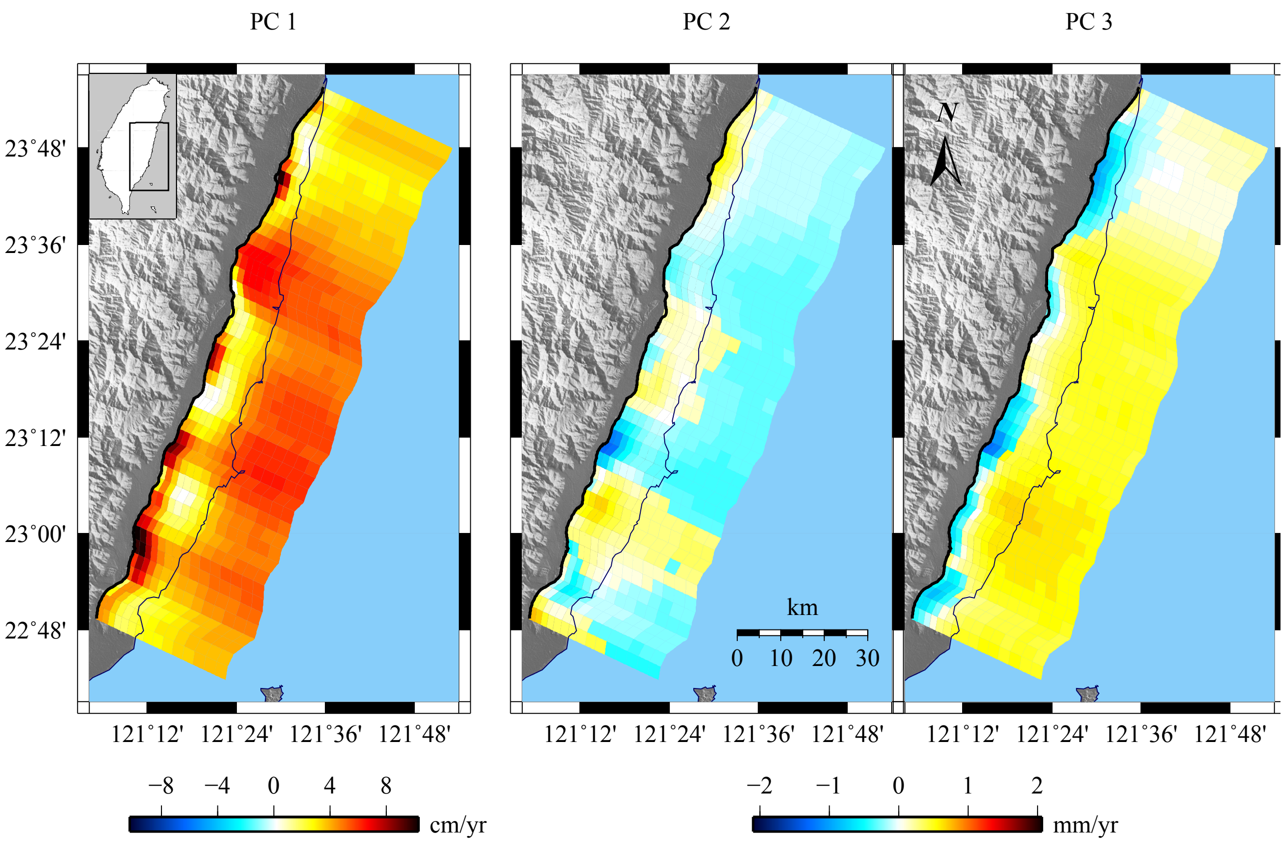

Figure S10: Preseismic principal slip distribution for the three first principal components (PC). Plots display the cumulative slip on the LVF the 1/1/1997 to 12/12/2003 period, determined from PCAIM inversion of principal components. The range of the color scale is 50 times smaller for PC2 and PC3 than for PC1. Therefore most of the slip is accommodated by the first principal component, as comparison with Figure 18a demonstrates.

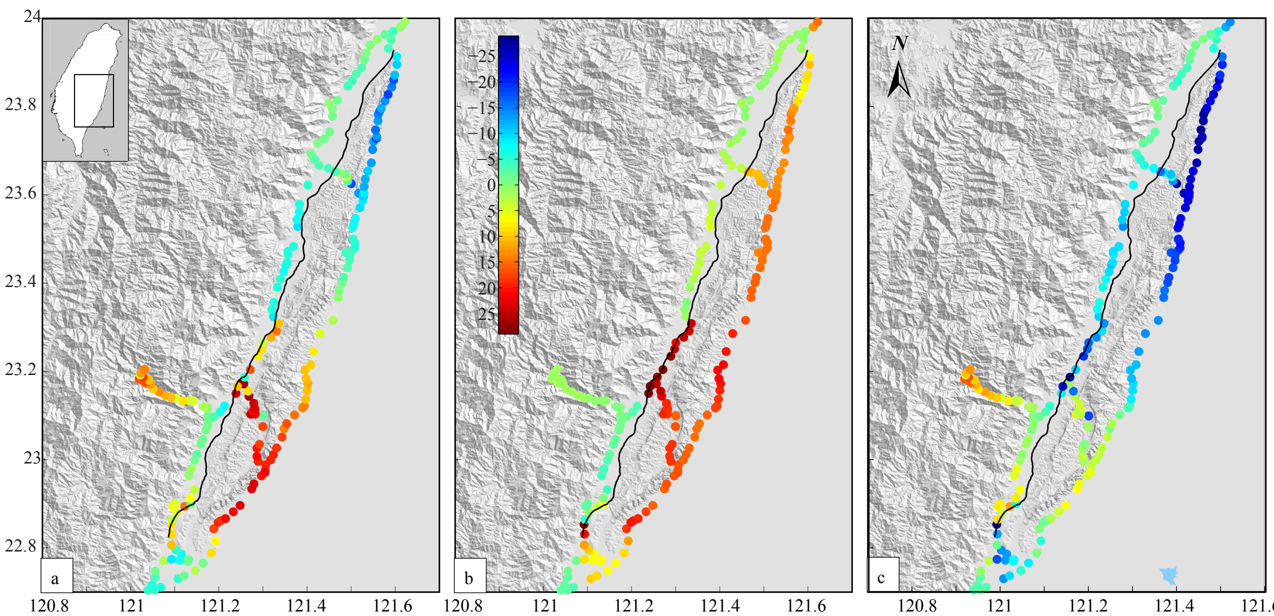

Figure S11: Leveling data from *Ching et al.* (2011).(a) Published Dataset.*Ching et al.* (2011) have removed the coseismic motion due to the chenkung earthquake. Same color scale as in (b). (b) Vertical velocities predicted from the PCAIM preseismic and postseismic models for the same time period.(c) Residuals from the inversion with same color scale as in (a) and (b). Our model does not predicted subsidence in the north, which is linked to Okinawa subduction zone. Residuals in south might be explained by a difference in the coseismic model.

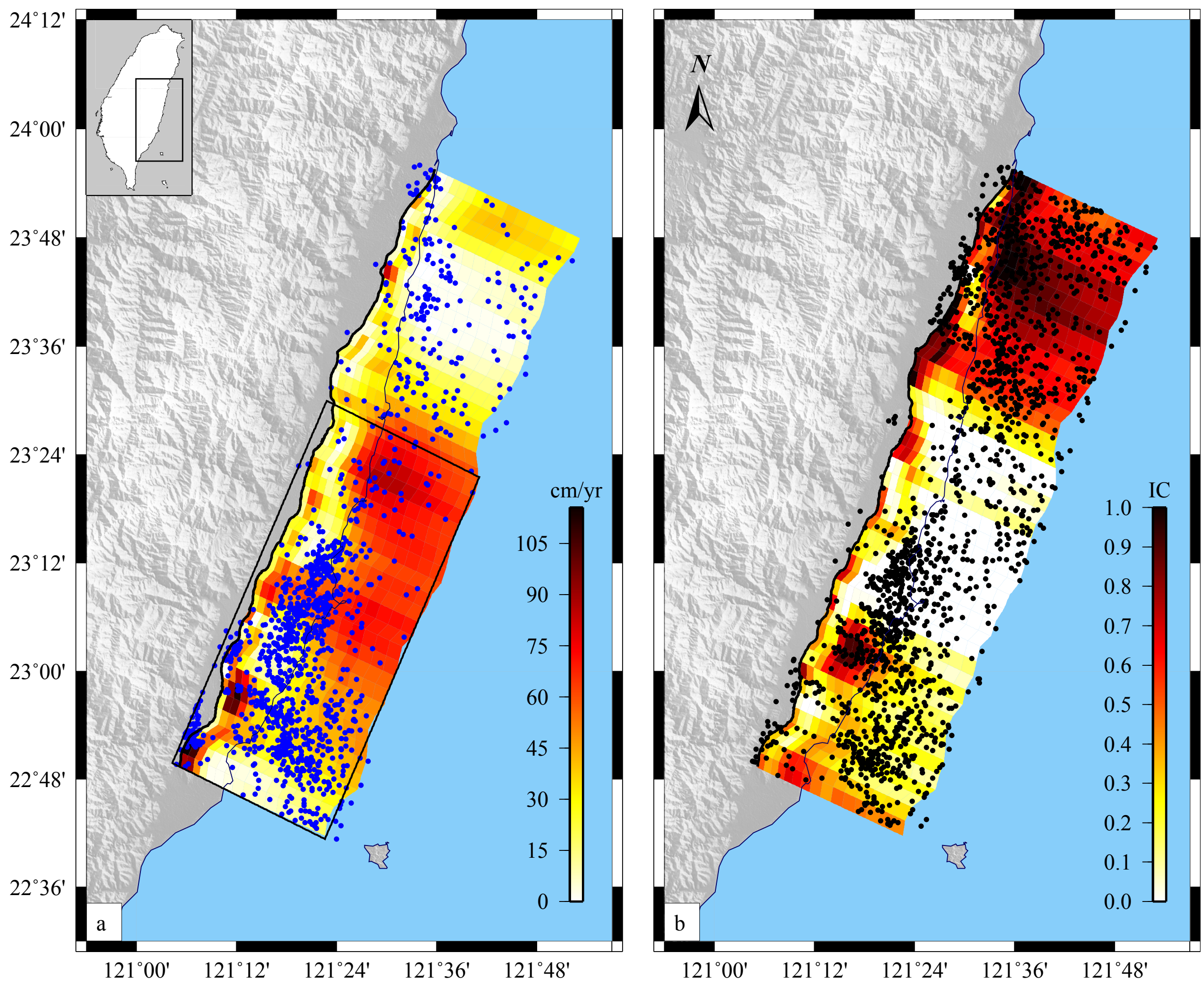

Figure S12: Seismicity around the LVF from 1991 to 2010. (a) Blue dots represents the seismicity recorded on the LVF since the Chengkung earthquake (12/10/2003) until December 2010, for events $M_w > 3$. The black boxe defined the soutern segment of the lVF, for which we compute the Gutenberg-Richter plot (Figure 21). The inversion model underneath corresponds to the cumulative slip on the LVF over the period between 12/11/2003 and 11/26/2010, determined from PCAIM inversion of CGPS and creepmeters time series, leveling data (from 9/1/2007 to 31/20/2010) and PS ALOS cumulative displacement between 1/29/2007 and 6/2/2010. (a) Black dots represents the seismicity recorded on the LVF from January 1991 to the day before the Chenkung earthquake, for events $M_w > 3$. Underneath, we plot the ISC model quantifying the degrees of locking of the LVF fault. If $ISC = 1$, then patch is fully locked, whereas $ISC = 0$ means that the patch is creeping at the long-term slip rate.

Chapter 3

Lithological control on the deformation mechanism and the mode of fault slip on the Longitudinal Valley Fault, Taiwan

Marion Y. Thomas, Jean-Pierre Gratier, Jean-Philippe Avouac, and Jian-Cheng Lee

Abstract

The Longitudinal Valley Fault (LVF) in Taiwan is creeping at shallow depth along its southern half, where it is bounded by the Lichi Mélange. By contrast, the northern segment of the LVF is locked where it is bounded by forearc sedimentary and volcanoclastic formations. Structural and petrographic investigations show that the Lichi Mélange most probably formed as a result of internal deformation of the forearc when the continental shelf of South China collided with the Luzon arc as a result of the subduction of the South China Sea beneath the Philippine Sea Plate. The forerac formations constitute the protolith of the Lichi Mélange. It seems improbable that the mechanical properties of the minerals of the matrix (illite, chorite, kaolinite) in themself explain the aseismic bevavior of the LVF. Microstructural investigations show that deformation within the fault zone must have resulted from a combination of frictional sliding at grain boundaries, cataclasis (responsible for grain size comminution) and pressure solution creep (responsible for the development of the scaly foliation and favored by the mixing of soluble and insoluble minerals). The microstructure of the gouge formed in the Lichi Mélange favors effective pressure solution creep, which inhibits strain-weakening brittle mechanisms and is probably responsible for the dominantly aseismic mode of fault slip. Since the Lichi Mélange is analogous to any unlithified subduction mélanges, this study sheds light on the mechanisms which favor aseismic creep on subduction megathrust.

3.1 Introduction

Geodetic and seismological observations show that fault slip can be either seismic or aseismic. The observation that locked fault patches tend to coincide with seismic ruptures, combined with numerical studies, suggests that the partitioning between aseismic and seimic slip is an influential and perhaps determining factor governing the spatial extent, size and timing of earthquake ruptures (e.g., *Barbot et al.*, 2012; *Hsu et al.*, 2009a; *Kaneko et al.*, 2010; *Noda and Lapusta*, 2010; *Perfettini et al.*, 2010; *Harris and Segall*, 1987; *Hashimoto et al.*, 2009; *Loveless and Meade*, 2011; *Chlieh et al.*, 2008; *Moreno et al.*, 2010). However, the factors that determine the mode of fault slip, and hence the seismogenic potential of faults, are still poorly understood. Ascertaining those factors by defining the spatial and temporal variability of frictional properties, and understanding the deformation mechanisms and their relative importance are therefore major goals in seismotectonics.

We propose to address this problematic by investigating the deformation mechanisms that control aseismic slip on the Longitudinal Valley Fault (LVF) in Taiwan. This fault runs parallel to the East coast of Taiwan and defines the plate boundary between the Chinese continental margin, considered to be part of the Eurasian plate, and the oceanic Philippine Sea Plate (*Lee et al.*, 2001; *Chang et al.*, 2009) (Figure 3.1). This fault is known to creep near the surface (*Angelier et al.*, 1997; *Lee et al.*, 1998, 2000, 2001, 2005; *Chang et al.*, 2009; *Champenois et al.*, 2012; *Thomas et al.*, to be submitted) but has also produced large earthquakes, with five $M_w > 6.8$ events in 1951 and 2003 (*Shyu et al.*, 2007; *Wu et al.*, 2006a; *Hsu et al.*, 2009a; *Mozziconacci et al.*, 2009; *Thomas et al.*, to be submitted). Modeling of the spatio-temporal evolution of seismic and aseismic slip on the LVF, derived from the inversion of geodetic, remote-sensing and accelerometric data, has demonstrated that as much as 80-90% of the 4.5 cm/yr slip rate on the LVF, in the 0-26 km seismogenic depth range (as defined by local seismicity), is actually the result of aseismic creep(*Thomas et al.*, to be submitted). The spatial pattern of aseismic creep on the LVF is very heterogeneous, showing both along dip and along strike variations. Creep is observed at the surface along the southern portion of the LVF, where it seems to correlate with Lichi Mélange (Figure 3.1), a formation which has received various debated interpretations (*Biq*, 1971; *Huang and Yin*, 1990; *Huang et al.*, 1992; *Reed et al.*, 1992; *Malavieille et al.*, 2002; *Huang et al.*, 2008; *Wang*, 1976; *Ernst*, 1977; *Page and Suppe*, 1981; *Lin and Chen*, 1986; *Chang et al.*, 2000, 2001, 2009; *Huang et al.*, 2006a).

The objective of this study is to investigate the potential factors that favor aseismic slip on the LVF based on structural and micro-structural analysis of the various formations along the LVF and of rocks from the fault zone. The study is based on field investigations and analysis of samples collected at the outcrop and from drill cores (*Chen*, 2009; *Mu et al.*, 2011). Hereafter, we first describe the different stratigraphic units that compose the Longitudinal vValley area and discuss the nature and origin of the Lichi Mélange. We next discuss its correlation with the creeping section

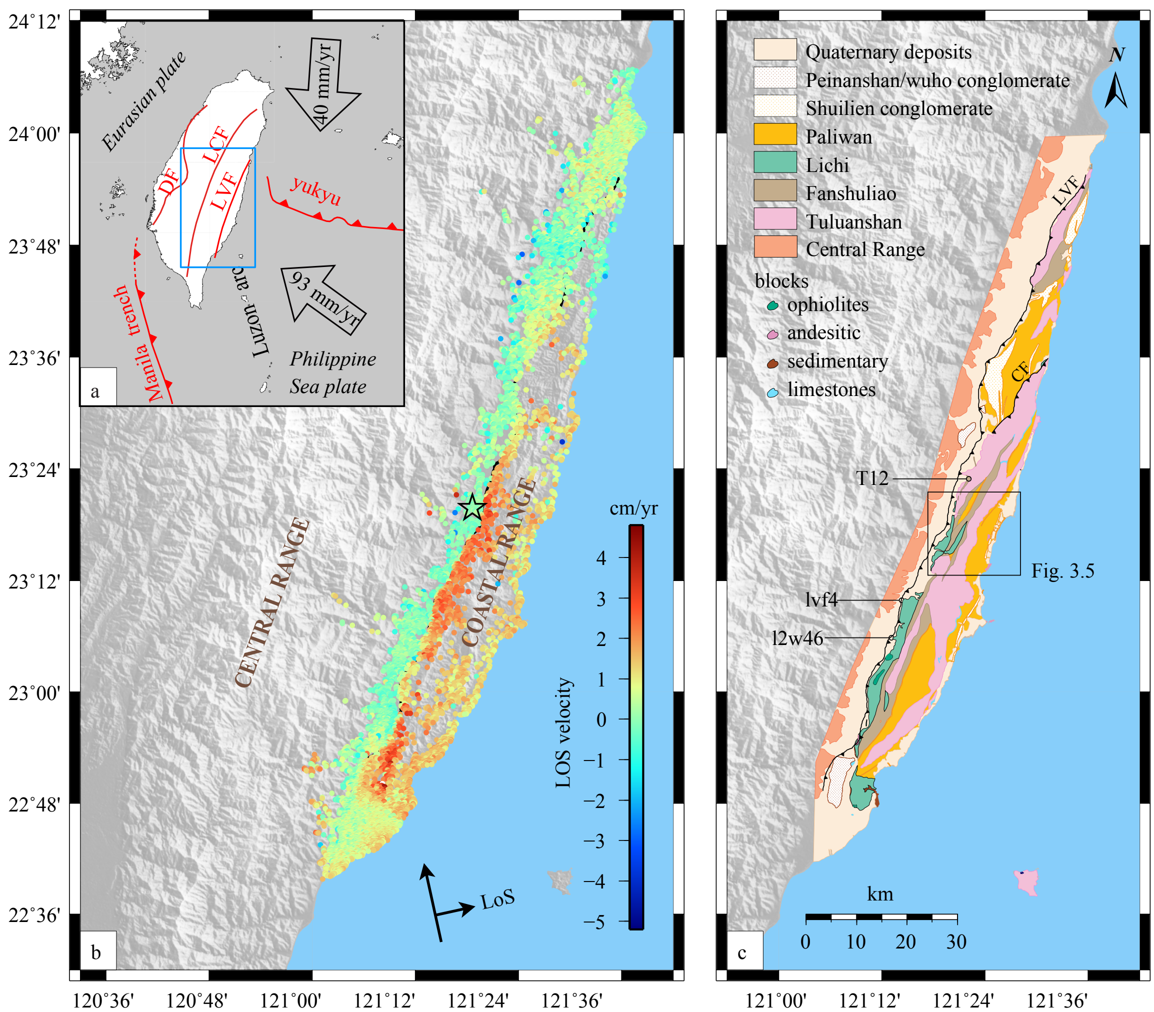

Figure 3.1: (a) Regional tectonic setting of the Longitudinal Valley Fault. The blue rectangle corresponds to the location of subfigure (b). (b) Mean line of sight (LOS) velocity (in cm/yr) around the Longitudinal Valley Fault derived from the Persistent Scatter (PS) technique applied to PALSAR ALOS data acquired between 1/29/2007 and 6/2/2010 (*Champenois et al.*, 2012; *Thomas et al.*, to be submitted). Velocities are expressed relative to the mean velocity of a reference area, indicated by the black star. Black arrows show the ascending track direction and the LOS, which has an incidence of about 35° on average (relative to the vertical). (c) Geological map of eastern Taiwan (modified from *Wang and Chen* (1993)). The Coastal Range is composed of three accreted Mio-Pliocene volcanic islands (Tuluanshan formation), three remnants of Plio-Plesitocene forearc basins and intra-arc basins (Fanhsuliao and Paliwan), and the Pliocene collision Lichi Mélange, which is related to the suturing of the subduction zone due to the collision between the Luzon arc (see subfigure (a)) and the continental margin of South China (*Chang et al.*, 2000, 2001, 2009; *Huang et al.*, 2006a, 2008). Peinanshan and the Wuho are post-collision conglomerates. Central Range formations that border the Longitudinal Valley, include slates and schist *Wang and Chen* (1993). DF-deformation front; LCF-Lishan-Chaochou Fault; LVF-Longitudinal Valley Fault; CF Chimei Fault.

of the LVF, and we investigate the potential deformation mechanisms which could explain shallow creep on the LVF, based on structural and microstructural observations.

3.2 Stratigraphic and tectonic setting of the Coastal Range

The Coastal Range consists of the Luzon arc volcanic basement and forearc basins, which were accreted to the passive Chinese continental margin during the arc-continent collision, which started about 7 millions years ago (*Liu et al.*, 2000; *Suppe*, 1984; *Huang et al.*, 2006a). We describe here the various rock formations outcropping in their area, their stratigrahic and structural relationships and their mineralogical constituents. This discussion is based on the information available from the literature and our own observations. The location of the sites where observations were carried out and samples collected are indicated in supplemental Figure S1. We conducted two field surveys and collected samples (73 total) for chemical and micro-structural analysis (80 thin sections). We used BSE and SEM to indentify the microstrucrures and X-ray diffraction to characterize the mineralogy. Figure 3.2 shows our revised version of the geological map and sections of the area where most of the field work was focused in order to better constrain the nature and origin of the Lichi Mélange as well as its stratigraphic relationship to the other formations of the Coastal Range.

With regard to the stratigraphy, five rock units can be distinguished in the Coastal Range. The Tuluanshan arc formation, the Fanshuliao volcanoclastic deposits, and the Lichi Mélange are pre-collision island-arc lithofacies, whereas the Paliwan lithic flysch and the Peinanshan and Wuho conglomerates (molasse) are later syn/post-collision lithofacies (Figure 3.1c).

3.2.1 The Tuluanshan arc formation

Stratigraphic and geochemical studies have shown that the Costal Range is composed of three accreted Miocene-Pliocene volcanic islands, from north to south: Yuehmei, Chimei and Chengkuangao (*Huang et al.*, 2006a, 2008). The volcanic rocks of the Tuluanshan formation represent the former Luzon arc (*Teng and Lo*, 1985). They are distributed all along the Coastal Range (Figure 3.1c) and usually form mountain ridges, covering an area over 1/3 of the Coastal Range. The Tuluanshan formation is considered to be the oldest formation of the Coastal Range. Most of the radiometric dates fall in the range from 23 to 5 Ma with some extending to late Oligocene (29 Ma) and early Pliocene (4.4 Ma) (*Ho*, 1969; *Juang and Bellon*, 1984; *Yang et al.*, 1988; *Chen et al.*, 1990; *Lo et al.*, 1994).

A combined geochronological, geochemical and geophysical study of the Luzon arc has demonstrated that the Luzon arc presents a clear double arc structure related to the eastward shift in volcanism (5-4 Ma ago), most probably due to a change in the dip angle of the slab, which leads to the creation of a new volcanic chain (*Yang et al.*, 1996). As the volcanism in the accreted islands

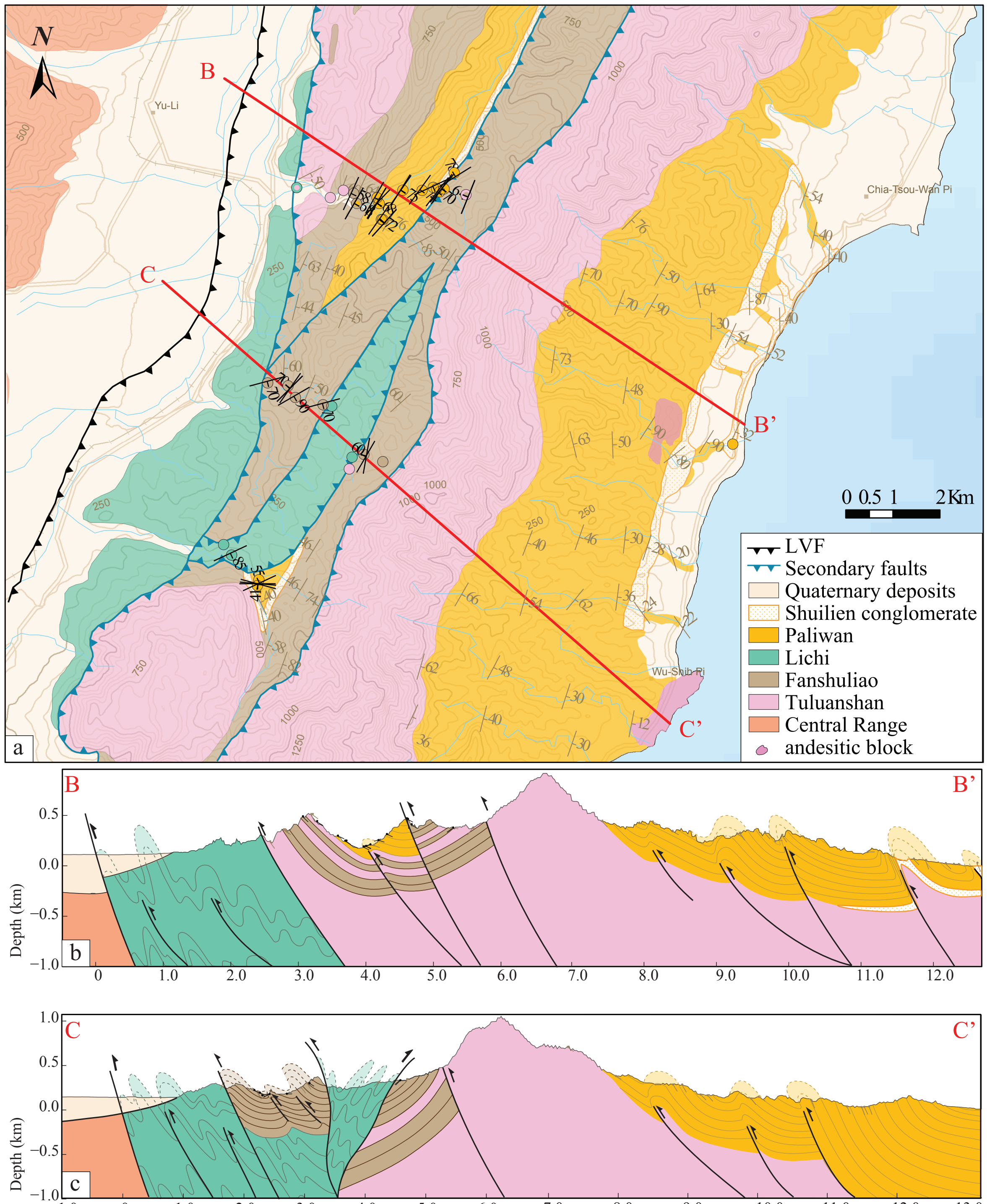

Figure 3.2: Geological map and cross-sections for the central part of the Longitudinal Valley, Taiwan. For location see Figure 3.1. (a) Geological map is modified from Wang and Chen (1993) based on our field observations. Colored-circles show locations of samples. Field-measured dip angles are displayed in black, and measurements from Wang and Chen (1993) are shown in light brown. BB and CC show locations of cross-sections displayed in(b) and (c), respectively. Color coding for the different lithological formations of the Coastal Range are given in (a).

had ceased before then, it is likely that the earlier volcanic centers were, in the early stage of the collision, closer to the trench than the current active volcanic islands. Therefore the three independent islands (Yuehmei, Chimei and Chengkuangao) were not aligned with the present Lutao and Lanshu Islands, south-east of Taiwan.

Volcanic features of the Tuluanshan formation indicate that most were produced by submarine eruptions and a small fraction by subaeraial extrusion (*Teng and Lo*, 1985). The following lithofacies have been documented (i) lava, (ii) pyroclastics, and (iii) limestones (*Teng and Lo*, 1985; *Teng et al.*, 1988; *Chen*, 1997a). A whole spectrum of rocks ranging from basalts, basaltic andesites and andesites can be found, among which andesites are the more voluminous (*Teng and Lo*, 1985). Phenocrysts are generally less than 50 %, of which plagioclase is usually the predominant phase. Hypersthene and pyroxene are inferior to 5 %.

3.2.2 Forearc and intra-arc basins: the Paliwan and the Fanshuliao formations

Three Plio-Plesitocene remnant forearc basins (Shuilien, Loho, Taiyuan) and two intra-arc basins (Chingpu and Chengkung) have been recognized in the Coastal Range (*Huang et al.*, 2008, 2006a). Submarine-fan channel deposits, together with paleocurrent measurements (*Teng*, 1982; *Chen and Wang*, 1988), indicate that the three forearc basins were originally one single basin before the Pliocene arc-continent collision (*Huang et al.*, 1995). On the contrary, the Pliocene Chingpu and Pleistocene Chengkung intra-arc basins display no continuity in sediments deposits. They are believed to have developed as a pull apart basin, due to the oblique convergence, on the eastern part of the Neogene Chimei and Chengkuangao volcanic islands, respectively, prior to their accretion on the Coastal Range (*Huang et al.*, 1995, 2006a).

Except limestones, most of the sedimentary deposits found in the forearc basin and intra-arc basins display primary sedimentary structures characteristic of turbidites, such as rhythmic alternations of thin persistent sandstone and shale beds, graded beds, sole marks and slump structures. According to the modal composition *Teng* (1979) has distinguished three types of sedimentary rocks, reflecting the variation of sedimentary sources with time. Based on comparison with biostratigraphic studies of the area (*Chang*, 1967, 1968, 1969, 1975; *Chi et al.*, 1981), Type I and II correspond to the so-called Fanshuliao formation, and Type III to the Paliwan formation (Figure 3.1c).

3.2.2.1 Fanshuliao formation

Well exposed in the northern part of the Coastal Range, the Fanshuliao formation conformably overlies the Tuluanshan volcanics with a sometimes interfingering contact (*Teng and Lo*, 1985) (Figure 3.2). The Fanshuliao formation is considered to consist of sediments which accumulated in

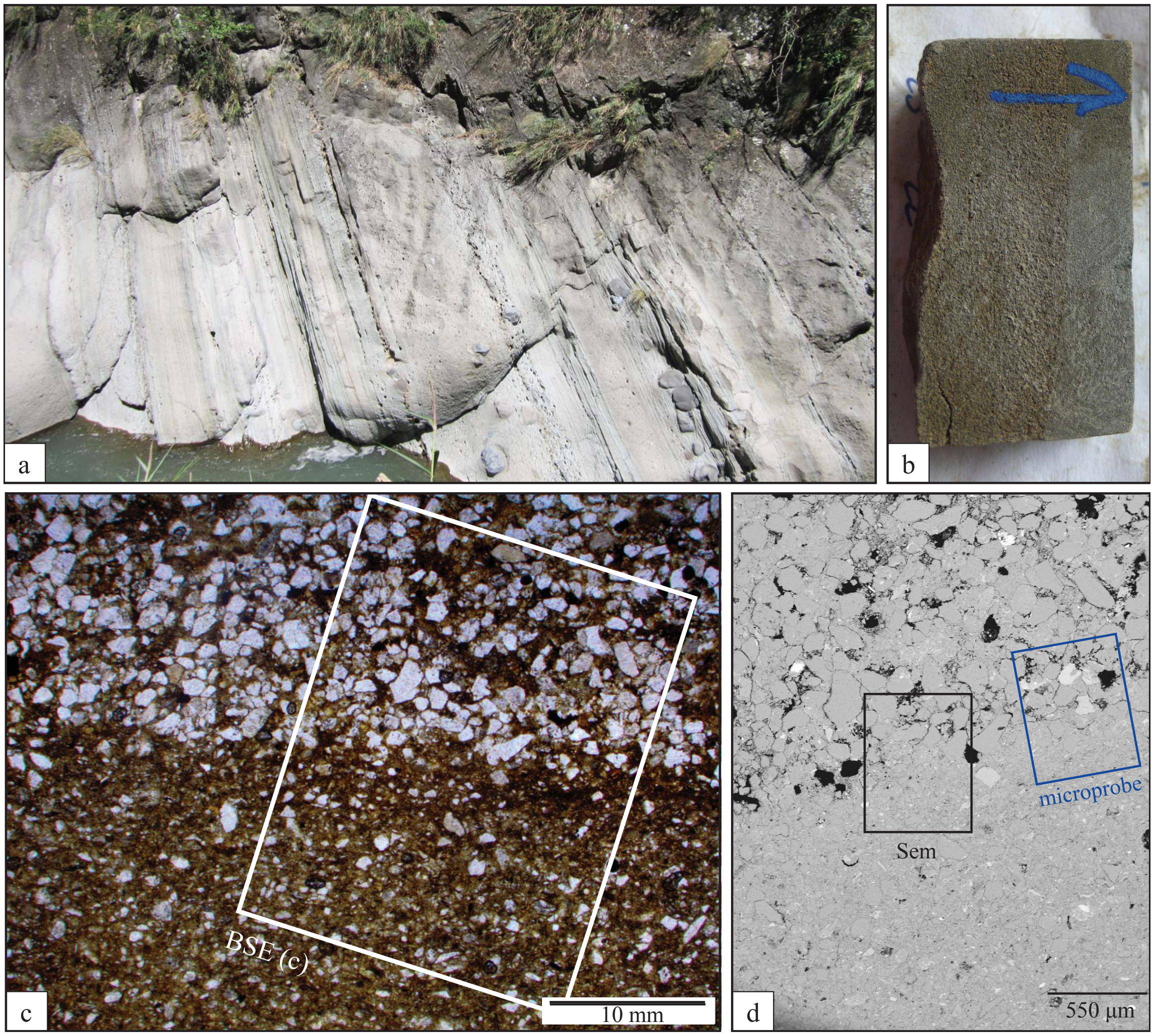

Figure 3.3: Fanshuliao formation. (a) Field view of a Fanshuliao outcrop along the Le-Ho River displaying a typical turbiditic Bouma sequence. (b) T12, a representative Fanshuliao sample collected in the field at longitude 121°22'25"E and latitude 23°22'55"N. See Figure 3.1c for location. (c) Optical micrograph in plane polarized light. Sample exhibits a distinctive layering (s0) with variation in granulometry, characteristics of turbiditic deposits. The white rectangle displays the location of subfigure (d). (d) BSE image from the SEM. Black and blue boxes indicate location of pointshoot X-ray analysis with the SEM (Figure S1 in supplements) and electron probe compositional maps in Figure 3.9, respectively.

the forearc basin between the backstop of the accretionary prism and the Luzon arc islands (*Huang et al.*, 2006b) (Figure 3.6a). Biostratigraphic studies (*Huang*, 1969; *Chang*, 1967, 1968, 1969, 1975; *Chi et al.*, 1981) show that the age of this formation roughly spans the latest Miocene to early Pliocene. Rythmic alternation of thin sandstone and mudstone beds (Figure 3.3), together with common slump features (meter to hundred meters) are the dominant facies, but characteristic basal mudstone, which represents the draping mud over the volcanic arc in the early Pliocene, can locally be observed. Based on probable source origin, the Fanshuliao formation can be further subdivided into two petrographic types, namely the calcarenaceous volcaniclastic sandstone (Type I) and the quartwacke sandstone (Type II) (*Teng*, 1979; *Teng and Wang*, 1981; *Chen and Wang*, 1988).

In terms of mineralogy content, Type I rocks are marked by a quasi-absence of quartz, a large proportion of volcanic origin feldspar plagioclase (10-40%), the omnipresence of hornblende, some augite and opaques, occasional glauconite and chlorite, and few coalified wood fragments. The epiclastic content of volcanic origin is remarkable (over 50% of the total rock). A large quantity of carbonated bioclasts (20-70% of the total rock) are also found, together with a micritic calcitic cement. Since the mineralogy contents is very similar to the Tuluanshan formation (*Teng and Wang*, 1981; *Chen*, 1997a), arc islands are likely the major source for these sedimentary rocks, transported by turbidity currents to the final depositional basin (*Teng*, 1979, 1980b). Moreover, the lack of terrigenous sediments combined with the abundance of fossil remains lead to the hypothesis of a primary inner, shallow-water shelf environment of deposition, far from the continent.

Unlike in rocks of Type I, quartz is an essential mineral of the quartwacke sandstone (Type II), constituting 10 to 50 % of the total rocks. Nevertheless, plagioclases still dominate, and K-feldpars also occur. With regard to accessory minerals, serpentine is more abundant than hornblende. Augite, chlorite, glauconite and micas can be also found, as well as zircon, tourmaline, garnet and monazite in the heavy fraction. Volcanic fragments are still the prevalent epiclasts, even though the relative quantity of lithic fragments is reduced. Slate fragments occasionally occur in Type II sandstone, and carbonated fossils are still present, but much less abundant than in Type I rocks. Carbonate cement forms an appreciable amount of these sandstones; nonetheless, the detrital clay matrix constitutes 4 to 47 % of the total rock based on the *Teng* (1979) study. Pointshoot X-ray analysis with the SEM is presented in supplementary material (Figure S4).

In the field, Type I and Type II rock units are interbedded, occur evenly and show similar textures. Therefore, they are hardly distinguishable without a petrographic analysis (*Teng*, 1979, 1980b). The main difference is in quartz and fossils content, as well as clay quantity. Consequently, Type II sandstone can be regarded as Type I rocks mixed, to a various extent, with a quartz and alkali feldspar-rich source, likely the non-metamorphic cover sequences of the proto-Taiwan island (*Teng et al.*, 1988) (Figure 3.6b).

3.2.2.2 Paliwan formation

Plio-Pleistocene in age, the Paliwan formation conformably overlies both the Fanshuliao and the Tuluanshan formations (*Teng et al.*, 1988) (Figure 3.1 and 3.2). Grayish in color, this formation includes the whole range of possible facies of deep-sea fan systems and corresponds to Type III sandstones, as described by *Teng* (1979). In terms of mineralogy content, quartz represents 7 to 32 % of the total rock, feldspar is a minor accessory mineral, but serpentine is very common (*Teng*, 1979, 1980b). Detrital grains of pyroxenes are found as well, whereas amphibole is rare. The principal content of those rocks are epiclasts of different origin (14 to 90 % of the total rock) with a relative abundant matrix, composed mainly of pelitic fragments and detrital clays in a smaller amount. Unlike in the Fanshuliao formation, bioclastic grains and calcareous cement are very limited in those rocks (*Teng*, 1979). The dominant type of lithic fragments is basic to ultrabasic igneous rocks, more or less serpentinized. Andesitic fragments are rarely present. The other epiclasts are slate and metasandstones (*Teng*, 1979, 1980b), with a progressive decrease through time in sedimentary lihtic fragments and an increase first in low-grade and later in medium-grade methamorphic lithic fragments (*Dorsey et al.*, 1988). The voluminous content of strained quartz, slate and metasandstone are undoubtedly derived from a low-grade metamorphic terrain, more likely the exposed Central Range (*Teng*, 1979; *Dorsey et al.*, 1988). The source of the basic rocks is less certain. They might come from the erosion of ophiolite-bearing rock. Finally, the small amount of andesitic epiclasts tells us that the area of deposition was still not far from the arc.

3.2.3 The Lichi Mélange

The Lichi Mélange crops out on the western side of the Coastal Range (Figure 3.1). Its stratigraphic thickness is quite variable and can reach up to $\sim$ 2 km. Biostratigraphic studies (*Chang*, 1967; *Chi et al.*, 1981; *Chi*, 1982; *Barrier and Muller*, 1984; *Huang et al.*, 2008) show a consistent early Pliocene age, which restrains the time of deposition of the protolith to a narrow range (5.5 to 3.7 Ma). Therefore, the Lichi Mélange is coeval with the lower forearc basin sequence but older than the upper deposits of the Paliwan formation.

The Lichi Mélange is a characteristic block-in-matrix mélange with preferred foliation in a scaly argillaceous matrix with slickensided surfaces (Figures 3.4a and b) and boudinage structures in the sandstone blocks (*Chen*, 1997b; *Chang et al.*, 2000). Different sheared facies are observed in the Lichi Mélange: from weakly sheared/broken to highly sheared mélange facies (*Chang et al.*, 2000, 2001; *Huang et al.*, 2008). The weakly sheared, broken formation facies still preserves a distinct turbidite sedimentary structure with a basal layer primarily composed of quartz, like in the lower forearc sequences. However, slate chips, which are commonly found in the upper part of the forearc basin turbidite deposits (< 3 Ma) (*Teng*, 1982), are generally absent in the Lichi Mélange (*Huang*

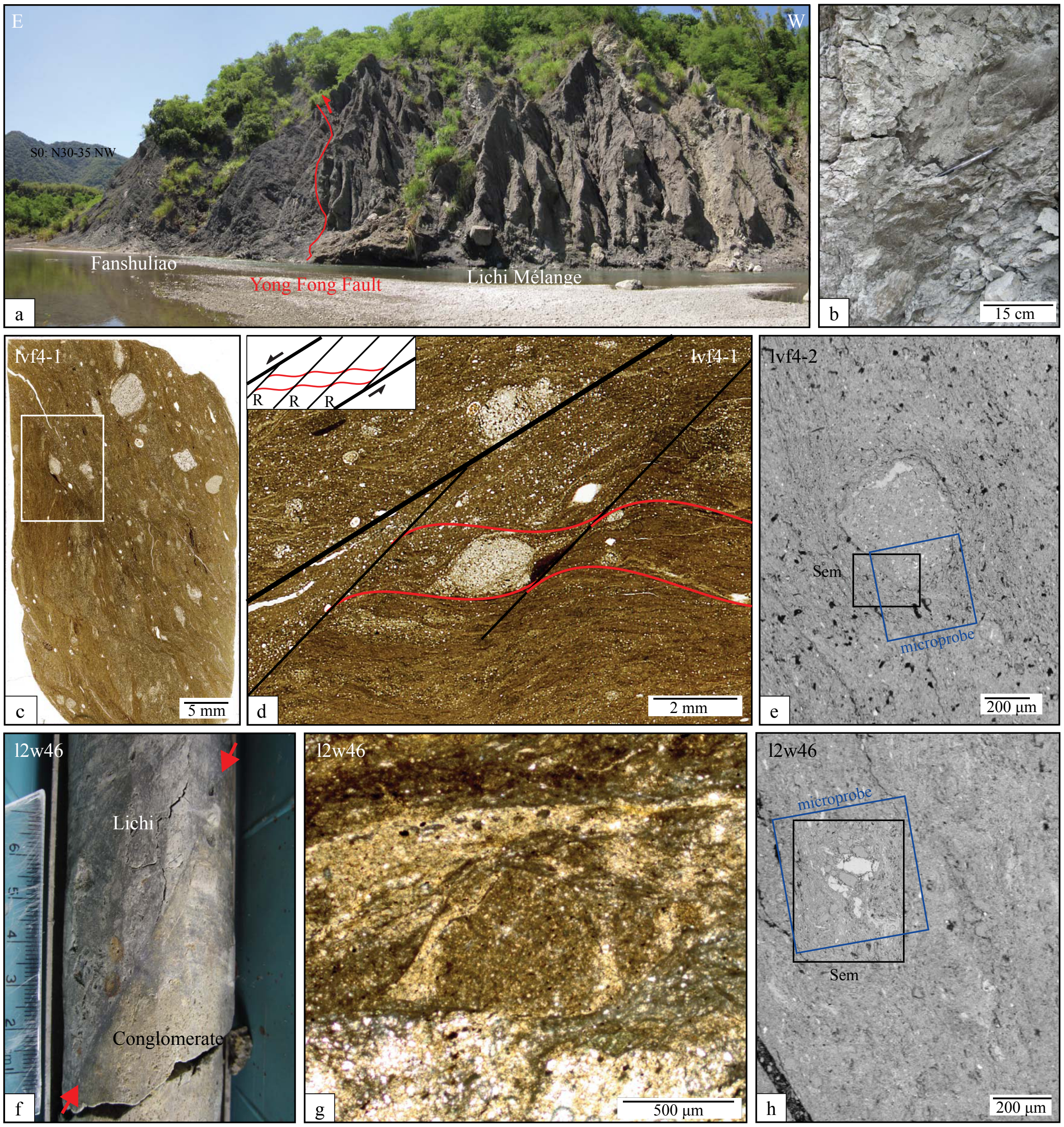

Figure 3.4: Lichi Mélange formation. (a) Contact between the Lichi Mélange and the Fanshuliao formation, near Fuli (121°15'48"E and 23°8'35"N). The Lichi Mélange is highly erodible and exhibits characteristic v-shape erosion features in the field. (b) Outcrop of Lichi Mélange displaying the typical scaly argillaceous matrix with slickensided surfaces. (c) Thin section of lvf4 sample collected in the field (121°14'32"E and 23°9'56"N) showing the block-in-matrix structure with penetrative foliation. See Figure 3.1c for location. The white rectangle displays the location of subfigure (d). (d) Typical sigmoid-shaped microstructure with microlithons enmeshed in an clay-rich gouge and oriented along R-type Riedel shear fractures. (f) Borehole core Wan-2 (46.4 m depth along the core section) (*Chen*, 2009; *Mu et al.*, 2011) displaying the tectonic contact(LVF) between the quaternary conglomerate and the Lichi Mélange. l2w46 samples the main fracture zone highligthed with red arrows.(g) Optical micrograph in transmitted light showing a sigmoid-shaped clast of sandstone. (e) and (h) BSE image from the SEM. Black rectangles indicate the location of the pointshoot X-ray analysis with the SEM (Figure S2 for (e) and S3 for (h) in supplements). Blue boxes correspond to the location of the electron probe compositional maps in Figure 3.7 and 3.8 for (e) and (h), respectively.

et al., 2008).

The exotic blocks inside the formation are of various size (millimeters to kilometers) and lithology (arc products, ophiolites, sedimentary rocks). The volcanic products derived from the Luzon volcanic arc include andesite, volcanic breccias, tuffs and volcanoclastic turbidites. Pillow basalts and gabbro, sometimes serpentinized, composed the dismembered ophiolite suite. The sedimentary blocks show two different facies. One consists of weakly lithified Pliocene turbidite with similar lithology, age and sedimentary turbidite structures as the forearc basin strata (Fanshuliao). The Lichi Mélange also includes metric to kilometric size angular blocks of well-lithified, whitish quartz-rich, feldspathic sandstones, which are late Miocene in age. They have only been observed in the intensely sheared facies of the Lichi Mélange and zircon a fission track study has shown that they are similar to the non-metamorphosed deep-sea fan sandstones of the upper accretionary prism in the Hengchun Peninsula (*Huang et al.*, 1997, 2008). Therefore, those whitish blocks are believed to have been incorporated by eastward thrusting into the deformed forearc strata (*Huang et al.*, 2008).

Clay mineral composition (< 2 m) of the muddy matrix and the sedimentary blocks is similar in all samples, regardless of shearing intensity (*Huang et al.*, 2008). They are characterized by illite, chlorite, mixed-layer clay minerals (mica/smectite) and kaolinite (*Lin and Chen*, 1986) (Figure 3.5 and S2 and S3 in supplements). Smectite alone or serpentine are found as traces or are completely absent. Therefore, the Lichi Mélange must have two sources: one continental with slightly metamorphosed sediments from the exhumed accretionary prism to provide illite and chlorite, and one volcanic to provide the kaolinite. The clay mineral assemblage in the turbidites of the remnant forearc basin is very similar in composition except for the kaolinite, which is absent in the Fanshuliao formation (*Lin and Chen*, 1986). *Huang et al.* (2008) claimed that the occurrence of kaolinite shows the tectonic involvement (thrusting, fragmentation and mixing) of the volcanic basement beneath the forearc basin, during the formation of the Lichi Mélange, with incorporation of the kaolinite from the arc formation by fluid flow along the sheared plan or fractures. Therefore, kaolinite is absent in the forearc basin strata because they did not experience intense deformation.

3.2.4 Stratigraphic relations between the Coastal Range formations

Wherever overlain by the Fanshuliao deposits, the Tuluanshan formation is composed of debris-flow type breccias and turbidites. Moreover, although overlying the arc formation, the Fanshuliao deposits are contemporary to limestones and upper deposits of the Tuluanshan formation (*Teng et al.*, 1988; *Huang et al.*, 1988, 1995). This coevalness suggests that the Tuluanshan limestones and tuffs represent the shallow-water volcanic and fringing reefs environment, and the Fanshuliao turbidites and underlying Tuluanshan debris-flow deposits represent the deep-water deposits in the forearc basin (*Teng and Wang*, 1981; *Teng et al.*, 1988; *Teng and Lo*, 1985; *Chen*, 1997a).

The Paliwan sequences conformably overlie both the Fanshuliao and the Tuluanshan formations

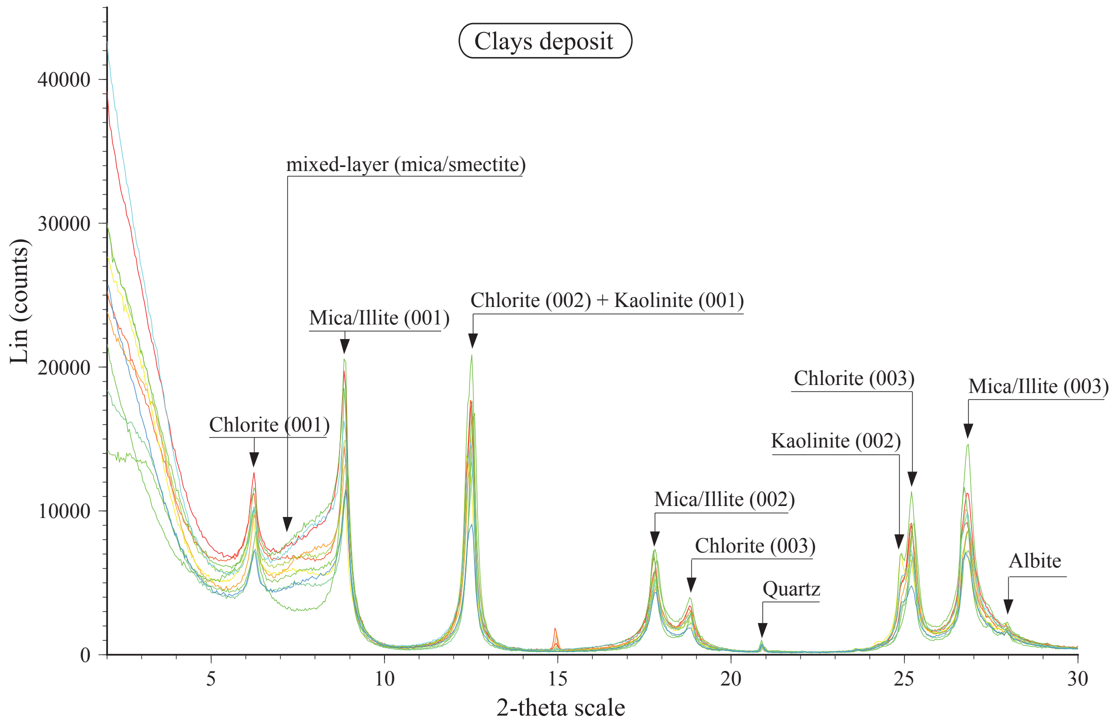

Figure 3.5: X-ray powder diffraction pattern of some oriented clay from Lichi Mélange matrix.

(Figure 3.2). Where it is observed in direct contact with Tuluanshan deposits, the Paliwan formation generally consists of deep-marine mudstones and turbidites resting on either limestones or tuffs (*Teng et al.*, 1988). The facies change associated with this contact is rather drastic and involves significant basin deepening (*Teng et al.*, 1988; *Huang et al.*, 1988, 1995). The contact between the Fanshuliao and the Paliwan formation varies with the facies character of the latter (*Teng et al.*, 1988). While the boundary between the two sequences is a depositional contact in the southern Coastal Range, represented by one layer of pebby sandstone (*Chen and Wang*, 1988), we clearly observe a sharp, erosional contact in the northern Coastal Range (*Teng and Lo*, 1985; *Chen and Wang*, 1988). Moreover, the formation exhibits overall a southward fining trend, with conglomerates dominating in the north and sandstones in the south (*Teng*, 1982; *Teng et al.*, 1988). These observations lead to the hypothesis of a northern source for the sediments.

The Lichi Mélange is mostly in faulting contact with the coherent forearc basin strata (Fanshuliao, Paliwan) and the Tuluanshan arc formation (*Hsu*, 1956; *Teng and Lo*, 1985) (Figure 3.1 and 3.4b). Nevertheless, depositional contact between the Lichi and Fanshuliao were reported (*Page and Suppe*, 1981; *Barrier and Muller*, 1984; *Huang et al.*, 2008). The Lichi Mélange has been intensely studied, and several origins have been proposed. It was first interpreted as a subduction complex, developed in the former Manilla Trench during the subduction of the South China Sea oceanic crust (*Biq*, 1971). But this interpretation is in contradiction to the position of the Lichi

Mélange, which lies east of the accretionary wedge instead of within the accretion prism (*Huang and Yin*, 1990; *Huang et al.*, 1992; *Reed et al.*, 1992; *Malavieille et al.*, 2002; *Huang et al.*, 2008). The Lichi Mélange was later interpreted as an olistostrome (*Wang*, 1976; *Ernst*, 1977; *Page and Suppe*, 1981; *Lin and Chen*, 1986) due to slumping into the western part of the forearc basin of the exposed accretionary prism (proto-Central Range). However, marine seismic investigations in the early 1990s, combined with previous biostratrigraphic studies, clays composition and lithology of the exotic blocks inside the mélange, questioned this model and led instead to the proposal of a tectonic collision origin, where the protolith of the mélange is the forearc basin, and the exotic blocks have been incorporated during the early stage of the collision (*Chang et al.*, 2000, 2001, 2009; *Huang et al.*, 2006a, 2008). Indeed, the marine seismic profile in the south of Taiwan shows synchronous deformation and sedimentation in the western part of the forearc basin: once the sediments are deposited in the Luzon trough, the sequence is deformed and then covered unconformably by the overlying sequence (*Huang et al.*, 2008) (Figures 1.1 and 1.3). On the other hand, in the eastern part of the forearc basin, sedimentation is continuous regardless of active deformation in the west. Near the southern tip of Taiwan, seismic profiles reveal the progressive closure of the forearc basin by arcward thrusting of the forearc basin strata (*Huang et al.*, 2008; *Malavieille et al.*, 2002; *Reed et al.*, 1992). The accumulation of deformation and shortening of the forearc basin would have led to the development of the Huatung Ridge, which connects northward with the Lichi Mélange in the southern Coastal Range (*Huang et al.*, 2008).

Finally, based on the petrographic features and stratigraphic relations described above, it is likely that the Tuluanshan, the Fanshuliao and the Lichi Mélange formations can be grouped as the pre-collision island-arc lithofacies and the Paliwan formation corresponds to the syn-post collision lithofacies (*Teng*, 1979, 1980b), and, consequently, should instead be considered as a flysch. The effect of this initial collision is well recorded by the deposition of voluminous coarse-grained continent-derived clastics of the Shuilien Conglomerate (Figure 3.1) in the northern Coastal Range (*Teng and Wang*, 1981; *Teng*, 1982), which started at about 3.5 Ma (*Teng*, 1982).

3.2.5 Tectonic scenario

The mineralogic content and field observations of the stratigraphic relations between the Coastal Range sequences give us clues as to the environment of deposition and tectonic history of the Coastal Range, which allow us to precisely locate the formations with regard to the creeping zone, and the following scenario can be proposed (Figure 3.6):

Intra-Oceanic Subduction

Rifting within the Eurasian continent in the Oligocene ($\sim$ 32 Ma) gave rise to the opening of the South China Sea until the Middle Miocene ($\sim$ 17 Ma) (*Briais et al.*, 1993). According to radiometric

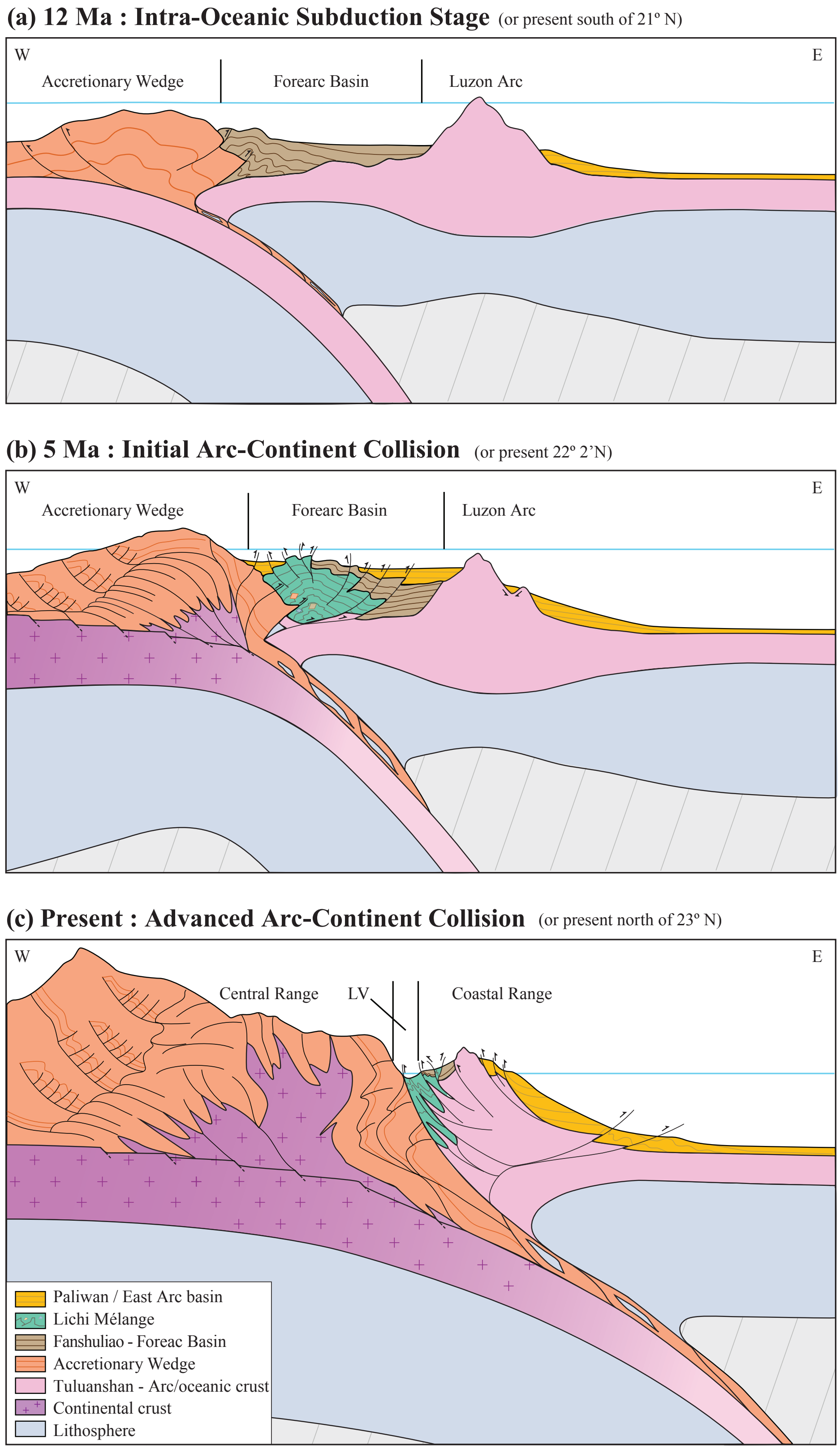

Figure 3.6: Tectonic sketching on the formation of the Coastal Range. (a) Tectonic setting at 12 Ma (or present south of 21°N): intra-oceanic subduction stage. (b) Tectonic setting at 5 Ma (or present 22°2'N): initial arc-continent collision. (c) Current tectonic setting (or present north of 23°N): advanced arc-continent collision.

dating (*Ho*, 1969; *Juang and Bellon*, 1984; *Yang et al.*, 1988; *Chen et al.*, 1990; *Lo et al.*, 1994), it was quickly followed by the eastward subduction of this basin, beneath the Philippine Sea Plate along the Manila Trench, leading to the creation of the volcanic Luzon arc. From Early Miocene (perhaps late Oligocene) to late Miocene, arc magmatism brought thick sequences of Tuluanshan volcanics and sediment offscraping, filling up the forearc basin (Figure 3.6a). As observed now south of 21°N (profil GMGS973 in Figure 1.3) (*Huang et al.*, 2008), once the sediments are deposited in the Luzon trough, the sequence is synchronously deformed and then unconformably overlain by new sequences.

Initial Arc-continent Collision

The initiation of the arc-continent collision starts with the closure of the forearc basin, leading to the formation of the Lichi Mélange (Figure 3.6b). At the same time, as the subduction continues, more and more continental sediments are added in the accretionary prism, which is finally exhumed, providing a new source of deposits for the forearc basin. Cessation of volcanism is also a good marker of the earliest stages of the collision, which suggests a southward propagation : 8-5 Ma for Chimei based on nanofossils (*Chi et al.*, 1981) and 3.3 for Chenkuangao based on fission track (*Yang et al.*, 1988). Subsequently, fringing reefs start to grow on volcanic islands providing evidences of the termination of volcanism. The oldest Kankgou limestone on the Chimei volcanic island has been dated to 5.2 Ma, and Tungho Limestone (in the south, on the Chengkuangao complex) returned an age of 2.9 Ma (*Huang et al.*, 1995, 1988). Based on those observations, it is reasonable to think that the initial arc-continent collision must have begun 7 to 8 Ma ago and that it had already reached 23°5N at 5.2 Ma (*Liu et al.*, 2000; *Suppe*, 1984; *Huang et al.*, 2006b). The equivalent state is located now at 22°2'N, as observed in seismic profile MW9006-31 in Figure 1.3 (*Huang et al.*, 2008). This southward propagation is consistent with the obliquity of the edge of the continental shelf of South China with respect to the subduction zone, which implies a southward migration rate of 90 mm/yr based on *Suppe* (1984) or 60 mm/yr based on *Byrne and Liu* (2002). (*Dorsey et al.*, 1988) study of the subsidence and uplift of the basins in the Coastal Range also concluded a migration rate of about 60 mm/yr.

Advanced Arc-Continent Collision

The westward thrusting and accretion of the Luzon arc and forearc sequences onto the Asian continent, conjointly with the exhumation of metamorphic basement in the Central Range, mark the final stage of the arc-continent collision (Figure 3.6c). This stage should be younger than the youngest strata found on the forearc basin sequences. Bio- and magnetostratigraphic studies (*Chang*, 1975; *Chi et al.*, 1981; *Horng and Shea*, 1997; *Lee et al.*, 1991) indicate that Coastal Range formations must have been accreted roughly 1.5 Ma ago in the north and 1.1 Ma in the south (*Huang et al.*, 2006b).

3.2.6 Origin of latitudinal variations in the occurrence of the Lichi Mélange

The Lichi Mélange is thus interpreted as the result of the deformation of the forearc strata and basement in the early stage of the collision. One might then wonder why there is almost no occurrence of the Lichi Mélange in the northern half of the Coastal Range.

The southward propagation of the arc-continent collision in Taiwan, as well as the indication that the volcanic activity within the Luzon arc shifted eastwards (*Yang et al.*, 1996) can today, south of Taiwan. Moroever, we should consider an increase over time of sediment supply in the foreac basin, with the exhumation of the accretionary prism and the continental basement. Consequently, a southward decrease of the thickness of the forearc basin sequences as well as a decrease in lithic content should be expected. Hence, the extent of the Lichi Mélange formation should be reduced northward.

Additionally, the northern termination of the Lichi Mélange outcrops correlates with a major tectonic feature of the Coastal Range, the Chimei Fault (Figure 3.1b and c), which splits the Coastal Range into northern and southern blocks. It is a left-lateral reverse fault with N-S compression, which separates the Tuluanshan and the Paliwan formations (Figure 3.1c) and which is ascribed a total offset of up to several kilometers (*Chen et al.*, 1991; *Kuo*, 2013). Therefore, the Chimei fault, and a probable northward decrease in thickness of the Lichi Mélange formation, might explain the rather abrupt termination of the Lichi Mélange outcrops.

Finally, it is also possible that the highly erodible Lichi Mélange would have been eroded away thanks to the thrusting component and the high erosion rate estimated to be more than 10 mm/yr in the Coastal Range (*Dadson et al.*, 2003). Therefore, the few spotty outcrops of potentially Lichi Mélange reported to the north of the Chimei Fault (Figure 3.1c) (*Teng*, 1980a) may well be the remnants of the Lichi formation, which was squeezed out upon land in the early stage of the collision.

3.3 Deformation mechanisms in the Lichi Mélange

3.3.1 Spatial correlation of aseismic slip with the Lichi Mélange

As mentioned in the introduction, the southern half of the LVF is clearly creeping at the surface. The lateral extent of the creeping segment is well revealed by the map of mean LOS velocity (in cm/yr) derived from the Permanent Scatter technique applied to PALSAR ALOS data acquired between 01/12/2007 and 09/07/2010 (*Champenois et al.*, 2012; *Thomas et al.*, to be submitted) (Figure 3.1b). This map shows a clear step in the LoS velocity field (positive toward the satellite) along the LVF, south of 23°30. The discontinuity is clear evidence of aseismic slip near the surface for the southern portion of the LVF, and comparison with surface geology supports earlier inferences (*Hsu et al.*, 2009a) that the Lichi Mélange would be responsible for promoting aseismic creep (Figure 3.1). By contrast, no clear discontinuity (at the detection level of the technique, estimated to be ~ 2 mm/yr at the 67% confidence level) is observed along the northern half of the LVF, suggesting that the shallow portion of the fault has remained locked over the 2007-2010 period. The lack of aseismic slip correlates with the disappearance of the collision mélange since only isolated outcrops of the Lichi Mélange have been recognized north of the Chimei Fault (*Teng*, 1980a) (Figure 3.1c). Therefore, in the particular case of the LVF, lithology seems to control the along strike variations of slip mode. We now examine the potential mechanisms which could explain enhanced aseismic creep where the fault is bounded by the Lichi Mélange. We examine in particular the difference of structure and mineralogical composition between the Lichi Mélange and the forearc formations.

3.3.2 Selection of field and core samples

Two field surveys and one core sampling have been conducted to study the different units of the Coastal Range. A total of 59 samples from the Lichi Mélange, Fanshuliao, Tuluanshan and Pailwan outcrops were collected, and 63 thin sections were prepared and analyzed (see Figure S1 in supplementary materials for location). We also sampled cores from shallow drillings, which were conducted near Chihshang (121°22E, 23°10N) (*Chen*, 2009; *Mu et al.*, 2011). We collected samples from the fault zone, as expressed by the intense macroscopic fracturation and foliation: 14 samples from the Wanan sites (Wan-1 and Wan-2) were selected, and the analysis of 16 thin sections has been carried out. All petrographic sections were polished sections to allow both optical and electron microscopy. Samples containing Lichi Mélange were impregnated with clear epoxy resin before cutting. We first resorted to optical transmitted and polarized light microscopy to examine the mineralogy contents and microstructures. A total of 11 field samples were also selected to perform a clay mineral analysis of the Lichi Mélange (Figure 3.5). High-resolution SEM combined with Energy-dispersive X-ray spectroscopy (EDS), as well as electron probe micro-analyzer were used for imaging the fault rock microstrures and determining the mineral phases of the Lichi samples from the fault zone (Figures 3.9, 3.7, 3.8 and S2, S3, S4 in supplementary materials). The selection of samples was based on microscopy anaylsis.

Hereafter we describe three representative samples for describing the LVF: (1) lvf4, a Lichi Mélange sample collected in the field (121°14'32"E and 23°9'56"N) on the LVF (Figure 3.4c-d), (2) l2w46, a sample from the borehole core Wan-2 at 46.4 m depth along the core section (*Chen*, 2009; *Mu et al.*, 2011), displaying the tectonic contact (LVF) between the quaternary conglomerate and the Lichi Mélange (Figure 3.4f-h) and (3) T12, a typical Fanshuliao sample collected in the field at longitude 121°22'25"E and latitude 23°22'55"N, as a protolith reference for the Lichi formation

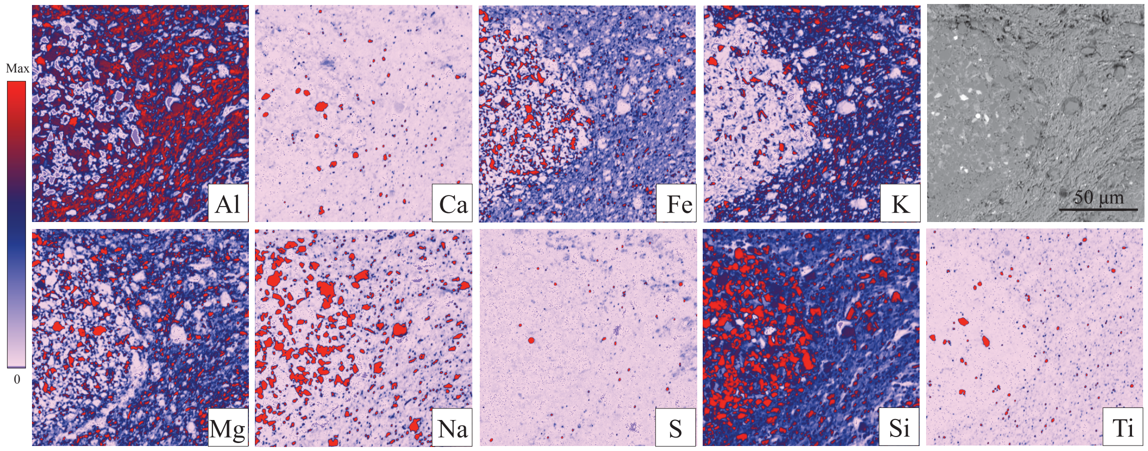

Figure 3.7: Electron probe micro-analyzer compositional maps of sample Lvf4, displaying a microlithon enmeshed in foliated matrix. The Lichi Mélange sample was collected in the field, inside the LVF fault gouge (Figure 3.1c). For location of the analysis, see Figure 3.4e. Red, blue and white colors indicates high, intermediate and missing contents respectively. The distribution of Aluminium indicates pervasive clay mineralization of the foliated matrix. The foliated gouge is also clearly depleted in Si, Ca and Na and passively concentrated in K, Al, Fe, Mg, Ti,and S compared to the microlithon (initial state), showing a deficit in soluble minerals that is likely related to pressure-solution diffusive mass transfer. The top-right corner figure is the corresponding BSE image of the area.

(Figure 3.3). See Figure 3.1c for the location of those three samples .

3.3.3 Microstructural and analytical observations

The fault gouge in the Lichi Mélange consists of altered, highly comminuted, scaly foliated rocks with slickensided surfaces and striations. All samples are pervasively sheared and display a characteristic anastomozing phyllosilicates foliation with sigmoidal microlithons and strain shadows (Figures 3.4d and c) that define R-type Riedel shear surface (*Rutter*, 1986). They provide a clear indication of bulk ductile flow. Foliation is defined by millimetric to sub-millimetric alternation of clay and quartz-rich bands (Figures 3.4a and b) that contain microstructural evidences of reworked cataclasites as well as mineralogic differentiation, which are likely related to pressure solution mass transfer (Figures 3.7 and 3.8). Pyrite minerals in the gouge provide evidence for hydrothermal fluid flow (Figures 3.8 and S2 in supplementary materials). Blocks in the matrix can be sub-millimetric to kilometric in size. In the thin sections we analysed they mostly consist of quartz-rich or calcite-rich lithic fragments with micro-fossils. Most remarkably, there are no veins in the gouge. By contrast, sandstone blocks in the foliated matrix are pervasively fractured with open fractures filled with calcite or breccias cemented by calcite (*Chen*, 1997b), which appear to have been injected, presumably under high fluid pressures.

The textural differences between the Fanshuliao formation (protolith equivalent) and the Lichi Mélange are emphasized by the electron probe micro-analyzer compositional maps presented in

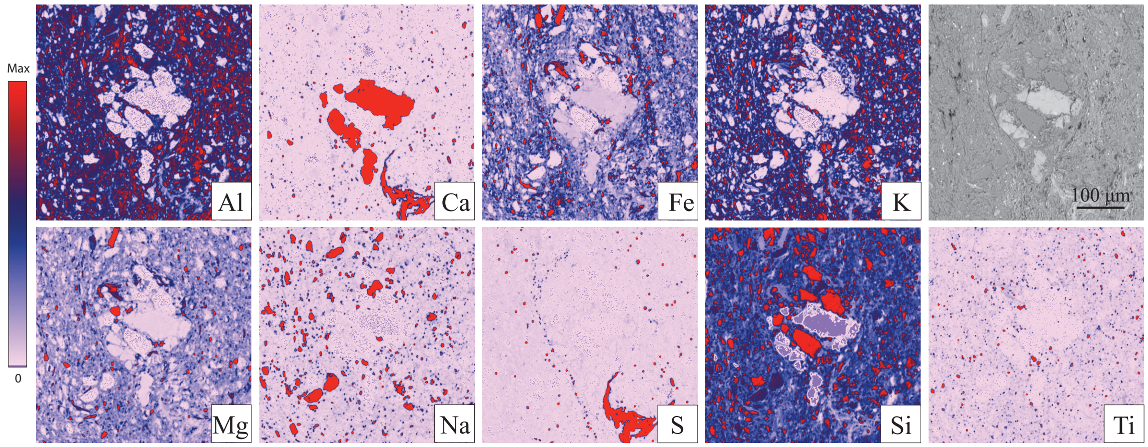

Figure 3.8: Electron probe micro-analyzer compositional maps of sample L2w46, displaying a sigmoidal microlithon embedded in foliated matrix. L2w46 was sampled on the borehole core Wan-2 at 46.4 m depth along the core section (Figure 3.1c). For the location of the analysis, see Figure 3.4h. Red, blue and white colors indicate high, intermediate and missing contents respectively. Distribution of Aluminium indicates pervasive clay mineralization of the foliated matrix. The foliated gouge is also clearly depleted in Si, Ca and Na, and passively concentrated in K, Al, Fe, Mg, Ti and S compared to the microlithon (initial state), showing a deficit in soluble minerals that is likely related to pressure-solution diffusive mass transfer. Evidence of pyrite masses in the gouge also favours the presence of hydrothermal fluid flow. The top-right corner figure is the corresponding BSE image of the area.

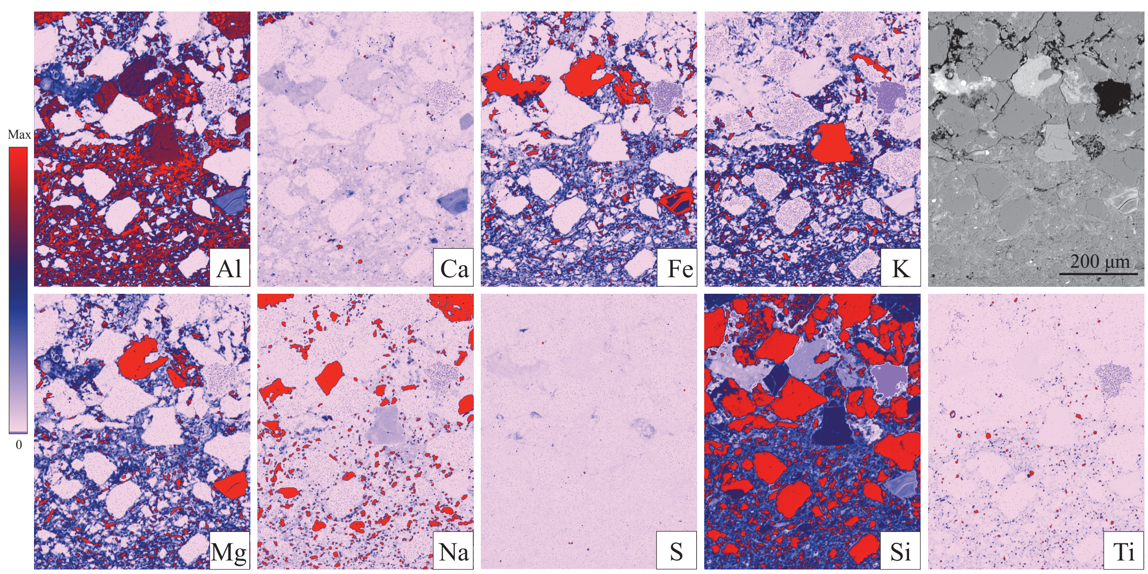

Figure 3.9: Electron probe micro-analyzer compositional maps of one typical foreac-basin formation sample (Fanshuliao) showing that no substantial differentiation is observed in the two sedimentary layers, which seems to display the same mineralogic contents (a slight increase in Ti may be inherited). The only difference stands in the grain size. For the location of the analysis, see Figure 3.3d. The top-right corner figure is the corresponding BSE image of the area, and red, blue and white colors in cthe ompositional map indicate high, intermediate and missing contents, respectively.

Figures 3.7, 3.8 and 3.9. The fault gouge, compared to sample T12 or the microlithons, which represent an initial state of the Lichi Mélange, is dominated by the development of a very fine grain matrix and foliation seams with a depletion of Si Ca and Na and a passive concentration of K, Al, Fe Mg, S, Ti. This corresponds to the dissolution of soluble minerals, such as quartz, feldspars and calcite, and the passive concentration of phyllosilicates and titano-ferro oxides associated with a possible recrystallization of the phyllosilicates. Quartz, calcite and feldspar are, on the contrary, preserved inside the microlithons and in the strain shadows of those grains (Figures 3.7 and 3.8).

3.4 Discussion

3.4.1 Deformation mechanisms of the Lichi Mélange and control on the aseismic behavior of the LVF

The microstructural study of the fault zone samples shows that the deformation on the LVF is accommodated by grain boundary sliding. Such a deformation mechanism can be operated by frictional sliding (with granular and/or cataclastic flows) or pressure-solution creep. The deformation observed in those fault zone rocks reflects the cumulative tectonic history since the onset of deformation of the Luzon forearc. The exhumed fault zone does not show much evidence for metamorphism, consistent with the low exhumation (less than 2km) (*Shyu et al.*, 2006) and relative cold conditions (Temperature less than 450°C in the 0-30 km depth range) inferred from the thermokinematic modeling of *Simoes et al.* (2007a). Note, however, that the estimated thermal structure is not well calibrated for the Coastal Range due to the lack of thermobarometric and thermochronological constraints in this area. However, it is likely that the deformation observed in the exhumed fault zone is representative of the ongoing deformation on the LVF at a relatively shallow depth (a few kilometers).

The primary fault zone processes observed in this study are the strong reduction of grain size and the pervasive foliation. Several processes might lead to grain-size reduction that include cataclasis, stress corrosion, dynamic recrystallization and neomineralization (*Snoke et al.*, 1998). the Lichi Mélange sample show evidence of cataclastic flow, which has been interpreted to be related to the early deformation of the foreac basin strata, based on the cross-cutting relation with the foliation (*Chen*, 1997b) (see section 3.2.4). On the other hand, the development of a strong anastomosing foliation inside the Lichi Mélange, the presence of sigmoidal porphyroclasts and microlithons and the evidence of strain shadows (Figures 3.4, 3.7 and 3.8) demonstrate the dominant role of pressure solution creep. Stress-driven dissolution is also strongly supported by the depletion in Ca-Na feldspar, quartz and calcite in the foliated matrix, whereas we observe an enrichment in phyllosilicates and oxydes (Figures 3.7 and 3.8). There is no evidence of redeposition in veins nearby; however, soluble species may have been transported away from the zone of dissolution and such fluid flow may likely be the source of the hydro-fracturing observed in sandstone blocks (*Chen*, 1997b).

Evidences of pressure-solution creep do not exclude the fact that part of the creep is accommodated by granular flows, involving friction. R-type Riedel slip surfaces in the clay-rich matrix surround the microlithons (Figure 3.4d) and demonstrate intrinsic material weakness. Aseismic slip might also occur by a granular flow mechanism that involves frictional sliding of microlithons in a matrix of phyllosilicates.

3.4.2 Influence of mineral frictional properties on fault slip mode

The matrix of the Lichi Mélange is rich in illite, chlorite, mixed-layer clay minerals (mica/smectite), which are also common constituents of subduction mélanges. Illite has long been thought to be dominantly velocity-weakening and smectite velocity-strengthening. The illitization of subducted sediments (smectite transforms to illite when the temperature get higher than about 450°C) was then considered to be the possible mechanism responsible for the updip limit of the seismogenic zone (*Hyndman et al.*, 1997). Recent experimental work has shown that the illite clay gouge is actually velocity-strenghtening in the $0 - 250$°C temperature range (*Saffer and Marone*, 2003; *Saffer et al.*, 2012; *den Hartog et al.*, 2012b,a). In fact, experimental studies show that, overall, unconsolidated and unlithified clay-rich gouges promote a velocity-strengthening behavior, and hence aseismic deformation, independently of their composition (in particular, the smectite/illite ratio) (*Rutter and Maddock*, 1992; *Saffer and Marone*, 2003; *Ikari et al.*, 2009; *Saffer et al.*, 2012). This result is consistent with the observation that the Lichi Mélange promotes aseismic slip at shallow depth on the LVF.

However, most intriguingly, there is no key mineralogical difference between the matrix of the Lichi Mélange along the creeping segment in the South and the forearc formations along the locked segment in the north. They only differ in the presence of kaolinite (see subsection 3.2.3), which displays both velocity-strengthening and velocity-weakening behavior at a low slip rate (11 μm/s), relatively low normal stress ($\sigma = 20 - 50$ MPa), and a high frictional strength ($f_o = 0.6$) (*Ikari et al.*, 2011a). In agreement with previous mineralogic studies (*Lin and Chen*, 1986) we did not find evidence for talc, serpentine or saponite (a form of smectite), which have been advocated to account for the aseismic creep on the San Andreas fault (e.g, *Solum et al.*, 2006; *Morrow et al.*, 2007; *Moore and Rymer*, 2007; *Lockner et al.*, 2011; *Carpenter et al.*, 2011). Therefore, it seems unlikely that the inherent frictional properties of the fault zone mineral constituents can explain why aseismic creep is favored at shallow depth on the southern segment of the LVF.

Nevertheless, the development of the foliation itself, as a microstructural weakening mechanism, could have substantially altered the mechanical properties of the Lichi Mélange compared to its undeformed protolith. The development of the foliation indeed favors low friction minerals, which, even though they might represent a very low mass fraction of the constituents, can turn out to dominate the mechanical properties of a fault zone (*Collettini et al.*, 2009; *Niemeijer et al.*, 2010a; *Ikari et al.*, 2011b). Besides, *Ikari et al.* (2011a) have found a systematic relationship between absolute frictional strength and the potential for unstable fault slip. Weak gouges, with coefficients of friction $\mu < 0.5$, exhibit only stable sliding behavior, whereas strong gouges, with $\mu \geq 0.5$, exhibit both stable and unstable slip (*Ikari et al.*, 2011a). Accordingly, even with similar mineralogic content, the well-foliated Lichi Mélange is more likely to display a velocity-strengthening behavior than the forearc basin strata that preserved the bedding structure.

3.4.3 Can pressure solution creep explain the lithological control of aseismic slip on the LVF?

The discussion above shows that the deformation of the Lichi Mélange along the LVF has involved pressure solution creep. For pressure-solution creep to develop and accommodate large creep rate, specific conditions are required. Soluble minerals such a quartz, calcite or feldspar, which have been proved to be abundant in the Lichi Mélange, must be present and interact with a fluid phase. Note that the solubility of these minerals varies with the temperature: calcite is more soluble at low temperature, whereas the dissolution of quartz and feldspar is more efficient at high temperature. Here we see on the outcrop the cumulative effect of this process since the Litchi Mélange, which is now at the surface, was dragged from depth along the thrust zone.

The rate of pressure solution creep is known to be inversely proportional to the cube of the grain size (*Rutter*, 1976). Therefore, very fine grained material decreases the distance of diffusive mass transfer and consequently increases the efficiency of the deformation mechanism (*Twiss and Moores*, 1992; *Gratier et al.*, 2011, 2013). Finally, the enhancement of pressure-solution creep under the influence of phyllosilicates has been recognized (*Weyl*, 1959; *Renard et al.*, 1997): clay minerals provide higher diffusivity in the contact layer and prevent the sealing of grains, which keep fast diffusive paths along solution seams (*Niemeijer and Spiers*, 2005; *Gratier et al.*, 2011). Therefore, the Lichi Mélange, compared to others lithological formations in the Coastal Range, gathers the specific conditions for pressure solution creep to exist, to persist in time and to accommodate large strain rates.

Pressure-solution creep has been shown to be a key factor in promoting aseismic deformation of synthetic fault gouge (*Niemeijer et al.*, 2010b). This experimental study demonstrates that pressure-solution creep tends to inhibit the strain-weakening behavior associated with pure mechanical deformation of the fault gouge. We suspect that such a mechanism could explain the large fraction of aseismic slip on the LVF. One objection to pressure-solution creep being the rate-controlling factor is that this mechanism predicts a linear viscous flow law (*Rutter*, 1976), while postseismic aseismic creep is highly non-linear in general, as was observed on the LVF, following the 2003 Chengkung Earthquake on the LVF (*Thomas et al.*, to be submitted; *Hsu et al.*, 2009b; *Chang et al.*, 2009). The abrupt acceleration of creep and the typical $1/t$ decay of afterslip rate following that earthquake is consistent with the behavior predicted by velocity-strengthening frictional sliding (*Marone et al.*, 1991; *Perfettini and Avouac*, 2004). However, it should be pointed out that velocity-strengthing friction is a phenomenological behavior that could result from a variety of different deformation mechanisms. Pressure-solution creep could actually be involved. *Gratier et al.* (2009) and *Gratier* (2011) have indeed demonstrated that micro-fractures development can drastically accelerate pressure solution creep rate: fracturing reduces the diffusive mass transfer distance, which is the rate-limiting effect. However, if the fractures are progressively sealed, this effect disappears and consequently reduces the displacement rate and shows exponential decrease (*Gratier et al.*, 2009). Such a mechanism would allow for reconciling the evidence for pressure-solution creep with the the acceleration of creep observed after the 2003 Chenkung earthquake and the later decay of afterslip rate.

Note that evidence of slickensides in the Lichi attest to cataclastic processes that must contribute to the creeping process. As the sliding occurs on relatively high friction minerals (see section 3.4.2) it must be associated with an increase in temperature. The partition between mass transfer through pressure-solution creep and friction process could be inferred, in theory, by measuring the temperature inside the creeping zone. This remains to be done, and it is not an easy process, due to the possible artifact effect of fluid cooling.

3.5 Conclusion

Based on the kinematic study of the LVF (*Thomas et al.*, to be submitted) and the tectonic analysis of the Coastal Range formations, we conclude that there is a strong lithological control of the mode of slip on the LVF: the presence of the Lichi Mélange clearly promotes aseismic creep. This finding is consistent with experimental studies which have demonstrated the velocity-strengtehing behavior of clay-rich gouges at low ($T < 250°$C) temperatures (*den Hartog et al.*, 2012a; *Saffer et al.*, 2012).

The lithological, meso- and microstructural evidences from the fault core samples suggest that it is likely that both frictional sliding (by cataclasis or granular flow) and pressure-solution creep concur to accommodate grain boundary sliding within the LVF gouge. A similar mode of deformation has been observed in experimental deformation of synthetic gouge (*Niemeijer et al.*, 2010b). Presumably, in such a context of competing deformation mechanisms, the less energy-consuming process should dominate (*Beeler et al.*, 1996). We argue that that pressure-solution creep is probably determining the creep rate, as in the experimental study, due to favorable conditions for pressure-solution creep inside the Lichi Mélange. As long as soluble minerals are present in the fault gouge, and those soluble species are transported away from the zone of dissolution, preventing restrengthening mechanisms such as cementation or fracture sealing, pressure-solution creep should be the dominating deformation mechanism. It is an efficient mechanism to accommodate aseismic creep through the entire upper crust down to more than 10 km (*Gratier et al.*, 2011). Episodic particle size reduction by cataclasis and alteration of feldspars to phyllosilicates are processes that would assist the pressure-solution creep mechanism and are likely to occur in the Lichi Mélange. The partition between dissolution and friction processes, which accommodate the sliding of the mineral elements, could be evaluated by measuring the temperature of the creeping zone, but this remains to be done.

This study suggests that aseismic creep is probably favored in the presence of any non-lithified subduction mélange, and that the internal structure of a fault gouge, namely the foliation, comminuted grain sizes, and the mixing of soluble and insoluble minerals, is more important in determining the mechanical properties of the fault zone than the mechanical properties of its mineral constituents, adding support to the view that fault zone fabric is essential in explaining fault mechanical properties (*Collettini et al.*, 2009; *Niemeijer et al.*, 2010a; *Ikari et al.*, 2011b).

Lithological control on the spatial evolution of fault slip on the Longitudinal Valley Fault, Taiwan - Supplementary materials

July 23, 2013

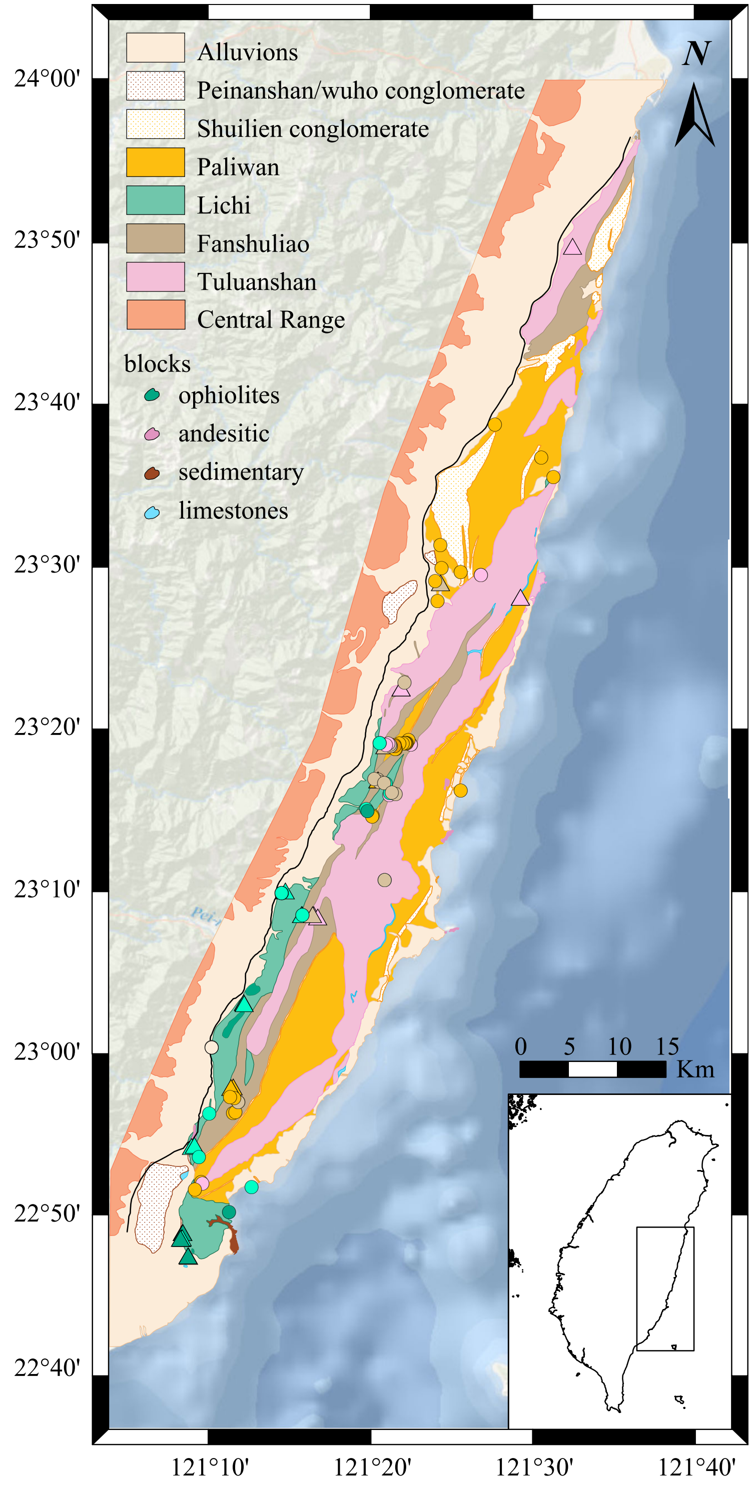

Figure S1: Geological map of eastern Taiwan (modified from Y. Wang and W.S Chen, 1993) and locations of samples collected in the field. Circle are samples collected in September 2012 while triangles gives the locations for the April 2010 sampling survey. Color attributions for samples and Lithological formations are identical.

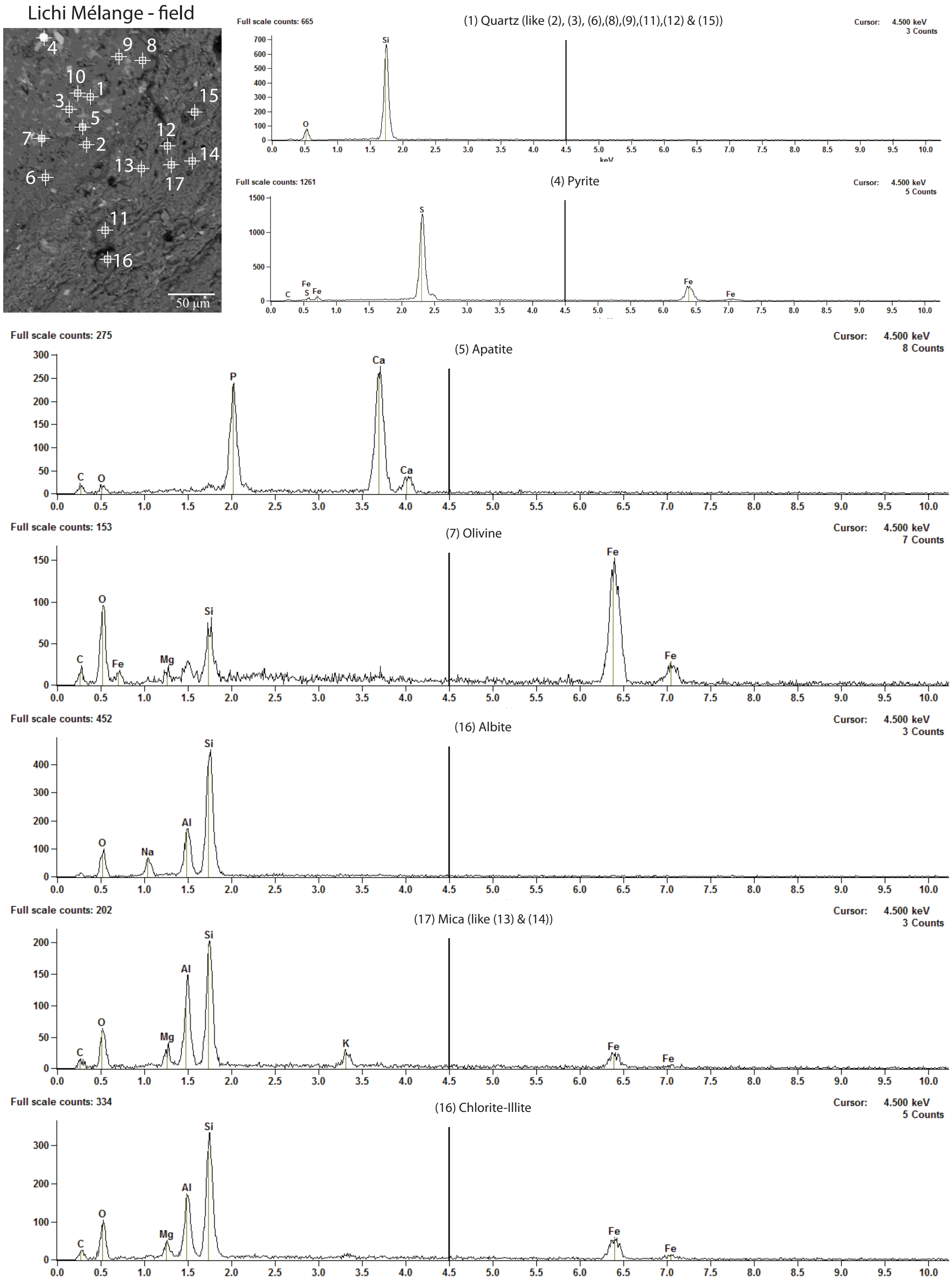

Figure S2: Representative EDS traces of grains inside de fault gouge, sample lvf4 (Lichi Mélange). For location of the analysis, see Figure 3.3e.

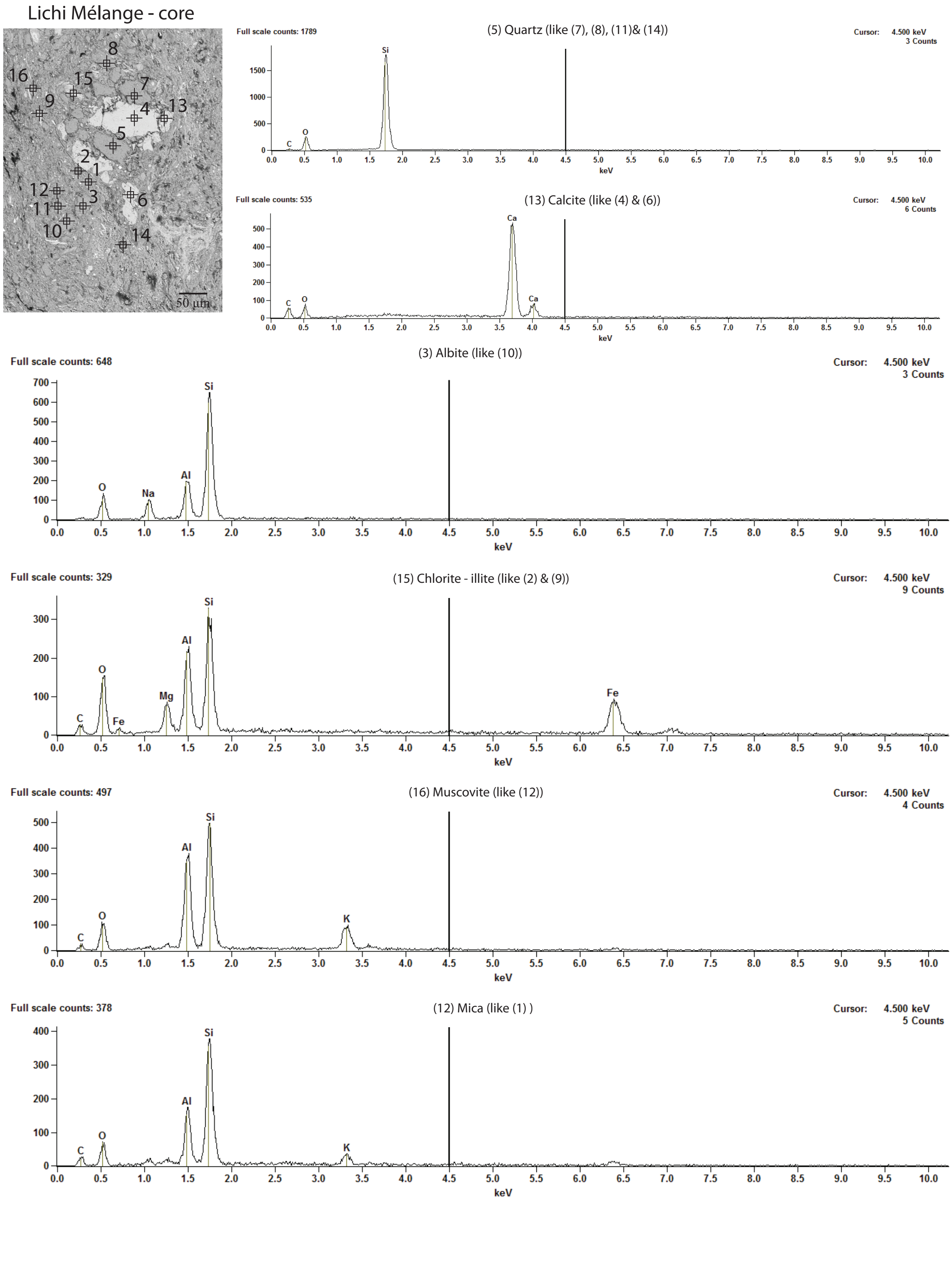

Figure S3: Representative EDS traces of grains inside de fault gouge, sample l2w46 (Lichi Mélange). For location of the analysis, see Figure 3.3h

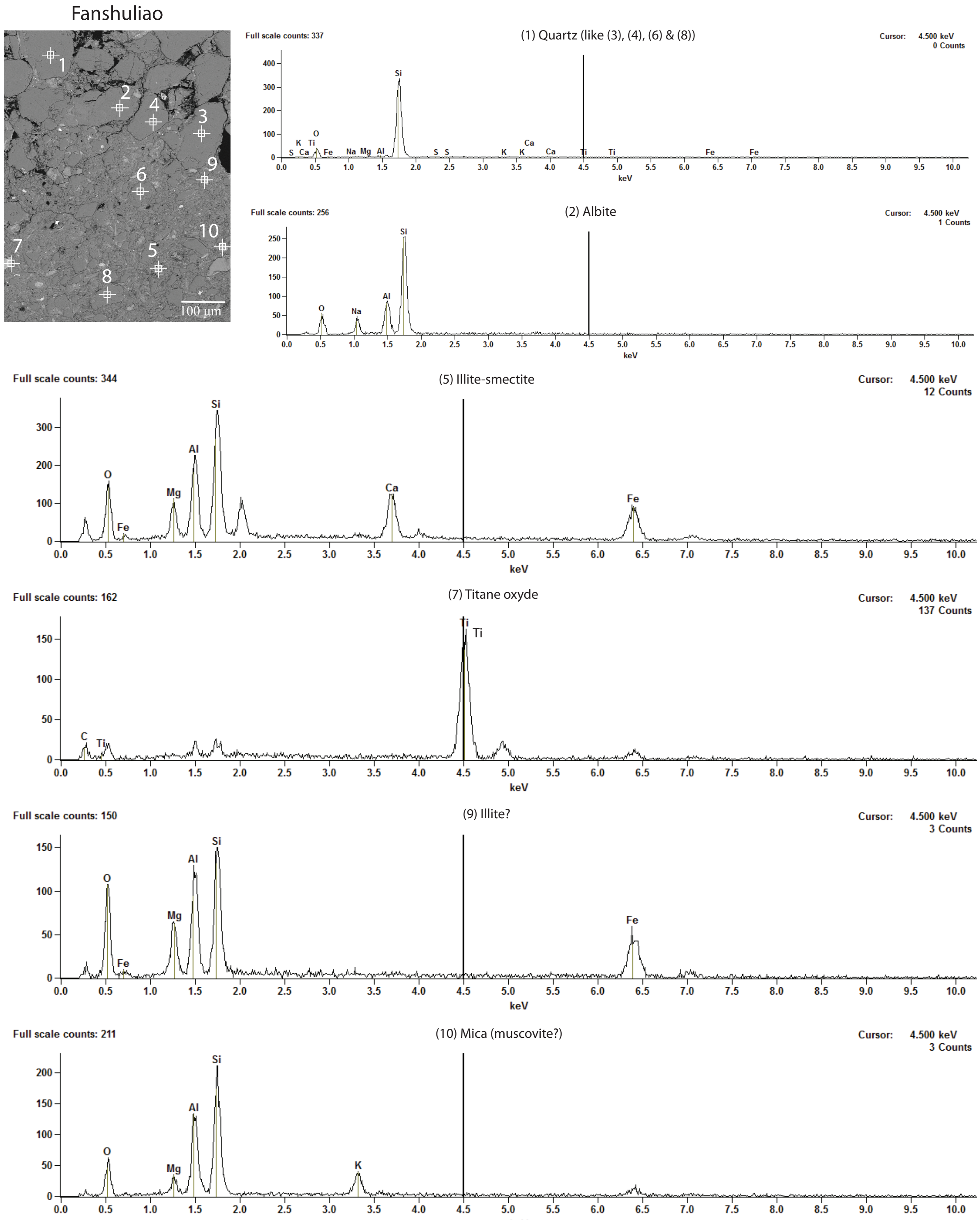

Figure S4: Representative EDS traces of grains inside the Fanshuliao formation, sample T12. For location of the analysis, see Figure 3.2d

Chapter 4

Quasi-dynamic versus fully-dynamic simulations of earthquakes sequences on heterogeneous faults with and without enhanced coseismic weakening

Marion Thomas, Nadia Lapusta, Hiroyuki Noda, and Jean-Philippe Avouac

Abstract

Theoretical fault models and computer simulations of fault slip can reveal the role and relative importance of different factors on the manner in which slip accumulates on faults. Such factors include various forms and parameters of friction laws, pore pressure evolution, and fault non-planarity. To study long deformation histories, most simulation methods do not incorporate full inertial effects during simulated fast slip. In quasi-static methods, a series of static problems is solved, with the loading advanced in time. However, such methods cannot simulate fast slip during seismic events, and earthquakes have to be added to such simulations in a kinematic fashion. That is why so-called quasi-dynamic methods have become increasingly popular, which approximately account for inertial effects (and hence seismic radiation) during simulated earthquakes through a radiation damping term. Such methods allow to continue simulations through the seismic phase, without having to pay significant additional memory and computational costs associated with modeling true wave-mediated effects.

In this study, we compare the results of quasi-dynamic simulations and fully-dynamic ones, in with all wave effects are accounted for during simulated earthquakes. We consider the long-term fault

behavior in two problems: (i) interaction of two velocity-weakening regions separated by a small velocity-strengthening patch and (ii) segments with additional pronounced rate-weakening during seismic slip. We find that, in the absence of additional seismic weakening, the two methods generally result in the same qualitative behavior, with similar slip patterns, although there are quantitative differences. In fact, in quasi-dynamic simulation, resulting seismic events tend to have much slower slip velocity and rupture speeds which may modify significantly the resulting seismic events and hence the long-term fault behavior. In simulations with additional coseismic rate weakening, the two methods produce qualitatively different long-term results with different slip patterns. Fully-dynamic solution generates pulse-like events, while quasi-dynamic formulation turns earthquakes to be more crack-like. Moreover, we observe that the levels of shear stress on the fault is significant different in both cases. In fully-dynamic simulations seismic events are able to nucleate and to propagate through the fault at a much lower level of shear stress than for quasi-dynamic ones.

4.1 Introduction

The expanding stream of seismic and geodetic observations on major faults provide increasingly better insight into the variability of fault slip behaviors over a wide range of temporal and spatial scales, from quasi-instant coseismic slip that generates seismic waves to slower interseismic and postseismic slips of the order of few cm/yr that can include transient events (few days to a few months) with sliding rates 10 to 100 times larger than the plate rate (e.g, *Kanamori and Hauksson*, 1992; *Kawasaki et al.*, 1995; *Linde et al.*, 1996; *Heki et al.*, 1997; *Freymueller et al.*, 2000; *Wallace et al.*, 2004; *Cross and Freymueller*, 2007; *Fournier and Freymueller*, 2007; *Chlieh et al.*, 2008; *Perfettini et al.*, 2010; *Loveless and Meade*, 2011; *Miyazaki et al.*, 2011; *Evans et al.*, 2012; *Burgmann et al.*, 2000; *Titus et al.*, 2006; *Murray et al.*, 2001; *Jolivet et al.*, 2012; *Kaneko et al.*, 2013). These observations suggest a complex pattern of slip in the 0-50 km seismogenic depth range, with the fault interface likely consisting of interfingered patches that either creep at a low rate, without seismic radiation, or remain locked during the interseismic period and rupture seismically. It has been observed that this segmentation have a strong influence on the seismic rupture patterns (*Burgmann et al.*, 2005; *Hetland and Hager*, 2006; *Chlieh et al.*, 2008; *Kaneko et al.*, 2010; *Perfettini et al.*, 2010; *Chlieh et al.*, 2011; *Loveless and Meade*, 2011): locked segments may rupture independently or together with neighboring patches, producing irregular earthquakes of different sizes. This complex behavior arises from the interaction of stress transfers, levels of prestress, and fault friction properties (*Rundle et al.*, 1984; *Cochard and Madariaga*, 1996; *Ariyoshi et al.*, 2009; *Kaneko et al.*, 2010).

Understanding the physics and mechanics of the fault behavior is an important issue in seismotectonics, since the seismic potential of any fault depends primarily on the partitioning between seismic and aseismic slip. Theoretical fault models and computer simulations of fault slip can reveal the role and relative importance of different factors on the manner in which slip accumulates on faults and can provide physical basis for understanding the entire earthquake sequence.

To study the factors controlling the fault behavior, it is essential to incorporate all the stages of the fault deformation into a single physics-based model. Simulating the behavior of the model requires algorithms that are able to treat all aspects of the observed fault slip, from long-duration deformation histories, with continuous aseismic creep throughout the loading period, to gradual nucleation of earthquakes, followed by dynamic propagation of ruptures and rapid post-dynamic deformation after such events. Indeed, prestress inherited from aseismic slip history and prior seismic events would determine where earthquakes would nucleate and how far the rupture would propagate. However, realistic simulations that account for full inertial (wave) effects during seismic events as well as long-term deformation history are challenging because of the variety of temporal and spatial scales involved. That is why many modeling efforts of long fault slip histories simplify the representation of the dynamic events (e.g, *Shibazaki and Matsuura*, 1992; *Cochard and Madariaga*, 1996; *Kato*, 2004; *Duan and Oglesby*, 2005; *Liu and Rice*, 2005; *Hillers et al.*, 2006; *Ziv and Cochard*, 2006). A common approximation is the quasi-dynamic (QD) model (*Rice*, 1993; *Ben-Zion and Rice*, 1995; *Rice and Ben-Zion*, 1996; *Hori et al.*, 2004; *Kato*, 2004; *Hillers et al.*, 2006; *Ziv and Cochard*, 2006) in which the wave-mediated stress transfers are ignored. In the QD simulations, inertial effects during simulated earthquakes are approximately accounted for through a radiation damping term. This method allows computing the long-term histories of fault slip, including the seismic phase, without having to pay significant additional memory and computational costs associated with modeling true wave-mediated effects. However, the question arises as to how the results of simulations are influenced by ignoring this part of the dynamic response (*Lapusta et al.*, 2000; *Lapusta and Liu*, 2009).

Here, we explore our hypothesis that the QD simulations can only be qualitatively useful in situations where the wave-mediated stress transfers do not produce qualitatively important features that define the model response. To that end, we study two conceptually different physical models. In the first one, only the standard rate-and-state friction laws (Dieterich, Ruina) are used, as in *Lapusta et al.* (2000); *Lapusta and Liu* (2009). In the other one, enhanced dynamic weakening is added motivated by flash heating (Rice 2006), which have been shown to result in self-healing pulses on low-prestressed faults (*Zheng and Rice*, 1998; *Noda et al.*, 2009). The self-healing mode is generated through appropriate stress transfers by dynamic waves, and hence the QD approach should not be able to capture it. We indeed find that the QD and fully dynamic (FD) simulations produce dramatically different results in the model with the enhanced weakening. Similarly dramatic differences between the QD and FD approach are expected in other situations where wave-mediated effects play a significant role, such as in the models with transitions to supershear speeds (e.g., *Andrews*, 1976; *Xia et al.*, 2004; *Liu and Lapusta*, 2008). We also consider how the QD and FD simulations compare with respect to rupture interaction with a potential local barrier in the form of a fault region with velocity-strengthening friction, following the study of *Kaneko et al.* (2010).

Our methodology is described in section 4.2, with a particular emphasis on the differences between the FD and QD approaches. Section 4.3 confronts the FD and QD simulations of earthquake sequences with the standard rate-and-state laws. In section 4.4, we consider how fault response compares when enhanced coseismic weakening is added in the FD and QD cases. The reasons for the dramatic differences between FD and QD simulations with enhanced weakening are discussed in section 4.5. In section 4.6 we explore the ability of the earthquake rupture to propagate over faults with heterogeneous properties for the two different friction laws models used in this paper, with or without full wave-mediated effects. Our findings are summarized in section 4.7.

4.2 Methodology

4.2.1 Fully dynamic vs quasi dynamic formulation

We consider a 2-D antiplane (Mode III) model, with 1D fault embedded in a 2D uniform, isotropic, elastic medium. Earthquakes occur spontaneously on the fault subject to slow tectonic loading. The model has been fully described by *Lapusta et al.* (2000). Nevertheless, in order to understand the difference between QD and FD formulation, it is useful to recall the underlying elastodynamic equations. We assume purely dip-slip motion on a fault which coincides with the $x-z$ plane of a Cartesian coordinate system xyz. The only non-zero displacement $u_x(y,z,t)$ is along-strike (parallel to the x direction). Then the time-dependent relative slip $\delta(z,t)$ corresponds to the displacement discontinuity $\delta(z,t) = u_x(0^+,z,t) - u_x(0^-,z,t)$. The relevant shear stress on the fault plane $\tau(z,t) = \sigma_{xy}(0,z,t)$ is expressed as the sum of a loading term $\tau^0(z,t)$, i.e. the stress that would act in absence of any displacement continuity on the fault plane $y = 0$, and some additional terms related to slip $\delta(z,t)$ (*Perrin et al.*, 1995; *Cochard and Madariaga*, 1996; *Lapusta et al.*, 2000):

$$\tau(z,t) = \tau^0(z,t) + f(z,t) - \frac{\mu}{2c_s}V(z,t), \tag{4.1}$$

where μ is the shear modulus, c is the shear wave speed and $V(z,t) = \partial\delta(z,t)/\partial t$ is the slip rate. In equation (4.1), the functional $f(z,t)$ incorporates most of the elastodynamic response and represents the stress transfer along the fault through waves. It is a linear functional of prior slip $\delta'(z',t')$ over the causality cone, that expresses the stress transfer due to a rupture. The third term, $\frac{\mu}{2c}V(z,t)$ represents the radiation damping term (energy radiated by waves in the medium) (*Rice*, 1993). Explicit extraction of that term from the functional $f(z,t)$ avoids singularities of the convolution integrals (*Cochard and Madariaga*, 1996).

The difference between FD and QD models lies in the expression of the stress-transfer functional

$f(z,t)$, which involves a double convolution integral in space and time. In the spectral domain, $f(z,t)$ is related to $\delta(z,t)$ by a single convolution integral in time when slip and the functional are represented as truncated Fourier series in space (*Perrin et al.*, 1995). This is very advantageous, as convolution integrals are the most computationally demanding part of the elastodynamic analysis. Let us write:

$$\delta(z,t) = \sum_{n=-N/2}^{N/2} D_n(t) e^{ik_n z}, \tag{4.2}$$

$$f(z,t) = \sum_{n=-N/2}^{N/2} F_n(t) e^{ik_n z}, \quad k_n = \frac{2\pi n}{\lambda}, \tag{4.3}$$

where λ is the length of the fault domain, replicated periodically and discretized into N (even) elements. The period λ has to be larger than the domain over which the seismic rupture takes place, to avoid influence of waves arriving from periodic replicates of the rupture. To satisfy the elastodynamic equations, the Fourier coefficients $D_n(t)$ and $F_n(t)$ are related by:

$$F_n(t) = -\frac{\mu\,|k_n|}{2} D_n(t) + \frac{\mu\,|k_n|}{2} \int_0^t W(|k_n|\, ct')\dot{D}_n(t-t')dt', \tag{4.4}$$

$$\dot{D}_n(t) = \frac{dD_n(t)}{dt}, \tag{4.5}$$

$$W(p) = \int_0^\infty \left[\frac{J_1(\xi)}{\xi}\right] d\xi, \quad \text{with} \quad W(0) = 1, \tag{4.6}$$

where $J_1(\xi)$ is the Bessel function of order 1. The first term in equation (4.4) represents the static redistribution of stress after a certain amount of slip, while the second term captures the wave-mediated stress transfer. This term depends on slip rate and its history, and it is computed in the time interval of the length T_w for which the elastodynamic effect are considered. We called equations (4.1-4.6) the fuly dynamic formulation. T_w is of the order of the time needed for the waves to propagate through the entire fault (further details about the convolution truncation can be found in *Lapusta et al.* (2000)). Relative to the fully-dynamic formulation, the quasi-dynamic models ignore this transient wave-propagation effect that influences the rupture (e.g., enhancing the stress concentration at the rupture tip). Equations (4.1-4.6) with $T_w = 0$ (no convolution) correspond to the quasi-dynamic procedure of *Rice* (1993), *Ben-Zion and Rice* (1995) and *Rice and Ben-Zion* (1996). They lead to the static calculation of stress transfers but account for dynamic radiation away from the fault through the radiation damping term; that is why those models are described as quasi-dynamic procedures. Then, the stress-transfer functional $f(z,t)$ for the quasi-dynamic models can be expressed as follows:

$$f(z,t) = \sum_{n=-N/2}^{N/2} -\frac{\mu\,|k_n|}{2} D_n(t) e^{ik_n z}, \quad k_n = \frac{2\pi n}{\lambda}. \tag{4.7}$$

Note that, with no damping term $\mu V/(2c_s)$ the quasi-dynamic procedure would turn into a quasi-static one and it would not allow solutions to exist during inertially controlled slip (*i.e.*, fast seismic slip). In the quesi-static formulation the slip rates become infinite as the seismic event approaches.

4.2.2 Standart logarithmic rate-and-state laws

Laboratory-derived rate-and-state laws (*Dieterich*, 1979; *Ruina*, 1983; *Dieterich*, 2007, and references therein) have been successfully used to simulate the fault in its entirety, from the nucleation process to the dynamic rupture propagation, followed by postseismic slip, interseismic period and re-strengthening of the fault between earthquakes (*Lapusta et al.*, 2000; *Noda and Lapusta*, 2010; *Kaneko et al.*, 2010; *Noda and Lapusta*, 2013). We first adopt the laboratory-derived rate-and-state laws with the aging law proposed by *Dieterich* (1979); *Ruina* (1983) which assumes constant normal stress σ:

$$\tau = \bar{\sigma} f = (\sigma - p)\left[f_0 + a \ln\left(\frac{V}{V_0}\right) + b \ln\left(\frac{V_0 L}{\theta}\right)\right], \tag{4.8}$$

$$\frac{d\theta}{dt} = 1 - \frac{V\theta}{L}, \tag{4.9}$$

where τ is the shear stress, f is the friction coefficient, V is the slip velocity, p is the pore pressure, θ is the state variable, L is the characteristic slip for state variable evolution, f_0 is the value of the friction coefficient corresponding to the reference slip rate V_0 and $a > 0$ and $b > 0$ are the constitutive parameters. At constant slip velocity V, the shear stress τ and the state variable θ evolve to their steady state values τ_{ss} and θ_{ss} respectively:

$$\theta_{ss}(V) = \frac{L}{V}, \tag{4.10}$$

$$\tau_{ss} = (\sigma - p)\left[f_0 + (a-b)\ln\left(\frac{V}{V_0}\right)\right]. \tag{4.11}$$

Hence, the value of the parameter combination $(a - b)$ defines the fault behavior at steady-state: $(a-b) > 0$ corresponds to velocity-strengthening friction properties, which lead to stable slip with the imposed loading rate, while $(a - b) < 0$ defines potentially seismogenic velocity-weakening regions of the model. We further refer to velocity-strengthening or velocity-weakening regions with the implicit understanding that this is the steady-state behavior.

Equation (4.8) is not definied for $V = 0$. To remedy this issue, we use the regularization following the physically-based approach based on an Arrhenius activated rate process describing creep at asperity contacts (*Lapusta et al.*, 2000; *Rice et al.*, 2001, and references therein):

$$\tau = \bar{\sigma} f(V, \theta) = (\sigma - p) f(V, \theta), \tag{4.12}$$

$$f(V, \theta) = a \sinh^{-1}\left[\frac{V}{2V_0} \exp\left(\frac{f_0 + b\ln(V_0\theta/L)}{a}\right)\right]. \tag{4.13}$$

4.2.3 Additional coseismic weakening

The standard logarithmic rate-and-state law has been derived from laboratory experiments at relatively low slip velocity, from 10^{-9} to 10^{-3} m/s, and small slips (of order centimeters) (*Dieterich*, 1979; *Ruina*, 1983). At seismic slip velocity of the order of 1 m/s, additional weakening mechanism can contribute. Several of the proposed additional processes are related to shear heating that unavoidably occurs during fast sliding that accumulates significant slip. With flash heating, fault gouge grains heat up at asperity contacts and substantially weaken, a phenomenon that has both theoretical and experimental support (e.g. *Lim and Ashby*, 1987; *Lim et al.*, 1989; *Tsutsumi and Shimamoto*, 1997; *Molinari et al.*, 1999; *Rice*, 1999; *Goldsby and Tullis*, 2002; *Beeler et al.*, 2008; *Rice*, 2006; *Tullis and Doldsby*, 2003; *Goldsby and Tullis*, 2011, and references therein). If the shear strain rate is sufficiently high, flash heating can occur even for small slip on the fault plane (of the order of 100 microns). Hence this mechanism might influence even the smallest earthquake. Pore fluid pressurization is another shear-heating-related weakening mechanism that might take place during seismic slip (e.g. *Sibson*, 1973; *Lachenbruch*, 1980; *Mase and Smith*, 1987; *Rudnicki and Chen*, 1988; *Sleep*, 1995; *Andrews*, 2002; *Bizzarri and Cocco*, 2006a,b; *Rice*, 2006; *Noda and Lapusta*, 2010). In that case, pore fluid expands faster in the shearing layer than the surrounding porous space, which increases the pore fluid pressure and hence decreases the effective normal stress, unless counteracted by fluid escape from the shearing zone and other potential processes such as inelastic dilatancy. Other suggested weakening processes include frictional melting (e.g. *Tsutsumi and Shimamoto*, 1997; *Hirose and Shimamoto*, 2005), dynamics of sliding between dissimilar materials (e.g. *Andrews and Ben-Zion*, 1997; *Adams*, 1998; *Cochard and Rice*, 2000), gel formation (*Goldsby and Tullis*, 2002; *Di Toro et al.*, 2004), and elastohydrodynamic lubrication (*Brodsky and Kanamori*, 2001).

For the purpose of this study, we we incorporate the effect of flash heating only. The logarithmic rate and state formulation at steady state (4.11) is modified to (*Noda and Lapusta*, 2010; *Lapusta et al.*, 2013):

$$f_{ss}(V) = f(V, \theta_{ss}(V)) = \frac{f(V, L/V) - \text{sign}(V) f_w}{1 - \text{sign}(V) V/V_w} + \text{sign}(V) f_w, \tag{4.14}$$

$$\text{with} \quad \frac{d\theta}{dt} = \frac{V\theta_{ss}(V)}{L} - \frac{V\theta}{L} = \frac{V}{L}\left(\theta_{ss}(V) - \theta\right), \tag{4.15}$$

where V_w is the characteristic slip velocity at which flash heating becomes significant (Figure 4.1b) and f_w is the residual friction coefficient. Based on laboratory experiments and flash heating theories, V_w is of the order of 0.1 m/s. Selecting much larger values of V_w would effectively disable the additional weakening due to flash heating and it would be equivalent to the formulation with the standard but regularized rate-and-state laws (equations 4.12-4.13).

4.2.4 Fault geometry and computational procedures

Fault geometry and properties in our simulations have been selected to follow *Kaneko et al.* (2010) study for comparison purposes (Figure 4.1c and Table 4.1). The fault is therefore 240 km long, subdivided into three VS segments (80 km each on both sides and 15 km in the middle), that surround two VW regions each 72.5 km long. The length of the central VS segment is varied in our simulations. We assign the rate-and-state parameter as follows: a is 0.01 for the entire fault and b varies to define VS and VW areas. b is 0.015 is in the VW regions and -0.01 and 0.008 for VS segments on the side and in the middle respectively. Uniform time-independent effective normal stress $\bar{\sigma} = (\sigma - p) = 50$ MPa is applied on the entire fault. The reference slip velocity $V_0 = 10^{-6}$ m/s, characteristic slip distance $L = 8$ mm, Poisson's ratio $\nu = 0.25$, and shear wave speed $c_s = 3.3$ km/s are also constant over the fault. The fault is loaded from the sides by steady motion at the long-term slip rate $V_{pl} = 50$ mm/yr. In the case of additional weakening, we set V_w and f_w to be 0.14 m/s and 0, respectively. The weakening is disabled in the VS regions by assigning $V_w = 10^9$ m/s.

In simulations with the standard rate-and-state law, the shear prestress τ_0 is equal to taht of *Kaneko et al.* (2010), which is 26.1 MPa for the VS patches on both sides of the fault, 28.2 MPa for the VS patch in the middle and two different values for the VW areas (28.5 MPa for the left one and 28.8 MPa for the right one) so that nucleation of the first earthquake preferentially starts at one side (left) rather at the two sides at the same time (Figure 4.1). In the case of simulations with additional weakening, we apply different τ_0 to avoid getting large slips in the very first event. Indeed, the shear stress history (Figure 4.2) shows that, in the case of additional weakening, earthquakes nucleate at lower average stress than for the regular rate-and-state law. Therefore, to be closer to the long-term behavior, the following initial shear stress values have been applied for the cases with enhanced weakening: 23.6 MPa for the VS areas on the sides, 29.4 MPa for the central VS patch, and 9 MPa for the VW segment.

The reference friction coefficient f_0 is set to be 0.6 everywhere, except for the simulations with additional weakening, where use f_0 to define a nucleation-prone patch. At the boundary between

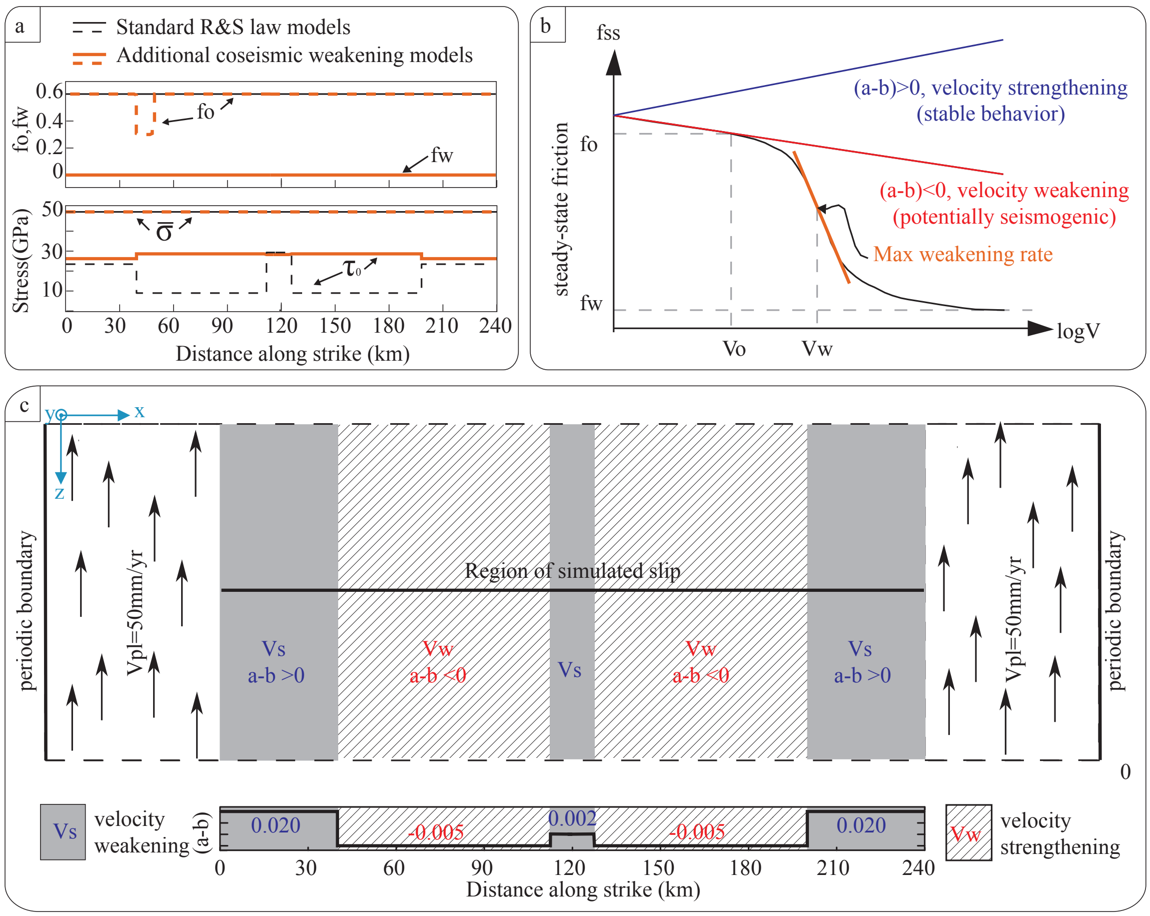

Figure 4.1: Schematics and parameters of the simulated fault. (a) Along-strike distribution of the reference friction coefficient (f_0), residual friction coefficient (f_w), effective normal stress ($\bar{\sigma}$), and initial shear stress (τ_0). Values for the standard rate-and-state law models are plotted in black while parameters for models with additional coseismic weakening are displayed in orange. (b) Schematics showing the dependence of the steady-sate friction coefficient on slip velocity in velocity-weakening (VW) areas for rate-and-state law models with (black) and without (red) flash heating. The blue curve illustrates the rate dependence of velocity-strengthening (VS)segments. (c) Schematics of the simulated fault. Rate-and-state friction acts on the 240-km-long fault, subdivided into two VW and three VS segments. Fault is loaded from the sides by steady motion at the long-term slip rate V_{pl} = 50 mm/yr. Along-strike variation of the friction parameter $(a - b)$ is given for the main cases plotted in Figures 4.3 and 4.5. In the other cases, only the size and $(a - b)$ value of the middle VS patch vary.

Parameter	Symbol	Value
Fault length along strike	λ	240 km
VW region length (total)	W_{VW}	145 km
VS region length (total)	W_{VS}	95 km
Loading slip rate	V_{pl}	50 mm/yr
Shear wave speed	c_s	3.3 km/s
Possion's ratio	ν	0.25
Effective normal stress	$\bar{\sigma} = (\sigma - p)$	50 MPa
Reference slip velocity	V_0	10^{-6} m/s
Reference friction coefficient	f_0	0.6
Rate-and-state direct effect	a	0.01
Rate-and-state parameters		
in VW regions	b	0.015
in VS regions	b	-0.01 /0.008
Characteristic slip	L	8 mm
Residual friction coefficient	f_w	0
Characteristic slip velocity	V_w	0.14 m/s
Cell size	Δx	29 m

Table 4.1: Parameters for our simulations

VS and VW regions, continuous creep in VS segments concentrates the shear stress, promoting nucleation near these rheological transitions. For simulations with flash heating, we create on a 10 km weaker patch next to the boundary between the VS and VW regions, where f_0 is decreased to 0.3 (Figure 4.1a). This weaker patch promotes earlier nucleation and therefore leads to more puse-like ruptures. In our study, the weaker patch helps to get less unrealistic seismic events for QD simulations with additional weakening (section 4.4).

4.3 Simulations of earthquake sequences with standard R&S law: FD vs QD

4.3.1 Fault response: common features

Histories of slip for representative QD and FD simulations with standard rate-and-rtate law are displayed in Figure 4.3. Accumulation of slip during interseismic periods is represented by blue lines, which are plotted every 50 years. Red lines display cumulative slip every 2 seconds when the maximum slip velocity on the fault exceeds 1 mm/s, illustrating the end of earthquake nucleation and slip during seismic events.

Despite their relatively simple geometry and distribution of friction properties, the numerical models produce realistic complex fault behavior. They both show seismic and aseismic slip including transients. As expected from stability properties of fault with rate-and-state law (e.g., *Rice and Ruina*, 1983), the VS areas are steadily slipping at the slip rate comparable to the plate veloc-

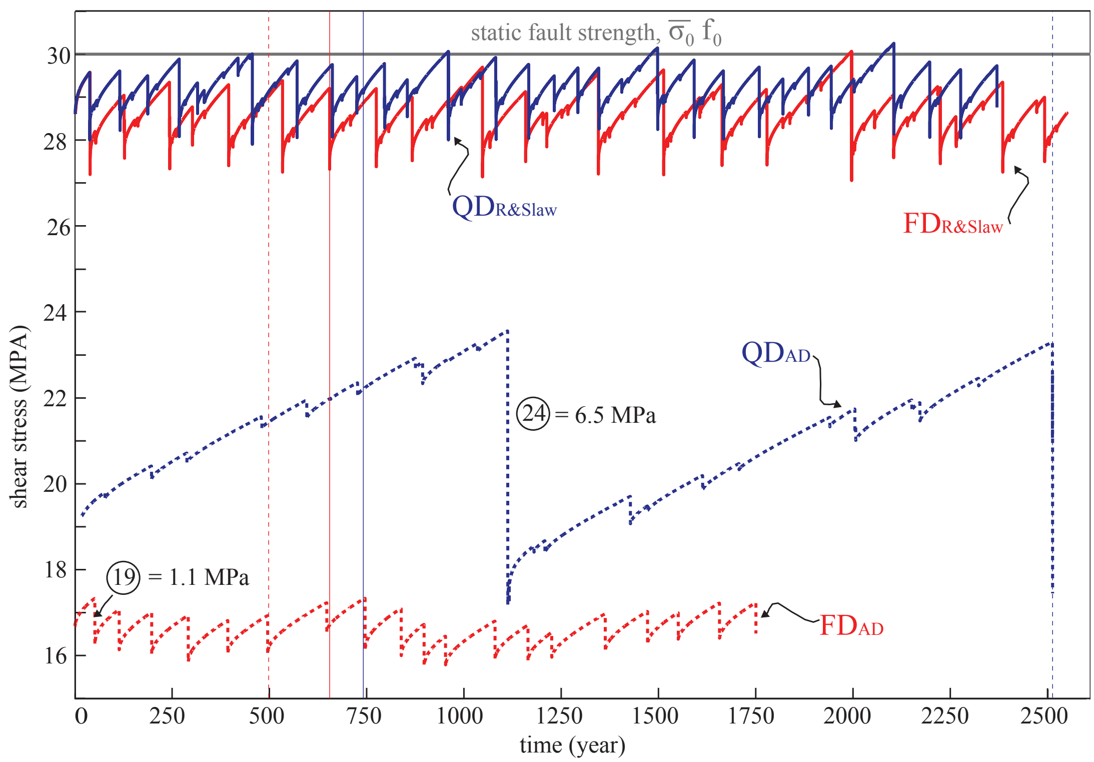

Figure 4.2: Shear stress levels on the fault over many earthquakes. The solid curves correspond to the QD (blue) and FD (red) standard rate-and-state (R&S) simulations. The corresponding vertical lines show the time limit for which we plot accumulation of slip on the fault in Figure 4.3. The dashed lines represent the stress levels for the QD (blue) and FD (red) simulations with additional coseismic weakening. Similarly, the corresponding vertical lines show the time over which we plot cumulative slip in Figure 4.5. The grey line gives a representative fault-averaged quasi-static fault strength ($\bar{\sigma} f_0$). In both cases (FD and QD), for the standard R&S law simulations, the average fault prestress before large, fault-spanning events is close to the representative static fault strength. In contrast, when models account for flash heating, the average fault prestress is significantly below the static fault strength, particularly for the FD case.

ity, whereas VW regions are almost fully locked during interseismic periods and accumulate the slip mainly during seismic events. Earthquakes nucleate where the fault undergoes local stress concentrations due to either rheological transitions from VS to VW regions or arrest of previous earthquakes. Depending on the level of prestress caused by previous slip, some events remains small, rupturing only a fraction of the VW area, while others grow large and propagate through the middle VS barrier. The larger VS regions on both sides of the model act as permanent barriers and coseismic ruptures penetrate into them only a little. The central VS patch affects rupture propagation, as shown by *Kaneko et al.* (2010): sometimes it acts as a barrier, and sometimes coseismic rupture goes through. The behavior depends on a number of factors, as discussed in *Kaneko et al.* (2010) and section 4.6. When only one VW segment ruptures, static stress increases at the tip of the previous rupture area, promoting propagation of the subsequent event through the VS patch and leads to the stress transfer into the neighbouring VW segment. This often leads to the nucleation of another event, shortly after the first one, at the boundary between the central VS patch and the unruptured VW area, which is a type of clustering.

4.3.2 QD vs FD: differences

The QD and FD simulations also exhibit important quantitative and qualitative differences. The first observation is that the final slip is smaller in the QD case than for the FD simulation. As a consequence, fewer events are needed in the FD case to accumulate the same amount of slip. Furthermore, the rupture speed and slip velocity, which are related to the horizontal and vertical spacing of red lines, respectively, are much lower for the QD simulation than for the FD one. If we compute the average rupture speed between black arrows in Figure 4.3, we find 3.56 km/s and 0.98 km/s for the FD and QD simulation respectively. This phenomenon is also illustrated in Figure 4.4a, which display the maximum sliding velocity recorded during one event. These differences have already been pointed out by *Lapusta et al.* (2000) and *Lapusta and Liu* (2009).

To quantify the evolution of the stress state on the fault for the two models, we consider the average shear stress $\tau_{av}(t)$ defined as follows:

$$\tau_{av}(t) = \frac{1}{z_2 - z_1} \int_{z_1}^{z_2} \tau(z,t) dz, \tag{4.16}$$

where the spatial integration is taken over the VW regions plus the central patch, excluding the VS areas on the sides. Therefore, $z_1 = 40$ km and $z_2 = 200$ km for the two examples shown in Figure 4.3 (see Figure 4.1 for fault geometry). The time evolution of the average stress for the standard rate-and-state laws is plotted in Figure 4.2 with solid curves. The vertical solid lines correspond to the time limit for which the accumulation of slip on the fault in shown in Figure 4.3. The variations in the average shear stress display steady interseismic accumulation of stress due to the tectonic

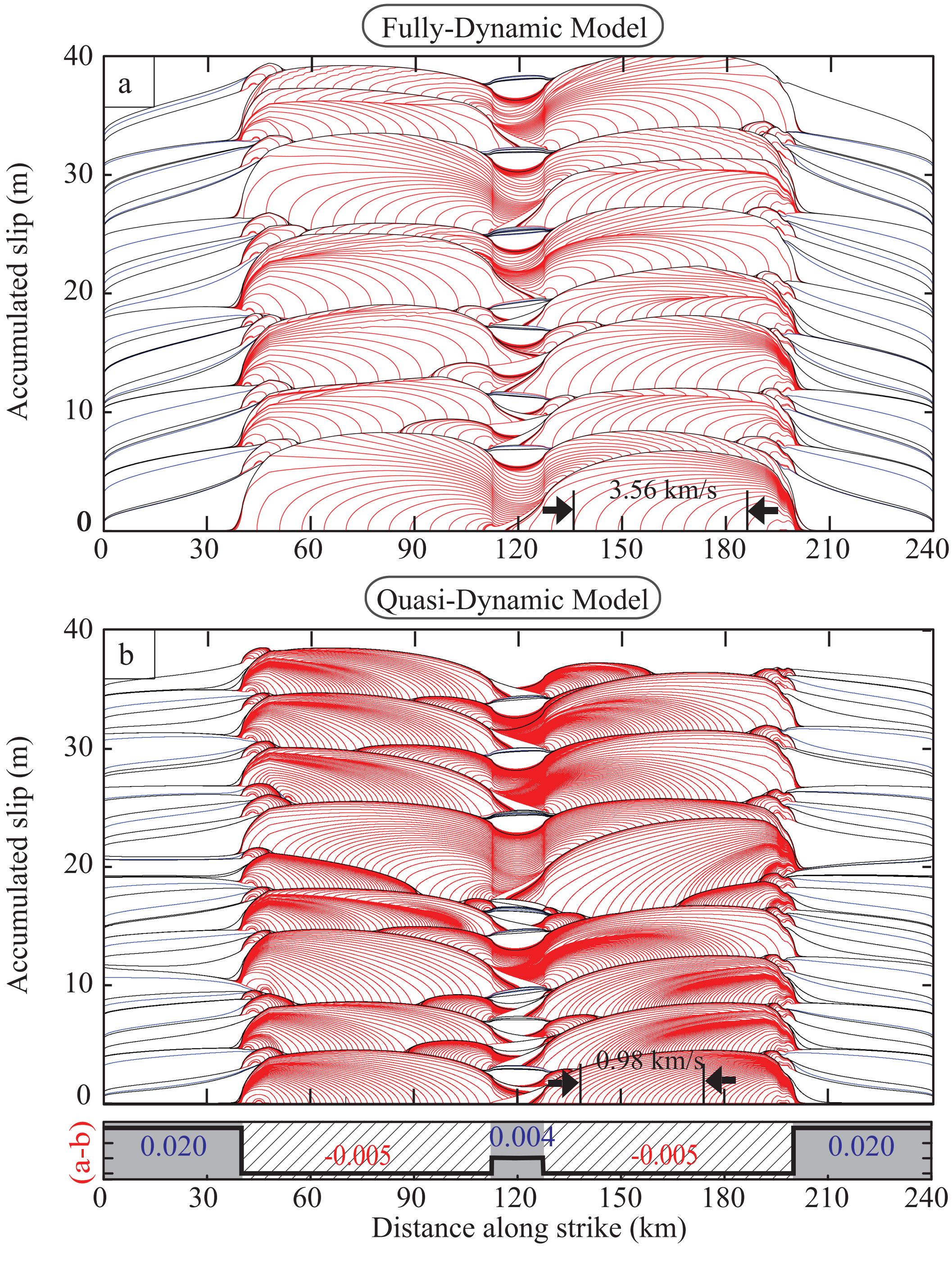

Figure 4.3: Cumulative slip on the fault for (a) FD and (b) QD simulations with the standard rate-and-state law. Red lines are plotted every 2 s during seismic events, when the maximum slip velocity exceeds 1 mm/s, while blue lines (every 50 years) illustrate the aseismic behavior of the fault. Black lines represent the cumulative slip after each seismic event. The middle VS patch creates complexity in both FD and QD cases. The FD events are bigger in general, display higher rupture speed (computed between black arrows), and are more likely to rupture the middle VS asperity as discussed in section 6.

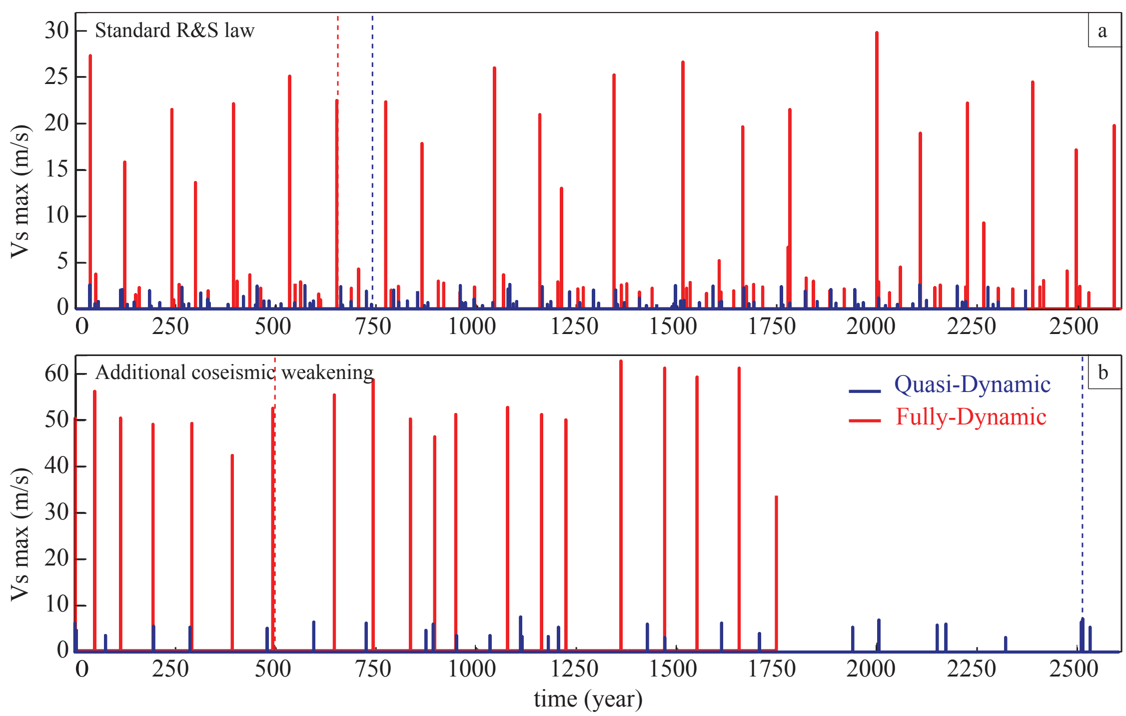

Figure 4.4: The maximum slip velocity over the fault for the QD and FD simulations (a) without and (b) with additional coseismic weakening for the reference cases plotted in Figures 4.3 and 4.5, respectively. In both cases, the maximum velocity is much higher (about 10 times) in the FD simulations than in in the QD ones. Accounting for additional coseismic weakening also increases significantly the slip velocity (about 2 times) for both QD and FD formulations but the ratio between the two stays similar. The vertical dashed lines illustrate the time limit for which we plot the cumulative slip on the fault in Figures 4.3 and 4.5.

loading, with occasional abrupt drops representing the simulated earthquakes. Consequently, local peaks of the average shear stress correspond to the level of stress on the fault before earthquakes nucleate. For both curves, the peaks are close to the representative quasi-static (or low-velocity) fault strength $\bar{\sigma} f_0 = 30$ MPa (the grey line in Figure 4.2) averaged over the seismogenic part of the fault (VW segments + VS asperity), but the FD simulation displays a slightly smaller value compared to the QD model. This shows that the FD formulation promote the nucleation, with the wave-mediated stress transfer enhancing the stress concentration in the nucleation zone and promoting the transition to rapid expansion at lower values of prestress. If one divides the shear stress peak values by the effective normal stress (50 MPa) to estimate the equivalent friction coefficient, one finds a value of 0.55 for the QD simulation and 0.54 for the FD case, which is close to the representatuve quasi-static friction coefficient ($f_0 = 0.6$). The stress drop for the larger events is, on average, ~ 0.99 MPa and ~ 1.26 MPa for the QD and the FD simulations, respectively, which is consistent with the difference in the cumulative slip per event observed in Figure 4.3. Note that we estimate the stress drop directly from the fault-averaged shear stress change from Figure 4.2. Such fault-averaged stress is not exactly equal to the seismologically estimated moment-based stress drop (*Noda and Lapusta*, 2013). However, for the relatively uniform slips that we have in our models, the two estimates are quite close.

Overall, the FD and QD models in the case of standard rate-and-state law are qualitatively similar but quantitatively different. We will see in the following section that the differences are much more dramatic in the presence of enhanced coseismic weakening.

It has been hypothesized (*Lapusta et al.*, 2000) that smaller radiation damping terms in the QD formulation can make the comparison with FD models more favourable. In that case, constant β_s is added to equation (4.1):

$$\tau(z,t) = \tau^0(z,t) + f(z,t) - \frac{\mu}{2c_s\beta s}V(z,t), \tag{4.17}$$

with $\beta_s \geq 1$. *Lapusta and Liu* (2009) have explored this hypothesis for 3D cases and found that indeed, the rupture speed in the QD simulations increases with the higher values of β_s, however, the slip velocity remains small in comparison with the FD events. Moreover, final slip, average slip per event, and static stress drop are smaller for all the QD simulations they have explored ($\beta_s =$1, 2 or 4). *Lapusta and Liu* (2009) also emphasized that increasing β_s further is not a promising approach, since the rupture speed for $\beta_s = 4$ is already higher than that in the FD case. Therefore, the QD approach can be used to explored the fault behavior qualitatively in somes cases (see section 4.7 for more discussion) but it cannot be precise quantitatively.

4.4 Simulations of earthquake sequences with additional weakening: FD vs QD

4.4.1 Fault response : seismic and aseismic slip including transient

Despite having the same model parameters, QD and FD simulations display drastic differences in cases with additional dynamic weakening. Slip history for representative QD and FD simulations is displayed in Figure 4.5. As for Figure 4.3, the accumulation of slip during the intersesimic period is plotted every 50 years in blue, whereas the accumulation of slip during seismic events is displayed every 2 s with red lines. For plotting purposes, we increase four times the ordinate axis for the QD simulation, but we keep the same scale as in Figure 4.3 for the FD case. Both FD and QD simulations show seismic and aseismic slip, including transients, but earthquake ruptures are very different in size, recurrence, and propagation mode.

The first observation is that earthquake events can become unrealistic in the QD simulation if the friction law includes coseismic weakening mechanisms. For example, event 24 in the QD model (Figure 4.5) displays a maximum slip of 75 m while FD simulations records $\sim$ 6 m of slip on average with the peak at 7 m. Moreover, despite the simple geometry and the same parametrization, QD simulations produce a more complex earthquake sequence behavior. In the FD model, for this particular setup, all events are able to propagate through the VS region in the middle and look very similar to one another. In the QD solution, depending on the level of prestress, some events remains small, rupturing only a fraction of the VW area, while others grow large and propagate through the middle VS barrier (Figure 4.5).

4.4.2 Pulse-like ruptures in FD vs crack-like ones in QD simulations

The mode of rupture for the largest events in the two simulations are radically different: the FD solution generates pulse-like events, while the QD formulation results in crack-like events. To illustrate this phenomenon, Figure 4.5 shows in grey the spatial extend of fault slipping during 2 sec interval, close to the end of the rupture. For event 19 in the FD simulation, only a small part of the fault ($\sim$ 10 km out of 160 km) slips during those 2 sec, while in the QD simulation (event 24), the slipping area is 140 km out of 160 km, with most of the seismogenic part of the fault slipping. We see that, for the QD cases, the region where the earthquake nucleated keeps slipping as the rupture propagates further.

Evolution of slip rate through time for the two events is another way to emphasize the difference (Figure 4.6 for the FD event 19 and Figure 4.7 for the QD event 24). Both seismic events nucleate similarly, but thereafter they display a very different story. In the FD dynamic case (Figure 4.6), while propagating through the VW area, the slipping region is consistently narrow and the second

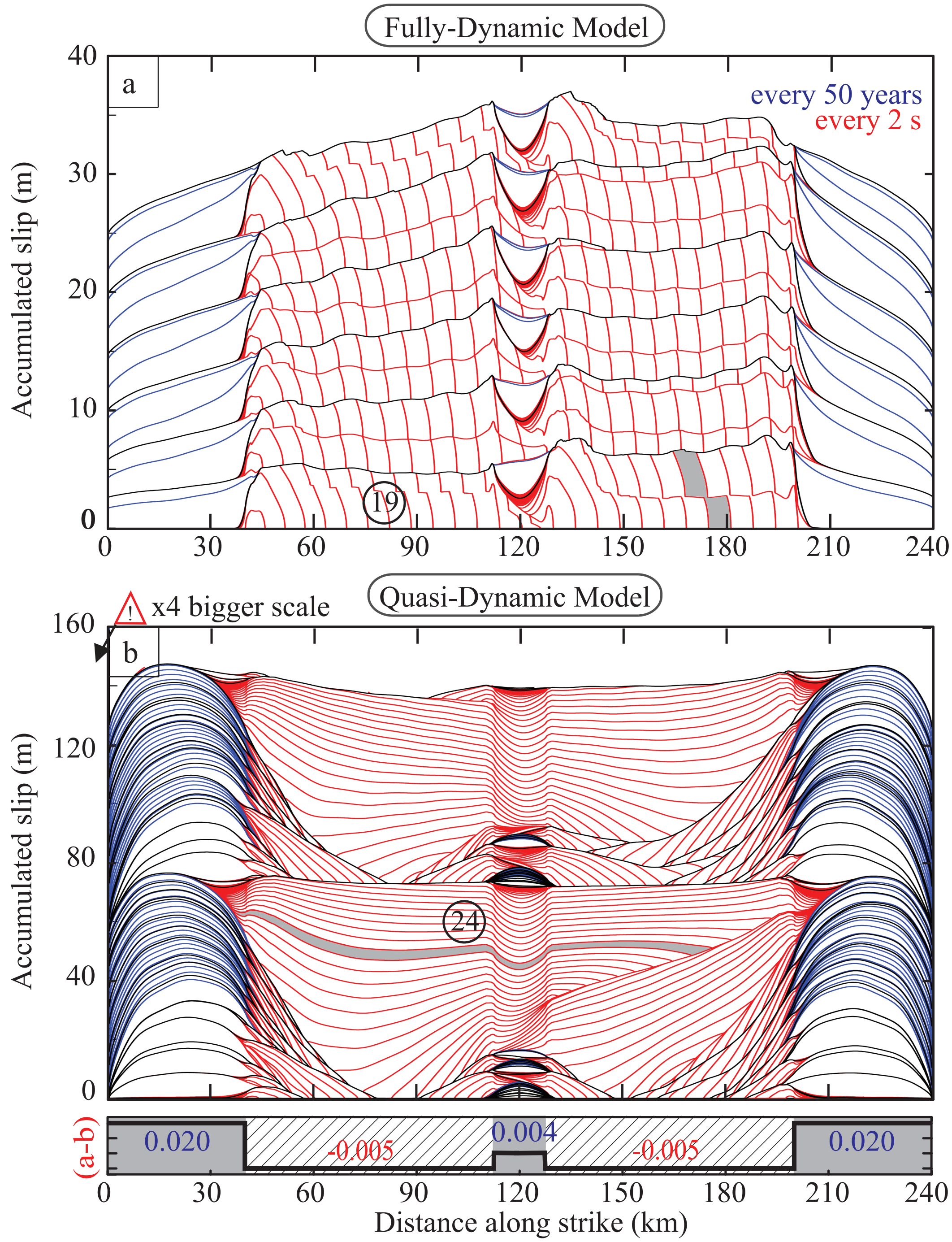

Figure 4.5: Cumulative slip on the fault for the a) FD and (b) QD simulations with the rate-and-state law and additional coseismic weakening. Note that the y-axis has four times larger values in (b) than in (a). Red lines are plotted every 2 s during seismic events while blue lines are plotted every 50 years. Black lines represent the cumulative slip after each seismic event. The FD and QD events are very different in size, recurrence, and propagation mode. The FD solution generates pulse-like events, while the QD formulation results in smaller events in the form of dying pulses and large crack-like events. The slip-rate snapshots for events 19 in (a) and 24 in (b) are displayed in Figures 4.6 and 4.7, respectively.

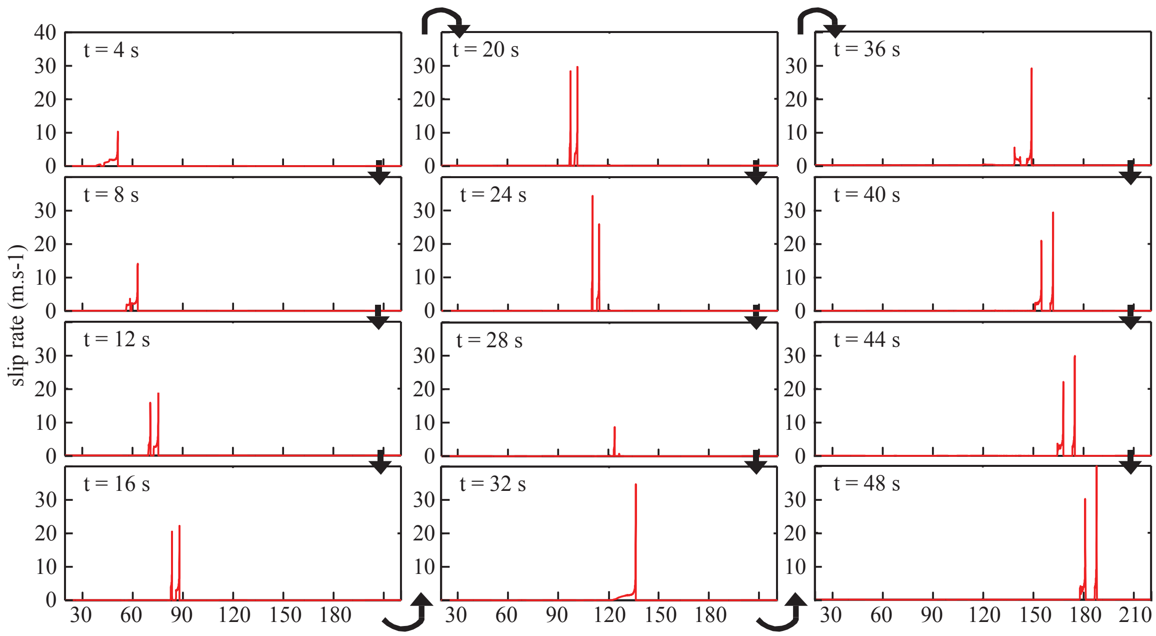

Figure 4.6: Snapshots of slip rate on the fault for a representative FD event with enhanced coseismic weakening. The slip rate is non-zero only on a small portion of the fault at a time, indicating that the rupture propagates as a narrow self-healing slip pulse (which is actually a double pulse in most snapshots). The slip rate increases as the rupture propagates through the first (right) VW segment, but then decreases when the rupture encounters the VS middle patch. Propagation in the second VW patch leads to the slip rate increasing again . For the cumulative slip history of this seismic event (number 19), see Figure 4.5.

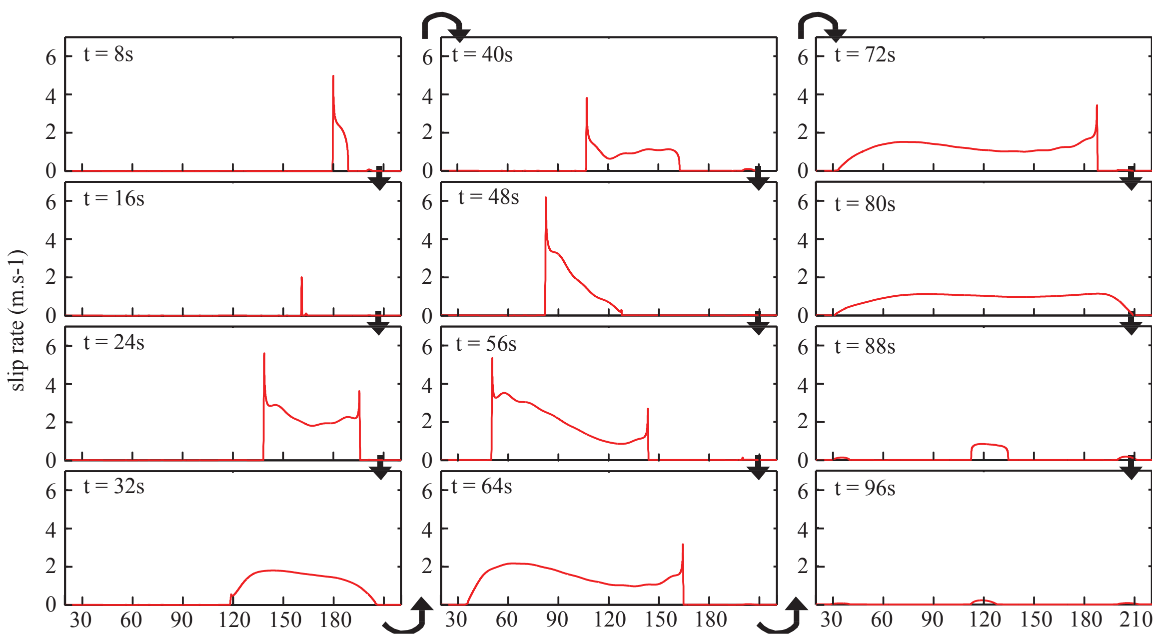

Figure 4.7: Snapshots of slip rate on the fault for a representative model-spanning QD event with enhanced coseismic weakening. As the rupture propagates through the fault, segments that have already sustained seismic motion still accumulate more slip, which leads to the development of a crack-like rupture. The middle VS patch decreases the slip rate but does not stop the rupture. For the cumulative slip history of this seismic event (number 24), see Figure 4.5.

pulse is developed ($t = 8$ s to $t = 29$ s). When the rupture encounters the central VS patch ($t = 28$ s), the slip rate drastically decreases. Propagation in the second VW patch leads again to the creation of a double pulse and slip rate increases up to 40 m/s. For the QD event number 24 (Figure 4.7), nucleation starts within the right VW region, then the rupture extends bilaterally in a crack-like modes. The rupture becomes less vigorous as it propagates through the central VS patch, then re-surges on the other side, with large slips that promote the re-rupturing of the right VW patch.

Note that the smaller events in the QD case, the ones that nucleate at the sides of the seismogenic region and arrest before reaching the middle of the fault, propagate as dying pulses.

4.4.3 Average shear stress level on the fault

The state of stress on the fault is strongly influenced by the FD vs QD modeling procedures. The time evolution of average shear stress (equation 4.16) for the QD and FD models with additional weakening mechanisms is plotted in Figure 4.2 with the dashed blue and red curves, respectively. The corresponding vertical lines show the time limit for which the accumulation of slip is illustrated (Figure 4.5). Unlike for simulations that assume the standard rate-and-state logarithmic-type coseismic weakening, the average shear stress on the fault with additional coseismic weakening is much smaller than the quasi-static strength $\bar{\sigma} f_0$. Accounting for full inertial effects reduces even more the average stress level. In the simulation with additional weakening and wave-mediated stress transfers (dashed red curves), the peaks of the average shear stress are between 16.5 and 17.3 MPa, with the equivalent friction coefficients of 0.33 and 0.35, respectively. The seismic events are very similar, with the return period of ~ 92 years on average and stress drop of ~ 0.78 MPa. The QD simulation displays a very different behavior. Interseismic increase of average shear stress, punctuated by stress drop due to smaller events, is observed over a period of ~ 1100 years until the stress reaches a peak of 23.6 MPa. During that time, smaller events can occur on the sides of the fault and their stress drops appear smaller on this plot due to averaging over the entire fault. The equivalent coefficient of friction in this QD case is close to 0.47. Thereafter, the fault records a large event with the stress drop of 6.5 MPA, 8.3 times bigger than that of a representative FD event (Figure 4.2).

4.5 Reasons for the dramatic differences between FD and QD simulations with enhanced weakening

It is clear that the QD simulations produce qualitatively different outcome from the FD ones in the cases with enhanced coseismic weakening, unlike our findings for the models with standard rate-and-state weakening only, as in section 4.3. In all cases, the exclusion of the wave-mediated stress transfers lowers stress concentration at the rupture tip, hence lowering slip rates there. In the case of the standard rate-and-state law, this mostly leads to slower rupture speeds, consistent with dynamic fracture mechanics (e.g., *Freund*, 1990); however, the amount of weakening the fault experiences is virtually unchanged, since the weakening in the standard rate-and-state friction laws is only logarithmically dependent on the slip rate. In the case of enhanced coseismic weakening, however, the dependence of fault weakening on the slip rates is much stronger, and the reduction of slip rates in the QD simulations has a profound effect on how the fault weakens with slip. In essence, the FD simulations have more intense fault weakening than the QD ones, promoting low-stress fault operation and pulse-like rupture mode as consistent with the previous theories and numerical findings (*Zheng and Rice*, 1998; *Noda et al.*, 2009; *Lapusta et al.*, 2013). As the result, the FD simulations have the fault operating under low overall prestress (section 4.4.3) with all ruptures propagating in the pulse-like mode (section 4.4.2), while the QD simulations produce a mixture of smaller events that arrest as dying pulses and much larger, model-spanning, crack-like ruptures under larger prestress.

The differences between the FD and QD simulations manifest themselves even during the nucleation processes. As mentioned in section 4.2.4 for the simulations with additional weakening, the reference friction coefficient f_0 is defined to be 0.6 everywhere, except for the nucleation-prone patch near the transition zone between the VW and VS segments (at $x \simeq 45$ km in Figure 4.1). In the FD models, all events nucleate at that particular location. In the QD simulations, events nucleate on both sides of the VW fault and even at the boundary with the VS barrier in the middle of the fault (Figure 4.5), while the weaker patch simply produces more numerous small events. This can be linked to the level of stress at which events are able to propagate, which varies in the two models. In both cases, earthquakes can nucleate in the nucleation-prone patch while most of the fault is far from its static strength. By the time the rupture reaches the statically stronger parts of the faults (where $f_0 = 0.6$), it must be able to cope with the high mismatch between the prestress and the higher static strength of the fault to keep propagating. This is possible for the FD simulations, due to higher slip rates and associated more intense weakening, but not in the QD simulations that can only support the dying pulse-like and the crack-like mode. This is why we observe the interseismic average stress increases over a period of ~ 1100 in the QD simulation (Figure 4.2), which brings the VW segments to a stress level closer to its quasi-static strength value.

4.6 Quantifying the effect of VS patches on seismic ruptures

As mentioned in the introduction, a important question in seismotectonics is the ability of the earthquake rupture to propagate over faults with heterogeneous properties. In particular, a case of seismogenic patches separated by creeping barriers has emerged as that of significant practical interest based on observations (e.g., *Burgmann et al.*, 2005; *Hetland and Hager*, 2006; *Chlieh et al.*, 2008; *Perfettini et al.*, 2010; *Chlieh et al.*, 2011; *Loveless and Meade*, 2011). *Kaneko et al.* (2010) explored the dependence of earthquake rupture patterns and interseismic coupling on spatial variations of fault friction using FD simulations. Here we consider the importance of accounting for full wave-mediated effects in modeling of that kind.

Following the study of *Kaneko et al.* (2010), we analyze the probability P of an earthquake to rupture the VS middle patch in QD dynamic simulations, to compare with the statistics computed for FD models. We start each simulation with arbitrary initial conditions (described in subsection 4.2.4) and then simulate the fault behavior for 10,000 years. Based on the study of *Kaneko et al.* (2010), the probability P is estimated from the percentage of earthquakes that propagate through the VS patch relative to the number of earthquakes that rupture entirely one or two of the VW segments (*Kaneko et al.*, 2010). *Kaneko et al.* (2010) identified a non-dimensional parameter, B, which correlates with the probability P. The parameter B relates the amount of stress that is needed by the VS patch to sustain the rupture and the amount of stress that the incoming rupture can provide to the VS patch. It is given by:

$$B = \frac{\Delta\tau_{prop} D_{vs}}{\beta \Delta\tau_{vw} D_{vw}}, \tag{4.18}$$

which can be approximated as:

$$B \simeq \frac{\ln\left(V_{vs}^{dyn}/V_{vs}^{i}\right)\bar{\sigma}_{vs}(a_{vs} - b_{vs})D_{vs}}{\beta \Delta\tau_{vw} D_{vw}}, \tag{4.19}$$

where $\Delta\tau_{prop}$ is the stress required by the VS patch, D_{vs} and D_{vw} are the sizes of the VS patch and VW segment, respectively, $\Delta\tau_{vw}$ is the average coseismic stress drop over the VW segment from which the rupture is attempting to enter the VS patch, $\bar{\sigma}_{vs}$ is the normal stress in the VS patch, V_{vs}^{dyn} and V_{vs}^{i} are the seismic and pre-event (interseismic) velocity in the VS patch, respectively, $a_{vs} - b_{vs} > 0$ is the velocity-strengthening parameter in the VS patch, and β is a model-dependent geometric factor that specifies the fraction of the stress transferred onto the VS patch; following *Kaneko et al.* (2010) we use $\beta = 0.5$ for the 2D model considered here. As B increases from 0 to ~ 1, the percentage P drops from 100% to 0% (*Kaneko et al.*, 2010).

4.6.1 Models with standard rate-and-state friction

For simulations with the standard rate-and-state law, the dependence of the propagation probability P on the parameters of the VS patch displays similar trends in the FD and QD simulations (Figure 4.8a and 4.8b). For both approaches, the higher the value of $(a_{vs} - b_{vs})$ and/or the larger the size D_{vs}, the more efficient the patch is in stopping earthquake rupture, which is consistent with the prediction based on the parameter B. Moreover, if we look at the distributions of slip in individual events (cases Q1-3 and F1-3 in Figure 4.9), the overall rupture pattern is qualitatively similar.

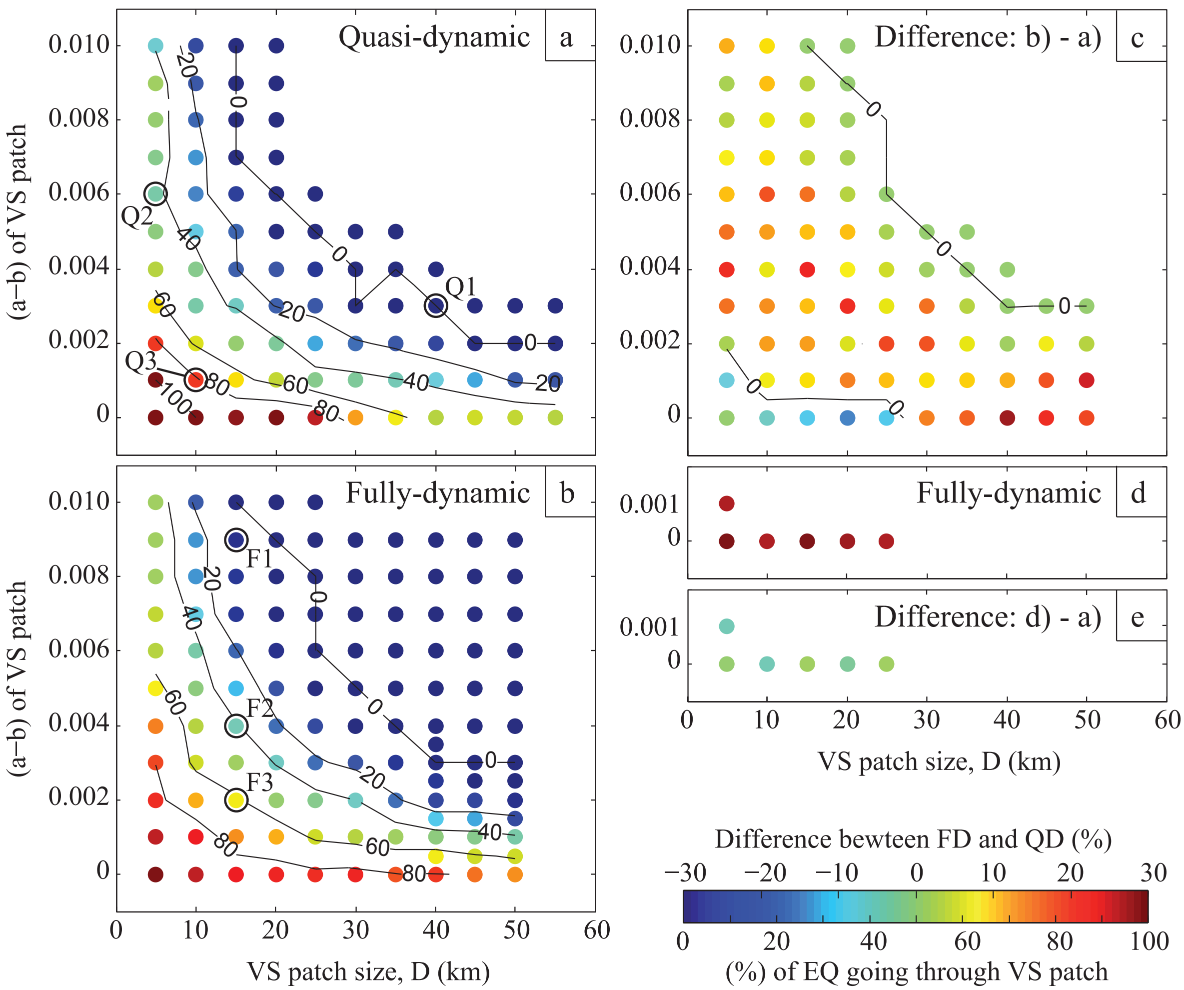

Figure 4.8: The ability of seismic ruptures to propagate through an unfavorable fault region in the form of a VS patch in simulations with the rate-and-state friction only. The relation between the properties of the VS patch and the probability P (in color) that an earthquake would propagate through it is shown for the (a) QD approach (this study) and (b) FD approach (modified from (*Kaneko et al.*, 2010)). Each colored dot corresponds to a 10,000-year simulation of fault slip with more than 50 events that rupture either one or both VW segments. P = 0% means that the VS patch is a permanent barrier. Black lines are the isocontours of P. Slip distributions in seismic events for cases Q1-3 and F1-3 are displayed in Figure 4.9. (c) The difference in probability P between the QD and FD cases. (d) Several FD simulations recomputed with the same code and computational cluster as the QD simulations (see the text for more explanation). (e) The difference in probability P between the QD and FD cases from (d).

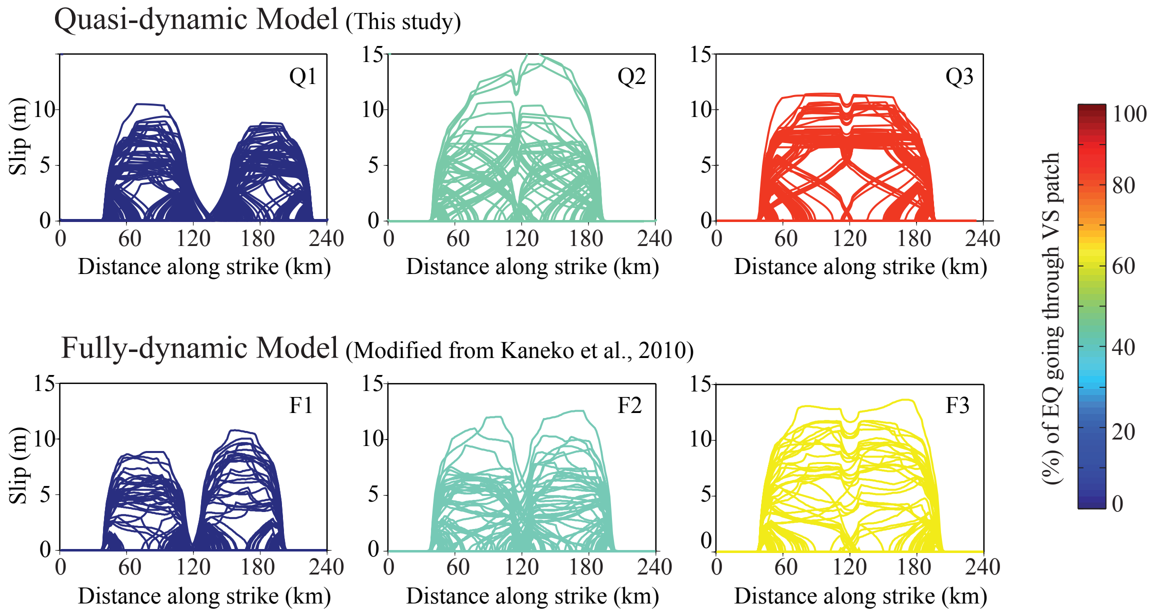

Figure 4.9: Slip distributions of the seismic events corresponding to cases Q1-3 (QD simulations) and F1-3 (FD simulations) from Figure 4.8, illustrating the range of fault behaviors that both QD and FD simulations can produce but not for the same properties of the VS region. The VS patch can either act as a permanent barrier (Q1 and F1) or let some of the earthquakes to propagate through (Q2-3 and F2-3).

Nevertheless, there are important quantitative differences. In the QD simulations, the VS patch acts as a permanent barrier for smaller values of $(a_{vs} - b_{vs})$ and/or D_{vs} (Figure 4.8a) than in the FD simulations. Furthermore, for most cases in which the VS patch is a partial barrier, up to 30% more events propagate through the VS patch in the FD simulations that incorporate full inertial effects (Figure 4.8c). These results are likely due to two factors. First, the stress drop $\Delta\tau_{vw}$) in equation 4.18 is higher for the FD simulations (Figure 4.2 and section 4.3.2), leading to smaller B and hence higher probability of propagation P. Second, incorporating all wave-mediated stress transfers - as in the FD simulations - leads to higher stress concentration at and in front of the rupture tip and hence promotes rupture propagation through unfavorable regions such as the VS patch. This latter effect is not completely accounted for by parameter B which is based on quasi-static consideration of stress transfer.

Note that, in the particular case of a velocity-neutral patch ($(a_{vs} - b_{vs}) = 0$) and for another case where the velocity strengthening of the patch is small ($(a_{vs} - b_{vs}) = 0.001$, $D_{vs} = 5$ km), we observe the opposite trend: the QD formulation seems to slightly enhance rupture propagation through the patch (Figure 4.8c). Since our QD computations (Figure 8a) have been executed on a different computational cluster and with an updated code compared to the FD simulations of *Kaneko et al.* (2010), we first check whether there might be small computational differences between the two types of simulations. To that end, we redo the FD computations for the cases in question (Figure 4.8d) and indeed find that the results are slightly different, by 0 to 5% in the propagation probability P. This is not surprising, since small differences in the order of the computational operations accumulate and can lead to rupture arrest or propagation over the VS patch in these highly nonlinear problems. Comparing the FD and QD calculations done with the same code on the same computational cluster, we still find that the QD simulations lead to slightly more ruptures propagating through the VS patch in some cases (e.g., $(a_{vs} - b_{vs}) = 0$, $D_{vs} = 10$ km), although the difference is smaller, up to at most 5% (Figure 4.8e), while for some other cases (e.g., $(a_{vs} - b_{vs}) = 0$, $D_{vs} = 15$ km)), the FD simulations have a slight edge of up to 0.5%. Overall, these results imply that the difference between FD and QD simulations for rupture propagation over the velocity-neutral patch is near zero. This is consistent with our simulations without the patch, where large events, once they reach the middle of the fault, propagate to the other end of the fault in both FD and QD simulations, implying 100% propagation probability (recall that P is computed based only on those events that fully rupture one of the VW sides of the fault). The addition of a patch with properties close to the rest of the fault cannot change this behavior much, at least for relatively small patches, and the FD and QD simulations both have near-100% probability of propagation through the patch in those cases.

Overall, the effect of FD vs. QD simulations with the standard rate and state friction on the ability of rupture to propagate through an unfavorable patch is similar to the comparison discussed in section 3: the results are qualitatively similar but quantitatively different.

4.6.2 Models with enhanced coseismic weakening

For the models with enhanced coseismic weakening, we explore a smaller representative subset of cases to shorten the computational time. We consider a 15-km-long VS patch with a range of velocity-strengthening $(a_{vs} - b_{vs})$ values (Figure 4.10a).

As expected based on the results of section 4.4, the two simulation approaches display more dramatic differences in the models with enhanced coseismic weakening. For smaller values of $(a_{vs} - b_{vs})$, the large events still propagate through the patch in almost 100% in both cases, as in the models with the standard rate-and-state friction (section 4.6.1). However, the behavior deviates for larger values of $(a_{vs} - b_{vs})$. In the QD cases, the decrease in probability P is essentially gradual with $(a_{vs} - b_{vs})$ and relatively slow, with about 50% of ruptures propagating through the VS patch for the largest value, 0.01, of $(a_{vs} - b_{vs})$ explored. In the FD case, near-100% propagation persists until $(a_{vs} - b_{vs}) \leq 0.005$, and then the propagation probability P relatively rapidly drops, with the VS patch essentially becoming a permanent barrier for $(a_{vs} - b_{vs}) \geq 0.008$.

The differences between the rupture-patch interaction in the FD and QD simulations can be explained by the differences in the rupture propagation mode and size detailed in section 4.4. The FD simulations produce similar pulse-like ruptures that initiate on the side of the VW segment away from the patch, and attempt to propagate over the patch after entirely rupturing one of the VW

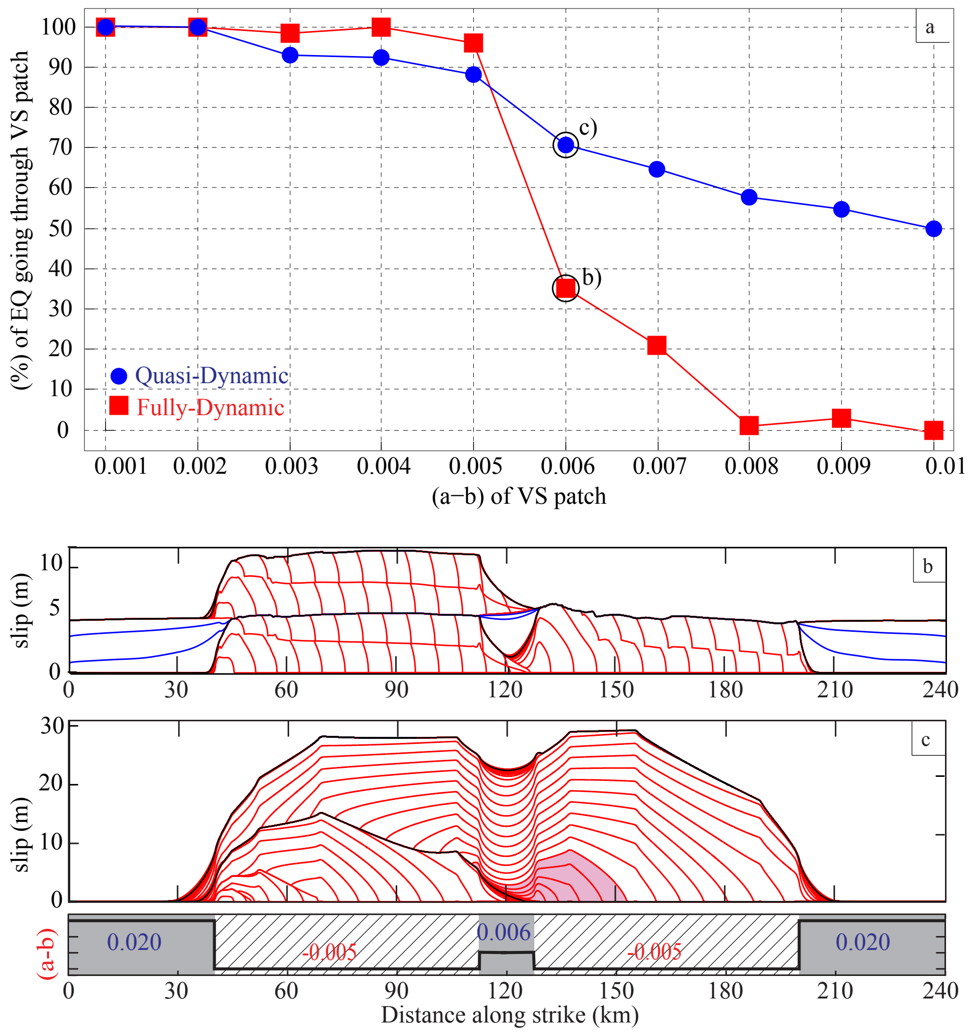

Figure 4.10: The ability of seismic ruptures to propagate through an unfavorable fault region in the form of a VS patch in simulations with additional coseismic weakening. (a) Probability P that an earthquake propagates through a 15-km patch is plotted against the friction parameter $(a - b)$ of the patch. Each red squares correspond to a 10,000-year FD simulation of fault slip with more than 50 events that rupture either one or both VW segments. Events spanning the entire fault are more rare with the QD simulations (blue dots), therefore the QD statistics has been computed over at least 20 events that arrest at or propagate through the VS patch. The FD and QD results are quite different, as discussed in the text. (b) and (c): Cumulative slip on the fault for representative events in the FD and QD simulations, respectively, when $(a_{vs} - b_{vs}) = 0.006$. Red lines are plotted every 2 s during seismic events while blue lines are plotted every 50 years.

segments (e.g., Figure 4.5; Figur 4.10b). Such behavior results in a relatively stable value of $\Delta\tau_{vw}$, of about 3 MPa in our cases. Using this value in the approximate expression of B, equation 4.19, with the typical value of $\ln\left(V_{vs}^{dyn}/V_{vs}^{i}\right) = 20$ (*Kaneko et al.*, 2010), and determining the value of $(a_{vs} - b_{vs})$ that corresponds to $B = 1$ results in 0.007. The value of $(a_{vs} - b_{vs}) = 0.007$ is indeed close to the value of 0.008 at which the VS patch becomes a permanent barrier in the fully dynamic case (Figure 10). The decay of the probability over a range of $(a_{vs} - b_{vs})$ values, from 0.005 to 0.008, is likely related to the variability of events and inter-event times - and hence values of $\Delta\tau_{vw}$ and V_{vs}^{i} - observed in the FD simulations (Figures 4.5a and 4.2).

In the QD simulations, the larger events that attempt to break the VS patch nucleate at different distances from the VS patch, including right next to it, and hence are in a different state of their development when they reach the VS patch. This results in different relevant values of $\Delta\tau_{vw}$ and effective ruptured D_{vw} (Figure 4.10c, where the relevant region is shaded), and hence complexifies the application of equations 4.18-4.19 for B to this case. Furthermore, many of the events that cross the VS patch occur right after other attempts, benefiting from elevated slip rate and stress on the VS patch from the previous attempt (as in Figure —4.10c), which significantly affects the slip rate V_{vs}^{i} in equation 4.19. However, the expression for the parameter B is still helpful in understanding why the QD simulations in the models with enhanced weakening are more likely to result in rupture propagation over the VS patch than the FD simulations. This is because the largest events that attempt to propagate over the patch have much larger values of $\Delta\tau_{vw}$ in the QD simulations than in the FD simulations, up to a factor of 8 in the case considered in section 4.4.

Overall, the ability of the rupture to propagate over the VS patch is significantly affected by the FD vs. QD simulations in the models with enhanced dynamic weakening, as expected based on the significant differences between the simulations documented in section 4.4. Furthermore, the effect is not intuitive. One might intuitively think that the FD ruptures would be more likely to propagate through the patch, as observed in the cases with the standard rate-and-state friction, but this is not true in these models, since the QD simulations result in artificially large crack-like ruptures with much larger slip and stress drops, and hence have a significant edge in terms of their ability to propagate through the patch.

4.7 Conclusions

We have investigated the differences between the fully-dynamic (FD) simulations that properly incorporate the wave-mediated stress transfers and the quasi-dynamic (QD) simulations that ignore the transient nature of the stress transfers. The results support our hypothesis that the QD simulations can only be qualitatively useful in situations where the wave-mediated stress transfers do not produce important features that define the model response.

In the models with the standard rate-and-state friction and relatively uniform fault properties (section 4.3), the FD and QD simulations indeed produce qualitatively similar fault behaviors, with crack-like ruptures and similar earthquake patterns. There are also quantitative differences, with the FD simulations having fractionally larger amounts of slip per event, correspondingly larger stress drops, and significantly higher slip velocities and rupture speeds. These findings are similar to those of previous studies with simlar models (*Lapusta et al.*, 2000; *Lapusta and Liu*, 2009). In terms of the ability of the rupture to propagate over the unfavorable spots such as the VS patch considered in this study, the trends with respect to the patch parameters are similar in the FD and QD simulations, but the events in the FD simulations are more likely to propagate over the patch for most cases considered, consistently with their higher stress drops, which is an important parameter, based on the study of *Kaneko et al.* (2010), and their higher slip rates and hence stress concentration.

However, the results of the FD and QD simulations become qualitatively different for the models with enhanced dynamic weakening, where we expect the wave-mediated stress changes to contribute to the formation of self-healing slip pulses (*Zheng and Rice*, 1998). Indeed, we find the FD simulations produce similar pulse-like ruptures that nucleate at the provided weaker site, whereas the QD simulations produce numerous smaller events at the edges of the seismogenic part of the model, until a much larger crack-like event spans the entire seismogenic part of the fault. The largest events in the QD simulations have much larger average slip and stress drop than the largest FD events, up to a factor of 8 in the cases considered. This finding is a clear reversal of what is observed in models with the standard rate-and-state friction, where the FD events are larger in slip and stress drop. Similarly to the models with the standard rate-and-state friction, the slip rate and rupture speed is significantly higher in the FD simulations with enhanced coseismic weakening than in the QD ones. However, unlike in the models with the standard rate-and-state friction, where the coseismic fault resistance is minimally affected, the higher slip rates in the models with enhanced coseismic weakening result in more pronounced fault weakening, and hence substantially change the fault behavior. In part, the average shear stress on the fault is significantly lower in the FD simulations, including before the largest model-spanning events, leading to self-healing pulse-like ruptures (*Zheng and Rice*, 1998; *Noda et al.*, 2009). As a result of their much larger slip and stress drop, the large events in the QD simulations are more likely to propagate through the unfavorable fault patch, again, contrary to the models with the standard rate-and-state friction. Note that the inability of the QD simulations to produce large sustained pulse-like events is particularly troubling in the view of observations that such mode of rupture propagation may be the one that operates on most mature faults (e.g., *Heaton*, 1990).

We expect similarly dramatic differences between the FD and QD simulations in other cases where wave-mediated transient effects can lead to qualitative differences. One of such cases is the models with transitions to supershear speeds (e.g., *Andrews*, 1976; *Xia et al.*, 2004; *Liu and Lapusta*, 2008), in which the wave-mediated stress transfers either produce a secondary supershear rupture ahead of the main one or induce the main rupture front to jump to the supershear speeds (*Liu and Lapusta*, 2008). Another case is that of strong local heterogeneities that can produce local arrest waves and cause short local rise time (e.g., *Beroza and Mikumo*, 1996), a phenomenon that may not be captured by the QD simulations.

Considering both models, we find that ignoring the transient wave-mediated stress transfers, which are a significant part of inertial effects, may lead to (1) mis-prediction of the size and recurrence of earthquakes; (2) incorrect average stress levels on the fault, and (3) missed characteristic features such as the sustained pulse-like mode of rupture propagation. Note that even the postseismic slip may be significantly affected, due to the differences in the coseismic rupture and its interaction with the potentially creeping VS fault areas.

We conclude that, to interpret correctly observations of individual earthquakes and the entire fault slip cycle, or to draw inferences regarding fault friction, it is important to use the right modeling approach. Under certain conditions, such as the standard rate-and-state friction and relatively homogeneous faults with no possibility of supershear transition, the QD simulations could be appropriate. However, since it is difficult to predict the outcome of the FD simulations and hence the presence or absence of certain features, it is important to verify the results with the FD approach at least for some representative cases.

Chapter 5

Summary and dynamic modeling of earthquakes sequences on the Longitudinal Valley Fault: implications for friction properties

5.1 Introduction

The kinematic analysis performed over the 1997-2011 period (chapter 2, *Thomas et al.*, to be submitted) suggests that the slip on the Longitudinal Valley Fault (LVF) is controlled by a complex patchwork of velocity-weakening (VW) patches where the Chengkung earthquake, the background seismicity and the aftershocks can nucleate, and velocity-strengthening (VS) patches, which produce aseismic creep in the interseismic period or during postseismic transients. The interseimic, coseismic and postseismic models complement each other and, to the first order, this simple picture compares well with theoretical models of earthquakes sequences based on rate-and-state friction laws, where the slip mode on the fault is controlled by the lateral and depth variation of frictional properties (e.g., *Dieterich*, 1979; *Ruina*, 1983; *Dieterich*, 1992, 1994; *Lapusta et al.*, 2000; *Lapusta and Liu*, 2009; *Rice and Ben-Zion*, 1996; *Scholz*, 1998; *Kaneko et al.*, 2010; *Barbot et al.*, 2012).

In this last chapter, we propose to analyse further the results from the kinematic inversion of geodetic and seismological data on the LVF (chapter 2, *Thomas et al.*, to be submitted), to evaluate the fault friction properties and to develop a realistic 3D dynamic model of the seismic "cycle" on the southern section of the LVF.

5.2 Slip history on the LVF over the 2003 earthquake area

In chapter 2, we were able to determine the time evolution of slip on the LVF over the period 1997-2011, encompassing the 2003 Chengkung earthquake and the pre- and postseismic period. We now focus on the southern section, around the Chengkung earthquake rupture area, which is best constrained and displays the most noticeable temporal and spatial variations of slip.

The results discussed in chapter 2 are summarized in Figure 5.1, which provides a synthetic view of the time evolution of fault slip in the Chengkung earthquake area over the study period. The map view displays the coupling model (see Figure 2.10a for location), and the time evolution of slip at 6 representative patches is plotted on the right side of figure 5.1 (see section 2.7 in chapter 2 for a description of the time series). The cumulative slip vector at each epoch is projected onto the direction of the long-term slip vector, predicted by the block motion of the Coastal Range relative to the Central Range. As discussed in chapter 2, the spatial resolution of the inversion is typically of the order of less than 1 km near the surface. It increases to about 5 km beneath the coastline, where the fault depth is about 20 km, and it increases gradually to about 15 km at the downdip extent of the model, at the depth of ~ 30 km.

Along-dip variations of slip through time, for three vertical sections on the LVF, are displayed on the left side of Figure 5.1 (see map view for location). For each graph, we average the slip along strike determined at all the patches at the same depth, within a swath spanning three to four patches. Then we plot the cumulative slip along dip with an increment of one year for the preseismic and postseismic periods. The last preseismic curve was chosen to represent the total slip accumulated right before the Chenkung earthquake, and the first postseismic curve represents the cumulative slip one year after the main event. Therefore, the areas in red represent the slip due to the coseismic event only. North of the locked patch, section A1 averages over 3 patches along strike. Section A2 is a four-patches-wide swath, centered right on the zone of maximum coseismic slip. Section A3 averages the cumulative slip over 3 patches and it is located south of the locked zone.

Northern section A1

The northern section A1 displays mostly creep before and after the main event, at shallow depth (less than 5km) as well as on the deep (more than 20 km) portion of the fault, but also records coseismic slip (~ 25 cm at the maximum). Near the surface, the average creep rate is estimated to be around 5 cm/yr before the event. It increases abruptly at the time of the Chengkung earthquake and decreases gradually during the postseismic period. In contrast, the Chengkung earthquake seems to have only slightly enhanced the creep rate on the deeper section of the fault (more than 18 km), and postseismic relaxation is hardly visible over the 7-year postseismic period. At the intermediate depths (between about 7 km and 18 km) section A1 shows that the fault was partially locked, with a creep rate about half the long term slip rate, before and after the Chengkung earthquake.

Middle section A2

Section A2 spans the area with the highest coupling and corresponds to the area where most of the coseismic slip occurs. Before December 2003, this section of the fault behaves in a fashion very similar to A1, though with a slower creep rate ($\sim$ 4 cm/yr at shallow depth and for the deep creeping part). In the 8 - 15 km depth range, the fault was $\sim$ 80% locked in the preseismic period and relocks nearly immediately after the Chengkung Earthquake. The rupture area of the 2003 earthquake coincides approximately with the area which was locked in the preseismic period, although somewhat offset to larger depths. In contrast, the rupture hardly reaches the surface. Coseismic slip reaches a maximum of $\sim$ 0.8 m at 18 km depth. As we illustrated in Figure 2.20 (chapter 2), the overlap at depth could be partially due to the smoothing induced by the regularization of our inversions, but not entirely. After the Chengkung earthquake, aseismic slip occurs at shallow depth, with a creep rate $\sim$ 2 times higher than during the preseismic period, and it relaxes to nearly its pre-seismic value within a year. Some increase of creep rate is also inferred at depth, but no clear relaxation is observed over the 7 years following the main event.

Southern section A3

Section A3 shows a large creep rate at shallow depth (less than 5 km) both before and after the 2003 earthquake, of about 8 cm/yr. At greater depth, the fault is also creeping throughout the study period, though at a lower rate of about 4.5 cm/yr. During the Chengkung earthquake, this section of the LVF seems to have produced some slip with a maximum of $\sim$ 0.6 m at 20 km depth and no significant coseismic slip in the 0-5 km depth range. High postseismic slip is observed at shallow depth (3-12 km) during the first few years following the main chock, with a maximum rate of 23.5 cm/yr around 7.5 km, but the creep rate rapidly slows down to interseimic values. Some afterslip is inferred in the first year at intermediate depths (from 12 to 22 km), but the fault apparently locks up later on. The deepest portion of the fault(from 22 km to 30 km) displays constant slip rate, with a value slightly higher than before the 2003 earthquake.

Altogether, the kinematic model shows that this portion of the fault has been mostly creeping over the study period, with the Chengkung earthquake and aftershocks accounting for only about 20% of the released moment (or equivalent slip potency) (chapter 2). Creep is, however, non-uniform, with a clear deficit of creep in a 10 km $\times$ 12 km partially locked zone. The Chengkung earthquake 12 km $\times$ 16 km rupture area approximately coincides with the locked fault zone, although it is broader and offset the deeper portion of the fault. The overlap between the creeping zone and the rupture area could partly be due to the smearing induced by the spatial resolution of our inversions. Hence, to he first order, it seems that it would be appropriate to represent this fault segment as essentially one VW patch embedded in a creeping zone displaying VS friction. Over the 15 years of the study period, coseismic and aseismic slip do not quite even out to uniform slip. In fact, the cumulative slip is, on average, larger than the 0.7 m that would have occurred if the fault had been creeping at its long term slip rate of about 4.5 cm/yr. This is consistent with the finding that the return period of M_w 6.5 earthquakes, similar to the Chengkung earthquake, needs to be of the order of 36 years, so that the moment released by afterslip and coseismic slip adds up to compensate the deficit of the moment accumulating during the interseismic period (chapter 2). The kinematic model does, however, suggest a somewhat more complicated seismic cycle pattern than the repetition of Chengkung-like earthquakes. In particular, it looks like the coseismic slip and afterslip do not compensate for the deficit of slip on the upper part of the locked fault zone, along sections A1 an A2. Presumably, recurring earthquakes must have different but complementary slip distributions to even out the heterogeneities of slip recorded for a single event. In spite of this complexity, the kinematic model is relatively simple and compares well enough with the idealized seismic cycle models presented next, so that a quantitative comparison with prediction from dynamic modeling simulations is possible.

Figure 5.1: Slip on the fault through time from inversions of pre- and postseismic period and coseismic slip due to the Chengkung earthquake (chapter 2). (See next Page). The map view shows a close-up view of the coupling model on the LVF (see Figure 2.10a for location), with the contour lines of the coseismic slip model (black lines) and epicenter (star) of the 2003 Chengkung earthquake. Graphs around the map view show the time evolution of slip at 6 patches along the direction of the slip vector predicted by the block motion of the Coastal Range relative to the Central Range. Blue, red and green curves represent, respectively, the pre-, co- and postseismic periods. Patches 331, 301, and 228 sample the upper creeping zone. Patch 291 is characteristic of the zone which was locked before the Chengkung earthquake, slipped during the event, and relocked immediately after. Patches 314 and 354 illustrate the behavior of the deeper fault portion which is most poorly resolved. Black curves correspond to the fit of the retrieved patch time series, following the relaxation law as described in *Perfettini et al.* (2010) (equation 5.1). The three panels on the left display the average cumulative slip (in meters) along the three vertical swath sections A1, A2 and A3 located in the map view. Isochrons of cumulative slip are plotted with an increment of one year for the preseismic (blue) and the postseismic (green) periods, whereas red shading shows coseismic slip due to the 2003 earthquake.

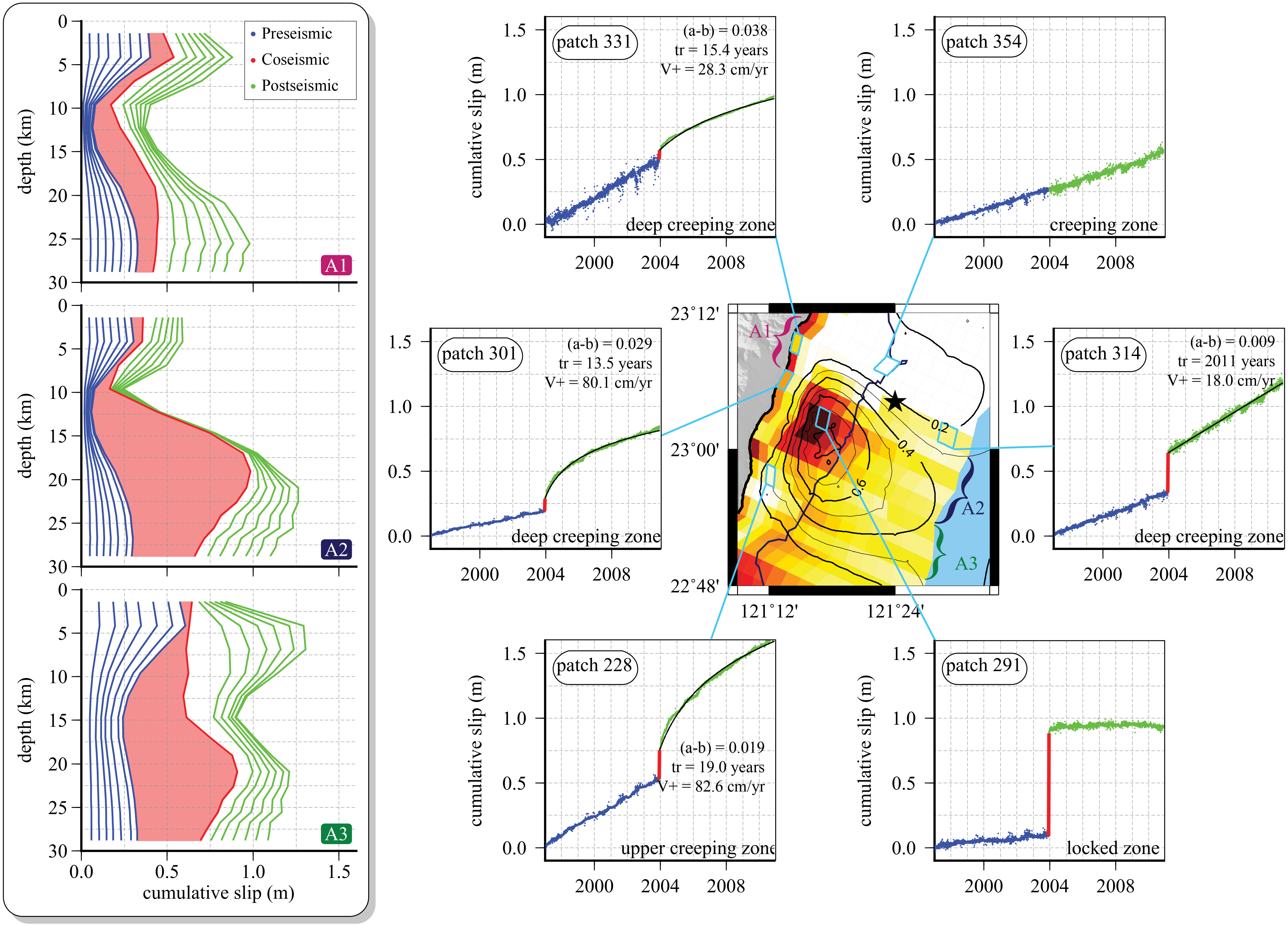

Preseismic
Coseismic
Postseismic
A1
A2
A3
depth (km)
cumulative slip (m)
patch 331
(a-b) = 0.038
tr = 15.4 years
V+ = 28.3 cm/yr
deep creeping zone
patch 354
creeping zone
patch 301
(a-b) = 0.029
tr = 13.5 years
V+ = 80.1 cm/yr
deep creeping zone
patch 314
(a-b) = 0.009
tr = 2011 years
V+ = 18.0 cm/yr
deep creeping zone
patch 228
(a-b) = 0.019
tr = 19.0 years
V+ = 82.6 cm/yr
upper creeping zone
patch 291
locked zone
23°12'
23°00'
22°48'
121°12'
121°24'
0.2
0.4
0.6

5.3 Prediction of friction parameters from velocity-strengthening friction law

The kinematic analysis displays a spatio-temporal evolution of fault slip qualitatively consistent with seismic cycle models (*Rice*, 1993; *Lapusta et al.*, 2000) based on laboratory-derived rate-and-state laws (*Dieterich*, 1979; *Ruina*, 1983; *Dieterich*, 1992, 1994, and references therein). Here, we estimate the frictional parameters that would allow for predicting quantitatively the observed postseismic relaxation. We assume that the fault obeys a rate-and-state friction law (for details see section 4.2.2 in chapter 4).

We compare the time evolution of slip deduced from the inversions of the geodetic data with that predicted from a velocity-strengthening friction law. We assume steady state, since the slip-at-depth time functions retrieved from the inversions do not sample the transient early increase of postseismic slip rate, which would reflect the adjustment of the state variable (*Perfettini and Avouac*, 2007; *Perfettini and Ampuero*, 2008; *Fukuda et al.*, 2009). The analysis of this short-lived transient would probably require better temporal resolution than the daily resolution of the kinematic model obtained in chapter 2. In the steady-state approximation, for a VS material, the friction law only depends on the slip velocity, and the frictional stress τ increases linearly with the logarithm of the sliding velocity $\dot{U}$. If elastic interactions among the various creeping patches are ignored an analytical solution can be derived (*Perfettini and Avouac*, 2004), which can then be used to infer the fault friction properties, as it has been done in a number of studies (*e.g.*, *Perfettini et al.*, 2010; *Hsu et al.*, 2006). This model predicts that postseismic slip $U(t)$ evolves as:

$$U(t) \approx V_{pl} t_r log \left[1 + \frac{V^+}{V_{pl} t_r} t \right], \tag{5.1}$$

where t_r is the relaxation time, V_{pl} the long-term slip rate, and V^+ is the sliding velocity on the fault immediately after the earthquake. According to this law, the ratio $\frac{V^+}{V_{pl}}$ depends on the friction parameters $(a-b)$, the normal stress $\bar{\sigma}$, and the static Coulomb stress change induced by the main shock (ΔCFF) (*Perfettini and Avouac*, 2004; *Perfettini et al.*, 2010)), as follows:

$$(a-b) = \frac{\Delta CFF}{\bar{\sigma} log \left(\frac{V^+}{V_{pl}} \right)}. \tag{5.2}$$

The relaxation time, t_r, depends on the frictional parameters but also on the stressing rate, $\dot{t}au$, according to:

$$t_r = \frac{(a-b)\sigma}{\dot{\tau}}. \tag{5.3}$$

An estimation of the friction parameters $(a-b)$ can therefore be deduced by computing the static Coulomb stress change from our coseismic model (section 2.5 in chapter 2) and fitting the

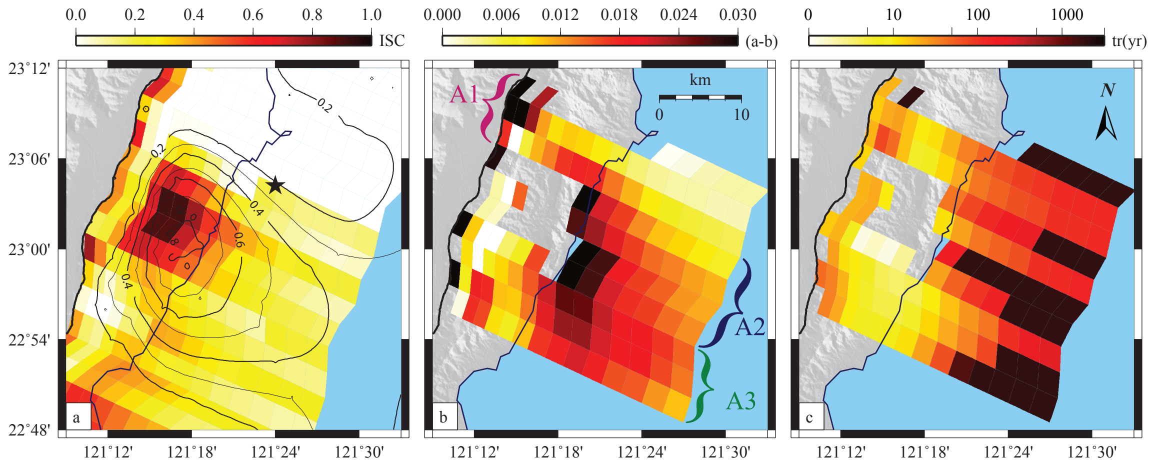

Figure 5.2: (a) The map view shows the coupling model on the LVF for the Chengkung area (see Figure 2.10a for location), with contour lines of the coseismic slip model (black lines) and epicenter (star) of the 2003 Chengkung earthquake. (b) Frictional parameters $(a-b)$ and (c) relaxation time t_r predicted from the velocity-strengthening friction law (equation 5.1). Only patches that show accelerated creep after the Chengkung earthquake were selected.

time evolution of slip for all patches that record postseismic slip (Figure 5.1 and 5.2). This calculation can be done based on the semi-analytical solution of *Okada* (1992). The values for upper patches should, however, be taken with caution, since $(a-b)$ grows toward infinity for small values of $\bar{\sigma}$.

The frictional parameter $(a-b)$, calculated assuming the hydrostatic pore pressure and rock density of 2800 kg/m^3, varies with depth from near velocity-neutral to 0.03. This is comparable to the values obtained in laboratory experiments for illite-rich lithology, similar in lithology to the Lichi Mélange, and assumed to be representative of subduction mélanges in general (*den Hartog et al.*, 2012a; *Ikari et al.*, 2011a) (Figures 5.3, 5.2 and 5.4a). If we plot those values against the temperature derived from the thermokinematic model of *Simoes et al.* (2007a) (Figure 5.3), we observe a trend similar to that observed experimentally on illite-rich gouges (*den Hartog et al.*, 2012a) (Figure 5.4a), for panels A3 and A2. The values of$(a-b)$ derived for patches in section A1 are not as well constrained, since almost no postseismic relaxation occurs on that section of the fault (see section 5.2 and Figure 5.1). Therefore, the rate-dependency of friction derived from our kinematic model (Figure 5.3) seems comparable to the values measured in the lab for a clay-rich fault zone lithology (Figure 5.4). In addition, we observe that patches, inferred to be VW patches, fall into the $250-400$°C range for which a VW behavior is observed in the laboratory. So the temperature may well be the factor explaining along-dip variations of frictional properties: from VS at $150-250$°C to VW at $250-375$°C, and VS again for temperatures higher than 380°C. This temperature dependency of illite-fault gouges could be applied to the section A2 in particular, but fails to explain the observed lateral variations, since the temperature is probably quite uniform along strike on the LVF. This discussion shows that some of our results are quite consistent with results

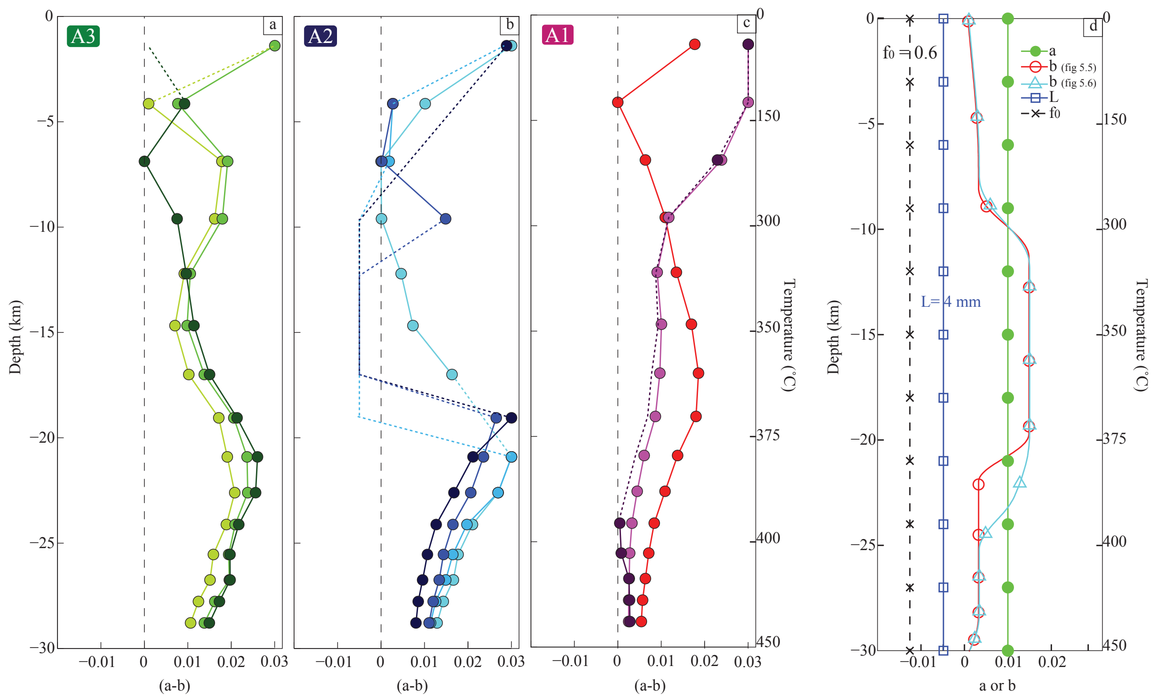

Figure 5.3: (a), (b) and (c): along-dip variations of frictional parameters $(a-b)$ predicted from a velocity-strengthening friction law (equation 5.1) for patches within swath sections A1, A2 and A3, respectively (see Figure 5.2 for location). Dashed lines show hypothetical interpolated values of $(a-b)$ based on the coupling model (Figure 5.2a), *i.e.*, if the patch is locked ($ISC > 0.8$) we assume that the friction law is velocity-weakening, and if the patch was creeping before the Chenkung earthquake, we interpolate with the nearby values. The temperature on the LVF is retrieved from *Simoes et al.* (2007a). (d) Down-dip variations of a, b, L and f_0 vs temperature and depth assumed in the dynamic simulations (Figures 5.5 and 5.6) for the fault portion that models segment A2.

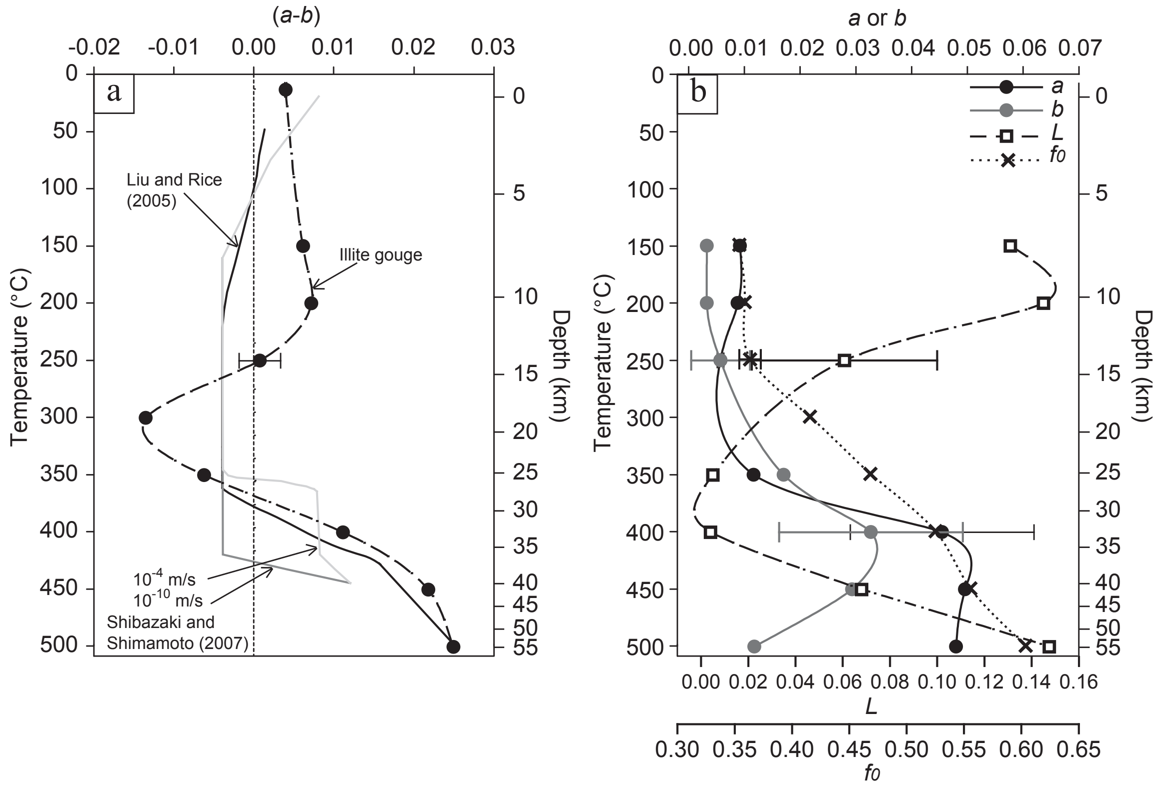

Figure 5.4: Figure from *den Hartog et al.* (2012a) (slight modification). (a) The values of $(a-b)$ for illite-rich gouge derived from the laboratory measurements in *den Hartog et al.* (2012b), shown as dots. The error bars represent plus or minus one standard deviation. The dashed trend line emphasizes the data trend for clarity. The pressuretemperature path for Shikoku of *Peacock* (2009) is used. For comparison, the profile of *Liu and Rice* (2005) for the example of the Shikoku subduction zone plus two profiles of *Shibazaki and Shimamoto* (2007) are given, for different sliding velocities. The profiles given in the two respective studies are based in part on the data for wet granite (*Blanpied et al.*, 1998) and dry halite (*Shimamoto*, 1986), respectively. (b) Profiles of a, b, L, and f_0 vs temperature. Values of a, b, and L (in mm) are derived from velocity steps from 1 to 10 mm/s. Error bars represent plus or minus one standard deviation.

from experimental laboratory studies. We should, however, forewarn that the thermokinematic model is not well-constrained for the LVF, given the lack of thermometric and thermochronological data from the Coastal Range. Consequently, those observations should be taken with caution. An alternative possible explanation for the presence of VW patches inside a VS matrix can also be related to the presence of competent blocks (*Fagereng and Sibson*, 2010), which we know can be of kilometric size in the Lichi Mélange (see section 3.2.3).

Finally, the $(a - b)$ values obtained at shallow depth ($\sim$ 5 km) from our inversion compare well with the estimated values of 0.013 before the Chengkung EQ and 0.0066 after the main event, derived from the modeling of seasonal variations of slip rate induced by pore-fluid pressure variations *Chang et al.* (2009).

5.4 Dynamic modeling of earthquake sequences

The analysis based on the analytical formula described above (equation 5.1 and 5.2) (*Perfettini and Avouac*, 2004; *Perfettini et al.*, 2010), derived from the equation of motion of a one-degree-of-freedom spring-and-slider system, may be too simplistic, in particular because it ignores the interactions between neighboring patches due to elastic stress transfer. In addition, this analysis does not provide any insight on the frictional properties of the VW patches or on the reference friction coefficient f_0. To improve our understanding of the factors that govern the slip behavior of the LVF, we therefore carry out numerical fully-dynamic (FD) simulations of earthquake sequences and slow slip to qualitatively reproduce the wide range of observations for the southern segment of the LVF.

The model set up is designed based on the kinematic model summarized in Figure 5.1 (Chapter 2, *Thomas et al.*, to be submitted). We follow an approach similar to that of *Barbot et al.* (2012) who developed a model calibrated to reproduce the seismic cycle on the Parkfield segment of the San Andreas fault. As discussed in chapter 4, a quasi-dynamic approximation would be less costly but the inferences made could be biased. We therefore conduct only FD simulations.

The model assumes a thrust fault segment embedded into an uniform, isotropic, elastic medium, loaded at the average long-term slip rate on the fault (4.5 cm/yr) and governed by the rate-and-state friction law. A patch with the VW friction ($a - b = -0.005$), where seismic slip can nucleate, is embedded in a VS area for which we apply the value ($a - b = 0.0066$) determined by (*Chang et al.*, 2009) (Figures 5.3d, 5.5a and 5.6a). To account for the listric shape of the fault, we definy the normal stress as if we were along-dip on the LVF (Figures 5.5b and 5.6b). Hereafter, to facilitate the comparison with the kinematic inversion of fault slip, we plot the equivalent depth (computed from the formula $\rho g z$) rather than the "true" depth of our model. In our simulations, the characteristic slip distance $L = 4$ mm, the Poisson ratio $\nu = 0.25$, and the reference friction coefficient $f_0 = 0.6$

are constant over the fault (Figure 5.3d). The pre-stress τ_0 is uniform on the fault, except for one location where τ_0 is slightly increased over a 1×1 km^2 patch, at the right-bottom boundary between the VS and VW regions. This set-up promotes the nucleation of the first event. More details about the elastodynamic relations and the constitutive laws of those models can be found in chapter 4 (section 4.2) and in *Lapusta and Liu* (2009).

The frictional parameters within the VW zone are adjusted so that ruptures of the whole patch would produce M_w 6.8 earthquakes with a return period comparable to our estimate of 36 years. Because of the computational cost of the FD simulations, we assume a relatively large value of the critical slip-weakening distance L of 4 mm. This choice yields a nucleation size h^* of about 1.5 km. We develop two models: one with a sharp boundary between the VW patch and the surrounding VS area, and the other with a more smooth transition down-dip to allow propagation of seismic slip into the deeper VS zone (Figure 5.3d). Results are presented in Figures 5.5 and 5.6, respectively.

The models predict a relatively simple seismic cycle with the quasi-periodic return of similar earthquakes, rupturing the whole VW patch. The relatively large value of the nucleation size, compared to the size of the VW patch, prevents generating smaller size earthquakes. As a result, the model does not produce much complexity. Nevertheless, these simple models succeed in reproducing some key aspects of the seismic cycle on the LVF. First, they both yield seismic events with a magnitude close in M_w to that of the Chengkung earthquake, although slightly smaller: 6.4 on average for the abrupt transition (Figure 5.5c), and 6.5 for the model with enhanced down-dip seismic slip (Figure 5.6c). The recurrence time of those events are 35.4 and 36.2 years, respectively, consistent with our estimate of the return period of Chengkung-type earthquake on the LVF, *i.e*, 36 years.

In both models, the seismic ruptures do not reach the surface (Figures 5.5e and 5.6e), indicating that the VS friction on the shallow patch is strong enough, given its down-dip extent, to arrest up-dip propagation of seismic ruptures, as it happened during the Chengkung earthquake. The model with the smooth transition of $(a - b)$ parameters allows for the ruptures to propagate further down-dip (Figure 5.6e), leading to a slightly larger M_W. This model is therefore closer to reproducing the down-dip extent of the Chengkung earthquake (Figure 5.1).

Afterslip in the models is equivalent to about half of the coseismic moment, which is a smaller ratio than for the Chengkung eartquake, and the creep rate is back to the interseimic velocity after 5 years, as observed on the LVF at shallow depth, but not on the deep creeping section. These remarks suggest that a better fit would be obtained with a lower value of $(a-b)$ beneath the VW patch. This would allow the rupture to extend deeper and hence to yield a larger magnitude. Another option to increase the magnitude of the earthquakes rupturing the whole VW patch would be to increase b within the VW patch, but coherently decrease the parameters L to hold to the estimated 36 years recurrence time (See *Barbot et al.* (2012) for discussion). Also, a lower value of L would yield more complexity and more diversity of the slip distributions.

5.5 Conclusion

The spatio-temporel evolution of fault slip on the LVF over the 1997-2011 period is consistent, to the first order, with predictions from a simple model in which a VW patch is embedded in a VS area. We show that the time evolution and spatial distribution of afterslip can be quantitatively explained based on such a model and used to estimate the velocity-dependency of friction at steady-state $(a - b)$. We obtain values relatively consistent with the laborabory measurements on clay-rich fault zone gouges comparable to the Lichi Mélange, which borders the southern segment of the LVF. The $a - b$ parameter varies along-dip, possibly as result of temperature as the laboratory results suggest, but it also varies along-strike, probably for some reason other than temperature variations. A more realistic model of the seismic cycle on the LVF would require adding complexity to the model set-up, for example, by assuming more heterogeneous frictional properties and reducing the nucleation size to get a wider range of earthquake magnitudes. Hence, although the models shown here are relatively satisfying given their simplicity, the model geometry and parameters could certainly be further improved to better quantitatively reproduce the wide range of observations available from the LVF. Note also that another modeling technique than the Boundary Integral Method would be more appropriate to take into account the effect of the free surface (this effect can be correctly taken into account with the Boundary Integral Method only for a vertical fault in mode II) and nonplanar geometry.

Finally, it should be underlined that there is no firm evidence that strong weakening mechanisms, such as thermal pressurization (*Rice*, 2006), occurred during the Chengkung earthquake. However, enhanced seismic weakening could explain that the rupture was able to propagate down-dip beyond the locked VW patch(*e.g. Sibson*, 1973; *Lachenbruch*, 1980; *Mase and Smith*, 1987; *Rudnicki and Chen*, 1988; *Sleep*, 1995; *Andrews*, 2002; *Bizzarri and Cocco*, 2006a,b; *Rice*, 2006; *Noda and Lapusta*, 2010). In that case, parameters such as the permeability, friction coefficient, or shear zone width should vary with depth to enhance the thermal pressurization effect in the deeper part but not near the surface.

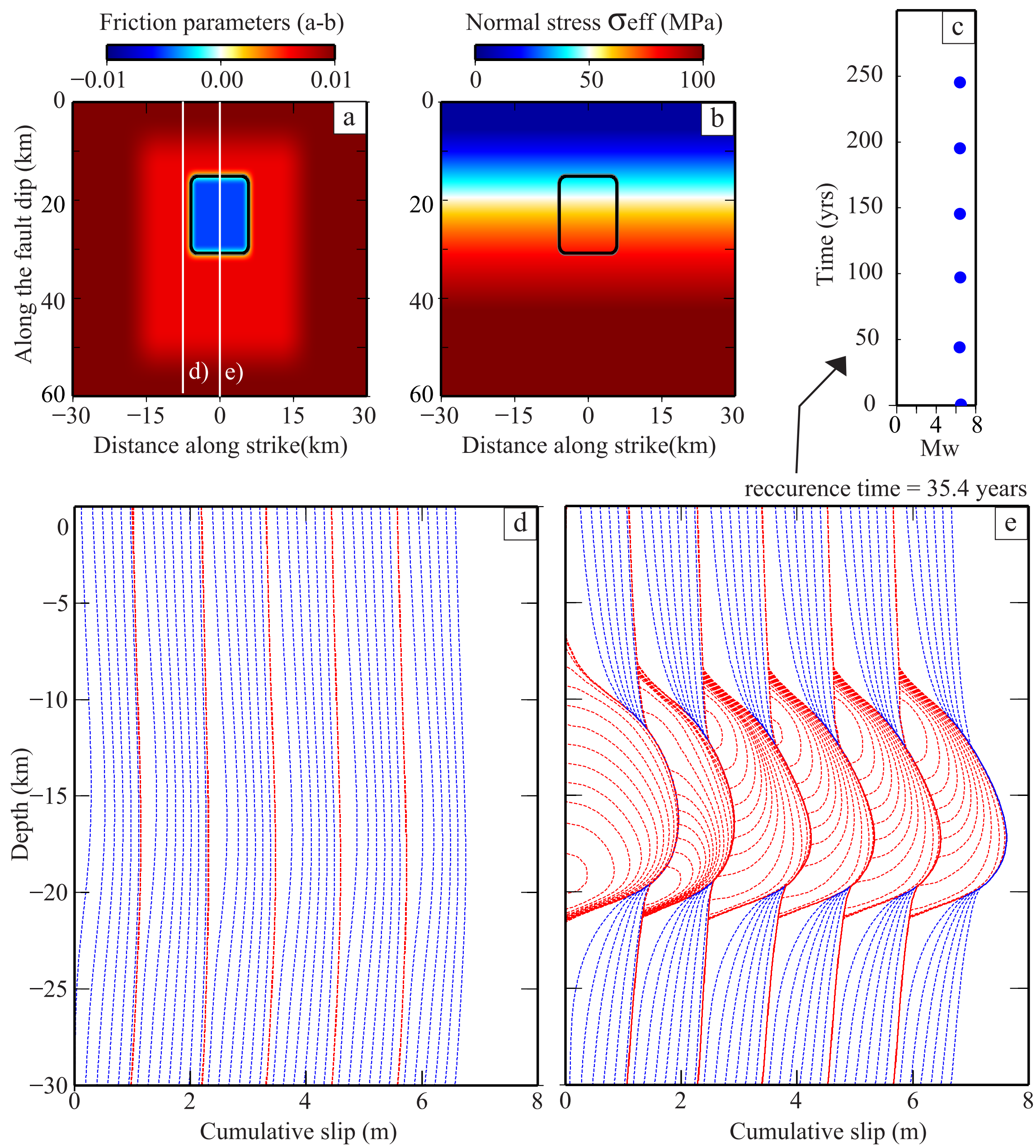

Figure 5.5: 3D simulations of earthquake sequences, with abrupt transition of $(a-b)$ parameters at depth. (a) Variation of friction parameters $(a-b)$. (b) Along-dip variation of normal stress. (c) Catalogue of simulated seismic events. (d) and (e) Cumulative slip on the fault for two depth profiles, one in the middle of the fault (e) and one on the left side (d). See subfigure (a) for the locations. Red lines are plotted every 2 s when maximum slip velocity exceeds 1 mm/s, while blue lines (every 5 years) illustrate the aseismic behavior of the fault.

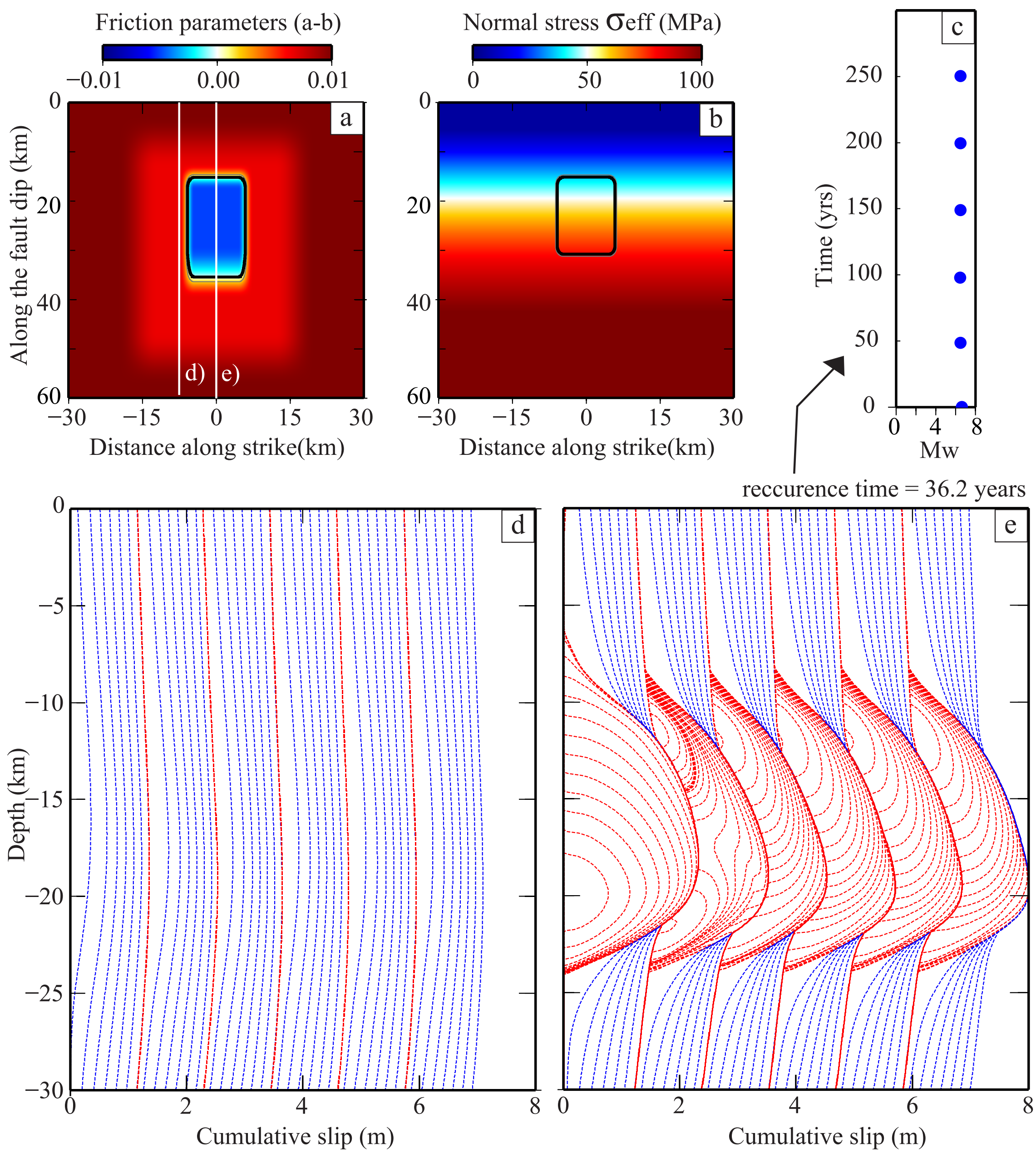

Figure 5.6: 3D simulations of earthquake sequences, with smooth transition of $(a-b)$ parameters at depth. (a) Variation of frictional parameters $(a-b)$. (b) Along-dip variation of normal stress. (c) Catalogue of simulated seismic events. (d) and (e) Cumulative slip on the fault for two depth profiles, one in the middle of the fault (e) and one on the left side (d). See subfigure (a) for the locations. Red lines are plotted every 2 s when maximum slip velocity exceeds 1 mm/s, while blue lines (every 5 years) illustrate the aseismic behavior of the fault.

Appendix A

Evidences for aseismic slip in the seismogenic depth range, in other geological contexts

Measurements of surface deformation have shown that stress on faults is either released seismically or as aseismic slip, called fault creep. This has been observed along a number of subduction zones including Japan, Sumatra, Peru, Chile and Alaska (*e.g. Freymueller et al.*, 2000; *Igarashi et al.*, 2003; *Chlieh et al.*, 2008; *Moreno et al.*, 2008; *Hashimoto et al.*, 2009; *Kaneko et al.*, 2010), but also on continental faults such as in California, Turkey, the Philippines, China and Taiwan (e.g. *Thomas et al.*, to be submitted; *Titus et al.*, 2006; *Galehouse and Lienkaemper*, 2003; *Richards-Dinger and Shearer*, 2000; *Jolivet et al.*, 2012; *Kaneko et al.*, 2013; *Duquesnoy et al.*, 1994). In this section we review continental faults for which aseismic creep occurs in the seismogenic zone.

A.1 San Andreas Fault system, California

Creep on the San Andreas fault (SAF) system, which is a major component of the active transform plate boundary between the North America and the Pacific Plates (*Chester et al.*, 1993), has been monitored at several locations.

Although anticipated by *Louderback* (1942), creep was not observed in California until the early 1960s (*Steinbrugge and Zacher*, 1960; *Tocher*, 1960), when very localized deformed anthropogenic features were observed at a winery near Hollister, California. This 175-km-long Parkfield creeping segment of the SAF, between San Juan Bautista and Cholame, separates the locked sections of the fault that ruptured during the Fort Tejon earthquake of 1857 and the San Francisco earthquake of 1906 (*Titus et al.*, 2006). Following the recognition of aseismic slip on that fault, periodic and continuous measurement of creep have been performed using alignment arrays (*Burford and Harsh*, 1980; *Lienkaemper and Prescott*, 1989; *Titus et al.*, 2005, 2006), trilateration networks (*Lisowski and Prescott*, 1981; *Prescott et al.*, 1981; *Lienkaemper and Prescott*, 1989), creepmeters (*Schulz et al.*, 1982; *Titus et al.*, 2006; *Lienkaemper and Prescott*, 1989), GPS (*Langbein and Bock*, 2004; *Titus et al.*, 2005, 2006; *Rolandone et al.*, 2008) and InSAR data (*Ryder and Burgmann*, 2008; *de Michele et al.*, 2011). A combination of geodetic measurements have demonstrated that faster slip rates are observed at greater distances from the fault. Creepmeters and alignment arrays document an average minimum creep rate of 21-26 mm/yr on the fault trace. Motion between continuous GPS sites return 28.2 ± 5.0 mm/yr for two sites 1 km apart and 33.6 ± 5.0 mm/yr for two sites that are 70 km apart (*Titus et al.*, 2006). This pattern implies that either part of the deformation occurs off the San Andreas Fault or that strain accumulates along the creeping segment due to partial coupling on the fault, or some combination thereof (*Titus et al.*, 2006). The good agreement between today's measurement from cGPS stations 1 km apart and geological slip rate estimates at Wallace Creek, California (34 ± 3 mm/yr) (*Sieh and Jahns*, 1984), implies little or no interseismic stress build-up to be released seismically on the creeping section. Moreover, all creeping rate measurements are slower than the 39 ± 2 mm/yr predicted motion between the Sierra Nevada-Great Valley Block and the Pacific Plate. Therefore, deformation must occur off the San Andreas Fault, either seismically or aseismically. Detailed mapping of the spatio-temporal evolution of aseismic creep on the Parkfield segment are found in recent published papers based on geodetic, seismological and/or remote sensing data (e.g. *Nadeau and McEvilly*, 1999; *Murray et al.*, 2001; *Titus et al.*, 2006; *Ryder and Burgmann*, 2008; *Barbot et al.*, 2009; *de Michele et al.*, 2011; *Tong et al.*, 2013).

In the San Francisco Bay Area (SFBA), motion between the Pacific Plate and Sierra Block is partitioned across 7 major subparallel right-lateral faults with < 20 km spacing (e.g. *Freymueller et al.*, 1999; *Evans et al.*, 2012). From West to East these include the San Gregorio, the San Andreas, the Hayward, the Rodgers Creek, the Calaveras, the Concord/Green Valley and the Greenville Faults. The San Andreas Fault is fully locked northwest from San Juan Bautista, *i.e*, at the southern end of the 1906 earthquake rupture (*Galehouse and Lienkaemper*, 2003). Likewise, the San Gregorio fault shows no creep. On the other end, several faults within the SFBA have long been known to exhibit interseismic creep, including the Hayward Fault (4.6 mm/yr) (*Prescott et al.*, 1981; *Lienkaemper et al.*, 1991; *Schmidt et al.*, 2005; *Kanu and Johnson*, 2011; *Evans et al.*, 2012), the Calaveras Fault (14 ± 2 in south, ~ 10 mm/yr in the central part and 3-4 mm/yr in north)(*Rogers and D.*, 1971; *Prescott et al.*, 1981), the Concord Fault (2.5-3.5 mm/yr) and its northward continuation, the Green Valley Fault (4.4 mm/yr) (*Galehouse and Lienkaemper*, 2003). More recently, PS-InSAR data from *Funning et al.* (2007) has demonstrated that aseismic creep also occurs on the Rodgers Creek Fault, at a rate up to 6 mm/yr. This particular fault is aligned with the Hayward Fault (South) and the Maacama Fault (North) which has been proved to slip aseismically as well (4.4 to 6.5 mm/yr) (*Galehouse and Lienkaemper*, 2003). Based on two decades of alinement array measurements of creep in the SFBA, *Galehouse and Lienkaemper* (2003) have demonstrated that if the central and southern segments of the Calaveras Fault are predominantly creeping, the Hayward Fault, the Northern

Calaveras Fault and the Maacama Fault are partly locked, generating sufficient elastic strain to produce major earthquakes. Indeed, the Hayward Fault generated a severely damaging earthquake (M 6.8) in 1868 with a reported surface rupture from Fremont in the South to San Leandro in the North (*Evans et al.*, 2012). Based on seismic and geodetic data, the partial coupling of the Hayward Fault has been discussed furthermore by *Schmidt et al.* (2005) and *Evans et al.* (2012).

Finally, trilateration network have revealed aseismic slip on the southern section of the San Andreas fault system (*Louie et al.*, 1985). The Banning, Coyote Creek, Imperial and Superstition Hills fault have been recognized to creep but at the time of survey some of the one-going slip could have been related to the postseismic relaxation following the 1979 Imperial Valley and 1968 Borrego Mountain earthquakes (*Louie et al.*, 1985). Recent permanent scattereers InSAR study by *Lyons and Sandwell* (2003) along the seismic gap on San Andreas fault near the Salton Sea (*Richards-Dinger and Shearer*, 2000) reveal a diffuse secular strain buildup, punctuated by localized interseismic creep of 4-6 mm/yr line of sight, 12-18 mm/yr horizontally (if assumed pure strike-slip motion). This section of the San Andreas fault has undergone four large slip events between 1000 and 1700 A.D. (*Sieh*, 1986) with a reccurence interval of about 230 years. The last major events has been inferred to have happened in 1700 (*Sieh*, 1986), therefore significant seismic event along this portion of the San Andreas Fault is consider to be overdue (*Lyons and Sandwell*, 2003).

A.2 Haiyuan Fault, Gansu, China

The Haiyuan Fault is part of a major left-lateral fault system at the northeastern edge of the Tibet-Qinghai plateau. Two M_w 8 earthquakes ruptured locked sections of this fault system in the last century (1920 and 1927), bracketing an unbroken section of the fault identified as the Tianzhu seismic gap (*Gaudemer et al.*, 1995). Interferometric synthetic aperture radar data have been used to infer interseismic velocity field along the Haiyuan Fault system, and they revealed the existence of a shallow, 35 km-long, slipping zone near the junction between the Tianzhu seismic gap and the fault section, which broke in the 1920, M_w 8 Haiyuan earthquake (*Cavalie et al.*, 2008; *Jolivet et al.*, 2012). Inferred average shallow slip-rate ($\sim$ 5 mm/yr) is comparable in magnitude with the estimated loading rate at depth, assumed to be constant along the fault (*Jolivet et al.*, 2012).

A.3 North Anatolian Fault, western Turkey

Evidence of creep along the North Anatolian Fault (NAF) at Ismetpasa (Turkey) was first mentioned by *Ambraseys* (1970), but until the last decade little was known about its lateral extent and rate. InSAR studies and elastic dislocation models have revealed discontinuities of up to $\sim$ 5 mm/yr across the Ismetpasa segment of the NAF, implying surface creep at a rate of $\sim$ 9 mm/yr (*Kaneko et al.*,

2013) or 8 ± 3 mm/yr based on *Cakir et al.* (2005). This is a large fraction of the inferred long-term slip rate of the NAF (22 ± 3 mm/year) (*McClusky et al.*, 2000). The lateral extent of significant surface creep is about 75 km, starting at the western termination of the Tosya 1943 (M = 7.6) earthquake rupture (*Barka*, 1996) and overlapping with the eastern part of the 1944 Bolu-Gerede (M = 7.3) earthquake rupture (*Barka*, 1996; *Cakir et al.*, 2005; *Kaneko et al.*, 2013). Instrumental measurements (*i.e.*, local triangulation networks and creepmeters) between 1982-1992 give a rate of 7.7 ± 1.1 mm/yr (*Deniz et al.*, 1993), which is in good agreement with the InSAR data (*Cakir et al.*, 2005). Ground-based LiDAR measurements ($6.0 - 10.1 \pm 4.0$ mm/yr) are also consistent with other datasets (*Karabacak et al.*, 2011). It is not known whether or not the fault was creeping before the 1944 earthquake. However, based on the study of *Cakir et al.* (2005), the rate of creep appears to have exponentially decreased with time since 1944, suggesting that creep may have started after the Bolu-Gerede event as postseismic relaxation, and hence aseismic slip on the NAF is transient.

More recently, SAR and GPS measurements reveal afterslip displacement triggered by the 1999 M7.4 earthquake that progressively slowed down to reach a steady rate ten years after the earthquake with a rate comparable to the pre-earthquake rate (*Cakir et al.*, 2012; *Reilinger et al.*, 2000; *Ergintav et al.*, 2009).

A.4 Philippine Fault system, Leyte island

Geodetic, trilateration and GPS measurements in the central part of the Philippine Fault system on Leyte island (Philippines) have revealed asesimic creep at a rate of at least 26 mm/yr (left-lateral) on two segments: the north Central Leyte Fault and the south Central Leyte Fault (*Duquesnoy et al.*, 1994; *Besana and Ando*, 2005). Creep in this particular case is believed to be linked to the mechanical strength of the crust, which is supposed to be weak in this area where the fault intersects the volcanic arc. High geothermal gradient and strong geothermal flows are also observed there (*Duquesnoy et al.*, 1994).

A.5 Asal Rift, Djibouti

Interferometry study in the Asal Rift (Djibouti) has revealed that creep behavior can also occur on normal faults (*Doubre and Peltzer*, 2007). Surface displacement maps show that the asysmmetric subsidence of the inner floor of the rift (with respect to the bordering shoulders) is accommodated by three main active faults. Slip on faults occurs either as steady creep or during sudden slip events conjointly with an increase in seismicity. *Doubre and Peltzer* (2007) suggest that slip on the faults is controlled by the small pressure changes in fluid-filled fractures connected to the faults.

A.6 Geological setting and aseismic behavior

These examples show that aseismic creep can occur in a variety of geological settings (e.g., *Graymer et al.*, 2005; *Holdsworth et al.*, 2011; *Bradbury et al.*, 2007; *Janssen et al.*, 2012, and chapter 3). While no systematics arise from this compilation, one might note that some of these examples involved subduction zone formations (e.g., *Holdsworth et al.*, 2011; *Huang et al.*, 2006a; *Teng*, 1980a). This observation comforts the view that subduction related clay-rich mélanges favor the occurrence of aseismic creep patches. By contrast, continental clastic formations seem to result in settings that are generally well locked in the 0-20km depth range (*Ader et al.*, 2012; *Hsu et al.*, 2009a). It also seems that the hythrothermalism in volcanic contexts favors aseismic creep, as the Philippine Fault through Leyte island and the Asal rift examples suggest (*Doubre and Peltzer*, 2007; *Duquesnoy et al.*, 1994; *Besana and Ando*, 2005). This would be consistent with the general observation that the ridge and transform faults in the oceanic lithosphere setting are dominantly aseismic (e.g., *Bird and Kagan*, 2004).

Appendix B

A brief review of rock deformation mechanisms

A number of mechanisms could potentially contribute to aseismic deformation. We briefly review these mechanisms, the conditions under which they operate (depending on temperature, strain rate, stress, confining pressure, grain size and chemical composition) and the criteria which might be used to detect them from observation of fault-zone rocks. They include cataclastic flows, pressure solution creep, dislocation creep, diffusion creep, and granular flow (*Snoke et al.*, 1998). Each mechanism displays a characteristic set of microstrutures, occurs at a specific set of pressure-temperature-fluid conditions (over which it is dominant) and displays a distinct form of flow law (*Snoke et al.*, 1998). Most of these mechanisms result in non-linear flow laws of the form:

$$\dot{\epsilon} = A\frac{\sigma^n}{d^m}\exp\left(\frac{Q}{RT}\right), \tag{B.1}$$

describing how the stress rate, $\dot{\epsilon}$, depends on the differential stress, σ, and grain size, d. The various mechanisms differ in the exponent n, dependency on grain size, represented by the exponent m, and activation energy Q. The diagram below qualitatively maps the domains of operation of these mechanisms as a function of strain rate and differential stress level (modified from *Davis et al.* (1996)). Similar diagrams that consider strain rates and grain size as mapping variables can be found in the literature.

B.1 Granular flows

Granular flows involve the rolling and sliding of rigid particles (relative to each other) of unlithified sediments layers or slurries (*Gifkins*, 1976; *Twiss and Moores*, 1992; *Stunitz and Gerald*, 1993). It occurs only at low effective confining pressures and involves friction; therefore it is an upper surface process, unless high pore fluid pressure lowers the effective confining pressure by reducing σ_n. Granular flow is an important soft-sediment deformation mechanism that must play a predominant role

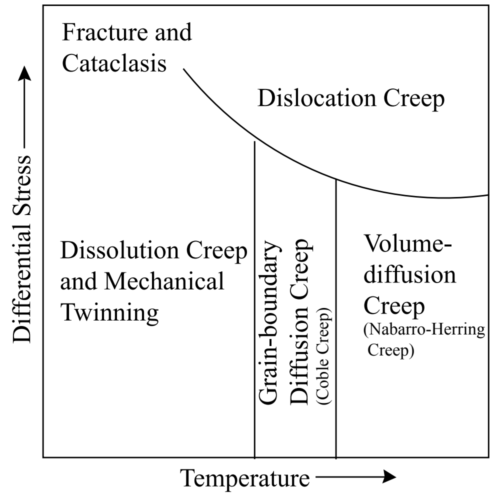

Figure B.1: Simplified deformation mechanism maps (Modified from *Davis et al.* (1996)). Plot of differential stress vs temperature, showing the field in which different mechanisms dominate relative to one another.

in deforming accretionary prisms in subduction zones (*Twiss and Moores*, 1992). Grains themselves show no evidence of granular flow (no characteristic microfabrics), only rocks are deformed. Hence, it is a mechanism difficult to detect based on the structural observation of fault-rocks.

B.2 Cataclastic flows

Cataclastic flow, in which crystal structure remains undistorted, involves continuous brittle fracturing and communition of grains with frictional sliding and rolling of the fragments with respect to one another (*Engleder*, 1974; *Rutter*, 1986; *Twiss and Moores*, 1992; *Hadizadeh et al.*, 2012). The process necessarily involves dilatancy and is therefore pressure sensitive (*Rutter*, 1986). This is a mechanism that operates under low to moderate temperatures, low confining pressure and relatively high strain rates, which leads to a progressive diminution of grain size (*Twiss and Moores*, 1992). Cataclastic flow occurs instead of granular flow when effective confining pressure is too high to promote granular flow, *i.e*, when the work required to fracture grains is less that the work required to slide or roll them past one another (*Twiss and Moores*, 1992). In term of microfabrics, cataclasis are characterized by the presence of pervasive cracks and sharp angular clasts/grains which can be very different in size, and commonly by the absence of any foliation (*Twiss and Moores*, 1992).

B.3 Stress corrosion

Stress corrosion is the growth of cracks associated with chemical reactions of the host material. It involves atomic bond rupture enhanced by stress and the chemical activity of the fluid produced at the vicinity of the crack tip such that the energy requirements for crack propagation are reduced (*Kerrich et al.*, 1981). However, while it may reduce the size of blocks, it cannot alone accommodate large deformations (*Gratier et al.*, 2013). Stress corrosion is thermally activated but can occur in a broad range of conditions depending of the rock fluid content.

B.4 Dislocation creep

Intracrystalline plasticity is another fundamental deformation mechanism in which grains become internally distorted (*Rutter*, 1986) at high strain rates and over a large temperature range. Dislocation creep, which involves the motion of dislocation through a crystal lattice, is probably the most important mechanism for producing ductile deformation in crystalline materials (*Twiss and Moores*, 1992; *Snoke et al.*, 1998). However, steady-state deformation (creep) involves both a strain-producing process and a recovery process (*Snoke et al.*, 1998). Strain is produced by the glide of line defects (dislocations) through the lattice (unit cell of a grain). The process, called dislocation glide, tends to be brought to a halt by an obstacle (point defect), and this produces strain hardening (*Nicolas and Poirier*, 1976; *Twiss and Moores*, 1992; *Snoke et al.*, 1998). Recovery processes act to offset strain-hardening by allowing the material to restore a state of lower internal energy. Both dislocation glide and recovery processes are thermally activated and depend little on pressure (*Snoke et al.*, 1998). Recovery processes are dislocation climb and dynamic recrystallization processes (subgrain rotation or grain boundary migration) by which new crystals grains form from old grains during deformation processes. Dislocation climb causes the dislocation to climb out of the glide plane (to overcome the point defect) through vacancy diffusion; therefore it is more efficient at high temperatures *Twiss and Moores* (1992). Ductile deformation by dislocation creep produces characteristic microfabrics, including: preferred orientations of mineral crystallographic axes, dislocations microstructures (linear features, undulatory extinction) and grain textures (deformation lamellae, ribbon-shaped grains, subgrains, higly serrated grains boundaries) which varies depending on the strain rate, the temperature and the differential stress undergone by the rock (*Twiss and Moores*, 1992; *Snoke et al.*, 1998). Dislocation creep involves thermal activation, and therefore the process is unlikely to develop before 400°C at the low natural deviatoric stresses (*Rutter*, 1976).

B.5 Twin gliding or mechanical twinning

Twin gliding is another process that involves intracrystalline plasticity, whereby twins are produced from an original structure by simple shearing parallel to the twin plane (*Twiss and Moores*, 1992; *Snoke et al.*, 1998). However, it requires minerals capable of forming twins across its crystallographic planes, and total strains associated with this mechanism are typically not large and depend on the crystal structure. Great strains must be sustained by other mechanisms (*Twiss and Moores*, 1992; *Burkhard*, 1993; *Snoke et al.*, 1998; *Gratier et al.*, 2013).

B.6 Diffusion creep

The third mechanism that can accommodate creep includes flow by diffusive mass transfer, in which changes of shape of the deforming grains involve the transfer of material from areas of high compressive stress to areas of low compressive stress (*Rutter*, 1986; *Twiss and Moores*, 1992). In the particular case of diffusion creep, the deformation of a crystalline solid takes place by the diffusion of point defects through their crystal lattice (Nabarro-Herring creep) or the the diffusion of atoms or ions along grain boundaries (Coble creep) (*Twiss and Moores*, 1992). Point defects in crystal lattices include both interstitials (extra atoms) and vacancies. The lattice is deformed around interstitials (expand) and vacancies (collapse), creating high-energy defects to be overcomed. With Nabarro-Herring creep, vacancies are created at the surface of the crystal, where the compressive stress is minimum and moves towards the surface of high compressive stress. The flux of atoms is opposite to that of the vacancies, and the shape change of the grain occurs by accumulation of atoms on the low-stressed face (*Twiss and Moores*, 1992). Nabarro-Herring creep is an effective deformation mechanism only at high temperatures and low stress with the strain-rate inversely proportional to the square of the grain size (*Twiss and Moores*, 1992). Coble creep occurs when diffusion (dry) of atoms takes places along the grain boundaries rather than through the volume. Atoms diffuse away from high stressed surfaces to accumulate on a surface of low compressive stress. Coble creep is effective at high temperatures, but lower than for Nabarro-Herring creep, since the diffusion is more rapid because of smaller activation energy (*Twiss and Moores*, 1992). In natural deformation, the minimum temperature, even for very fine grain aggregates, is 500°C for Coble creep and 600°C for Nabarro-Herring (*Rutter*, 1976). Flow law for Coble creep is strongly grain-size dependent, with the strain-rate inversely proportional to the cube of the grain size. Therefore, in both cases (Nabarro-Herring and Coble creep), diffusion creep is suppressed for large grains (*Twiss and Moores*, 1992).

B.7 Pressure-solution creep

Pressure solution is an important deformation mechanism at shallow to intermediate depth in the crust that also involves mass transfer. Deformation of the aggregate is accomplished by (1) stress-induced dissolution in the presence of fluid at relatively high-stress sites, (2) diffusion through interconnected grain-boundary fluid phase and (3) precipitation at potentially dilatant, low-stress sites (pores, veins) (*Rutter*, 1976; *Robin*, 1978; *Rutter*, 1983; *Gratier et al.*, 2013). Diffusion transfer may occur at the grain scale or over considerable distances (*Snoke et al.*, 1998). Pressure solution creep is very similar to Coble creep, only the activation energy of fluid phase diffusion is much lower than along dry grain boundaries (*Fischer and Elliott*, 1974; *Twiss and Moores*, 1992; *Gratier et al.*, 2013). Therefore, pressure-solution is the dominant mechanism at temperatures ranging from 20 to $350° - 400°$C, at tectonic strain rate 10^{-10} to 10^{-15} s^{-1} (*Twiss and Moores*, 1992). (*Rutter*, 1976) have inferred that where diffusion is the rate-limiting step, the rate of pressure solution creep should be inversely proportional to the cube of the grain size. There are abundant mircostructral evidences of pressure solution in rocks, found ubiquitously from near the surface down to 10-15 km depth (*Gratier et al.*, 2013). It includes dissolution features (dissolutions seams, stylolites, impressed grains, fossils and pebbles) as well as evidences of precipitations (solution cleavage associated with veins, fibers precipitated in pressure shadows) (*Snoke et al.*, 1998; *Gratier et al.*, 2013).

B.8 Grain-boundary sliding or superplastic creep

Sliding on the grain boundaries can accommodate large strain values; however, it cannot operate alone (*Poirier*, 1985; *Twiss and Moores*, 1992; *Snoke et al.*, 1998; *Gratier et al.*, 2013): there must be an accommodation mechanism to prevent gaps and overlaps at grain boundaries. Therefore, the shape of the grain must change slightly as they pass one another, and this deformation can be accommodated by diffusion or local dislocation motion (*Twiss and Moores*, 1992; *Snoke et al.*, 1998). This mechanism, which has been linked with the development of superplasticity (*Ashby and Verrall*, 1973; *Boullier and Guguen*, 1975; *Konstantinidis and Herrmann*, 1998) is characterized by very rapid strain rates at low stresses compared to other mechanisms of ductile deformation, and a power-law rheology with a stress exponent varying from 1 to 2 (*Twiss and Moores*, 1992). It is traditionally considered as a high-temperature mechanism when sliding is accommodated at dry conditions (*Boullier and Guguen*, 1975; *Gratier et al.*, 2013), so it is not expected to be commonly found in the upper crust. However, *Gratier et al.* (2013) have demonstrated that pressure-solution creep may accommodate grain boundary sliding when a trapped fluid phase activates diffusion along the grain boundary through the entire upper crust.

Appendix C

Nature and origin of the Lichi Mélange

The Lichi Mélange is a ~ 2 km wide formation, cropping out on the western side of the Coastal Range, mainly south of Yuli (Figure 1.5 and 1.6). It is a characteristic block-in-matrix mélange with preferred foliation in a scaly argillaceous matrix and extensional web and boudinage structures in the sandstone blocks (*Chen*, 1997b; *Chang et al.*, 2000). The exotic blocks inside the formation are various in size (millimeters to kilometers) and lithology (arc products, ophiolites, sedimentary rocks). The Lichi Mélange has been intensely studied, and several origins have been proposed. It was first interpreted to be a subduction mélange, developed in the former Manilla Trench during the subduction of the South China Sea oceanic crust (Biq, 1971). But this model is in contradiction with the position of the Lichi Mélange, east of the accretionary wedge (*Huang and Yin*, 1990; *Huang et al.*, 1992; *Reed et al.*, 1992; *Malavieille et al.*, 2002; *Huang et al.*, 2008). Afterwards, it was suggested that the Lichi Mélange was a former olistostrome (*Wang*, 1976; *Ernst*, 1977; *Page and Suppe*, 1981; *Lin and Chen*, 1986) where the sedimentary slumping deposits in the western part of forearc basin were coming from the exposed accretionary prism (proto Central Range). However, marine seismic investigations in the early 1990s combined with previous biostratrigraphic studies, clay composition and lithology of the exotic blocks inside the mélange questioned this model and led instead to the proposal of a tectonic collision origin (*Chang et al.*, 2000, 2001, 2009; *Huang et al.*, 2006a, 2008).

C.1 Marine seismic investigations

Southeastern Taiwan marine seismic investigations in the forearc basin, which lies between the backstop of the accretionary prism and the Luzon arc, have shown key features that help us to understand the origin of the Lichi Mélange. GMGS976 profile at 21N (*Huang et al.*, 2008) (Figure 1.1 and 1.3) shows synchronous deformation and sedimentation in the western part of the forearc basin:

once the sediments are deposited in the Luzon trough, the sequence is deformed and then covered unconformably by the overlying sequence. Consequently, folding and thrusting seem to have occurred since the early history of the forearc sedimentation. On the other hand, in the eastern part of the forearc basin, sedimentation is continuous regardless of active deformation in the west. Further to the north, seismic profiles reveal the progressive closure of the forearc basin by arcward thrusting of the forearc basin strata (*Huang et al.*, 2008; *Malavieille et al.*, 2002; *Reed et al.*, 1992). The accumulation of deformation and shortening of the forearc basin leads to the development of the Huatung Ridge which connects northward with the Lichi Mélange in the southern Coastal Range (Figure 1.1). Those observations support the tectonic collision model where the protolith of the mélange is the forearc basin deposits, and the exotic blocks were incorporated during the early stage of the collision.

C.2 Field observations

Field observations show that the Lichi Mélange lies on the western side of the Coastal Range, mostly in faulting contact with the coherent forearc basin strata and the Tuluanshan (arc) (*Hsu*, 1956; *Teng and Lo*, 1985). Nevertheless, depositional contact between the Lichi and Fanshuliao were reported (*Page and Suppe*, 1981; *Barrier and Muller*, 1984; *Huang et al.*, 2008). Different sheared facies are observed in the Lichi Mélange: from weakly sheared/broken to highly sheared mélange facies (*Chang et al.*, 2000, 2001; *Huang et al.*, 2008). The weakly sheared, broken formation facies still preserves a distinct turbidite sedimentary structure with a basal layer primarily composed of quartz, as in the lower forearc sequences. On the other hand, slate chips, which are commonly found in the upper part of the forearc basin turbidite deposits ($<$ 3 Ma) (*Teng*, 1982), are almost absent in the Lichi Mélange (*Huang et al.*, 2008). Moreover, in the weakly sheared broken facies, we can observe sub-angular to sub-rounded metasandstone conglomerates in pebbly mudstone layers, very similar to the Shuilien Conglomerate, a stratigraphic horizon in the remnant forearc basin sequences of the Coastal Range (*Huang et al.*, 2008; *Page and Suppe*, 1981). Those observations are coherent with a tectonic collision model with reworked material from the forearc basin deposits and its underlying bedrock.

C.3 Constraints from biostratigraphic studies

Biostratigraphic studies have placed a lot of constraints on the origin of the Lichi Mélange (*Chang*, 1967; *Chi et al.*, 1981; *Chi*, 1982; *Barrier and Muller*, 1984; *Huang et al.*, 2008). Planktic foraminifers and calcareous nanoplankton found in the Lichi Mélange and its tributaries show a consistent early Pliocene age which restrains the time of deposition of the protolith to a narrow range (5.5 to 3.7

Ma). Therefore, the Lichi Mélange is coeval with the lower forearc basin sequence, but older than the upper deposits. Consequently, the deformation must have occurred as soon the turbidites were deposited and it was then followed by continuous deposition of younger turbidites (3.5-1 Ma) in the upper part of the forearc basin. This scenario is very similar to what has been deduced from seismic profiles, south of the Coastal Range. Moreover, the benthic foraminifers study of (*Huang et al.*, 2008) have proved that, despite the shearing intensity, microfossils within the Lichi Mélange are similar and compatible with the fauna of the remnant forearc basin to the east. Besides, a comparative study between the Lichi Mélange, the remnant forearc basin strata and the present hemipelagic muds of the North Luzon Trough (Huang, 1993) has shown that the indigenous deep-marine benthic foraminifers are similar in the three formations. Consequently, all of these observations based on the biostratigraphic content of the Coastal Range formations favor a forearc basin protholith for the Lichi Mélange.

C.4 Clay composition

Clay mineral composition (< 2 m) of the muddy matrix and the sedimentary blocks is similar in all samples, regardless of shearing intensity (*Huang et al.*, 2008). They are characterized by illite, chlorite, mixed-layer clay minerals (mica/semectite) and kaolinite (*Lin and Chen*, 1986). Smectite is found as trace or is completely absent. Therefore, the Lichi Mélange must have two sources: one continental, with slightly metamorphosed sediments from the exhumed accretionary prism to provide illite and chlorite, and one volcanic, to derive the kaolinite. The clay mineral assemblage in the turbidites of the remnant forearc basin is very similar in composition except for the kaolinite, which is absent in the Fanshuliao formation (*Lin and Chen*, 1986). *Huang et al.* (2008) claimed that the occurrence of kaolinite shows the tectonic involvement of the volcanic basement beneath the forearc basin, during the formation of the Lichi Mélange. Thrusting, fragmentation and mixing of volcanic rocks within the mélange allowed the incorporation of the kaolinite from the arc formation by fluid flow along the sheared plan or fractures. Therefore, kaolinite is absent in the forearc basin strata because it did not undergo intense deformation.

C.5 Origin of exotic blocks

To understand how the Lichi Mélange was formed, another important matter is the origin of exotic blocks. As mentioned earlier in the text, different lithologies can be observed: arc products, ophiolites and sedimentary deposits. The volcanic products derived from the Luzon volcanic arc include andesite, volcanics breccias, tuffs and volcanoclastic turbidites. Pillow basalts and gabbro, sometimes serpentinized, composed the dismembered ophiolite suite. The larger block (several hundreds of meters) is known as the East Taiwan Ophiolite (ETO). Ophiolitic blocks appear to be restricted to the intensely sheared facies. They may represent the oceanic crust of either the South China Sea (*Suppe et al.*, 1981; *Jahn*, 1986; *Chung and Sun*, 1992) or the Philippine Sea Plate beneath the Luzon forearc-arc (*Juan et al.*, 1980; *Malavieille et al.*, 2002). The source and emplacing mechanism of these basic products are still highly debated. Microfossil records from intercalated shale within the ophiolites gave an age of 15 Ma (*Huang et al.*, 1979), which is younger than, but close in age, to the youngest South China Sea crust (opening 32-17 Ma) (*Briais et al.*, 1993). However, if the ophiolites came from the South China Sea, it is not clear how they were incorporated within the Lichi Mélange. Indeed, ophiolitic blocks inside the accretionary prism are only observed in the Kenting mélange, *i.e.*, west of the Hengchun Peninsula (southern extension of the Central Range), but not in the Central Range. Moreover, they differ from ETO in composition (*Huang et al.*, 2008). The second potential source of these ophiolites is the basement of either the Luzon arc or the forearc basin. The microfossils are coeval with the age of the Luzon arc formation, which is not older than mid-Miocene (*Huang et al.*, 2008). In that case, ophiolites would have been incorporated within the mélange at the same time as the arc products, during the shortening phase of the forearc basin (Huatung ridge equivalent).

Finally, the sedimentary blocks show two different facies. We can observe weakly lithified Pliocene turbidite units (tens of meters to a kilometer size blocks) with lithology, age and sedimentary turbidite structures simlar to those of the coherent remnants of forearc basin strata of the Coastal Range. The Lichi Mélange also includes metric to kilometric size angular blocks of well-lithified, whitish quartz-rich, feldspathic sandstones. They are late Miocene in age. Zircon fission track studies have shown that they are similar to the non-metamorphosed deep-sea fan sandstones of the upper accretionary prism in the Hengchun Peninsula, but they display a very different age record from the Bouma TA part of the Taiyuan remnant forearc-basin turbidites (*Huang et al.*, 1997, 2008). The whitish sandstone blocks in the Lichi Mélange show a partial annealing feature with two age peaks concentrated at the early-middle Miocene (9-18 Ma) and late Mesozoic (66-130 Ma), whereas the zircon grains in the Fanshuliao formation show either a complete reset (2.08 Ma) or partial reset with a young peak of Pliocene age (2.5 Ma) and an old tail of Mesozoic age (64-100 Ma) (*Huang et al.*, 2008). Those whitish blocks have only been observed in the intensely sheared facies of the Lichi Mélange, not in the weakly sheared, broken facies nor in the remnant forearc basin formation. Consequently, to get a different zircon fission track record and a classification based on shearing intensity, it is hard to imagine that they were delivered to the Lichi Mélange by turbiditic current. They were more probably incorporated by eastward thrusting into the deformed forearc strata (*Huang et al.*, 2008).

Bibliography

Adams, G. G. (1998), Steady sliding of two elastic half-spaces with friction reduction due to interface stick-slip, *Journal of Applied Mechanics*, *65*(2), 470–475.

Ader, T., J. P. Avouac, J. Liu-Zeng, H. Lyon-Caen, L. Bollinger, J. Galetzka, J. Genrich, M. Thomas, K. Chanard, S. N. Sapkota, S. Rajaure, P. Shrestha, L. Ding, and M. Flouzat (2012), Convergence rate across the nepal himalaya and interseismic coupling on the main himalayan thrust: Implications for seismic hazard, *Journal of Geophysical Research-Solid Earth*, *117*, n/a–n/a.

Ambraseys, N. N. (1970), Some characteristic features of the anatolian fault zone, *Tectonophysics*, *9*(2-3), 143–165.

Andrews, D. J. (1976), Rupture velocity of plane strain shear cracks, *Journal of Geophysical Research*, *81*(32), 5679–5687.

Andrews, D. J. (2002), A fault constitutive relation accounting for thermal pressurization of pore fluid, *Journal of Geophysical Research-Solid Earth*, *107*(B12), 2363.

Andrews, D. J., and Y. Ben-Zion (1997), Wrinkle-like slip pulse on a fault between different materials, *Journal of Geophysical Research-Solid Earth*, *102*(B1), 553–571.

Angelier, J., H. T. Chu, and J. C. Lee (1997), Shear concentration in a collision zone: kinematics of the chihshang fault as revealed by outcrop-scale quantification of active faulting, longitudinal valley, eastern taiwan, *Tectonophysics*, *274*(1-3), 117–143.

Ariyoshi, K., T. Matsuzawa, Y. Yabe, N. Kato, R. Hino, A. Hasegawa, and Y. Kaneda (2009), Character of slip and stress due to interaction between fault segments along the dip direction of a subduction zone, *Journal of Geodynamics*, *48*(2), 55–67.

Ashby, M., and R. Verrall (1973), Diffusion-accommodated flow and superplasticity, *Acta Metallurgica*, *21*, 149–163.

Barbot, S., Y. Fialko, and Y. Bock (2009), Postseismic deformation due to the m-w 6.0 2004 parkfield earthquake: Stress-driven creep on a fault with spatially variable rate-and-state friction parameters, *Journal of Geophysical Research*, *114*(b7), B07,405.

Barbot, S., N. Lapusta, and J. P. Avouac (2012), Under the hood of the earthquake machine: Toward predictive modeling of the seismic cycle, *Science*, *336*(6082), 707–710.

Barka, A. (1996), Slip distribution along the north anatolian fault associated with the large earthquakes of the period 1939 to 1967, *Bulletin of the Seismological Society of America*, *86*(5), 1238–1254.

Barrier, E., and J. Angelier (1986), Active collision in eastern taiwan: The coastal range, *Tectonophysics*, *125*, 39–72.

Barrier, E., and C. Muller (1984), New observations and discussion on the origin and age of the lichi mélange, *Memoir of the Geological Society of China*, *6*, 303–325.

Beeler, N. M., T. E. Tullis, M. L. Blanpied, and J. D. Weeks (1996), Frictional behavior of large displacement experimental faults, *Journal of Geophysical Research-Solid Earth*, *101*(B4), 8697–8715.

Beeler, N. M., T. E. Tullis, and D. L. Goldsby (2008), Constitutive relationships and physical basis of fault strength due to flash heating, *Journal of Geophysical Research-Solid Earth*, *113*(B1), B01,401.

Ben-Zion, Y., and J. R. Rice (1995), Slip patterns and earthquake populations along different classes of faults in elastic solids, *Journal of Geophysical Research-Solid Earth*, *100*(B7), 12,959–12,983.

Beroza, G. C., and T. Mikumo (1996), Short slip duration in dynamic rupture in the presence of heterogeneous fault properties, *Journal of Geophysical Research-Solid Earth*, *101*(B10), 22,449–22,460.

Besana, G. M., and M. Ando (2005), The central philippine fault zone: Location of great earthquakes, slow events, and creep activity, *Earth Planets and Space*, *57*(10), 987–994.

Biq, C. (1971), Comparison of mélange tectonics in taiwan and in some other mountain belts, *Petroleum Geology of Taiwan*, *9*, 79–106.

Bird, P., and Y. Y. Kagan (2004), Plate-tectonic analysis of shallow seismicity: Apparent boundary width, beta, corner magnitude, coupled lithosphere thickness, and coupling in seven tectonic settings, *Bulletin of the Seismological Society of America*, *94*(6), 2380–2399.

Bizzarri, A., and M. Cocco (2006a), A thermal pressurization model for the spontaneous dynamic rupture propagation on a three-dimensional fault: 1. methodological approach, *Journal of Geophysical Research-Solid Earth*, *111*(B5), B05,303.

Bizzarri, A., and M. Cocco (2006b), A thermal pressurization model for the spontaneous dynamic rupture propagation on a three-dimensional fault: 2. traction evolution and dynamic parameters, *Journal of Geophysical Research-Solid Earth*, *111*(B5), B05,304.

Blanpied, M. L., C. J. Marone, D. A. Lockner, J. D. Byerlee, and D. P. King (1998), Quantitative measure of the variation in fault rheology due to fluid-rock interactions, *Journal of Geophysical Research-Solid Earth*, *103*(B5), 9691–9712.

Boullier, A. M., and Y. Guguen (1975), S.p.-mylonites: origin of some mylonites by superplastic flow, *Contributions to Mineralogy and Petrology*, *50*, 93–104.

Bradbury, K. K., D. C. Barton, J. G. Solum, S. D. Draper, and J. P. Evans (2007), Mineralogic and textural analyses of drill cuttings from the san andreas fault observatory at depth (safod) boreholes: Initial interpretations of fault zone composition and constraints on geologic models, *Geosphere*, *3*(5), 299–318.

Briais, A., P. Patriat, and P. Tapponnier (1993), Updated interpretation of magnetic-anomalies and sea-floor spreading stages in the south china sea - implications for the tertiary tectonics of southeast-asia, *Journal of Geophysical Research-Solid Earth*, *98*(B4), 6299–6328.

Brodsky, E. E., and H. Kanamori (2001), Elastohydrodynamic lubrication of faults, *Journal of Geophysical Research-Solid Earth*, *106*(B8), 16,357–16,374.

Burford, R. O., and P. W. Harsh (1980), Slip on the san andreas fault in central california from alignment array surveys, *Bulletin of the Seismological Society of America*, *70*(4), 1233–1261.

Burgmann, R., D. Schmidt, R. M. Nadeau, M. d'Alessio, E. Fielding, D. Manaker, T. V. McEvilly, and M. H. Murray (2000), Earthquake potential along the northern hayward fault, california, *Science*, *289*(5482), 1178–1182.

Burgmann, R., M. G. Kogan, G. M. Steblov, G. Hilley, V. E. Levin, and E. Apel (2005), Interseismic coupling and asperity distribution along the kamchatka subduction zone, *Journal of Geophysical Research - Solid Earth*, *110*, B07,405–B07,416.

Burkhard, M. (1993), Calcite twins, their geometry, appearance and significance as stress-strain markers and indicators of tectonic regime - a review, *Journal of Structural Geology*, *15*(3-5), 351–368.

Byrne, T., and C. Liu (2002), *Geology and geophysics of an arc-continent collision, Taiwan*, chap. Preface: Introduction to the geology and geophysics of Taiwan, pp. v–viii, Geological Society of America Special Paper.

Cakir, Z., A. M. Akoglu, S. Belabbes, S. Ergintav, and M. Meghraoui (2005), Creeping along the ismetpasa section of the north anatolian fault (western turkey): Rate and extent from insar, *Earth and Planetary Science Letters*, *238*(1-2), 225–234.

Cakir, Z., S. Ergintav, H. Ozener, U. Dogan, A. M. Akoglu, M. Meghraoui, and R. Reilinger (2012), Onset of aseismic creep on major strike-slip faults, *Geology*, *40*(12), 1115–1118.

Carpenter, B. M., C. Marone, and D. M. Saffer (2011), Weakness of the san andreas fault revealed by samples from the active fault zone, *Nature Geoscienceence*, *4*(4), 251–254.

Cavalie, O., C. Lasserre, M. . P. Doin, G. Peltzer, J. Sun, X. Xu, and Z. . K. Shen (2008), Measurement of interseismic strain across the haiyuan fault (gansu, china), by insar, *Earth and Planetary Science Letters*, *275*(3-4), 246–257.

Champenois, J. (2011), Caractérisation des déformations tectoniques inter-sismiques de l'île de taiwan par interférométrie radar, Ph.D. thesis, Paris Est.

Champenois, J., B. Fruneau, E. Pathier, B. Deffontaines, K. C. Lin, and J. C. Hu (2012), Monitoring of active tectonic deformations in the longitudinal valley (eastern taiwan) using persistent scatterer insar method with alos palsar data, *Earth and Planetary Science Letters*, *337*, 144–155.

Chang, C. P., J. Angelier, and C. Y. Huang (2000), Origin and evolution of a mélange: the active plate boundary and suture zone of the longitudinal valley, taiwan, *Tectonophysics*, *325*(1-2), 43–62.

Chang, C. P., J. Angelier, C. Y. Huang, and C. S. Liu (2001), Structural evolution and significance of a mélange in a collision belt: the lichi mélange and the taiwan arc-continent collision, *Geological Magazine*, *138*(6), 633–651.

Chang, L. (1967), A biostratigraphic study of the tertiary in the coastal range, eastern taiwan, based on smaller foraminifera (i. southern part), *Proceeding of the Geological Society of China*, *10*, 64–76.

Chang, L. S. (1968), A biostratigraphic study of the tertiary in the coastal range, eastern taiwan, based on smaller foraminifera (ii. northern part), *Proceeding of the Geological Society of China*, *11*, 19–33.

Chang, L. S. (1969), A biostratigraphic study of the tertiary in the coastal range, eastern taiwan, based on smaller foraminifera (iii. midlle part), *Proceeding of the Geological Society of China*, *12*, 89–101.

Chang, L. S. (1975), Tertiary biostratigraphy of taiwan, *Geology and Paleontology of SE Asia*, *15*, 337–361.

Chang, S. H., W. H. Wang, and J. C. Lee (2009), Modelling temporal variation of surface creep on the chihshang fault in eastern taiwan with velocity-strengthening friction, *Geophysical Journal International*, *176*(2), 601–613.

Chen, C. H., Y. N. Shieh, T. P. Lee, and S. A. Mertzman (1990), Nd-sr-o isotopic evidence for source contamination and an unusual mantle component under luzon arc, *Geochimica Et Cosmochimica Acta*, *54*(9), 2473–2483.

Chen, H. Y., S. B. Yu, L. C. Kuo, and C. C. Liu (2006), Coseismic and postseismic surface displacements of the 10 december 2003 (m-w 6.5) chengkung, eastern taiwan, earthquake, *Earth Planets and Space*, *58*(1), 5–21.

Chen, H. Y., Y. J. Hsu, J. C. Lee, S. B. Yu, L. C. Kuo, Y. L. Jiang, C. C. Liu, and C. S. Tsai (2009), Coseismic displacements and slip distribution from gps and leveling observations for the 2006 peinan earthquake (m-w 6.1) in southeastern taiwan, *Earth Planets and Space*, *61*(3), 299–318.

Chen, H. Y., J. C. Lee, H. Tung, S. B. Yu, Y. J. Hsu, and H. Lee (2012), Determination of vertical velocity field of southernmost longitudinal valley in eastern taiwan: A joint analysis of leveling and gps measurements, *Terrestrial Atmospheric and Oceanic Sciences*, *23*(4), 355–376.

Chen, W. S. (1997a), Lithofacies analyses of the arc-related sequence in coastal range, eastern taiwan, *Journal of the Geological Society of China*, *40*(2), 313–338.

Chen, W. S. (1997b), Mesoscopic structures developed in the lichi mlange during the arc-continent collision in the taiwan region, *Journal of the Geological Society of China*, *40*(415-434).

Chen, W.-S. (2009), The fault slip long term velocity and recurrence period. report of central geological survey, *Tech. rep.*, Report of Central Geological Survey, pp. 31-40.

Chen, W. S., and Y. Wang (1988), Development of deep-sea fan systems in coastal range basin, eastern taiwan, *Acta Geologica Taiwanica*, *26*(37-56).

Chen, W. S., M. T. Huang, and T. K. Liu (1991), Neotectonic significance of the chimei fault in the coastal range, eastern taiwan, *Proceeding of the Geological Society of China*, *34*(1), 43–56.

Cheng, L.-W., J.-C. Lee, J.-C. Hu, and H.-Y. Chen (2009), Coseismic and postseismic slip distribution of the 2003 mw = 6.5 chengkung earthquake in eastern taiwan: Elastic modeling from inversion of gps data, *Tectonophysics*, *466*(3-4), 335–343.

Chester, F. M., J. P. Evans, and R. L. Biegel (1993), Internal structure and weakening mechanisms of the san andreas fault, *Journal of Geophysical Research-Solid Earth*, *98*(B1), 771–786.

Chi, W. (1982), The calcareous nannofossils of the lichi mélange and the kenting mélange and their significance in the interpretation of plate tectonics of the taiwan region, *Ti-Chih*, *4*, 99–112.

Chi, W., J. Namson, and J. Suppe (1981), Stratigraphic record of plate interactions in the coastal range of eastern taiwan, *Memoir of the Geological Society of China*, *4*, 155–194.

Ching, K. E., R. J. Rau, and Y. H. Zeng (2007), Coseismic source model of the 2003 m-w 6.8 chengkung earthquake, taiwan, determined from gps measurements, *Journal of Geophysical Research-Solid Earth*, *112*(B6), 31.

Ching, K. E., M. L. Hsieh, K. M. Johnson, K. H. Chen, R. J. Rau, and M. Yang (2011), Modern vertical deformation rates and mountain building in taiwan from precise leveling and continuous gps observations, 2000-2008, *Journal of Geophysical Research-Solid Earth*, *116*, B08,406.

Chlieh, M., J. P. Avouac, K. Sieh, D. H. Natawidjaja, and J. Galetzka (2008), Heterogeneous coupling of the sumatran megathrust constrained by geodetic and paleogeodetic measurements, *Journal of Geophysical Research-Solid Earth*, *113*(B5), 31.

Chlieh, M., H. Perfettini, H. Tavera, J.-P. Avouac, D. Remy, J.-M. Nocquet, F. Rolandone, F. Bondoux, G. Gabalda, and S. Bonvalot (2011), Interseismic coupling and seismic potential along the central andes subduction zone, *Journal of Geophysical Research-Solid Earth*, *116*, B12,405.

Chuang, R. Y., M. M. Miller, Y. G. Chen, H. Y. Chen, J. B. H. Shyu, S. B. Yu, C. M. Rubin, K. Sieh, and L. H. Chung (2012), Interseismic deformation and earthquake hazard along the southernmost longitudinal valley fault, eastern taiwan, *Bulletin of the Seismological Society of America*, *102*(4), 1569–1582.

Chung, L. H., Y. G. Chen, Y. M. Wu, J. B. H. Shyu, Y. T. Kuo, and Y. N. N. Lin (2008), Seismogenic faults along the major suture of the plate boundary deduced by dislocation modeling of coseismic displacements of the 1951 m7.3 hualien-taitung earthquake sequence in eastern taiwan, *Earth and Planetary Science Letters*, *269*(3-4), 415–425.

Chung, S. L., and S. S. Sun (1992), A new genetic model for the east taiwan ophiolite and its implications for drupal domains in the northern hemisphere, *Earth and Planetary Science Letters*, *109*(1-2), 133–145.

Cochard, A., and R. Madariaga (1996), Complexity of seismicity due to highly rate-dependent friction, *Journal of Geophysical Research-Solid Earth*, *101*(B11), 25,321–25,336.

Cochard, A., and J. R. Rice (2000), Fault rupture between dissimilar materials: Ill-posedness, regularization, and slip-pulse response, *Journal of Geophysical Research-Solid Earth*, *105*(B11), 25,891–25,907.

Collettini, C., C. Viti, S. A. F. Smith, and R. E. Holdsworth (2009), Development of interconnected talc networks and weakening of continental low-angle normal faults, *Geology*, *37*(6), 567–570.

Copley, A., J. Hollingsworth, and E. Bergman (2012), Constraints on fault and lithosphere rheology from the coseismic slip and postseismic afterslip of the 2006 m(w)7.0 mozambique earthquake, *Journal of Geophysical Research-Solid Earth*, *117*, B03,404.

Cross, R. S., and J. T. Freymueller (2007), Plate coupling variation and block translation in the andreanof segment of the aleutian arc determined by subduction zone modeling using gps data, *Geophysical Research Letters*, *34*(6), L06,304.

Dadson, S. J., N. Hovius, H. G. Chen, W. B. Dade, M. L. Hsieh, S. D. Willett, J. C. Hu, M. J. Horng, M. C. Chen, C. P. Stark, D. Lague, and J. C. Lin (2003), Links between erosion, runoff variability and seismicity in the taiwan orogen, *Nature*, *426*(6967), 648–651.

Davis, G. H., S. J. Reynolds, and C. F. Kluth (1996), *Structural Geology of Rocks and Regions. 2nd Edition*, John Wiley & sons, inc.

de Michele, M., D. Raucoules, F. Rolandone, P. Briole, J. Salichon, A. Lemoine, and H. Aochi (2011), Spatiotemporal evolution of surface creep in the parkfield region of the san andreas fault (1993-2004) from synthetic aperture radar, *Earth and Planetary Science Letters*, *308*(1-2), 141–150.

DeMets, C., R. G. Gordon, and D. F. Argus (2010), Geologically current plate motions, *Geophysical Journal International*, *181*(1), 1–80.

den Hartog, S. A. M., A. R. Niemeijer, and C. J. Spiers (2012a), New constraints on megathrust slip stability under subduction zone p-t conditions, *Earth and Planetary Science Letters*, *353*, 240–252.

den Hartog, S. A. M., C. J. Peach, D. A. M. de Winter, C. J. Spiers, and T. Shimamoto (2012b), Frictional properties of megathrust fault gouges at low sliding velocities: New data on effects of normal stress and temperature, *Journal of Structural Geology*, *38*, 156–171.

Deniz, R., A. Aksoy, D. Yalin, H. Seeger, P. Franke, O. Hirsch, and P. Bautsch (1993), Determination of crustal movements in turkey by terrestrial geodetic methods, *Journal of Geodynamics*, *18*(1-4), 13–22.

Di Toro, G., D. L. Goldsby, and T. E. Tullis (2004), Friction falls towards zero in quartz rock as slip velocity approaches seismic rates, *Nature*, *427*(6973), 436–439.

Dieterich, J. (1994), A constitutive law for rate of earthquake production and its application to earthquake clustering, *Journal of Geophysical Research*, *99*(B2), 2601–2618.

Dieterich, J. H. (1979), Modeling of rock friction .1. experimental results and constitutive equations, *Journal of Geophysical Research*, *84*(NB5), 2161–2168.

Dieterich, J. H. (1992), Earthquake nucleation on faults with rate-dependent and state-dependent strength, *Tectonophysics*, *211(1-4)*(1-4), 115–134.

Dieterich, J. H. (2007), Applications of rate- and state-dependent friction to models of fault slip and earthquake occurrence, *Treat. Geophys.*, *4*, 107–129.

Dorsey, R. J., E. J. Buchovecky, and N. Lundberg (1988), Clay mineralogy of pliocene-pleistocene mudstones, eastern taiwan - combined effects of burial diagenesis and provenance unroofing, *Geology*, *16*(10), 944–947.

Doubre, C., and G. Peltzer (2007), Fluid-controlled faulting process in the asal rift, djibouti, from 8 yr of radar interferometry observations, *Geology*, *35*(1), 69–72.

Duan, B. C., and D. D. Oglesby (2005), The dynamics of thrust and normal faults over multiple earthquake cycles: Effects of dipping fault geometry, *Bulletin of the Seismological Society of America*, *95*(5), 1623–1636.

Duquesnoy, T., E. Barrier, M. Kasser, M. Aurelio, R. Gaulon, R. S. Punongbayan, C. Rangin, B. C. Bautista, E. Delacruz, M. Isada, S. Marc, J. Puertollano, A. Ramos, M. Prevot, A. Dupio, I. Eto, F. G. Sajona, D. Rigor, F. G. Delfin, and D. Layugan (1994), Detection of creep along the philippine fault - 1st results of geodetic measurements on leyte island, central philippines, *Geophysical Research Letters*, *21*(11), 975–978.

Engleder, J. T. (1974), Cataclasis and the generation of fault gouge, *Geol. Soc. Am. Bull.*, *85*, 1515–1522.

Ergintav, S., S. McClusky, E. Hearn, R. Reilinger, R. Cakmak, T. Herring, H. Ozener, O. Lenk, and E. Tari (2009), Seven years of postseismic deformation following the 1999, m=7.4 and m=7.2, izmit-duzce, turkey earthquake sequence, *Journal of Geophysical Research-Solid Earth*, *114*, B07,403.

Ernst, W. (1977), Olistostromes and included ophiolite debris from the coastal range of eastern taiwan, *Memoir of the Geological Society of China*, *2*, 97–114.

Evans, E. L., J. P. Loveless, and B. J. Meade (2012), Geodetic constraints on san francisco bay area fault slip rates and potential seismogenic asperities on the partially creeping hayward fault, *Journal of Geophysical Research-Solid Earth*, *117*, B03,410.

Fagereng, A., and R. H. Sibson (2010), Mélange rheology and seismic style, *Geology*, *38*(8), 751–754.

Ferretti, A., C. Prati, and F. Rocca (2001), Permanent scatterers in sar interferometry, *IEEE Transactions On Geoscience and Remote Sensing*, *39*(1), 8–20.

Fischer, G. W., and D. Elliott (1974), *Geochemical transports and kinetics*, chap. Criteria for quasi-steady diffusion and local equilibrium in metamorphism., pp. 77–89, Carnegie Inst. Washington Publ.

Fournier, T. J., and J. T. Freymueller (2007), Transition from locked to creeping subduction in the shumagin region, alaska, *Geophysical Research Letters*, *34*(6), 5.

Freund, L. B. (1990), *Dynamic Fracture Mechanics*, Cambridge University Press.

Freymueller, J. T., M. H. Murray, P. Segall, and D. Castillo (1999), Kinematics of the pacific north america plate boundary zone, northern california, *Journal of Geophysical Research-Solid Earth*, *104*(B4), 7419–7441.

Freymueller, J. T., S. C. Cohen, and H. J. Fletcher (2000), Spatial variations in present-day deformation, kenai peninsula, alaska, and their implications, *Journal of Geophysical Research-Solid Earth*, *105*(B4), 8079–8101.

Fukuda, J., K. M. Johnson, K. M. Larson, and S. Miyazaki (2009), Fault friction parameters inferred from the early stages of afterslip following the 2003 tokachi-oki earthquake, *Journal of Geophysical Research-Solid Earth*, *114*, B04,412.

Funning, G. J., R. Buergmann, A. Ferretti, and F. Novali (2007), Creep on the rodgers creek fault, northern san francisco bay area from a 10 year ps-insar dataset, *Geophysical Research Letters*, *34*(19), L19,306.

Galehouse, J. S., and J. J. Lienkaemper (2003), Inferences drawn from two decades of alinement array measurements of creep on faults in the san francisco bay region, *Bulletin of the Seismological Society of America*, *93*(6), 2415–2433.

Gaudemer, Y., P. Tapponier, B. Meyer, G. Peltzer, S. M. Guo, Z. T. Chen, D. H. G., and I. Cifuentes (1995), Partitioning of crustal slip between linked, active faults in the eastern qilian shan, and evidence for a major seismic gap, the tianzhu gap, on the western haiyuan fault, gansu (china), *Geophysical Journal International*, *120*(3), 599–645.

Gifkins, R. (1976), Grain-boundary sliding and its accommodation during creep and superplasticity, *Metallurgical Transactions A*, *7*(8), 1225–1232.

Goldsby, D. L., and T. E. Tullis (2002), Low frictional strength of quartz rocks at subseismic slip rates, *Geophysical Research Letters*, *29*(17), 1844.

Goldsby, D. L., and T. E. Tullis (2011), Flash heating leads to low frictional strength of crustal rocks at earthquake slip rates, *Science*, *334*(6053), 216–218.

Gratier, J.-P. (2011), Fault permeability and strength evolution related to fracturing and healing episodic processes (years to millennia): The role of pressure solution., *Oil & Gas Science and Technology*, *66*(3), 491 – 506.

Gratier, J. P., R. Guiguet, F. Renard, L. Jenatton, and D. Bernard (2009), A pressure solution creep law for quartz from indentation experiments, *Journal of Geophysical Research-Solid Earth*, *114*, B03,403.

Gratier, J. P., J. Richard, F. Renard, S. Mittempergher, M. L. Doan, G. Di Toro, J. Hadizadeh, and A. M. Boullier (2011), Aseismic sliding of active faults by pressure solution creep: Evidence from the san andreas fault observatory at depth, *Geology*, *39*(12), 1131–1134.

Gratier, J. P., D. K. Dysthe, and F. Renard (2013), The role of pressure solution creep in the ductility of the earth's upper crust, *Advances In Geophysics, Vol 54*, *54*, 47–179.

Graymer, R. W., D. A. Ponce, R. C. Jachens, R. W. Simpson, G. A. Phelps, and C. M. Wentworth (2005), Three-dimensional geologic map of the hayward fault, northern california: Correlation of rock units with variations in seismicity, creep rate, and fault dip, *Geology*, *33*(6), 521–524.

Hadizadeh, J., S. Mittempergher, J. P. Gratier, F. Renard, G. Di Toro, J. Richard, and H. A. Babaie (2012), A microstructural study of fault rocks from the safod: Implications for the deformation mechanisms and strength of the creeping segment of the san andreas fault, *Journal of Structural Geology*, *42*, 246–260.

Hanks, T. C., and H. Kanamori (1979), Moment magnitude scale, *Journal of Geophysical Research*, *84*(NB5), 2348–2350.

Harris, R. A., and P. Segall (1987), Detection of a locked zone at depth on the parkfield, california, segment of the san andreas fault, *Journal of Geophysical Research-Solid Earth and Planets*, *92*(B8), 7945–7962.

Hashimoto, C., A. Noda, T. Sagiya, and M. Matsu'ura (2009), Interplate seismogenic zones along the kuril-japan trench inferred from gps data inversion, *Nature Geoscienceence*, *2*(2), 141–144.

Heaton, T. H. (1990), Evidence for and implications of self-healing pulses of slip in earthquake rupture, *Physics of the Earth and Planetary Interiors*, *64*(1), 1–20.

Heki, K., S. Miyazaki, and H. Tsuji (1997), Silent fault slip following an interplate thrust earthquake at the japan trench, *Nature*, *386*(6625), 595–598.

Hetland, E., and M. Simons (2010), Post-seismic and interseismic fault creep ii: transient creep and interseismic stress shadows on megathrusts, *Geophysical Journal International*, *181*(1), 99–112.

Hetland, E. A., and B. H. Hager (2006), Interseismic strain accumulation: Spin-up, cycle invariance, and irregular rupture sequences, *Geochemistry Geophysics Geosystems*, *7*, 28.

Hillers, G., Y. Ben-Zion, and P. M. Mai (2006), Seismicity on a fault controlled by rate-and-state dependent friction with spatial variations of the critical slip distance, *Journal of Geophysical Research-Solid Earth*, *111*(B1), B01,403.

Hirose, T., and T. Shimamoto (2005), Growth of molten zone as a mechanism of slip weakening of simulated faults in gabbro during frictional melting, *Journal of Geophysical Research-Solid Earth*, *110*(B5), B05,202.

Ho, C. S. (1969), Geological significance of k-ar ages of the chimei igneous complex of eastern taiwan, *Bulletin of the Geological Survey of Taiwan*, *20*, 63–74.

Holdsworth, R. E., E. W. E. van Diggelen, C. J. Spiers, J. H. P. de Bresser, R. J. Walker, and L. Bowen (2011), Fault rocks from the safod core samples: Implications for weakening at shallow depths along the san andreas fault, california, *Journal of Structural Geology*, *33*(2), 132–144.

Hooper, A., P. Segall, and H. Zebker (2007), Persistent scatterer interferometric synthetic aperture radar for crustal deformation analysis, with application to volcan alcedo, galapagos, *Journal of Geophysical Research-Solid Earth*, *112*(B7).

Hori, T., N. Kato, K. Hirahara, T. Baba, and Y. Kaneda (2004), A numerical simulation of earthquake cycles along the nankai trough in southwest japan: lateral variation in fictional property due to the slab geometry controls the nucleation position, *Earth and Planetary Science Letters*, *228*(3-4), 215–226.

Horng, C. S., and K. S. Shea (1997), Magnetobiostratigraphy of the mawu-chi section, southern coastal range, eastern taiwan, *Journal of the Geological Society of China*, *40*, 339–362.

Hsu, L., and R. Burgmann (2006), Surface creep along the longitudinal valley fault, taiwan from insar measurements, *Geophysical Research Letters*, *33*(6), 4 pp.–4 pp.

Hsu, T. (1956), Geology of the coastal range, eastern taiwan, *Bulletin of the Geological Survey of Taiwan*, *25*, 39–63.

Hsu, Y. J., M. Simons, S. B. Yu, L. C. Kuo, and H. Y. Chen (2003), A two-dimensional dislocation model for interseismic deformation of the taiwan mountain belt, *Earth and Planetary Science Letters*, *211*(3-4), 287–294.

Hsu, Y. J., M. Simons, J. P. Avouac, J. Galetzka, K. Sieh, M. Chlieh, D. Natawidjaja, L. Prawirodirdjo, and Y. Bock (2006), Frictional afterslip following the 2005 nias-simeulue earthquake, sumatra, *Science*, *312*(5782), 1921–1926.

Hsu, Y. J., J. P. Avouac, S. B. Yu, C. H. Chang, Y. M. Wu, and J. Woessner (2009a), Spatio-temporal slip, and stress level on the faults within the western foothills of taiwan: Implications for fault frictional properties, *Pure and Applied Geophysics*, *166*(10-11), 1853–1884.

Hsu, Y. J., S. B. Yu, and H. Y. Chen (2009b), Coseismic and postseismic deformation associated with the 2003 chengkung, taiwan, earthquake, *Geophysical Journal International*, *176*(2), 420–430.

Hu, J. C., L. W. Cheng, H. Y. Chen, Y. M. Wu, J. C. Lee, Y. G. Chen, K. C. Lin, R. J. Rau, K. C. Hao, H. H. Chen, S. B. Yu, and J. Angelier (2007), Coseismic deformation revealed by inversion of strong motion and gps data: the 2003 chengkung earthquake in eastern taiwan, *Geophysical Journal International*, *169*(2), 667–674.

Huang, B. S., W. G. Huang, Y. L. Huang, L. C. Kuo, K. C. Chen, and J. Angelier (2009), Complex fault rupture during the 2003 chengkung, taiwan earthquake sequence from dense seismic array and gps observations, *Tectonophysics*, *466*(3-4), 184–204.

Huang, C. Y., and Y. Yin (1990), Bathymetric ridges and troughs in the active arc-continent collision region off southeastern taiwan, *Proceeding of the Geological Society of China*, *33*, 351–372.

Huang, C. Y., P. B. Yuan, and L. S. Teng (1988), Sedimentology and paleontology of the kangkou. limestone, northern coastal range, eastern taiwan, *Acta Geologica Taiwanica*, *26*, 133–160.

Huang, C. Y., C. T. Shyu, S. B. Lin, T. Q. Lee, and D. D. Sheu (1992), Marine geology in the arc continent collision zone off southeastern taiwan - implications for late neogene evolution of the coastal range, *Marine Geology*, *107*(3), 183–212.

Huang, C. Y., P. B. Yuan, S. R. Song, C. W. Lin, C. S. Wang, M. T. Chen, C. T. Shyu, and B. Karp (1995), Tectonics of short-lived intraarc basins in the arc-continent collision terrane of the coastal range, eastern taiwan, *Tectonics*, *14*(1), 19–38.

Huang, C. Y., W. Y. Wu, C. P. Chang, S. Tsao, P. B. Yuan, C. W. Lin, and K. Y. Xia (1997), Tectonic evolution of accretionary prism in the arc-continent collision terrane of taiwan, *Tectonophysics*, *281*(1-2), 31–51.

Huang, C. Y., P. B. Yuan, and S. J. Tsao (2006a), Temporal and spatial records of active arc-continent collision in taiwan: A synthesis, *Geological Society of America bulletin*, *118*(3-4), 274–288.

Huang, C. Y., C. W. Chien, B. C. Yao, and C. P. Chang (2008), The lichi mélange: A collision melange formation along early arcward backthrusts during forearc basin closure, taiwan arc-continent collision, in *Formation and Applications of the Sedimentary Record in Arc Collision Zones*, *Geological Society of America Special Papers*, vol. 436, edited by A. E. Draut, P. D. Clift, and D. W. Scholl, pp. 127–154, Geological Soc Amer Inc, Boulder.

Huang, M. H., J. C. Hu, C. S. Hsieh, K. E. Ching, R. J. Rau, E. Pathier, B. Fruneau, and B. Deffontaines (2006b), A growing structure near the deformation front in sw taiwan as deduced from sar interferometry and geodetic observation, *Geophysical Research Letters*, *33*(12).

Huang, T. C., C. C. Chen, and W. R. Chi (1979), Calcareous nannofossils from the red shale of the ophiolite-mlange complex, eastern taiwan, *Memoir of the Geological Society of China*, *3*, 131–138.

Huang, T. Y. (1969), Some planktonic foraminifera from a borehole at shihshan, near taitung, taiwan, *Proceeding of the Geological Society of China*, *12*, 103–119.

Huang, W. J., K. M. Johnson, J. Fukuda, and S. B. Yu (2010), Insights into active tectonics of eastern taiwan from analyses of geodetic and geologic data, *Journal of Geophysical Research-Solid Earth and Planets*, *115*.

Hyndman, R. D., M. Yamano, and D. A. Oleskevich (1997), The seismogenic zone of subduction thrust faults, *Island Arc*, *6*(3), 244–260.

Igarashi, T., T. Matsuzawa, and A. Hasegawa (2003), Repeating earthquakes and interplate aseismic slip in the northeastern japan subduction zone, *Journal of Geophysical Research-Solid Earth*, *108*(B5), 9.

Ikari, M. J., D. M. Saffer, and C. Marone (2009), Frictional and hydrologic properties of clay-rich fault gouge, *Journal of Geophysical Research-Solid Earth*, *114*, B05,409.

Ikari, M. J., C. Marone, and D. M. Saffer (2011a), On the relation between fault strength and frictional stability, *Geology*, *39*(1), 83–86.

Ikari, M. J., A. R. Niemeijer, and C. Marone (2011b), The role of fault zone fabric and lithification state on frictional strength, constitutive behavior, and deformation microstructure, *Journal of Geophysical Research-Solid Earth*, *116*, B08,404.

Jahn, B. M. (1986), Midocean ridge or marginal basin origin of the east taiwan ophiolite - chemical and isotopic evidence, *Contributions to Mineralogy and Petrology*, *92*(2), 194–206.

Janssen, C., W. Kanitpanyacharoen, H. R. Wenk, R. Wirth, L. Morales, E. Rybacki, M. Kienast, and G. Dresen (2012), Clay fabrics in safod core samples, *Journal of Structural Geology*, *43*, 118–127.

Jolivet, R., C. Lasserre, M. P. Doin, S. Guillaso, G. Peltzer, R. Dailu, J. Sun, Z. K. Shen, and X. Xu (2012), Shallow creep on the haiyuan fault (gansu, china) revealed by sar interferometry, *Journal of Geophysical Research-Solid Earth*, *117*, B06,401.

Juan, V., H. Lo, and C. C. Chen (1980), Genetic relationships and emplacement of the exotic basic rocks enclosed in the lichi mélange, east coastal range, taiwan, *Proceeding of the Geological Society of China*, *23*, 56–68.

Juang, W. S., and H. Bellon (1984), The potassium-argon dating of andesites from taiwan, *Proceeding of the Geological Society of China*, *27*, 86–100.

Kanamori, H., and E. Hauksson (1992), A slow earthquake in the santa-maria basin, california, *Bulletin of the Seismological Society of America*, *82*(5), 2087–2096.

Kaneko, Y., J.-P. Avouac, and N. Lapusta (2010), Towards inferring earthquake patterns from geodetic observations of interseismic coupling, *Nature Geoscience*, *advance online publication*.

Kaneko, Y., Y. Fialko, D. T. Sandwell, X. Tong, and M. Furuya (2013), Interseismic deformation and creep along the central section of the north anatolian fault (turkey): Insar observations and implications for rate-and-state friction properties, *Journal of Geophysical Research-Solid Earth*, *in press*.

Kanu, C., and K. Johnson (2011), Arrest and recovery of frictional creep on the southern hayward fault triggered by the 1989 loma prieta, california, earthquake and implications for future earthquakes, *Journal of Geophysical Research*, *116*(B4), B04,403.

Karabacak, V., E. Altunel, and Z. Cakir (2011), Monitoring aseismic surface creep along the north anatolian fault (turkey) using ground-based lidar, *Earth and Planetary Science Letters*, *304*(1-2), 64–70.

Kato, N. (2004), Interaction of slip on asperities: Numerical simulation of seismic cycles on a two-dimensional planar fault with nonuniform frictional property, *Journal of Geophysical Research-Solid Earth*, *109*(B12), B12,306.

Kawasaki, I., Y. Asai, Y. Tamura, T. Sagiya, N. Mikami, Y. Okada, M. Sakata, and M. Kasahara (1995), The 1992 sanriku-oki, japan, ultra-slow earthquake, *Journal of Physics of the Earth*, *43*(2), 105–116.

Kerrich, R., T. La Tour, and R. Barnett (1981), Mineral reactions participating in intragranular fracture propagation: implications for stress corrosion cracking, *Journal of Structural Geology*, *3*(1), 77–87.

Konstantinidis, D. A., and H. J. Herrmann (1998), Morphological phenomena during superplastic deformation, *Physica*, *256*, 499–513.

Kositsky, A. P., and J. P. Avouac (2010), Inverting geodetic time series with a principal component analysis-based inversion method, *Journal of Geophysical Research-Solid Earth*, *115*.

Kuo, S.-T. (2013), Anatomy of folds in the damage zone of the chimei fault, eastern taiwan, in *EGU General Assembly*.

Kuochen, H., Y. M. Wu, Y. G. Chen, and R. Y. Chen (2007), 2003 mw6.8 chengkung earthquake and its related seismogenic structures, *Journal of Asian Earth Sciences*, *31*(3), 332–339.

Lachenbruch, A. H. (1980), Frictional heating, fluid pressure, and the resistance to fault motion, *Journal of Geophysical Research*, *85*(NB11), 6097–6112.

Langbein, J., and Y. Bock (2004), High-rate real-time gps network at parkfield: Utility for detecting fault slip and seismic displacements, *Geophysical Research Letters*, *31*(15), L15S20.

Lapusta, N., and Y. Liu (2009), Three-dimensional boundary integral modeling of spontaneous earthquake sequences and aseismic slip, *Journal of Geophysical Research-Solid Earth*, *114*, B09,303.

Lapusta, N., J. R. Rice, Y. Ben-Zion, and G. T. Zheng (2000), Elastodynamic analysis for slow tectonic loading with spontaneous rupture episodes on faults with rate-and-state dependent friction, *Journal of Geophysical Research-Solid Earth*, *105*(B10), 23,765–23,789.

Lapusta, N., H. Noda, and J. Rice (2013), Long-term behavior of quasi-statically strong but coseismically weak faults: low-stress/low-heat operation, typical stress drops, and importance of earthquake nucleation, *to be submitted to Journal of Geophysical Research*.

Lee, J. C., and J. Angelier (1993.), Location of active deformation and geodetic data analyses: an example of the longitudinal valley fault, taiwan, *Bulletin de la Société géologique de France*, *164*, 533–570.

Lee, J. C., J. Angelier, H. T. Chu, S. B. Yu, and J. C. Hu (1998), Plate-boundary strain partitioning along the sinistral collision suture of the philippine and eurasian plates: Analysis of geodetic data and geological observation in southeastern taiwan, *Tectonics*, *17*(6), 159–181.

Lee, J.-C., J. Fu-Shu, C. Hao-Tsu, J. Angelier, and H. Jyr-Ching (2000), A rod-type creepmeter for measurement of displacement in active fault zone, *Earth, Planets and Space*, *52*(5), 321–328.

Lee, J. C., J. Angelier, H. T. Chu, J. C. Hu, and F. S. Jeng (2001), Continuous monitoring of an active fault in a plate suture zone: a creepmeter study of the chihshang fault, eastern taiwan, *Tectonophysics*, *333*(1-2), 219–240.

Lee, J. C., J. Angelier, H. T. Chu, J. C. Hu, F. S. Jeng, and R. J. Rau (2003), Active fault creep variations at chihshang, taiwan, revealed by creep meter monitoring, 1998-2001, *Journal of Geophysical Research-Solid Earth*, *108*(B11), 21.

Lee, J. C., J. Angelier, H. T. Chu, J. C. Hu, and F. S. Jeng (2005), Monitoring active fault creep as a tool in seismic hazard mitigation. insights from creepmeter study at chihshang, taiwan, *Comptes Rendus Geoscience*, *337*(13), 1200–1207.

Lee, J. C., H. T. Chu, J. Angelier, J. C. Hu, H. Y. Chen, and S. B. Yu (2006), Quantitative analysis of surface coseismic faulting and postseismic creep accompanying the 2003, m-w=6.5, chengkung earthquake in eastern taiwan, *Journal of Geophysical Research-Solid Earth*, *111*(B2), 21.

Lee, T. Q., C. Kissel, E. Barrier, C. Laj, and W. R. Chi (1991), Paleomagnetic evidence for a diachronic clockwise rotation of the coastal range, eastern taiwan, *Earth and Planetary Science Letters*, *104*(2-4), 245–257.

Lee, Y. H., G. T. Chen, R. J. Rau, and K. E. Ching (2008), Coseismic displacement and tectonic implication of 1951 longitudinal valley earthquake sequence, eastern taiwan, *Journal of Geophysical Research-Solid Earth*, *113*(B4), 13.

Lienkaemper, J. J., and W. H. Prescott (1989), Historic surface slip along the san-andreas fault near parkfield, california, *Journal of Geophysical Research-Solid Earth and Planets*, *94*(B12), 17,647–17,670.

Lienkaemper, J. J., G. Borchardt, and M. Lisowski (1991), Historic creep rate and potential for seismic slip along the hayward fault, california, *Journal of Geophysical Research-Solid Earth*, *96*(B11), 18,261–18,283.

Lim, S. C., and M. F. Ashby (1987), Wear mechanism maps, *Acta Metallurgica*, *35*, 1–24.

Lim, S. C., M. F. Ashby, and J. F. Brunton (1989), The effect of sliding conditions on the dry friction of metals, *Acta Metallurgica*, *37*, 767–772.

Lin, S. B., and G. T. Chen (1986), Clay minerals from the lichi mélange and its adjacent formations in the coastal range, eastern taiwan, *Acta Geologica Taiwanica*, *24*, 319–356.

Lin, Y.-n. N., A. P. Kositsky, and J.-P. Avouac (2010), Pcaim joint inversion of insar and ground-based geodetic time series: Application to monitoring magmatic inflation beneath the long valley caldera, *Geophysical Research Letters*, *37*(23), L23,301.

Linde, A. T., M. T. Gladwin, M. J. S. Johnston, R. L. Gwyther, and R. G. Bilham (1996), A slow earthquake sequence on the san andreas fault, *Nature*, *383*(6595), 65–68.

Lisowski, M., and W. H. Prescott (1981), Short-range distance measurements along the san-andreas fault system in central california, 1975 to 1979, *Bulletin of the Seismological Society of America*, *71*(5), 1607–1624.

Liu, T. K., Y. G. Chen, W. S. Chen, and S. H. Jiang (2000), Rates of cooling and denudation of the early penglai orogeny, taiwan, as assessed by fission-track constraints, *Tectonophysics*, *320*(1), 69–82.

Liu, Y., and N. Lapusta (2008), Transition of mode ii cracks from sub-rayleigh to intersonic speeds in the presence of favorable heterogeneity, *Journal of the Mechanics and Physics of Solids*, *56*(1), 25–50.

Liu, Y. J., and J. R. Rice (2005), Aseismic slip transients emerge spontaneously in three-dimensional rate-and-state modeling of subduction earthquake sequences, *Journal of Geophysical Research-Solid Earth*, *110*(B8).

Lo, C. H., T. C. Onstott, C. H. Chen, and T. Lee (1994), An assessment of ar-40/ar-39 dating for the whole-rock volcanic samples from the luzon arc near taiwan, *Chemical Geology*, *114*(1-2), 157–178.

Lockner, D. A., C. Morrow, D. Moore, and S. Hickman (2011), Low strength of deep san andreas fault gouge from safod core, *Nature*, *472*(7341), 82–U107.

Lohman, R. B. (2004), The inversion of geodetic data for earthquake parameters, Ph.D. thesis, California Institute of Technology.

Louderback (1942), Faults and earthquakes, *Bulletin of the Seismological Society of America*, *32*(4), 305–330.

Louie, J. N., C. R. Allen, D. C. Johnson, P. C. Haase, and S. N. Cohn (1985), Fault slip in southern-california, *Bulletin of the Seismological Society of America*, *75*(3), 811–833.

Loveless, J. P., and B. J. Meade (2011), Spatial correlation of interseismic coupling and coseismic rupture extent of the 2011 m-w=9.0 tohoku-oki earthquake, *Geophysical Research Letters*, *38*, L17,306.

Lyons, S., and D. Sandwell (2003), Fault creep along the southern san andreas from interferometric synthetic aperture radar, permanent scatterers, and stacking, *Journal of Geophysical Research-Solid Earth*, *108*(B1), 2047.

Malavieille, J., S. E. Lallemand, S. Dominguez, A. Deschamps, C.-Y. Lu, C.-S. Liu, P. Schnuerle, J. Angelier, J. Y. Collot, B. Deffontaines, M. Fournier, S. K. Hsu, J. P. Le Formal, S. Y. Liu, J. C. Sibuet, N. Thareau, and F. Wang (2002), Arc-continent collision in taiwan: New marine observations and tectonic evolution, *Special Paper 358: Geology and Geophysics of an Arc-continent Collision, Taiwan*, *358*, 187–211.

Marone, C. J., C. H. Scholz, and R. Bilham (1991), On the mechanics of earthquake afterslip, *Journal of Geophysical Research-Solid Earth and Planets*, *96*(B5), 8441–8452.

Mase, C. W., and L. Smith (1987), The role of pore fluids in tectonic processes, *Reviews of Geophysics*, *25*(6), 1348–1358.

McClusky, S., S. Balassanian, A. Barka, C. Demir, S. Ergintav, I. Georgiev, O. Gurkan, M. Hamburger, K. Hurst, H. Kahle, K. Kastens, G. Kekelidze, R. King, V. Kotzev, O. Lenk, S. Mahmoud, A. Mishin, M. Nadariya, A. Ouzounis, D. Paradissis, Y. Peter, M. Prilepin, R. Reilinger, I. Sanli, H. Seeger, A. Tealeb, M. N. Toksoz, and G. Veis (2000), Global positioning system constraints on plate kinematics and dynamics in the eastern mediterranean and caucasus, *Journal of Geophysical Research-Solid Earth*, *105*(B3), 5695–5719.

Miyazaki, S., J. J. McGuire, and P. Segall (2011), Seismic and aseismic fault slip before and during the 2011 off the pacific coast of tohoku earthquake, *Earth Planets and Space*, *63*(7), 637–642.

Molinari, A., Y. Estrin, and S. Mercier (1999), Dependence of the coefficient of friction on the sliding conditions in the high velocity range, *Journal of Tribology-Transactions of the Asme*, *121*(1), 35–41.

Moore, D. E., and M. J. Rymer (2007), Talc-bearing serpentinite and the creeping section of the san andreas fault, *Nature*, *448*(7155), 795–797.

Moreno, M., M. Rosenau, and O. Oncken (2010), 2010 maule earthquake slip correlates with pre-seismic locking of andean subduction zone, *Nature*, *467*(7312), 198–U84.

Moreno, M. S., J. Klotz, D. Melnick, H. Echtler, and K. Bataille (2008), Active faulting and heterogeneous deformation across a megathrust segment boundary from gps data, south central chile (36-39 degrees s), *Geochemistry Geophysics Geosystems*, *9*, Q12,024.

Morrow, C., J. Solum, S. Tembe, D. Lockner, and T. . F. Wong (2007), Using drill cutting separates to estimate the strength of narrow shear zones at safod, *Geophysical Research Letters*, *34*(11), L11,301.

Mozziconacci, L., B. Delouis, J. Angelier, J. C. Hu, and B. S. Huang (2009), Slip distribution on a thrust fault at a plate boundary: the 2003 chengkung earthquake, taiwan, *Geophysical Journal International*, *177*(2), 609–623.

Mu, C.-H., J. Angelier, J.-C. Lee, H.-T. Chu, and J.-J. Dong (2011), Structure and holocene evolution of an active creeping thrust fault: The chihshang fault at chinyuan (taiwan), *Journal of Structural Geology*, *33*(4), 743–755.

Murray, J. R., P. Segall, P. Cervelli, W. Prescott, and J. Svarc (2001), Inversion of gps data for spatially variable slip-rate on the san andreas fault near parkfield, ca, *Geophysical Research Letters*, *28*(2), 359–362.

Nadeau, R. M., and T. V. McEvilly (1999), Fault slip rates at depth from recurrence intervals of repeating microearthquakes, *Science*, *285*(5428), 718–721.

Nicolas, A., and J. P. Poirier (1976), *Crystalline plasticity and solid state flow in metamorphic rocks*, 444 pp., Wiley.

Niemeijer, A., and C.-J. Spiers (2005), *High-strain zones: Structure and physical properties*, vol. 245, chap. Influence of phyllosilicates on fault strength in the brittle-ductile transition: Insight from rock analogue experiments, pp. 303–327, Geological Society of London Special Publication.

Niemeijer, A., C. Marone, and D. Elsworth (2010a), Fabric induced weakness of tectonic faults, *Geophysical Research Letters*, *37*, L03,304.

Niemeijer, A., C. Marone, and D. Elsworth (2010b), Frictional strength and strain weakening in simulated fault gouge: Competition between geometrical weakening and chemical strengthening, *Journal of Geophysical Research-Solid Earth*, *115*, B10,207.

Noda, H., and N. Lapusta (2010), Three-dimensional earthquake sequence simulations with evolving temperature and pore pressure due to shear heating: Effect of heterogeneous hydraulic diffusivity, *Journal of Geophysical Research*, *115*(B12), B12,314.

Noda, H., and N. Lapusta (2013), Stable creeping fault segments can become destructive as a result of dynamic weakening, *Nature*, *493*, 518–521.

Noda, H., E. M. Dunham, and J. R. Rice (2009), Earthquake ruptures with thermal weakening and the operation of major faults at low overall stress levels, *Journal of Geophysical Research-Solid Earth*, *114*, B07,302.

Okada, Y. (1985), Surface deformation to shear and tensile faults in a half space, *Bulletin of the Seismological Society of America*, *75*(4), 1135–1154.

Okada, Y. (1992), Internal deformation due to shear and tensile faults in a half-space, *Bulletin Of The Seismological Society Of America*, *82*(2), 1018–1040.

Page, B. M., and J. Suppe (1981), The pliocene lichi mélange of taiwan; its plate-tectonic and olistostromal origin, *American Journal of Science*, *281*(3), 193–227.

Peacock, S. M. (2009), Thermal and metamorphic environment of subduction zone episodic tremor and slip, *Journal of Geophysical Research-Solid Earth*, *114*, B00A07.

Perfettini, H., and J.-P. Ampuero (2008), Dynamics of a velocity-strengthening fault region: Implications for slow earthquakes and postseismic slip, *Journal of Geophysical Research-Solid Earth*, *113*(B9), B09,411.

Perfettini, H., and J. . P. Avouac (2007), Modeling afterslip and aftershocks following the 1992 landers earthquake, *Journal of Geophysical Research-Solid Earth*, *112*(B7), B07,409.

Perfettini, H., and J. R. Avouac (2004), Stress transfer and strain rate variations during the seismic cycle, *Journal of Geophysical Research*, *109*(B6), 8 pp.–8 pp.

Perfettini, H., J. P. Avouac, H. Tavera, A. Kositsky, J. M. Nocquet, F. Bondoux, M. Chlieh, A. Sladen, L. Audin, D. L. Farber, and P. Soler (2010), Seismic and aseismic slip on the central peru megathrust, *Nature*, *465*(7294), 78–81.

Perrin, G., J. R. Rice, and G. Zheng (1995), Self-healing slip pulse on a frictional surface, *Journal of the Mechanics and Physics of Solids*, *43*(9), 1461–1495.

Peyret, M., S. Dominguez, R. Cattin, J. Champenois, M. Leroy, and A. Zajac (2011), Present-day interseismic surface deformation along the longitudinal valley, eastern taiwan, from a ps-insar analysis of the ers satellite archives, *Journal of Geophysical Research*, *116*(B3), B03,402.

Poirier, J. P. (1985), *Creep of crystals.*, 260 pp., Cambridge University Press.

Prescott, W. H., M. Lisowski, and J. C. Savage (1981), Geodetic measurement of crustal deformation on the san-andreas, hayward, and calaveras faults near san-francisco, california, *Journal of Geophysical Research*, *86*(NB11), 853–869.

Reed, D. L., N. Lundberg, C. S. Liu, and B. Luo (1992), Structural relations along the margins of the offshore taiwan accretionary wedge: implications for accretion and crustal kinematics, *Acta Geologica Taiwanica*, *30*, 105–122.

Reilinger, R. E., S. Ergintav, R. Burgmann, S. McClusky, O. Lenk, A. Barka, O. Gurkan, L. Hearn, K. L. Feigl, R. Cakmak, B. Aktug, H. Ozener, and M. N. Toksoz (2000), Coseismic and postseismic fault slip for the 17 august 1999, m=7.5, izmit, turkey earthquake, *Science*, *289*(5484), 1519–1524.

Renard, F., P. Ortoleva, and J. P. Gratier (1997), Pressure solution in sandstones: influence of clays and dependence on temperature and stress, *Tectonophysics*, *280*(3-4), 257–266.

Rice, J. R. (1993), Spatiotemporal complexity of slip on a fault, *Journal of Geophysical Research-Solid Earth*, *98*(B6), 9885–9907.

Rice, J. R. (1999), Flash heating at asperity contacts and rate-dependent friction, *Eo*, *80(46)*, Fall Meeting Supplementary, F681.

Rice, J. R. (2006), Heating and weakening of faults during earthquake slip, *Journal of Geophysical Research-Solid Earth*, *111*(B5), B05,311.

Rice, J. R., and Y. Ben-Zion (1996), Slip complexity in earthquake fault models, *Proceedings of the National Academy of Sciences of the United States of America*, *93*(9), 3811–3818.

Rice, J. R., and A. L. Ruina (1983), Stability of steady frictional slipping, *Journal of Applied Mechanics*, *50*(2), 343–349.

Rice, J. R., N. Lapusta, and K. Ranjith (2001), Rate and state dependent friction and the stability of sliding between elastically deformable solids, *Journal of the Mechanics and Physics of Solids*, *49*(9), 1865–1898.

Richards-Dinger, K. B., and P. M. Shearer (2000), Earthquake locations in southern california obtained using source-specific station terms, *Journal of Geophysical Research-Solid Earth*, *105*(B5), 10,939–10,960.

Robin, P.-Y. (1978), Pressure solution at grain-to-grain contacts., *Geochimica et Cosmochimica Acta*, *42*, 1383–1389.

Rogers, T. H., and N. R. D. (1971), Active displacement on calaveras fault zone at hollister, california, *Bulletin of the Seismological Society of America*, *61*(2), 399–&.

Rolandone, F., R. Burgmann, D. C. Agnew, I. A. Johanson, D. C. Templeton, M. A. d'Alessio, S. J. Titus, C. DeMets, and B. Tikoff (2008), Aseismic slip and fault-normal strain along the central creeping section of the san andreas fault, *Geophysical Research Letters*, *35*(14), L14,305.

Rosen, P. A., S. Hensley, G. Peltzer, and S. M. (2004), Updated repeat orbit interferometry package released, *EOS, Transactions, American Geophysical Union*, *85*(5), 47.

Rudnicki, J. W., and C. H. Chen (1988), Stabilization of rapid frictional slip on a weakening fault by dilatant hardening, *Journal of Geophysical Research-Solid Earth and Planets*, *93*(B5), 4745–4757.

Ruina, A. (1983), Slip instability and state variable friction laws, *Journal of Geophysical Research*, *88*(NB12), 359–370.

Rundle, J. B., H. Kanamori, and M. K. C. (1984), An inhomogeneous fault model for gaps, asperities, barriers, and seismicity migration, *Journal of Geophysical Research*, *89*(NB12), 219–231.

Rutter, E. (1976), The kinetics of rock deformation by pressure solution., *Philosophical Transactions of the Royal Society of London*, *283*, 203–219.

Rutter, E., and R. Maddock (1992), On the mechanical properties of synthetic kaolinite/quartz fault gouge, *Terra Nova*, *4*(4), 489–500.

Rutter, E. H. (1983), Pressure solution in nature, theory and experiment., *Journal of the Geological Society of London*, *140*, 725–740.

Rutter, E. H. (1986), On the nomenclature of mode of failure transitions in rocks, *Tectonophysics*, *122*(3-4), 381–387.

Ryder, I., and R. Burgmann (2008), Spatial variations in slip deficit on the central san andreas fault from insar, *Geophysical Journal International*, *175*(3), 837–852.

Saffer, D. M., and C. Marone (2003), Comparison of smectite- and illite-rich gouge frictional properties: application to the updip limit of the seismogenic zone along subduction megathrusts., *Earth and Planetary Sciences Letters.*, *215*, 219–235.

Saffer, D. M., D. A. Lockner, and A. McKiernan (2012), Effects of smectite to illite transformation on the frictional strength and sliding stability of intact marine mudstones, *Geophysical Research Letters*, *39*, L11,304.

Savage, J. C. (1983), A dislocation model of strain accumulation and release at a subduction zone, *Journal of Geophysical Research*, *88*(NB6), 4984–4996.

Savage, J. C. (2007), Postseismic relaxation associated with transient creep rheology, *Journal of Geophysical Research-Solid Earth*, *112*(B5).

Schmidt, D. A., R. Burgmann, R. M. Nadeau, and M. d'Alessio (2005), Distribution of aseismic slip rate on the hayward fault inferred from seismic and geodetic data, *Journal of Geophysical Research-Solid Earth*, *110*(B8), B08,406.

Scholz, C. H. (1998), Earthquakes and friction laws., *Nature*, *391*, 37–42.

Schulz, S. S., G. M. Mavk, R. O. Burford, and W. D. Stuart (1982), Long-term fault creep observations in central california, *Journal of Geophysical Research*, *87*(NB8), 6977–6982.

Segall, P. (2010), *Earthquake and Volcano Deformation*, 464 pp., Princeton University Press.

Shibazaki, B., and M. Matsuura (1992), Spontaneous processes for nucleation, dynamic propagation, and stop of earthquake rupture, *Geophysical Research Letters*, *19*(12), 1189–1192.

Shibazaki, B., and T. Shimamoto (2007), Modelling of short-interval silent slip events in deeper subduction interfaces considering the frictional properties at the unstable-stable transition regime, *Geophysical Journal International*, *171*(1), 191–205.

Shimamoto, T. (1986), Transition between frictional slip and ductile flow for halite shear zones at room-temperature, *Science*, *231*(4739), 711–714.

Shyu, J. B. H., K. Sieh, Y.-G. Chen, and C.-S. Liu (2005), Neotectonic architecture of taiwan and its implications for future large earthquakes, *Journal of Geophysical Research*, *110*.

Shyu, J. B. H., K. Sieh, J. P. Avouac, W. S. Chen, and Y. G. Chen (2006), Millennial slip rate of the longitudinal valley fault from river terraces: Implications for convergence across the active suture of eastern taiwan, *Journal of Geophysical Research-Solid Earth*, *111*(B8), 22.

Shyu, J. B. H., L. H. Chung, Y. G. Chen, J. C. Lee, and K. Sieh (2007), Re-evaluation of the surface ruptures of the november 1951 earthquake series in eastern taiwan, and its neotectonic implications, *Journal of Asian Earth Sciences*, *31*(3), 317–331.

Sibson, R. H. (1973), Interactions between temperature and pore-fluid pressure during earthquake faulting and a mechanism for partial or total stress relief, *Nature-physical Science*, *243*(126), 66–68.

Sieh, K. E. (1986), Slip rate across the san andreas fault and prehistoric earthquakes at indio, california, *EOS, Transactions, American Geophysical Union*, *67*, 1200.

Sieh, K. E., and R. H. Jahns (1984), Holocene activity of the san-andreas fault at wallace-creek, california, *Geological Society of America Bulletin*, *95*(8), 883–896.

Simoes, M., J. P. Avouac, O. Beyssac, B. Goffe, K. A. Farley, and Y. G. Chen (2007a), Mountain building in taiwan: A thermokinematic model, *Journal of Geophysical Research-Solid Earth*, *112*(B11).

Simoes, M., J. P. Avouac, Y. G. Chen, A. K. Singhvi, C. Y. Wang, M. Jaiswal, Y. C. Chan, and S. Bernard (2007b), Kinematic analysis of the pakuashan fault tip fold, west central taiwan: Shortening rate and age of folding inception, *Journal of Geophysical Research-Solid Earth*, *112*(B3).

Sleep, N. H. (1995), Frictional heating and the stability of rate-and-state dependent frictional sliding, *Geophysical Research Letters*, *22*(20), 2785–2788.

Snoke, A. W., J. Tullis, and V. R. Todd (1998), *Fault-Related Rocks*, Princeton University Press.

Solum, J. G., S. H. Hickman, D. A. Lockner, D. E. Moore, B. A. van der Pluijm, A. M. Schleicher, and J. P. Evans (2006), Mineralogical characterization of protolith and fault rocks from the safod main hole, *Geophysical Research Letters*, *33*(21), L21,314.

Steinbrugge, R. M., and E. G. Zacher (1960), Creep on the san andreas fault-fault creep and property damage, *Bulletin of the Seismological Society of America*, *50*, 398–396.

Stunitz, H., and J. Gerald (1993), Deformation of granitoids at low metamorphic grade. ii: Granular flow in albite-rich mylonites, *Tectonophysics*, *221*(34), 299–324.

Suppe, J. (1984), Kinematics of arc-continent collision, flipping of subduction, and back-arc spreading near taiwan, *Geological Society of China Memoir*, *6*, 21–33.

Suppe, J., J. G. Liou, and W. G. Ernst (1981), Paleogeographic origins of the miocene east taiwan ophiolite, *American Journal of Science*, *281*(3), 228–246.

Teng, L. S. (1979), Petrographical study of the neogene sandstones of the coastal range, eastern taiwan (i. northern part), *Acta Geologica Taiwanica*, *20*, 129–155.

Teng, L. S. (1980a), On the origin and tectonic significance of the lichi formation, northern coastal range, eastern taiwan, *Ti-Chih*, *2*, 51–62.

Teng, L. S. (1980b), Lithology and provenance of the fanshuliao formation, northern coastal. range, eastern taiwan, *Proceeding of the Geological Society of China*, *23*, 118–129.

Teng, L. S. (1982), Stratigraphy and sedimentation of the shuilien conglomerate, northern coastal. range, eastern taiwan, *Acta Geologica Taiwanica*, *21*, 201–220.

Teng, L. S. (1990), Geotectonic evolution of late cenozoic arc-continent collision in taiwan, *Tectonophysics*, *183*(1-4), 57–76.

Teng, L. S., and H. Lo (1985), Sedimentary sequences in the island arc settings of the coastal range, eastern taiwan, *Acta Geologica Taiwanica*, *23*, 77–98.

Teng, L. S., and Y. Wang (1981), Island arc system of the coastal range, eastern taiwan, *Proceeding of the Geological Society of China*, *24*, 99–112.

Teng, L. S., W. S. Chen, Y. Wang, S. R. Song, and H. Lo (1988), Toward a comprehensive stratigraphic system of the coastal range, eastern taiwan, *Acta Geologica Taiwanica*, *26*, 19–35.

Thomas, M. Y., J. P. Avouac, J. Champenois, and J. C. Lee (to be submitted), Spatio-temporal evolution of seismic and aseismic slip on the longitudinal valley fault, taiwan, *Journal of Geophysical Research.*

Titus, S. J., C. DeMets, and B. Tikoff (2005), New slip rate estimates for the creeping segment of the san andreas fault, california, *Geology*, *33*(3), 205–208.

Titus, S. J., C. DeMets, and B. Tikoff (2006), Thirty-five-year creep rates for the creeping segment of the san andreas fault and the effects of the 2004 parkfield earthquake: Constraints from alignment arrays, continuous global positioning system, and creepmeters, *Bulletin of the Seismological Society of America*, *96*(4), S250–S268.

Tocher (1960), Creep on the san andreas fault: Creep rate and related measurements at vineyard, california:, *Bulletin of the Seismological Society of America*, *50*, 396–404.

Tong, X., D. T. Sandwell, and B. Smith-Konter (2013), High-resolution interseismic velocity data along the san andreas fault from gps and insar, *Journal of Geophysical Research-Solid Earth*, *118*(1), 369–389.

Tsutsumi, A., and T. Shimamoto (1997), High-velocity frictional properties of gabbro, *Geophysical Research Letters*, *24*(6), 699–702.

Tullis, T. E., and D. L. Doldsby (2003), Flash melting of crustal rocks at almost seismic slip rates, *EOS, Transactions, American Geophysical Union*, *84(46)*, Fall Meet. Suppl., abstract S51B–05.

Twiss, R. J., and E. M. Moores (1992), *Structural Geology*, first edition (april 15, 1992) ed., 532 pp., W. H. Freeman.

Wallace, L. M., J. Beavan, R. McCaffrey, and D. Darby (2004), Subduction zone coupling and tectonic block rotations in the north island, new zealand, *Journal of Geophysical Research-Solid Earth*, *109*(B12), B12,406.

Wang, C. S. (1976), The lichi formation of the coastal range and arc?continent collision in eastern taiwan, *Bulletin of the Geological Survey of Taiwan*, *25*, 73–86.

Wang, Y., and W. Chen (1993), Geological map of eastern coastal range, 1:100,000, *Central Geological Survey, MOEA, Taiwan.*

Weyl, P. K. (1959), Pressure solution and the force of crystallization - a phenomenological theory, *Journal of Geophysical Research*, *64*(11), 2001–2025.

Wiseman, K., P. Banerjee, K. Sieh, R. Buergmann, and D. H. Natawidjaja (2011), Another potential source of destructive earthquakes and tsunami offshore of sumatra, *Geophysical Research Letters*, *38*, L10,311.

Wu, Y. M., and C. F. Wu (2007), Approximate recovery of coseismic deformation from taiwan strong-motion records, *Journal of Seismology*, *11*(2), 159–170.

Wu, Y. M., Y. G. Chen, T. C. Shin, H. Kuochen, C. S. Hou, J. C. Hu, C. H. Chang, C. F. Wu, and T. L. Teng (2006a), Coseismic versus interseismic ground deformations, fault rupture inversion and segmentation revealed by 2003 mw 6.8 chengkung earthquake in eastern taiwan, *Geophysical Research Letters*, *33*, L02,312.

Wu, Y. M., Y. G. Chen, C. H. Chang, L. H. Chung, T. L. Teng, F. T. Wu, and C. F. Wu (2006b), Seismogenic structure in a tectonic suture zone: With new constraints from 2006 mw6.1 taitung earthquake, *Geophysical Research Letters*, *33*(22), L22,305.

Wu, Y.-M., C.-H. Chang, L. Zhao, J. B. H. Shyu, Y.-G. Chen, K. Sieh, and J.-P. Avouac (2007), Seismic tomography of taiwan: Improved constraints from a dense network of strong motion stations, *Journal of Geophysical Research-Solid Earth*, *112*(B8), B08,312.

Wu, Y. M., C. C. Chen, L. Zhao, and C. H. Chang (2008a), Seismicity characteristics before the 2003 chengkung, taiwan, earthquake, *Tectonophysics*, *457*(3-4), 177–182.

Wu, Y. M., C. H. Chang, L. Zhao, T. L. Teng, and M. Nakamura (2008b), A comprehensive relocation of earthquakes in taiwan from 1991 to 2005, *Bulletin of the Seismological Society of America*, *98*(3), 1471–1481.

Xia, K. W., A. J. Rosakis, and H. Kanamori (2004), Laboratory earthquakes: The sub-rayleigh-to-supershear rupture transition, *Science*, *303*(5665), 1859–1861.

Yang, T. F., T. Lee, C. H. Chen, S. N. Cheng, U. Knittel, R. S. Punongbayan, and A. R. Rasdas (1996), A double island arc between taiwan and luzon: Consequence of ridge subduction, *Tectonophysics*, *258*(1-4), 85–101.

Yang, T. Y., T. K. Liu, and C. H. Chen (1988), Thermal event records of the chimei igneous complex: Constraint on the ages of magma activities and the structural implication based on fission track dating, *Acta Geologica Taiwanica*, *26*, 237–246.

Yu, S. B., and L. C. Kuo (2001), Present-day crustal motion along the longitudinal valley fault, eastern taiwan, *Tectonophysics*, *333*(1-2), 199–217.

Yu, S. B., H. Y. Chen, and L. C. Kuo (1997), Velocity field of gps stations in the taiwan area, *Tectonophysics*, *274*(1-3), 41–59.

Zheng, G., and J. R. Rice (1998), Conditions under which velocity-weakening friction allows a self-healing versus a cracklike mode of rupture, *Bulletin of the Seismological Society of America*, *88*(6), 1466–1483.

Ziv, A., and A. Cochard (2006), Quasi-dynamic modeling of seismicity on a fault with depth-variable rate-and-state dependent friction, *Journal of Geophysical Research-Solid Earth*, *111*(B8), B08,310.